Development of a Three-Dimensional iPSC-Derived Cardiac Spheroid Model of Ischemia–Reperfusion Injury: From Classical Tissue Engineering to Closed-Loop Bayesian Optimized Engineering for Genotype-Dependent Drug Response Profiling

Zur Erlangung des akademischen Grades eines

DOKTORS DER NATURWISSENSCHAFTEN

(Dr. rer. nat.)

von der KIT-Fakultät für Chemie und Biowissenschaften

des Karlsruher Instituts für Technologie (KIT)

genehmigte

DISSERTATION

von

M.sc. Eric Pohl aus Bad Säckingen

1. Referent/Referentin: Prof. Dr. Ute Schepers
2. Referent/Referentin: PD. Dr. Beate Köberle
Tag der mündlichen Prüfung: 24.04.2026

Eidesstattliche Versicherung

Eidesstattliche Versicherung gemäß § 13 Absatz 2 Ziffer 3 der Promotionsordnung des Karlsruher Instituts für Technologie für die KIT-Fakultät für Chemie und Biowissenschaften

1. Bei der eingereichten Dissertation zu dem Thema

   „Development of a Three-Dimensional iPSC-Derived Cardiac Spheroid Model of Ischemia–Reperfusion Injury: From Classical Tissue Engineering to Closed-Loop Bayesian Optimized Engineering for Genotype-Dependent Drug Response Profiling“

   handelt es sich um meine eigenständig erbrachte Leistung.
2. Ich habe nur die angegebenen Quellen und Hilfsmittel benutzt und mich keiner unzulässigen Hilfe Dritter bedient. Insbesondere habe ich wörtlich oder sinngemäß aus anderen Werken übernommene Inhalte als solche kenntlich gemacht.
3. Die Arbeit oder Teile davon habe ich bislang nicht an einer Hochschule des In- oder Auslands als Bestandteil einer Prüfungs- oder Qualifikationsleistung vorgelegt.
4. Die Richtigkeit der vorstehenden Erklärungen bestätige ich.
5. Die Bedeutung der eidesstattlichen Versicherung und die strafrechtlichen Folgen einer unrichtigen oder unvollständigen eidesstattlichen Versicherung sind mir bekannt.

Ich versichere an Eides statt, dass ich nach bestem Wissen die reine Wahrheit erklärt und nichts verschwiegen habe.

Karlsruhe, den 11.03.2026 — Eric Pohl

Ort, Datum — Eric Pohl

Diese Arbeit wurde von November 2023 bis März 2026 unter der Leitung von Frau Prof. Dr. Ute Schepers am Institut für Funktionelle Grenzflächen des Karlsruher Institut für Technologie angefertigt.

“All models are wrong, but some are useful”

George E.P. Box

Danksagung

Mein besonderer Dank gilt Prof. Dr. Ute Schepers für die Betreuung dieser Arbeit. Ich danke ihr herzlich für die Möglichkeit, im Rahmen dieser Promotion an einem interdisziplinären und hochrelevanten Forschungsthema zu arbeiten. Ihre fachliche Unterstützung, die zahlreichen wissenschaftlichen Diskussionen sowie ihre konstruktiven Anregungen haben diese Arbeit maßgeblich geprägt. Besonders schätze ich zudem das Vertrauen und die Freiräume, die sie mir während der Promotionszeit gegeben hat.

Ich danke außerdem PD Dr. Beate Köberle für die freundliche Übernahme des Korreferats und ihr Interesse an dieser Arbeit.

Für die finanzielle Förderung dieses Projekts danke ich dem Exzellenzcluster 3D Matter Made To Order (3DMM2O). Darüber hinaus danke ich der HEiKA Graduate School on Functional Materials für die Unterstützung während der Promotionszeit sowie für die Möglichkeit, am MBA Fundamentals Program der HECTOR School of Engineering and Management teilzunehmen.

Ein großer Dank gilt allen Mitgliedern des AK Schepers für die angenehme Arbeitsatmosphäre, die kollegiale Zusammenarbeit und die vielen hilfreichen Diskussionen im wissenschaftlichen Alltag. Der Austausch im Labor sowie die gegenseitige Unterstützung haben wesentlich dazu beigetragen, diese Promotionszeit sowohl wissenschaftlich als auch persönlich bereichernd zu gestalten.

Mein herzlichster Dank gilt schließlich meiner Familie und meiner Freundin für ihre Geduld, ihren Rückhalt und ihre stetige Unterstützung während der gesamten Promotionszeit. Ihr Vertrauen und ihre Ermutigung haben mich auf diesem Weg stets begleitet.

Table of contents

Zusammenfassung

Ischämie-Reperfusionsschäden sind ein wesentlicher Faktor für Herzgewebeschäden nach Wiederherstellung der Durchblutung, doch wirksame kardioprotektive Therapien sind nach wie vor begrenzt. *In-vitro*-Herzmodellen mangelt es häufig an präziser zeitlicher Kontrolle, mechanistischer Tiefe oder Skalierbarkeit für systematische pharmakologische Untersuchungen. Das Ziel dieser Arbeit war es, ein zeitlich kontrolliertes dreidimensionales *In-vitro*-Modell der Ischämie-Reperfusionsschädigung zu entwickeln und es in eine adaptive Closed-Loop-Screening-Plattform für die pharmakologische und genotypabhängige Reaktionsanalyse zu integrieren. Aus humanen iPSCs gewonnene Herzsphäroide wurden einem schnellen Sauerstoffentzug durch Stickstofffluss sowie einer Restriktion metabolischer Substrate unter Verwendung von Tyrode-Lösung unterzogen, um eine Ischämie zu simulieren. Eine kontrollierte Reoxygenierung ermöglichte definierte Reperfusionsübergänge. Funktionelle, metabolische, strukturelle und transkriptionelle Analysen zeigten, dass die kombinierte Schädigung reproduzierbar eine akute Unterdrückung der Kontraktilität, eine intrazelluläre Calciumdysregulation, einen verzögerten metabolischen Abfall, eine sarkomerische Desintegration und eine remodellierungsassoziierte Genexpression induzierte. Eine isolierte Sauerstoff- oder Nährstoffentzug allein reproduzierte nicht den vollständigen Verletzungsphänotyp, was die multifaktorielle Natur der Reperfusionspathologie unterstreicht. Um eine systematische pharmakologische Untersuchung zu ermöglichen, wurde ein Bayesian Closed-Loop-Optimierungsframework implementiert, um maximale physiologische Konzentrationsbereiche zu bestimmen und das Dosis-Wirkungs-Verhalten direkt innerhalb des Sphäroid-Systems zu charakterisieren. Die Plattform zeigte eine adaptive Konzentrationsverfeinerung, eine Konvergenz in Richtung therapeutisch relevantem Konzentrationsbereich und die Fähigkeit, stimulierende und hemmende pharmakodynamische Muster ohne vordefinierte Annahmen aufzulösen. Eine gezielte Modulation des Calciumeinstroms (Verapamil) und des oxidativen Stresses (Ascorbinsäure) führte trotz kontinuierlicher Exposition vor und während der Schädigung nicht zu einer robusten Rettung unter vollständigen Reperfusionsbedingungen. Diese Ergebnisse deuten darauf hin, dass das Fortschreiten der Schädigung auf integrierten und teilweise refraktären Wechselwirkungen zwischen Calciumüberladung, mitochondrialer Destabilisierung und strukturellem Abbau beruht. Schließlich wurden genotypabhängige Arzneimittelreaktionen unter Verwendung von zwei genetisch unterschiedlichen, aus

iPSC gewonnenen Herzlinien bewertet. Eine medikamentenspezifische Divergenz wurde für die Natriumkanalblockade (Lidocain) und die β-adrenerge Stimulation (Adrenalin) beobachtet, während die Reaktionen auf die Hemmung des L-Typ-Kalziumkanals (Verapamil) konserviert waren. Diese Ergebnisse zeigen eine selektive pharmakodynamische Heterogenität und unterstreichen die Fähigkeit der Plattform, biologisch bedeutsame Variabilitäten zwischen den Linien unter standardisierten Bedingungen zu erkennen. Insgesamt schafft diese Arbeit einen integrierten Rahmen, der mechanistische Ischämie-Reperfusionsmodellierung, adaptive pharmakologische Optimierung und genotyp-sensitives Profiling in einem skalierbaren dreidimensionalen Herzsystem kombiniert. Die Ergebnisse unterstreichen die Komplexität von Reperfusionsschäden und weisen auf das Potenzial datengesteuerter Präzisionsansätze in kardialen *In-vitro*-Modellen hin.

Abstract

Ischemia–reperfusion injury is a major determinant of cardiac tissue damage following restoration of blood flow, yet effective cardioprotective therapies remain limited. *In vitro* cardiac models frequently lack precise temporal control, mechanistic depth, or scalability for systematic pharmacological investigation. The aim of this thesis was to develop a temporally controlled three-dimensional *in vitro* model of ischemia–reperfusion injury and to integrate it with an adaptive closed-loop screening platform for pharmacological and genotype-dependent response analysis.

Human iPSC-derived cardiac spheroids were subjected to rapid oxygen deprivation via nitrogen flux and metabolic substrate restriction using Tyrode solution to simulate ischemia. Controlled reoxygenation enabled defined reperfusion transitions. Functional, metabolic, structural, and transcriptional analyses demonstrated that the combined insult reproducibly induced acute suppression of contractility, intracellular calcium dysregulation, delayed metabolic decline, sarcomeric disintegration, and remodelling-associated gene expression. Isolated oxygen or nutrient deprivation alone did not reproduce the full injury phenotype, underscoring the multifactorial nature of reperfusion pathology.

To enable systematic pharmacological interrogation, a Bayesian closed-loop optimization framework was implemented to determine maximal physiological concentration ranges and characterize dose–response behaviour directly within the spheroid system. The platform demonstrated adaptive concentration refinement, convergence toward safety thresholds, and the ability to resolve stimulatory and inhibitory pharmacodynamic patterns without predefined assumptions.

Targeted modulation of calcium influx (verapamil) and oxidative stress (ascorbic acid) did not produce robust rescue under full reperfusion conditions, despite continuous exposure before and during injury. These findings indicate that injury progression arises from integrated and partially refractory interactions among calcium overload, mitochondrial destabilization, and structural degradation.

Finally, genotype-dependent drug responses were assessed using two genetically distinct iPSC-derived cardiac lines. Drug-specific divergence was observed for sodium channel blockade (lidocaine) and β-adrenergic stimulation (epinephrine), whereas responses to L-type calcium channel inhibition (verapamil) were conserved. These results demonstrate selective pharmacodynamic heterogeneity and highlight the

platform's capacity to detect biologically meaningful inter-line variability under standardized conditions.

Collectively, this work establishes an integrated framework combining mechanistic ischemia–reperfusion modelling, adaptive pharmacological optimization, and genotype-sensitive profiling within a scalable three-dimensional cardiac system. The findings emphasize the complexity of reperfusion injury and support the feasibility of data-driven precision approaches in cardiac *in vitro* models.

1. Introduction

1.1. Global Burden of Cardiovascular Disease

Over the last 30 years, rapid advancements in medicine, coupled with improvements in healthcare infrastructure, have led to a significant increase in life expectancy, from around 68 years in 2000 to roughly 74 years by 2026.[1,2] This achievement has largely been driven through a 50 % reduction in child mortality.[3,4] and the continuous development of therapeutic strategies to limit cancer[5] and infectious disease mortality. While these breakthroughs are remarkable achievements of modern medicine, they have also created what is sometimes referred to as a "success paradoxon."

As people live longer and survive many previously fatal diseases, they increasingly face cardiovascular diseases (CVD), which represent the primary cause of death in developed countries.[6,7] This trend is further amplified by the fact that, as therapies for other diseases improve, CVD now accounts for an even larger proportion of mortality.[8,9]

A striking example of this phenomenon is ischemic heart disease, historically the deadliest form of CVD. By 1970, 91 % of CVD associated deaths were caused by Ischemia.[10] Due to advances in medical treatments, such as percutaneous coronary intervention (PCI) and thrombolysis, which allow surgical removal of ischemic plugs, this fatality rate has gradually declined to just over 50 % today.[10] However, the increasing number of ischemia survivors has revealed a new clinical challenge: reperfusion injury. Previously nearly non-existent due to the high fatality of ischemia, reperfusion injury now affects a substantial proportion of survivor, approximately 10% die from the cellular damage caused by reperfusion,[11] while 25–35 % develop heart failure (HF) shortly afterward.[12]

The lack of targeted pharmacological therapies to mitigate the aftermath of ischemia and to limit reperfusion injury remains a major challenge. At the same time, the pharmaceutical industry has largely withdrawn from cardiovascular disease research due to high late-stage clinical trial failure rates,[13] primarily driven by poor translation from animal models to humans.[14] This underscores the urgent need for better models that more accurately recapitulate reperfusion injury and improve drug testing efficiency. In this context, tissue engineering has emerged as a promising approach to develop physiologically relevant *in vitro* systems that better mimic the structural, mechanical, and cellular complexity of native tissues.

1.2. Tissue Engineering

Tissue Engineering generally refers to the restoration, modification or enhancement of human tissue. The term gained significant public attention in 1997 following the "Vacanti mouse", a laboratory mouse with a cartilage resembling a human ear on its back, symbolizing the potential of the discipline.[15,16]

Although the formal nomenclature of tissue engineering is a modern development, its conceptual origins date back to ancient India. Documentations from as early as the 6th century BCE detail sophisticated reconstructive procedures, including skin grafts and nasal remodelling. These records resemble the first attempts to manipulate living tissue.[17]

Tissue engineering has evolved with increasing momentum over the past century. The origins of *in vitro* cell culture date back to 1907, when Ross Granville Harrison established a frog nerve fiber culture using the hanging drop technique. By incorporating extracellular matrix components, he effectively created a three-dimensional microenvironment.[18] While Harrison`s work predated modern terminology his system is built on the fundamental pillars of the tissue engineering triad: employing cells within a scaffold under specific environmental signals to facilitate growth.[19]

Despite the early use of three-dimensional systems, the focus of the field shifted toward two-dimensional (2D) monolayer cultures by the 1940s. This transition was driven by practical advantages, including improved compatibility with microscopy, greater scalability, and more predictable control of nutrient supply and waste removal.[20] However, as the demand for physiologically relevant models increased, interest gradually returned to three-dimensional (3D) cell culture systems.

Modern 3D culture utilizes either matrix-based scaffolds like hydrogels or scaffold-free aggregation to restore cellular dependencies and interactions lost in 2D. A significant advancement in this field is the development of organoids. In contrast to simple aggregates, organoids are derived from stem cells utilizing biological cues to self-organize into micro-scale tissues, successfully replicating key physiological functions.[21,22]

Since its inception tissue engineering has achieved significant milestones with engineered skin and bladders already transplanted into patients. However, the currently largest challenge limiting clinical breakthrough of *in vitro* generated tissues is vascularization. The inability to fabricate complex microvasculature networks *in vitro* limits construct size. The core size limitation is marked by the 200 μm hurdle.

This critical threshold is defined by oxygen diffusion limitations as every cell has to be within 200 µm of a blood vessel to ensure adequate nutrient delivery and metabolic waste removal.[23,24]

Beyond clinical transplantation, tissue engineering serves a second, increasingly important role: The development of advanced disease modelling and drug screening platforms. While animal models remain the current "gold standard" for preclinical testing, they often fail to accurately predict human physiological responses. Hence the increasing demand for iPSC derived disease models, offering better predictability of patient-specific physiological reactions.[25,26]

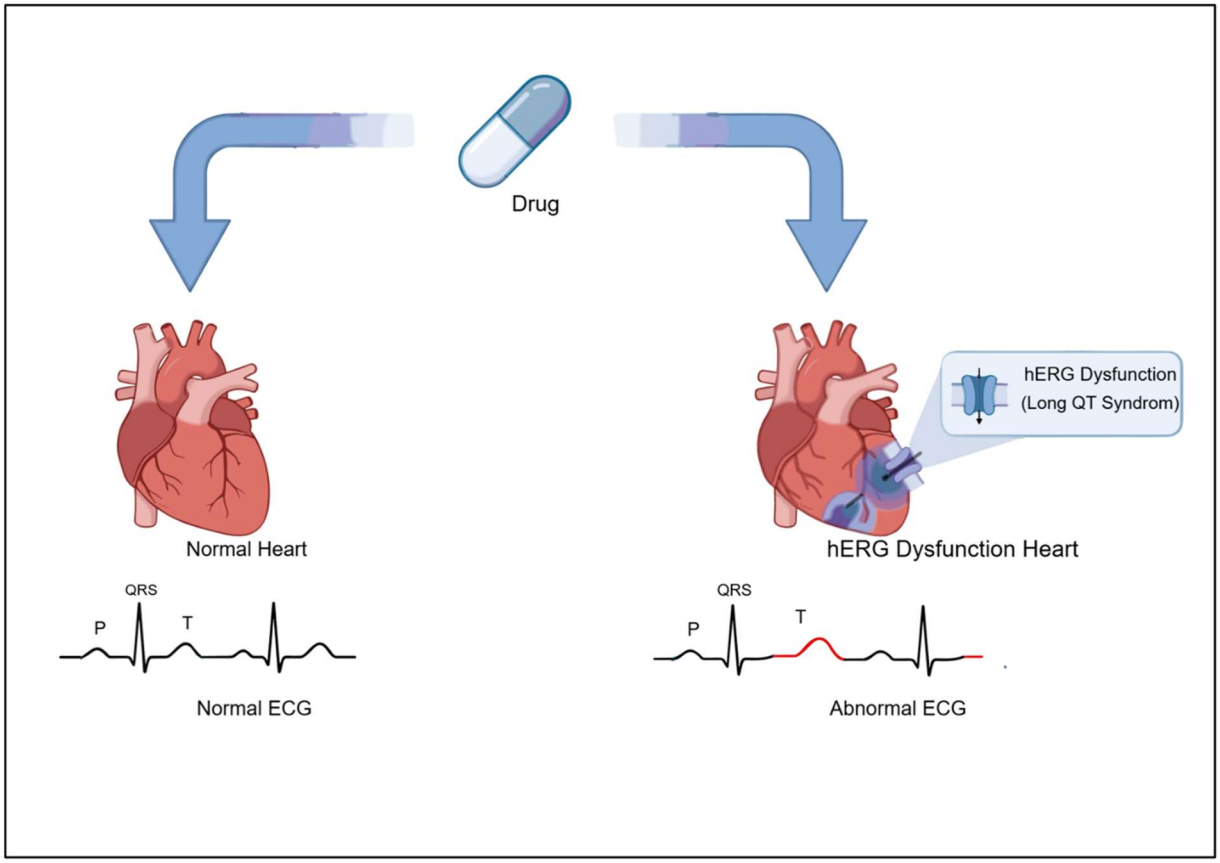

Figure 1: Translational complexity and inter-individual variability in cardiac electrophysiology. A standardized cardiac drug produces divergent clinical outcomes depending on the genotypical background. Dysfunction in the hERG channel can lead to long QT Syndrome, as visible in the ECG. This highlights the need for patient specific drugs. Created with FigureLabs March 2026.

Patient specificity is particularly crucial in cardiac research, given the exceptionally narrow therapeutic window characteristic of many cardiac medications. A dosage representing "gold standard" treatment for one individual may prove fatal for another, potentially triggering life-threatening arrhythmias or strokes.[27]

Prominent examples of the necessity of patient-specific pharmacotherapy include Digoxin and Warfarin. Digoxin is an anti-arithmetic possessing an exceptionally narrow therapeutic window where minor over-dosage can trigger heart failure.[28]

Similarly, the anticoagulant Warfarin is highly sensitive to genetic polymorphism, slight metabolic alterations can result in life-threatening haemorrhages.[29]

Perhaps the most critical target in cardiac drug safety is the human Ether-a-go-go-Related Gene (hERG) potassium channel (Figure 1). The gene of the channel protein is a frequent site of silent mutations, which under normal conditions remain asymptomatic with slightly increased repolarization phases. Given this preconditioning, standard doses of anti-arrythmic drugs can excessively extend the action potential (AP) duration and trigger "Torsades de Pointes", a ventricular tachycardia culminating in sudden cardiac death.[30,31] In order to reconstruct functional and personalized heart tissue, it is essential to understand the physiology and anatomy of the heart, including its tissue morphology.

1.3. The Human Heart

Early civilizations already recognized the heart as the body's central organ of circulation. Egyptian medical writings (~1500 BCE) linked the pulse to the heartbeat, identifying the heart as a pump driving blood through vessels.[32] Greek physicians, particularly Hippocrates (5th century BCE), provided the first anatomical descriptions of the heart's chambers and valves.[33–35] A decisive conceptual leap occurred during the Renaissance when Leonardo da Vinci accurately described the four heart chambers, myocardial fiber structure, coronary circulation, and functional valve dynamics, laying the foundation for modern cardiac anatomy and physiology.[36]

The human heart functions as the biomechanical engine of the circulatory system, operating as a dual-circuit pressure pump. Its primary role is the maintenance of high-pressure systemic perfusion alongside low-pressure pulmonary oxygenation.[37] To achieve this, the four heart chambers are clustered into two functional units. The right side of the heart acts as pulmonary pump, ensuring low-pressure for sufficient oxygenation, while the left side is the systemic pump, the main driving force of the cardiovascular system.[38] The pulmonary and systemic units are separated by an interventricular septum, which ensures strict separation of oxygenated and deoxygenated blood (Figure 2).[39]

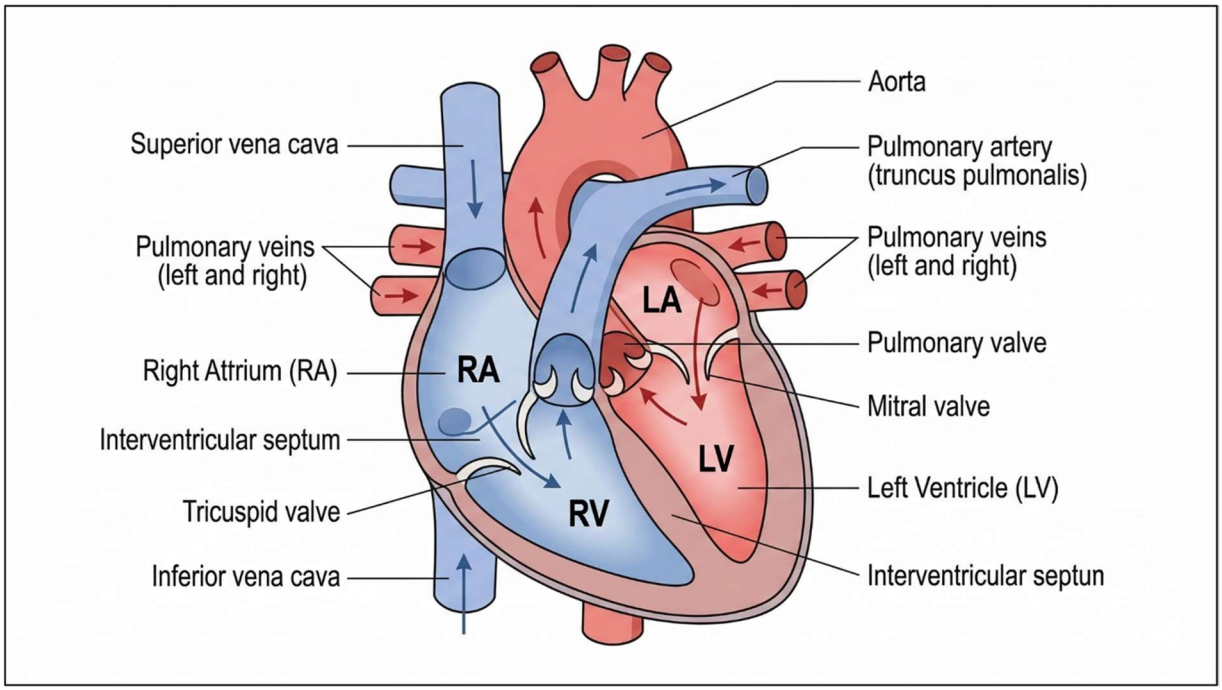

Figure 2: Anatomy of the heart. The heart consists of four chambers. Deoxygenated blood is collected in the right atrium (RA) and passes through the tricuspid valve into the right ventricle (RV). From there, the blood enters the pulmonary circulation via the pulmonary artery, where gas exchange occurs in the lungs. After reoxygenation, blood returns to the left atrium (LA) and flows through the mitral valve into the left ventricle (LV). The left ventricle then pumps oxygenated blood into the systemic circulation through the aorta. Created with FigureLabs March 2026.

Structurally, the heart is separated in atria and ventricles, atria serving as receiving chambers while the ventricles are the pumping chambers (Figure 2). The left atrium (LA) and the right atrium (RA) are thin-walled chambers serving as blood reservoirs, filling the ventricles with blood through diastolic under pressure, while also contributing through the atrial contraction to facilitate optimal ventricular filling.[40] The right ventricle (RV) and the left ventricle (LV) generate the mechanical force required for blood ejection. While the atria possess thin walls, a key characteristic of the ventricles are their thick walls, with the LV exhibiting significantly thicker walls then the RV, caused by elevated afterload during systemic circulation.[38]

The unidirectional blood flow is ensured by two valve systems, the atrioventricular valves prevent the retrograde flow during ventricular systole, while the semilunar valves regulate the outflow into the pulmonary vein and aorta.[41]

Apart from the valves, blood flow direction is governed by pressure gradients, which direct the flux through two interconnected circuits.[42] In the pulmonary circuit, the deoxygenated blood from the body returns to the RA via the superior and inferior venae cavae (Figure 2). It is then guided through the tricuspid valve into the RV and is ejected via the pulmonary artery towards the lungs, where gas exchange occurs.[43] The second circuit is the Systemic circuit, the oxygenated blood from the pulmonary vein is collected in the LA and flows through the mitral valve into the left ventricle. The LV

ejects the blood through the aortic valve into the aorta, while having to overcome systemic vascular resistance.[44] A precise coordination of contraction is mandatory to sustain the crucial interplay of the two circuits.[45]

1.4. Cardiac Conduction Pathway

In a healthy heart the conduction pathway is initiated by specialized pacemaker cells located in the sinoatrial (SA) node within the right atrium. These cells spontaneously generate electrical impulses spreading through the atrial myocardium to the left atrium, ensuring coordinated atrial contraction.[46]

The signal then merges at the atrioventricular (AV) node, the electrical gateway between atria and ventricles. The AV node introduces a critical physiological delay of approximately 100 ms ensuring completion of the atrial systole and ventricular blood loading before initiation of ventricular contraction. Following the delay, the impulse is rapidly transmitted through the bundle of His, located in the interventricular septum. At the apex the bundle branches into the Purkinje fiber network, a specialized system ensuring efficient simultaneous distribution over the ventricular myocardium.[46]

The electrophysiology of pacemaker cells is defined by the lack of stable resting membrane potential. Instead, they exhibit spontaneous diastolic depolarization primarily driven by funny currents (I_f), a special type of ionic current in heart pacemaker cells, mediated by the HCN channels.[47] These specialized sodium channels allow slow influx of Na^+ immediately after repolarization. Additionally, T-Type Ca^{2+} channels assist the terminal stage of diastolic depolarization through cation influx. This influx shifts the membrane potential from -60 mV toward a threshold of -40 mV. Upon reaching the threshold, L-type Ca^{2+} channels open.[48] This causes rapid influx of calcium, defining the depolarization slope of the action potential (AP). The heart rate is directly connected to the steepness of the AP slope.[49] Repolarization is achieved through the closing of Ca^{2+} channels and the voltage-gated opening of K^+ channels, allowing rapid K^+ efflux to restore the negative membrane potential.[50]

In contrast to the pacemaker cells, ventricular cardiomyocytes maintain a more negative resting potential of approximately -90 mV. Their AP generation primarily relies on external triggers and is characterized by a rapid depolarization phase 0, triggered by voltage-gated fast Na^+ channels, peaking at +50 mV. Closure of fast sodium channels initiates phase 1, repolarization. This is followed by a defining feature of ventricular AP, the prolonged plateau, phase 2, which lasts for

approximately 200 ms and ensures a long refractory period preventing tetanic contractions and allowing sufficient time for ventricular ejection. This phase is characterized by an inward current of Ca^{2+} through L-type channels, balanced by a delayed outward current of K^+. The plateau phase ends as Ca^{2+} channels close resulting in the K^+ efflux restoring membrane potential to -90 mV, known as phase 3. At resting potential Na^+/K^+-ATPase takes over, maintaining ionic homeostasis, marking phase 4.[51,52]

The coordinated activation of ventricular cardiomyocytes across the myocardium appears extracellularly as the QRS complex on the electrocardiogram. This signal reflects rapid ventricular depolarization and therefore serves as a functional indicator of intraventricular conduction. Under physiological conditions, the high conduction velocity of the His–Purkinje system ensures that ventricular activation occurs within a narrow time frame (Figure 3). Consequently, the QRS complex remains short, typically spanning 80 to 100 milliseconds, reflecting near-synchronous excitation of the ventricular myocardium and efficient electromechanical coupling.[53]

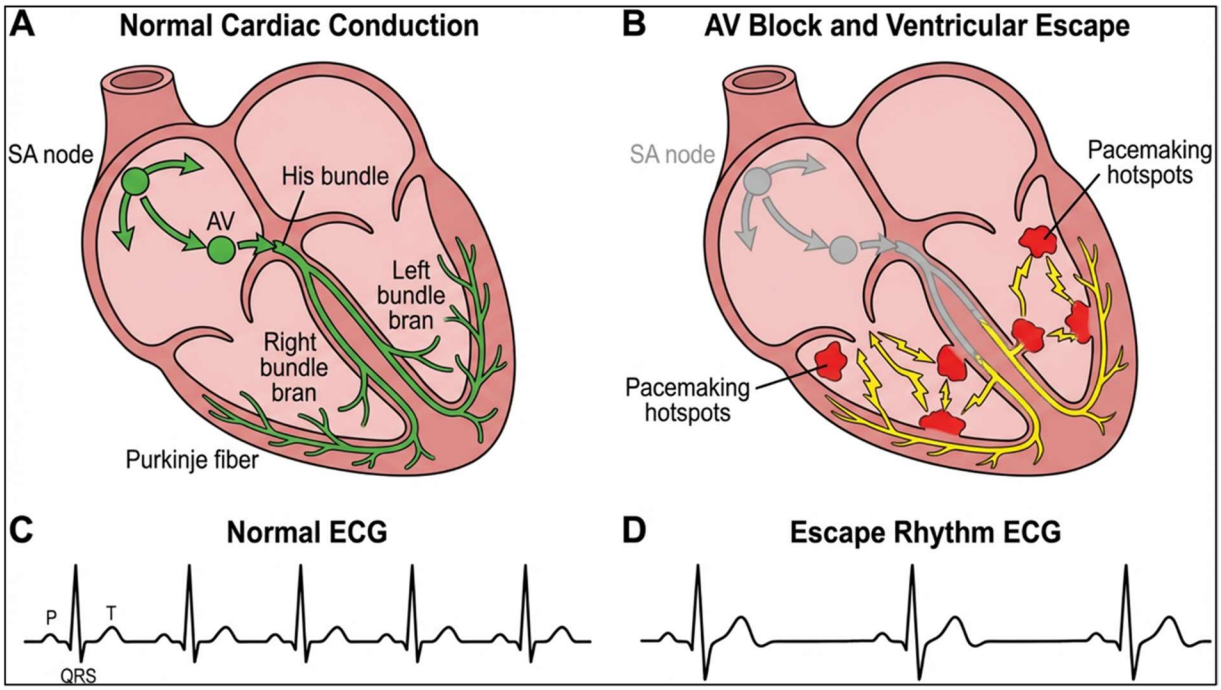

Figure 3: Normal sinus rhythm versus ventricular escape rhythm. Panel A illustrates physiological cardiac impulse propagation in a healthy heart. Electrical activity originates in the sinoatrial (SA) node, propagates through the atrioventricular (AV) node, and is rapidly conducted to the ventricles via the His–Purkinje system, resulting in synchronized ventricular contraction and a regular sinus rhythm as displayed in the ECG (Panel C). Panel B depicts pathological conduction in a diseased heart in which AV nodal conduction is blocked. In the absence of supraventricular input, a ventricular escape rhythm emerges. Electrical activation is propagated through slower cell-to-cell conduction rather than through the specialized Purkinje network. This leads to a reduced heart rate and altered ECG Wave patterns (Panel D). Created with Figurelabs March 2026.

Alongside the primary conduction system, the heart possesses backup mechanisms ensuring cardiac functionality. Under normal conditions, these backup mechanisms

are inhibited through a state of overdrive suppression. The faster SA node rate constantly resets latent pacemakers before reaching spontaneous depolarization.
However, if the SA node or AV conduction fail, the ventricles can initiate an escape rhythm, which has an intrinsic rate of 20-40 bpm (Figure 3).[54] This escape rhythm is triggered by a low density of HCN channels present in the ventricular myocardium. The lower density causes a significant prolongation of the "funny current" to reach the firing threshold, resulting in a slow but potentially life-saving backup heart rate (Figure 3).[55]
In contrast to the protective escape rhythms triggered activity arises from pathophysiological after depolarization, often linked to ischemia or electrolyte imbalance.[56] Triggered activity can be clustered into two groups: Early afterdepolarization (EAD) and delayed afterdepolarization (DAD). EAD occurs during the plateau or repolarization phase. It is characterized by early reopening of L-type Ca^{2+} channels. This can be caused by a prolonged AP triggering the activation of a second premature AP.[57] DAD occurs after complete repolarization of membrane potential and is defined by intracellular Ca^{2+} overload. The cells attempt to remove the Ca^{2+} via the Na^{+}/Ca^{2+} exchanger (NCX), importing 3 Na^{+} for every exported Ca^{2+}-ion. This net positive current can push the membrane potential above the threshold, triggering a spontaneous AP.[49]
Lastly, there is the pathophysiology of abnormal automaticity, typically occurring during heart failure (HF). The severe stress caused by HF can lead to ventricular membrane leakage, resulting in a change of resting potential from -90 mV to -60 mV. This significantly decreases potential difference to the firing threshold, resulting in generation of inefficient spontaneous beats.[58,59] Intensifying the issue of ventricular generated potentials is the loss of the Purkinje fiber system. Without this high-speed conduction network electrical impulses must travel from cell-to-cell via gap junctions through the myocardium. This slower propagation results in desynchronized contraction, reflected by widened QRS complexes in ECG.[60]

1.5. The Composition of the Heart

The continuous contractile function of the heart is sustained by a complex assembly of specialized cell types, with three populations contributing over 90 % of the cardiac tissue. The main cell types are cardiomyocytes. These muscle cells account for only roughly 30-50 % of the total cell count, while providing nearly 70 % of the total volume of cardiac tissue. As the primary engine of the heart, cardiomyocytes are generating

mechanical force and transducing electrical signals to ensure synchronized contraction.

The remaining cell population is dominated by endothelial cells and fibroblasts. In contrast to cardiomyocytes, endothelial cells account for 40 % of the total cell population, while contributing a mere 5 % of volume. They form the critical vascular network supplying the vast amounts of oxygen and nutrients necessary for cardiac functionality. Fibroblasts, commonly described as "architects" of the heart, make up roughly 20 % of the cell count while like the endothelial cells only contributing 2 % volume wise. They maintain structural integrity of the tissue by managing the collagenous extracellular matrix. The remaining fraction of the heart consists of supporting cells, including immune- and smooth muscle cells, regulating blood flow and tissue homeostasis.[61]

The following chapters provide a comprehensive analysis of the three main pillars of cardiac function: The contractile power of the cardiomyocyte, the structural framework of the fibroblasts and the life-sustaining vascular network of the endothelial cells.

1.5.1. Cardiomyocytes

Structurally cardiomyocytes contradict the linear, syncytial alignment of skeletal muscles, exhibiting a distinct branched cylindrical morphology. This branching is fundamental to facilitate the formation of a complex interconnected network allowing mechanical force to be distributed evenly across the myocardium (Figure 4).[62]

Ensuring mechanical and electrical continuity throughout the network is mediated by the intercalated disc (ICD). A specialized junctional complex employing desmosomes and fascia adherens to provide the robust mechanical adhesion required to withstand the immense contractile stress. Furthermore, the ICD facilitates rapid electrochemical communication between neighbouring cells via gap junctions ensuring synchronized contraction.[63]

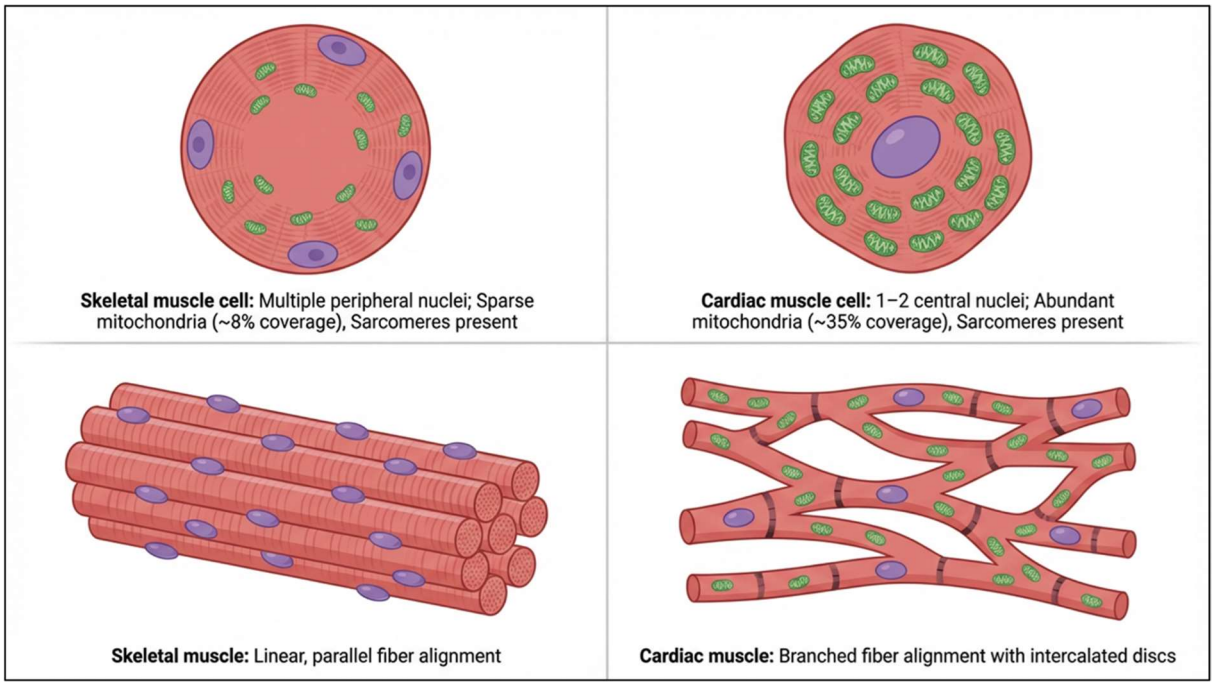

Figure 4: Histological comparison of skeletal muscle and cardiac muscle. The upper panel shows cross-sectional views of muscle cells. Skeletal muscle fibers (left) are multinucleated and exhibit a comparatively lower mitochondrial density. In contrast, cardiomyocytes (right) contain abundant mitochondria, reflecting their high oxidative capacity. The lower panel illustrates the architectural organization of the respective tissues. Skeletal muscle fibers are arranged in parallel, forming a highly ordered, linear structure. Cardiac muscle cells, however, display a characteristic branching morphology that contributes to the formation of an interconnected functional syncytium. Created with FigureLabs March 2026.

Intracellularly, the defining structure of Cardiomyocytes are myofibrils, highly ordered bundles of sarcomere serving as the fundamental contractile unit. To support the heart`s unmatched ATP demand, myofibrils are flanked by extraordinary density of mitochondria, accounting for up to 30 % of the total cellular volume.[64] This investment into metabolism is a key characteristic for cardiac tissue. In contrast skeletal muscles typically contain 3-8 % mitochondria, rarely exceeding 10 % even in elite endurance athletes (Figure 4).[64,65]

A defining hallmark of cardiomyocytes is their transition in regenerative capacity. During foetal development, cardiomyocytes possess high proliferation ability. Upon maturation however this potential decreases significantly since most cardiomyocytes exit the cell cycle. This exit is often marked by an incomplete division, resulting in a binucleated or polyploid state.[66] The binucleated state is highly species specific, in rodents up to 95 % of cardiomyocytes possess multiple nuclei, while in human only 25 % are binucleated, with the remainder often being polyploid.[67] It is hypothesized, that the increased genomic content facilitates the increased transcriptional and protein-synthesis demands of these large and highly active cells. Crucially this transition marks the shift from hyperplastic growth to hypertrophic growth. Hence the

mature heart adapts to physiological or pathophysiological pressures as described by Laplace`s Law primarily through hypertrophy rather than cell division.[68]

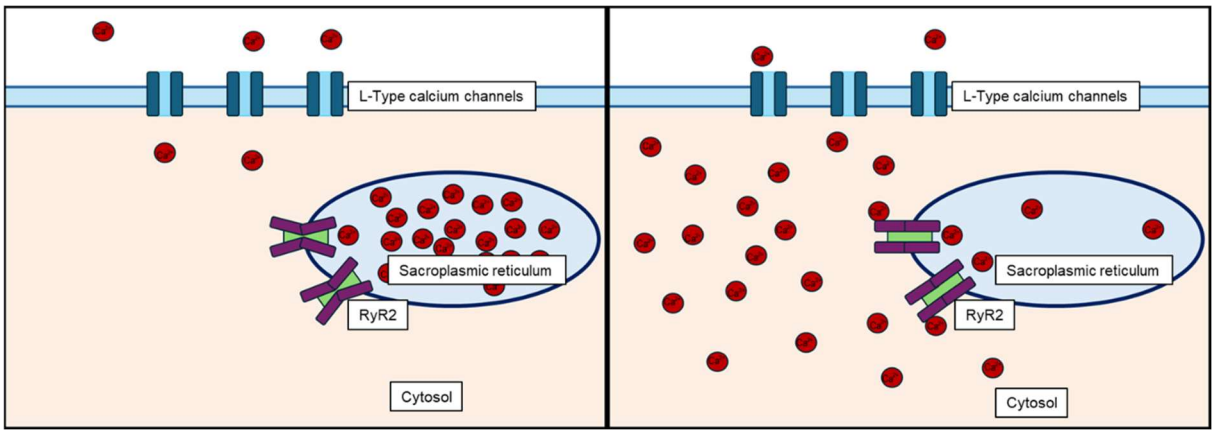

Figure 5: Calcium induced calcium release in cardiomyocytes. Calcium enters the Cytosol via L-type calcium channels (left panel). RyR2 channels are activated through cytosolic calcium and trigger large scale release of sarcoplasmic calcium (right panel).

Ion channels are tasked with a fundamentally important task in AP sensitive cells, managing membrane potential. While most channel types are present in all muscle- and brain cells, there are some distinct isoforms, defining the characteristics of cardiomyocyte AP. The most important is ryanodine receptor type 2 (RyR2) while most muscle cells rely on isoform 1, which supports voltage dependent opening of the Ca2+ efflux of the sarcoplasmic reticulum, the distinct isoform of cardiomyocytes is triggered by Ca2+ itself leading to a calcium-induced-calcium release (CICR) one of the crucial steps for rhythmic beating to sustain blood flow (Figure 5).[69,70] Furthermore, Nav1.5 (cardiac sodium channel) is a unique isoform to cardiomyocytes orchestrating the rapid depolarization of Phase 0.[71]

1.5.2. Cardiac Fibroblasts

Cardiac fibroblasts are characterized by a spindled-shaped or pleomorphic morphology. Unlike cardiomyocytes, they lack a basement membrane allowing them to remain highly sensitive to mechanical changes in the cardiac environment. They are located within the endomysial and perimysial spaces, forming an interconnected network that ensures nearly every cardiomyocyte is in direct contact with a fibroblast.[72] In contrast to cardiomyocytes fibroblasts maintain a high capacity for hyperplasia. This proliferative ability marks a cornerstone of cardiac wound healing. Following injury fibroblasts expand and differentiate into myofibroblasts to facilitate scaring and ensure the structural integrity of the heart wall.

The primary function of the cardiac fibroblast is the synthesis and constant remodelling of the extra cellular matrix (ECM). This matrix dictates the elastic

properties of the myocardium. In cardiac tissue the ECM mainly consists of two collagen types. Type I collagen provides the crucial tensile strength and stiffness, while Type III collagen modulates the flexibility and elasticity of the tissue. Maintaining a precise ratio between these two collagen types is crucial for healthy systolic and diastolic function. Beyond collagen, fibroblast secrete structural proteins such as laminin and fibronectin which serve as matrix proteins for the cardiomyocytes to connect to the surrounding scaffold.[73] For the remodelling they rely on a dynamic shift between matrix metalloproteinases (MMPs) and tissue inhibitor metalloproteinase (TIMPs) their direct counterpart. Fibroblast based Cardiac diseases often originate in an imbalance of these counterparts.[74,75]

Their architectural task exceeds mere scaffold production. They arrange the cardiomyocytes, thereby facilitating the characteristic "wringing" contraction. The endomysium marks the innermost layer, surrounding individual cardiomyocytes ensuring alignment and lateral transduction. The perimysium groups the endomysial units forming larger bundles known as fascicles. Their orientation is the fundamental structure allowing efficient blood ejection. The outermost layer, the epimysium, fulfils a protective role defining the boundaries of the muscle.[76]

1.5.3. Cardiac Endothelial Cells

While fibroblasts are responsible for the macroscopic scaffold of the heart, endothelial cells (ECs) play an equally important role in shaping the microenvironment and maintaining homeostasis. Cardiac ECs can be clustered into two functional groups, endocardial and microvasculature ECs.[77] Endocardial ECs are tasked with the formation of the specialized continuous monolayer that lines the interior chamber of the heart, the endocardium. This layer's smoothness plays a key role in facilitating blood flow as well as building the barrier to separate intracardiac blood and the myocardium.[78] The microvascular ECs provide the dense vascularization crucial to provide oxygen and nutrients in the vast amounts needed by the highly metabolic cardiomyocytes. Hence microvascular ECs outnumber cardiomyocytes at a rate of 3:1.[61] To facilitate the high oxygen diffusion needed to sustain the aerobic metabolism, the arrangement of coronary microvasculature ECs is highly optimized, guaranteeing direct physical contact of each cardiomyocyte with at least one EC. This ensures that the diffusion distance for oxygen is consistently below 20 μm.[79]

Beyond nutrient transport, ECs are contributing Type IV collagen and other essential glycoproteins, forming the basement membrane. This critical extracellular matrix

contact point, provides cardiomyocytes with essential biochemical cues for polarization and survival.[80]

Lastly, cardiac ECs are secreting paracrine factors like nitric oxide (NO) upon shear stress guiding fibroblast activity and cardiomyocyte contractility.[81]

1.6. The Limited Proliferative Capacity of the Heart

For much of the past century, the adult heart was widely regarded as a post-mitotic organ with little to no regenerative capacity. This view originated in 1925 when studies concluded cardiac growth was solely dependent on hypertrophy of existing fibers.[82] This hypothesis was overturned in 2003 with the identification of c-kit+ cells, suggesting the existence of an endogenous cardiac stem cell population capable of cardiomyocyte production.[83]

Current research confirms the presence of progenitor cells clustered in specialized "niches", with varying concentrations observed over specific anatomical regions. The highest density is reported in the right atrium, with some cultures showing up to 5 % stem cell content.[84] While the left ventricle, the region most prone to injury possesses the lowest regenerative capacity with stem cell population often falling below 0.6 %.[84]

To put the heart`s regenerative potential into perspective, intestinal tissue, which is known for its favourable reproductive ability's, with complete lining replacement every 5 days possess a stem cell population of 1-5 %.[85] Even more surprising is the Bone marrow, which produces millions of cells per second while containing only 0.1 % stem cells.[86] In sharp contrast, the myocardium`s turnover rate is negligible despite a progenitor population of approximately 1 %.[87]

The actual renewal rate has been determined through implementation of carbon-14 (14C) method.[88] The cumulative turnover throughout an entire human lifespan does not exceed 50 %.[89] At the age of 20 renewal rate is approximately 1 %, decelerating in an age-dependent manner to 0.3 % by age 75.[88]

Hence the role of c-kit+ has been subject of scientific debate. Recent lineage-tracing evidence indicate that the majority of new cardiomyocytes originate from the division of pre-existing cardiomyocytes rather than stem cell differentiation.[90] suggests that endogenous cardiac stem cell are primarily responsible for EC turnover and the maintenance of the vascular network.[91]

Rather than directly replacing muscle cells, c-kit + cells are now widely viewed as crucial support cells. They release paracrine factors enhancing the survival of existing cardiomyocytes, modulate inflammation and stimulate angiogenesis.[91,92]

1.7. Metabolism of Cardiomyocytes

To examine cardiac-specific metabolism, one must first understand the three primary interconnected pathways of eukaryotic energy production, glycolysis, the tricarboxylic acid (TCA) cycle and the oxidative phosphorylation (OxPhos).

Glycolysis describes the anaerobic breakdown of glucose into pyruvate occurring in the cytosol.[93] This pathway yields a net gain of 2 ATP and 2 NADH per glucose molecule. While glycolysis is oxygen-independent, its overall contribution to cardiac energy in healthy hearts is minor compared to oxidative pathways.[94]

The TCA cycle marks the central hub of metabolism. It takes place in the mitochondrial matrix and is the critical metabolic switching point between carbohydrate and lipid substrates.[95] Acetyl-Coenzym A (Acetyl-CoA), derived from either pyruvate or fatty acids, is oxidized (Figure 6). The oxidation results in the release of CO_2, which is disposed via exhaling, and the loading of high-energy electron carriers, resulting in 3 NADH and 1 $FADH_2$ per turn as well as 1 ATP.[96] Per molecule of glucose the TCA cycle can be run twice, while number of turns per fatty acid depends on chain length, they average 8 turns.[97]

Located on the inner mitochondrial membrane is the powerhouse of metabolism, OxPhos. OxPhos consists of the electron transport chain (ETC) and the ATP Synthase (Figure 6). The ETC utilizes the energy from NADH and $FADH_2$, generated through Glycolysis and the TCA cycle, to pump protons (H^+) across the membrane thus creating an electrochemical gradient.[98] This gradient creates a proton flow back into the matrix through the ATP synthase, driving the mechanical phosphorylation of ADP to ATP.[99] This process is strictly aerobic, as oxygen serves as the final electron acceptor to form H_2O. The approximate ATP yield is 30-32 ATP, making it the most efficient energy source.[100]

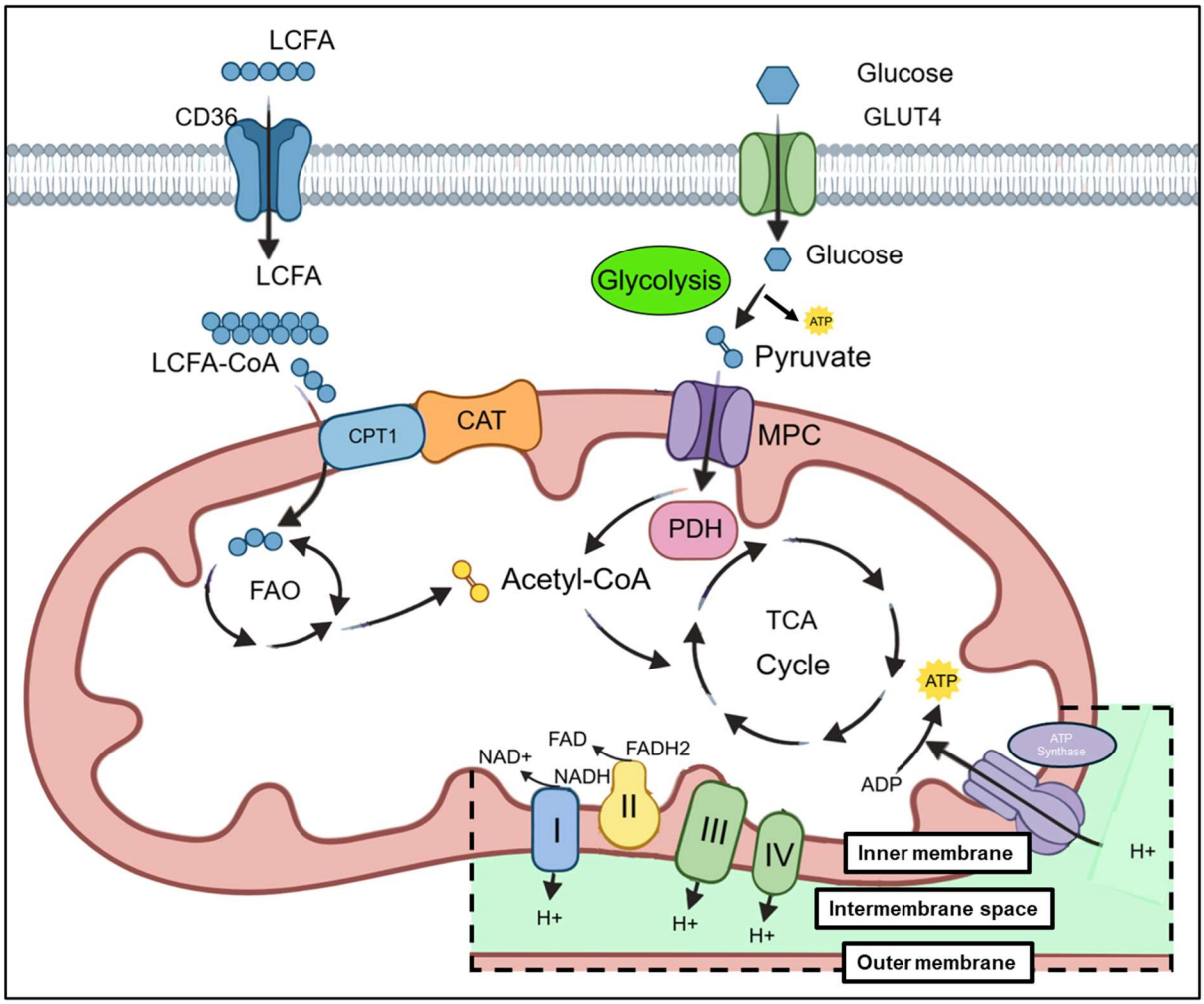

Figure 6: Metabolism of cardiomyocytes. The bottom left panel illustrates substrate uptake and intracellular processing in cardiomyocytes. Long-chain fatty acids (LCFAs) are transported into the cell via CD36, while glucose is taken up through Glut transporters. In the cytosol, LCFAs are converted to acyl-CoA and transported into the mitochondria via the carnitine shuttle, involving carnitine palmitoyltransferase I (CPT-I). Within the mitochondrial matrix, acyl-CoA undergoes β-oxidation, generating acetyl-CoA. Glucose, in contrast, is metabolized through glycolysis in the cytosol to form pyruvate. Pyruvate is transported into the mitochondria and converted to acetyl-CoA by the pyruvate dehydrogenase complex. Acetyl-CoA enters the tricarboxylic acid (TCA) cycle, shown in detail in the right panel. The reducing equivalents (NADH and $FADH_2$) generated by the TCA cycle are subsequently utilized by the electron transport chain (ETC) to drive oxidative phosphorylation and ATP production. Created with Figurelabs.

During development, the heart undergoes a profound metabolic transition to meet the increasing postnatal demands. Given the foetal heart operates in a relatively hypoxic environment with a steady supply of nutrients from the mother, it primary relies on glycolysis and lactate catabolism.[101] After birth it undergoes a postnatal transition supported by a high-fat diet and increased oxygen availability accompanied by gene expression changes resulting in a rapid up-regulation of the Fatty Acid β-Oxidation (FAO) pathway.[102] The adult heart, while metabolically flexible, derives 60-90 % of its ATP from the oxidation of Long-Chain fatty Acids (LCFAs).[103] While FAO is more energy dense, it requires significantly more oxygen per ATP molecule compared to glucose oxidation.[103]

The dependency on fatty acids together with the limited storage capacity of FAs relies on an efficient transport mechanism. The uptake is mediated by fatty acid transporter proteins (FATP) and fatty acid translocase (FAT/CD36), while the translocation into the mitochondria where the FAO takes place is regulated by the carnite palmitoyltransferase I (CPT I) system, which regulates the rate of long-chain fatty acid (LCFA) entry into the mitochondria (Figure 6).[101,104] As metabolic demand increases, there is a developmental switch in the dominant CPT I isoform, from the liver-type (L-type) isoform, which predominates in the embryo, to the muscle-type (M-type) isoform, which contributes approximately 90 % of total CPT I activity in the adult heart, thereby facilitating the high fatty acid oxidation (FAO) flux required for adult cardiac metabolism.[105,106]

The metabolic competition in cardiomyocytes is regulated by the Randle Cycle.[107] Mechanistically high rates of FAO increase mitochondrial Acetyl-CoA and Citrate levels. Acetyl-CoA inhibits the Pyruvate Dehydrogenase (PDH) complex, while Citrate accumulation leads to a down regulation of Phosphofructinase-1 (PFK-1) and glucose transporter type 4 (Glut-4) translocation.[108] The physiological purpose of the Randle Cycle is the glucose-sparing mechanism, which ensures preservation of blood glucose levels during fasting to sustain glucose -dependent tissues like the brain.[108–110]

During HF the reduced activity of the heart leads to excessive phosphorylation of the sarcoplasmic reticulum and an abundance of free fatty acids, uncoupling mitochondrial respiration after accumulation in the cardiomyocytes, while simultaneously downregulating Glut-4 translocation.[111] This leads to a further diminishing of contraction efficiency. FAO upregulation triggered by the abundance of LCFAs leads to further downregulation of glycolysis through inhibition of PDH. Which directly decreases ATP availability, causing even further diminishing of contractility.[112]

1.8. Cardiac Fibrosis

In healthy tissues, fibroblasts are essential for maintaining structural integrity. As the primary producers of collagen and other extracellular matrix (ECM) components, they regulate the composition and mechanical stiffness of the tissue. Upon severe stress or injury, fibroblasts become activated and differentiate into myofibroblasts, which increases ECM production (Figure 7). This response initially serves as a protective purpose by reinforcing tissue integrity. However, excessive or prolonged matrix

deposition leads to pathological scarring, which compromises tissue function rather than restoring it, also known as fibrosis.[113]

Progressive stiffening of the myocardial walls forces cardiomyocytes to generate greater contractile force, thereby increasing their energy demand. At the same time, reduced ventricular compliance limits diastolic filling and effective blood flow. The combination of elevated energy requirements and insufficient oxygen and nutrient supply promote cardiomyocyte loss, further amplifying fibrosis and establishing a vicious cycle that can ultimately result in heart failure.[114]

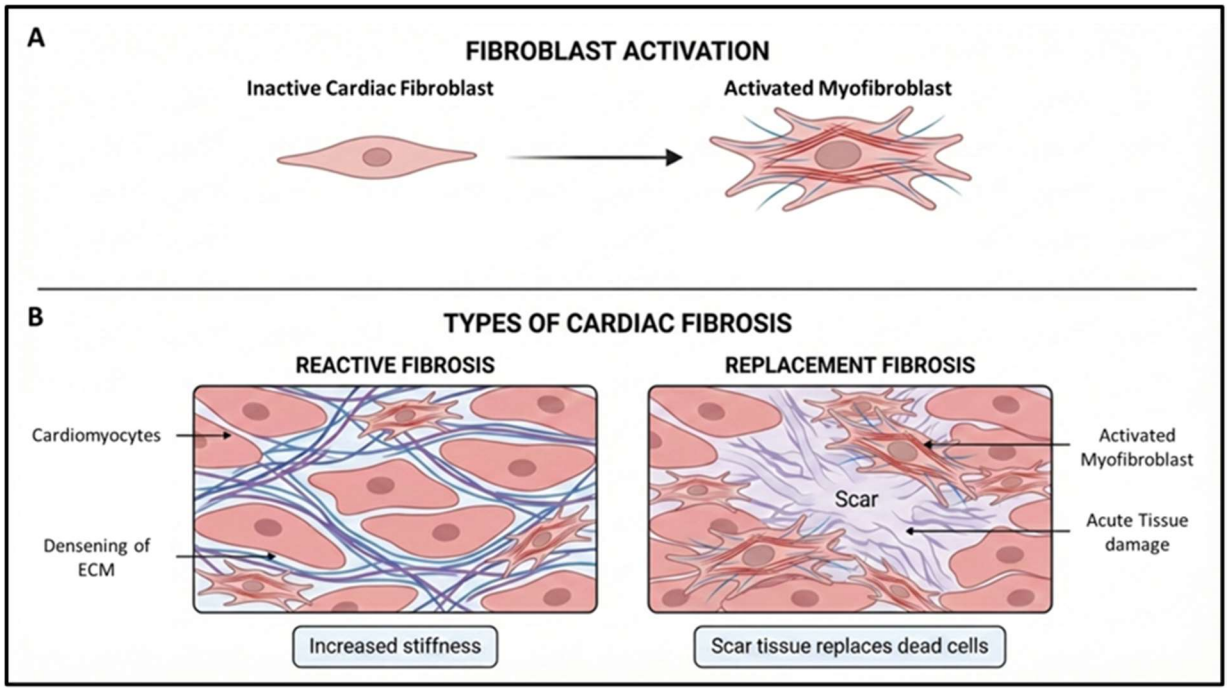

Figure 7: Cardiac fibroblast activation and types of cardiac fibrosis. Upon injury, quiescent cardiac fibroblasts differentiate into activated myofibroblasts characterised by prominent alpha-smooth muscle actin (α-SMA) expression and enhanced extracellular matrix (ECM) production (top panel). Reactive fibrosis occurs in the interstitial space between viable cardiomyocytes, increasing tissue stiffness without prior cell loss. Replacement fibrosis involves scar formation in areas of cardiomyocyte death, where necrotic tissue is substituted by dense ECM deposits (bottom panel). Created using Google Gemini (Image Generation Model: Nano Banana, February 2026); annotations added manually.

Cardiac fibrosis can be broadly classified into two forms: replacement fibrosis and reactive fibrosis (Figure 7). Replacement fibrosis occurs following cardiomyocyte death. Adult cardiomyocytes possess extremely limited regenerative capacity, hence they cannot be effectively replaced. To preserve the structural integrity of the myocardium, fibroblasts migrate to the site of injury and differentiate into cardiac myofibroblasts, depositing collagen and other ECM components to fill the resulting voids. While this prevents rupture of the ventricular wall, it also leads to permanent scar formation and reduced contractile capacity.[115]

Reactive fibrosis, in contrast, develops independently of cell death. It is primarily driven by chronic external stressors such as hypertension or pressure overload.

Sustained mechanical stress promotes fibroblast activation and excessive interstitial collagen deposition, which increases myocardial stiffness and is initially adaptive. Over time, however, this constant remodelling impairs cardiac compliance and function.[116]

Fibrosis is a common pathological feature of nearly all major cardiac diseases.[117] Reactive fibrosis is characteristic of hypertrophic heart disease, whereas replacement fibrosis is prominent following ischemic injury and reperfusion, where cardiomyocyte death triggers scar formation that further compromises cardiac performance. Some conditions, such as aortic stenosis, involve both forms of fibrosis at different stages of disease progression.[116,118]

Functionally, cardiac fibrosis contributes to heart failure through both diastolic and systolic dysfunction.[119,120] Increased stiffness impairs ventricular relaxation and filling during diastole, while excessive ECM accumulation can also reduce contractile efficiency during systole.

In addition to its mechanical consequences, fibrosis disrupts the electrical properties of the myocardium. Fibrotic tissue limits electrical signal transduction, increasing the risk of arrhythmias. Collagen-rich scar tissue acts as an electrical insulator, forcing action potentials to obviate fibrotic regions rather than travel through direct cell–cell pathways. This altered conduction leads to delayed and heterogeneous signal propagation, promoting delayed afterdepolarization, early afterdepolarization and potentially life-threatening arrhythmias.[121]

1.9. Ischemia

Cardiac ischemia describes a severe mismatch between oxygen and nutrient supply and metabolic demand in the myocardium. Under physiological conditions, coronary perfusion tightly matches myocardial energy requirements. However, in pathological states this balance becomes disrupted, resulting in insufficient substrate delivery and subsequent functional and structural impairment of cardiac tissue. The most frequent cause of ischemia is obstruction of the epicardial coronary arteries.

Obstruction of coronary arteries commonly originates from the formation of atherosclerotic plaques. The earliest step in plaque development is characterized by damage to the endothelial layer. Endothelial injury initiates an inflammatory cascade characterized by increased permeability, recruitment of inflammatory cells, and accumulation of lipids within the vessel wall.[122] Cholesterol deposition, macrophage

infiltration, and smooth muscle cell activation lead to the development of a lipid-rich necrotic core.

Simultaneously, the wound-healing response triggers the formation of fibrous tissue, thereby generating a protective structure known as the fibrous cap, separating the thrombogenic plaque contents from the circulating blood. While the fibrous cap stabilizes the lesion initially, the growing plaque inevitably leads to thickening of the arterial wall and progressive reduction of the effective lumen diameter.[123]

The structural narrowing limits coronary perfusion and increases shear stress within the vessel. During periods of stress or exercise, when myocardial demand rises, the hemodynamic load on the plaque increases further, gradually weakening the fibrous cap, eventually leading to a mechanical rupture. The Rupture of the fibrous cap exposes the necrotic core of the plaque, including tissue factors, lipids and pro-thrombotic factors directly to the blood stream (Figure 8). The exposure immediately triggers a coagulation cascade, causing platelet aggregation and fibrin-rich thrombus formation.

In severe cases, the thrombus completely clogs the coronary artery, abruptly terminating blood supply to the downstream myocardium (Figure 8). The region deprived of perfusion is known as rea at risk (AAR).[124]

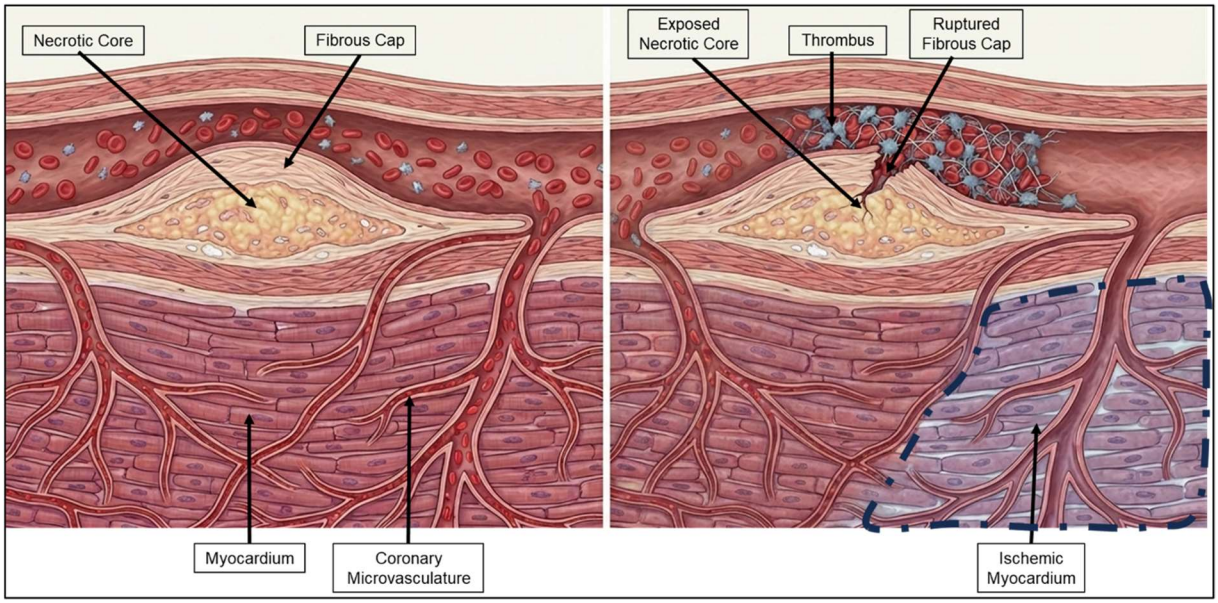

Figure 8: Pathophysiology of coronary plaque rupture and myocardial ischemia. Left panel shows a stable atherosclerotic plaque with an intact fibrous cap enclosing a lipid-rich necrotic core. Right panel illustrates plaque rupture, where disruption of the fibrous cap exposes the thrombogenic core to the bloodstream, triggering thrombus formation and vessel occlusion. The resulting loss of perfusion delineates a downstream area at risk (AAR, dashed outline), representing ischemic myocardium susceptible to irreversible injury. Created using Google Gemini (Image Generation Model: Nano Banana, February 2026); annotations added manually.

The myocardium within the AAR undergoes an almost immediate loss of contractile function. Within 15–30 seconds after the beginning of ischemia, the affected tissue

becomes akinetic or dyskinetic, a phenomenon often referred to as ischemic contractile shutdown or aperistalsis.

This shutdown is not simply a failure but also represents a protective metabolic adaptation. By suppressing mechanical activity, the cardiomyocytes significantly reduce ATP consumption by approximately 70 %.[125,126] This reduction conserves the limited remaining energy reserves for essential processes such as maintaining ion gradients and cellular integrity.[127]

The Aperistalsis is primarily mediated by metabolic alterations within the cardiomyocytes. The decline of ATP production paired with the continues basal ATP consumption, leads to intracellular rising levels of inorganic phosphate. The elevated inorganic phosphate levels directly reduce the calcium sensitivity of the myofibrils. This decreased affinity of troponin C for Ca^{2+} suppresses the cross-bridge cycling, shutting down the sarcomere.[128,129]

The effects of ischemia extend beyond the AAR. The non-contractile region effectively serves as a passive mechanical burden within the ventricular wall. During the systole, the AAR may undergo systolic bulging, a phenom in which upon contraction of the functional tissue, the non-functional tissue is pushed outwards. This paradoxical motion reduces effective stroke volume while increasing the mechanical workload of the remaining viable myocardium. Consequently, overall cardiac efficiency declines, even when large areas remain metabolically intact.[130]

The reduced pumping efficiency results in an accumulation of residual blood within the ventricle, stretching the remaining functional cardiomyocytes. According to the Frank–Starling law, increased ventricular filling leads to myocardial stretch, which enhances the calcium sensitivity of the contractile apparatus. As a result, contractile force increases, allowing the heart to adapt its stroke volume to changes in venous return.[131]

However, this compensatory effect comes at a cost. The increased wall stress significantly elevates oxygen demands in the non-ischemic myocardium. Experimental evidence suggests that metabolic demand in these regions may rise to 150-200 % of baseline levels. This enormous increase in oxygen consumption can trigger secondary ischemia even in well-perfused tissues, thereby expanding functional impairment beyond the original AAR.[132]

The duration of ischemia is the critical switch, determining whether the injury remains reversible or becomes permanent. When ATP levels fall below approximately 10 % of

normal values, cardiomyocytes lose the ability to detach myosin heads from actin filaments due to failure of the ATP-dependent cross-bridge cycle.[133]
This results in a pronounced stiffening of the tissue, a phenomenon known as ischemic contracture, closely resembling rigor mortis but occurring in living cells. This marks the key stage where the myocardium transitions from functional impairment to irreversible structural damage. Prolonged ischemic contracture hence serves as a potent marker of irreversible myocardial injury and cell death.[134]
Cardiac ischemia is not merely a consequence of reduced blood flow but a complex, multiscale pathological process including vascular pathology, metabolic adaptation, mechanical dysfunction, and ultimately cellular death. From endothelial injury and plaque formation to thrombotic occlusion, contractile shutdown, mechanical inefficiency, and ATP-dependent irreversible injury, each stage contributes to a self-reinforcing cascade of deterioration. Understanding these mechanisms in a mechanistic and quantitative framework is essential for the development of more effective therapeutic strategies.

1.10. Reperfusion

Ischemia–reperfusion injury represents the most critical phase of myocardial infarction. Paradoxically, the most severe cellular damage does not occur during the deprivation of oxygen and nutrients, but during their rapid restoration. While reperfusion itself is essential for tissue survival, it determines whether cardiomyocytes recover or sustain irreversible damage eventually leading to cell death. This determination is not solely done by reperfusion but mainly through the biochemical state established during ischemia. Hence to understand the reperfusion injury, ischemia and reperfusion must be considered as a continuous path.
The metabolic priming of ischemia plays a major role in determining reperfusion injury severity. Adult cardiomyocytes generate most of their ATP through mitochondrial oxidative phosphorylation of fatty acids. Under physiological conditions this provides an efficient and stable energy supply.[135] Hence isolated deprivation of nutrients in the presence of oxygen is relatively well tolerated. Cardiomyocytes can transition to endogenous energy stores such as lipid droplets and glycogen. During this state, AMP-activated protein kinase (AMPK) becomes activated, actively suppressing energy-consuming anabolic pathways and promoting catabolic processes.[136] Autophagy is substantially upregulated, allowing the cells to effectively recycle intracellular substrates maintaining viability for extended periods. Glykolysis

can be sustained for a limited time through stored glucose, afterwards controlled protein degradation contributes to maintaining basal cellular function.[137] As long as oxygen remains available, these mechanisms allow cardiomyocytes to adapt without severe structural damage.

However, the situation drastically changes with declining oxygen availability. Hypoxia forces the myocardium to abandon oxidative phosphorylation and rely solely on anaerobic glycolysis, which produces only a fraction of the ATP generated through mitochondrial OxPhos. This metabolic shift is accompanied by the rapid activation of AMPK, which enhances catabolic pathways and promotes the translocation of glucose transporters Glut1 and Glut4 to the membrane, thereby mediating a substantial increase in glucose uptake.[138] The stabilization of hypoxia-inducible factor 1α (HIF-1α), a key transcription factor activated under low oxygen conditions, further reinforces this metabolic reprogramming. It suppresses mitochondrial pyruvate entry and promotes glycolysis. Although the metabolic shift allows for short term survival, it inevitably leads to the accumulation of lactate and free protons, progressively lowering intracellular pH.[139]

When both oxygen and nutrients are absent, ATP production collapses. Glycolysis alone cannot sustain the energetic demands of cardiomyocytes. Ion pumps begin to fail, most notably the Na^+/K^+-ATPase, leading to intracellular sodium accumulation and osmotic swelling. Attempts to restore the intracellular pH via the Na^+/H^+ exchanger further intensify the sodium overload. These severely elevated sodium levels trigger the reverse activity of the Na^{2+}/Ca^{2+} exchanger, causing pathophysiological calcium influx. The rising intracellular calcium levels result in the locking of the sarcomeres in a rigor-like contracted state, while also destabilizing the mitochondrial membrane potential. The intensifying collapse of the proton gradient drives the ATP synthase into reverse mode, effectively transforming the mitochondria from the ATP-producing powerhouses of the cells into ATP-consuming organelles.[140,141]

Despite these severe dysfunctions, many cardiomyocytes remain structurally intact during ischemia.[142] The biochemical state established during this state, however, primes the cells for destruction upon reperfusion.

The rapid reintroduction of blood flow simultaneously initiates the restoration of nutrients and oxygen. Importantly, these two restorations have fundamentally different biological consequences. The return of nutrients is essential for recovery and is not responsible for the characteristic acute cell death observed during reperfusion. On the contrary, nutrient availability allows glycolysis to resume and supports the

restoration of ATP levels. The ATP generated during early reperfusion fuel the crucial ion pumps such as the Na^{2+}/K^{+}-ATPase, facilitating the correction of the ionic imbalance and importantly reducing the toxic intracellular calcium overload.[135] Experimental inhibition of glycolysis during early reperfusion markedly worsens cellular injury, highlighting the protective nature of nutrient restoration.[143,144]

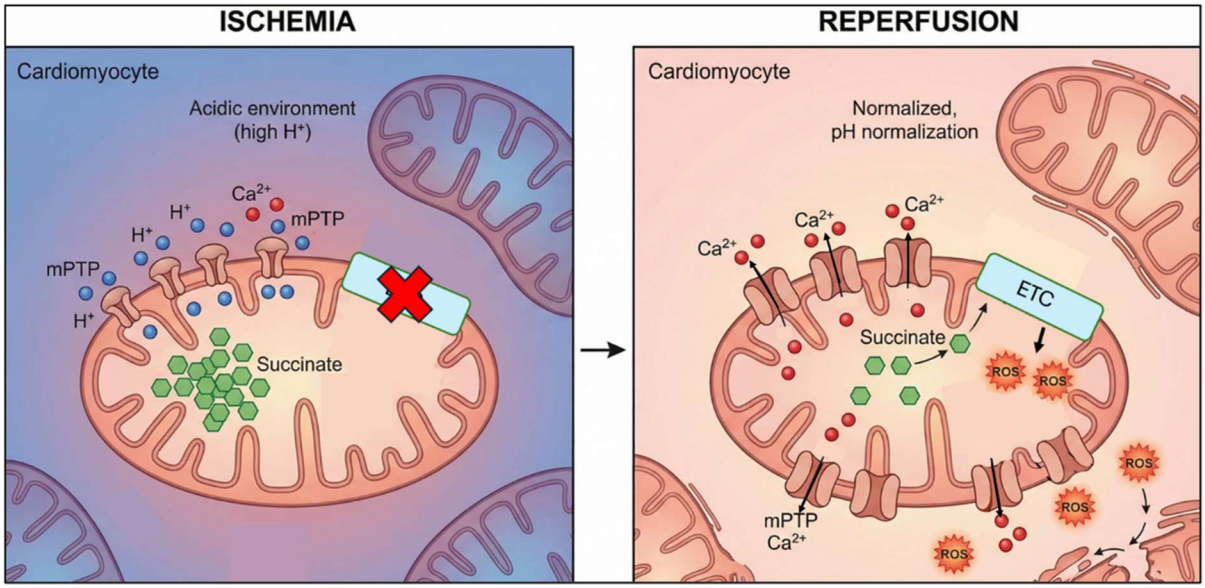

Figure 9: Cellular mechanisms of myocardial ischaemia-reperfusion injury. During ischaemia (left), impaired oxidative phosphorylation leads to anaerobic metabolism, intracellular acidosis, and accumulation of succinate. Disruption of ion homeostasis results in cytosolic calcium (Ca^{2+}) overload and increased reactive oxygen species (ROS) production from dysfunctional mitochondria. Upon reperfusion (right), rapid pH normalisation and continued Ca^{2+} overload trigger opening of the mitochondrial permeability transition pore (mPTP), leading to mitochondrial swelling, further ROS release, and ultimately cardiomyocyte death. Created using Google Gemini (Image Generation Model: Nano Banana, February 2026); annotations added manually.

In vast contrast, the return of oxygen acts as the critical trigger of irreversible damage. The central role in this damaging process is possessed by the mitochondrial permeability transition pore (mPTP), a non-specific high-conductance channel within the inner mitochondrial membrane.[145] Opening of the mPTP is triggered by severe cellular malfunction and leads to the immediate collapse of mitochondrial membrane potential, complete inhibition of ATP production, mitochondrial swelling, and the release of pro-death factors such as cytochrome c.[146] The opening of mPTP marks a functional point of no return in cardiomyocyte survival (Figure 9).

During Ischemia, calcium levels are severely elevated however widespread opening of mPTP is largely prevented by the acidic intracellular environment (Figure 9). There is a heavy competition between protons and calcium for the regulatory sites of mPTP and even a slight reduction in pH strongly inhibits pore opening.[147] Hence the ischemic acidosis caused by the lactate accumulation acts as a protective mechanism. However, upon reperfusion, lactate is rapidly washed out, and intracellular pH normalizes

within minutes. This sudden loss of acidosis removes the inhibitory constraint on the mPTP, facilitating acute sensitivity to the existing calcium overload (Figure 9).[148]
Simultaneously to the opening of the mPTP reperfusion induces a massive burst of oxygen species.[149] This phenomenon is caused by the oxygen paradox, while oxygen is indispensable for life it becomes severely toxic when reintroduced into metabolically damaged cells. A key mechanism underlying this oxidative burst is the accumulation of succinate during ischemia. In the absence of oxygen, succinate build ups within mitochondria due to the decoupling of OxPhos. Upon reperfusion, succinate is rapidly oxidized through complex II, delivering an excessive flux of electrons into the electron transport chain.[150] This saturates the coenzyme Q pool and promotes reverse electron transport through complex I. This is where electrons leak directly onto molecular oxygen, forming the dangerous superoxide. The resulting oxidative stress damages mitochondrial membranes, causing further opening of mPTP, amplifying necrotic and apoptotic pathways.[151]
Ischemia–reperfusion injury is best understood as a continuous mechanistic sequence rather than as two independent pathological states. Ischemia establishes a biochemical environment characterized by acidosis, calcium overload, and mitochondrial instability. Reperfusion abruptly removes the protective components of this environment while simultaneously reintroducing oxygen into a system no longer capable of safely processing it. The result is a highly coordinated collapse centred on mitochondrial dysfunction and mPTP opening. In this sense, mitochondria function not only as metabolic engines of the cardiomyocyte but also as the central decision point governing survival or death following ischemic injury.

1.11. State of the Art Reperfusion Models

Reproducing reperfusion injury experimentally demands precise control over oxygen, metabolism, and timing. Because available models differ in their ability to regulate these variables, each captures only selected aspects of the ischemic cascade while introducing characteristic limitations.
At the most physiologically representative end of the spectrum, *in vivo* coronary occlusion/reperfusion and ex vivo Langendorff-perfused hearts set the benchmark for ischemia–reperfusion injury research. In the Langendorff model, an isolated heart is rapidly excised and retrogradely perfused through the aorta with oxygenated buffer, allowing the coronary arteries to be supplied while the heart continues to beat ex vivo.[152–156] By preserving perfusion dynamics, neurohumoral signalling, and

multicellular architecture, they capture the integrated response to ischemia and reperfusion. However, this same strength imposes a key constraint: low throughput and limited flexibility for systematic parameter control or iterative screening. As a result, more controllable human cell–based *in vitro* platforms have gained interest.

The most common *in vitro* approach is hypoxia/reoxygenation (H/R) in 2D cardiomyocyte cultures using hypoxia chambers or controlled-gas incubators.[157–159] While oxygen reduction and reoxygenation can be defined, equilibration at the cellular level is often diffusion-limited through headspace, plastic, and media. As a result, the effective ischemic interval may not match intended timing, and rapid reperfusion transitions are difficult to achieve with minute-level precision.

Oxygen–glucose deprivation (OGD) combines hypoxia with glucose removal to approximate metabolic starvation.[160,161] Although simple to implement, glucose withdrawal alone incompletely models ischemia. Cardiomyocytes may transiently preserve ATP through endogenous or alternative substrates influenced by media composition and maturation state. This variability contributes to substantial inter-laboratory differences in OGD protocols and necessitates rigorous control of substrates and buffers to achieve physiological alignment.

To address these limitations, several groups have moved beyond substrate deprivation alone and adapted physiologically matched ischemic buffers that more comprehensively replicate the extracellular environment of ischemia.[162–164] This multi-parameter ischemic milieu more accurately reflects extracellular determinants of calcium dysregulation and mitochondrial stress. By incorporating coordinated changes in pH, ionic composition, and substrate availability, these systems improve biochemical fidelity relative to simpler hypoxia or OGD paradigms. However, unless oxygen concentration itself is actively regulated, the temporal dynamics of hypoxia and reoxygenation remain diffusion-governed, limiting precision in modelling rapid ischemia–reperfusion transitions.

Because oxygen availability in these systems remains governed by diffusion, alternative strategies have been developed to induce more rapid or controlled hypoxia. Chemical and enzymatic approaches attempt to directly deplete oxygen or activate hypoxia signaling pathways using agents such as sodium dithionite, cobalt chloride, or oxygen-scavenging systems.[165–167] While these methods can produce rapid hypoxic responses, they introduce additional variables, including off-target toxicity and unstable oxygen trajectories, complicating interpretation in the context of reperfusion injury.

To achieve greater spatiotemporal control without introducing chemical agents, microphysiological systems and heart-on-a-chip platforms have emerged as advanced *in vitro* models of ischemia–reperfusion injury.[168,169] By integrating microfluidic perfusion with engineered cardiac tissues, these systems enable controlled modulation of oxygen tension, nutrient delivery, and flow dynamics. This allows the generation of defined ischemic zones, oxygen gradients, and rapid transition kinetics that more closely approximate *in vivo* perfusion dynamics. Despite these advantages, such platforms require specialized fabrication and operational expertise, which can limit accessibility and scalability. Moreover, the increased physiological detail often comes at the expense of throughput, an important consideration when systematic screening or adaptive optimization is a central objective.

Overall, IRI modelling depends less on selecting a single optimal method than on matching temporal kinetics and multifactorial stressors to the mechanism under study. Diffusion-limited systems constrain transition precision, chemical hypoxia risks confounded interpretation, and microfluidics enhance realism at the cost of scalability. Together, these trade-offs underscore the challenge of simultaneously achieving precise temporal control, metabolic realism, and experimental scalability in ischemic reperfusion injury modelling.

1.12. Drug Specificity

The heart`s pharmacological response differs from other tissues, given its reliance on coordinated iron currents to facilitate rhythmic AP. Cardiac pharmacodynamics mainly focus on the modulation of these tissue specific ion channels.

The biological basis for individual drug response is genetically determined and mostly rooted in gene variations of drug-metabolizing enzymes, transporters or receptors. The most prominent is the Cytochrome P450 Superfamily, gene variations vastly alter the metabolism, potentially resulting in overdose or no effect, depending on the metabolic type.[170] In case of cardiac specificity, CYP2C19 and CYP2D6 are both highly deterministic on drug effect, hence testing for variations in these genes has nowadays become a cornerstone of precision anticoagulation.[171,172]

Several cardiac-specific ion channels exhibit high alteration rates. These include Nav1.5, which controls rapid depolarization; Cav1.2, which governs the plateau phase and is a major target for calcium channel blockers; hERG, commonly associated with QT prolongation; and KCNQ1, which provides a critical repolarization reserve.[173–177]

Together, these channels play a central role in cardiac electrophysiology, and drug exposure affecting any of them can increase the risk of arrhythmia.

The major issue with mutations or pharmacological interference in these channels lies in the delicate balance between inward depolarizing currents, primarily sodium and calcium, and outward repolarizing potassium currents.[178] The human heart can tolerate minor disturbances due to intrinsic repolarization reserve mechanisms.[179] However, drug-induced alterations may shift this equilibrium, prolong action potential duration or slow conduction, and thereby predispose to triggered activity and potentially catastrophic arrhythmic events.[180]

The vast landscape of possible genetic mutations, combined with the high risk of catastrophic drug-induced events such as arrhythmia or sudden heart failure, makes the development of patient-specific drug testing platforms essential. This need is further emphasized by the limitations of animal models, which often fail to accurately replicate human cardiac electrophysiology and action potential dynamics.[181]

Human induced pluripotent stem cell–derived cardiomyocytes (hiPSC-CMs) have therefore become a central focus in drug research.[182] Because they carry the patient's exact genetic background, they allow disease-specific phenotypes, such as Long QT syndrome, a disorder characterized by prolonged ventricular repolarization that increases the risk of arrhythmias, or Brugada syndrome, a genetic condition associated with impaired cardiac sodium channel function and a high risk of ventricular arrhythmias, to be reproduced *in vitro*. This enables more precise assessment of individual drug responses.[183]

2. Aim of the Thesis

Ischemia–reperfusion injury remains a major contributor to cardiac morbidity and mortality, yet the development of reproducible and mechanistically representative *in vitro* models remains challenging. Many existing systems lack precise temporal control over ischemic onset and reoxygenation, fail to recapitulate the multifactorial nature of reperfusion injury, or do not allow systematic pharmacological interrogation under scalable conditions.

The primary objective of this thesis was to establish a temporally controlled, mechanistically grounded three-dimensional *in vitro* model of cardiac ischemia–reperfusion injury using human iPSC-derived cardiac spheroids. Emphasis was placed on integrating rapid oxygen deprivation with defined metabolic substrate restriction to reproduce key aspects of reperfusion-associated injury progression.

A second objective was to implement and validate an adaptive closed-loop Bayesian optimization platform capable of automated concentration refinement and dose–response characterization directly within the 3D cardiac system. This framework was intended to enable efficient identification of physiologically relevant drug concentration ranges and to enhance reproducibility and scalability in cardiac pharmacological testing.

Finally, this work aimed to investigate genotype-dependent pharmacodynamic variability by comparing drug responses across distinct iPSC-derived cardiac lines. Through this approach, the study sought to assess whether the established platform is capable of detecting biologically meaningful inter-line differences in drug sensitivity.

Together, these objectives were designed to integrate mechanistic disease modelling, automated pharmacological optimization, and exploratory precision cardiac profiling within a unified experimental framework.

3. Results and Discussion

In order to implement the objectives the experimental section presents the stepwise establishment and application of a three-dimensional human iPSC-derived cardiac spheroid system. The results are organized into three conceptual blocks reflecting biological validation, pharmacological framework implementation, and exploratory genotype comparison.

The first block addresses the biological foundation of the model. Following directed cardiac differentiation, spheroids were structurally and functionally characterized to confirm cardiomyocyte identity and baseline properties. A temporally controlled ischemia–reperfusion protocol combining rapid oxygen deprivation and defined metabolic restriction was then established, and the resulting phenotype was assessed across functional, metabolic, structural, and transcriptional parameters. Targeted single-pathway interventions were subsequently examined to determine whether isolated modulation is sufficient to alter the integrated injury response.

The second block focuses on implementation of an adaptive Bayesian concentration refinement framework within the cardiac spheroid system. This approach enabled automated exploration of dose-dependent pharmacodynamic behaviour and convergence toward physiological concentration ranges without predefined assumptions.

The third block examines pharmacodynamic responses across two genetically distinct iPSC-derived cardiac lines in order to assess whether line-dependent differences in general drug responsiveness can be detected within the established three-dimensional system.

Together, these experimental components evaluate whether a scalable 3D cardiac platform can reproducibly model multifactorial stress responses while supporting adaptive pharmacological characterization and exploratory assessment of inter-line variability.

3.1. Validation of Differentiation

3.1.1. Confirming Pluripotency

The primary objective of this thesis was to establish a temporally controlled mechanistically grounded three-dimensional *in vitro* model of cardiac ischemia-reperfusion injury using human iPSC-derived cardiac spheroids. Human induced pluripotent stem cells (iPSCs) are somatic cells that have been reprogrammed to a

pluripotent state, enabling differentiation into a wide range of cell types, including cardiomyocytes. In this study, the WTCII-NGN2 iPSC line was used as the main iPSC line for differentiation experiments. Prior to cardiac differentiation, it was necessary to verify that the iPSC lines retained hallmark features of pluripotency. The differentiation potential and stability of stem cell populations directly influence downstream tissue formation and functional performance.[184] Consequently, a combination of morphological assessment and molecular characterization was employed to confirm pluripotent status.

iPSC strains were cultured according to 5.2.1.2. Colonies where fixed and permeabilised according to 5.2.5.1, 5.2.5.2. Immunostaining for the canonical pluripotency markers Oct4 and Nanog was performed by using anti-Oct4 and anti-Nanog (5.1.6) according to 5.2.5.5. Additionally, Hoechst staining was applied to verify cell integrity and morphology (5.2.5.3).

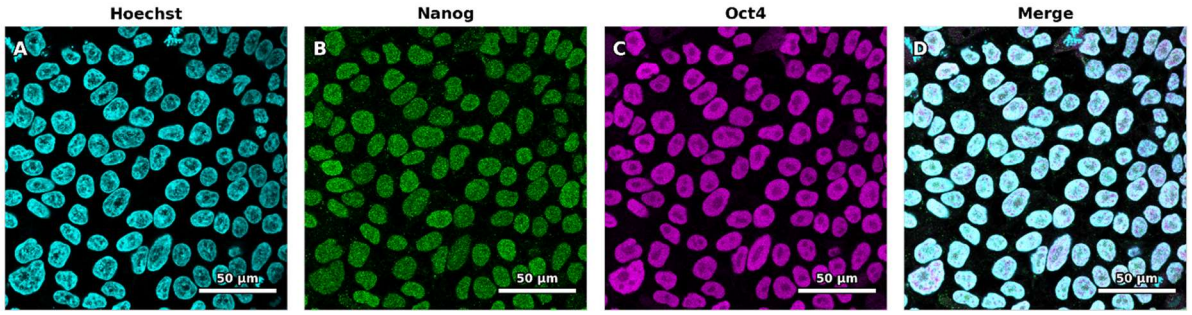

Figure 10 : Immunofluorescence staining of the hiPSC line WTC11-NGN2. Immunofluorescence staining was performed to visualize pluripotency markers in 2D-cultured hiPSCs of the WTC11-NGN2 line. The hiPSCs were cultured in Matrigel-coated wells of a 6-well plate at 37 °C and 5 % CO_2 for 3 days. Cells were subsequently fixed, permeabilized, and non-specific binding sites were blocked. Immunofluorescence staining was then carried out using primary antibodies against Oct-4 (anti-Oct-4 produced in rabbit, ab181537, Lot: GR3236296-2) and Nanog (anti-Nanog produced in mouse, ab62734, Lot: GR3209024-8). (A) Nuclear staining with Hoechst 33342, blue (λ_ex: 405 nm, λ_em: 415–480 nm). (B) Nanog, green (Alexa Fluor® 488 Goat Anti-Mouse, Invitrogen, Ref: A11001, Lot: 3148303; λ_ex: 488 nm, λ_em: 500–550 nm). (C) Oct-4, red (Alexa Fluor® 647 Chicken Anti-Rabbit, Invitrogen, Ref: A21443, Lot: 3188340; λ_ex: 635 nm, λ_em: 650–700 nm). (D) Merged image. Images were acquired using an inverted confocal microscope (Leica Stellaris 5). Scale bar: 50 µm.

As shown in Figure 10, the hiPSCs displayed typical pluripotent stem cell morphology, characterized by compact colony formation, high nucleus-to-cytoplasm ratio, and clearly defined nuclear borders. The average nuclear size was approximately 300 µm². No morphological abnormalities were observed.

Immunofluorescence analysis (Figure 10) demonstrated robust nuclear expression of the canonical pluripotency markers Oct4 and Nanog throughout the cell population. Both markers showed strong and homogeneous staining patterns, and merged images confirmed co-localization within the nuclei of the majority of cells.

These findings indicate maintenance of the undifferentiated state under the applied culture conditions and establish a defined baseline for subsequent differentiation experiments.

3.1.2. Cardiac Differentiation

Based on this validated pluripotency, directed cardiac differentiation was initiated to assess lineage-specific developmental potential. Cardiac differentiation from pluripotent stem cells is governed by tightly regulated developmental signalling pathways that recapitulate early embryonic cardio genesis.[185] Among these, modulation of the Wnt/β-catenin pathway plays a central role in directing lineage specification. Transient activation of Wnt signalling promotes early mesoderm formation, establishing the developmental foundation required for subsequent cardiac commitment.[186,187] Once mesoderm identity is established, inhibition of Wnt signalling becomes necessary to redirect cells toward a cardiac progenitor fate.[186]

This signalling transition is accompanied by coordinated changes in transcriptional regulators. Upregulation of cardiac-associated transcription factors, including GATA4, supports progression into a cardiac progenitor state, while downstream regulators such as TBX5 and MEF2C contribute to maturation toward a cardiomyocyte phenotype.[188] Controlled temporal modulation of these pathways forms the basis of the differentiation strategy used in this study. An overview of the signalling transitions and transcriptional milestones underlying cardiac specification is illustrated in Figure 11.

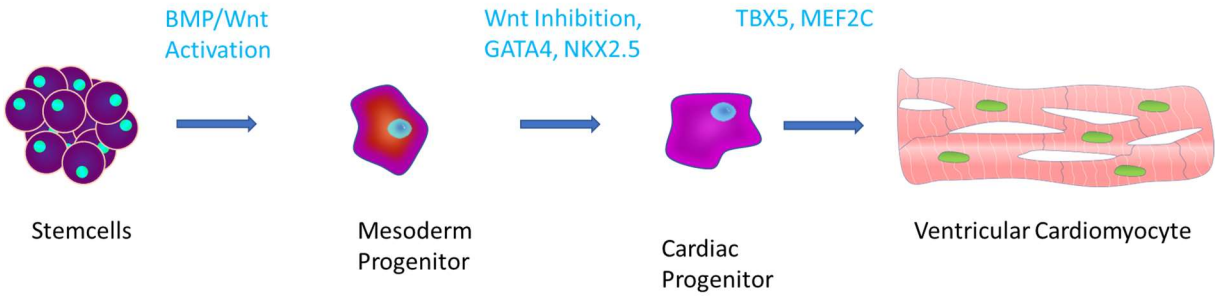

Figure 11: Schematic overview of Cardiac Differentiation. Transient activation of Wnt signaling promotes mesoderm formation from pluripotent stem cells. Subsequent Wnt inhibition drives commitment toward cardiac progenitor identity, accompanied by induction of transcriptional regulators such as GATA4. Downstream factors including TBX5 and MEF2C support maturation toward functional cardiomyocytes.

Cardiac troponin T (cTnT) represents a defining structural and functional marker of cardiomyocytes and is widely used to monitor progression toward a cardiac

phenotype.[189–191] Temporal evaluation of cTnT expression therefore provides a visual readout of differentiation status within developing cardiac spheroids.

Experimentally, spheroids were generated on differentiation day −2 (DD−2) using the hanging drop method described in Section 5.2.2.1. iPSCs were seeded as 10 μL droplets containing 1,000 cells supplemented with ROCK inhibitor and Matrigel, allowing the cells to self-aggregate into spheroids during a 48 h incubation period. Cardiac differentiation was subsequently initiated on differentiation day 0 (DD0) using the STEMCELL™ Technologies STEMdiff™ Ventricular Cardiomyocyte Differentiation Kit, which induces cardiac lineage specification through temporally controlled modulation of key developmental signalling pathways via stage-specific media formulations (Medium A–C). Samples were harvested at differentiation days 0, 2, 5, 9, and 21 to capture key stages of cardiac differentiation. To minimize variability, at least five spheroids were collected per time point. Samples were fixed in 4 % paraformaldehyde and stained for Cardiac troponin T together with Hoechst nuclear stain and phalloidin-TRITC to visualize cytoskeletal organization (5.2.5.1-5.2.5.5). Imaging was performed using fluorescent confocal imaging (Leica Stellaris 5 confocal microscope).

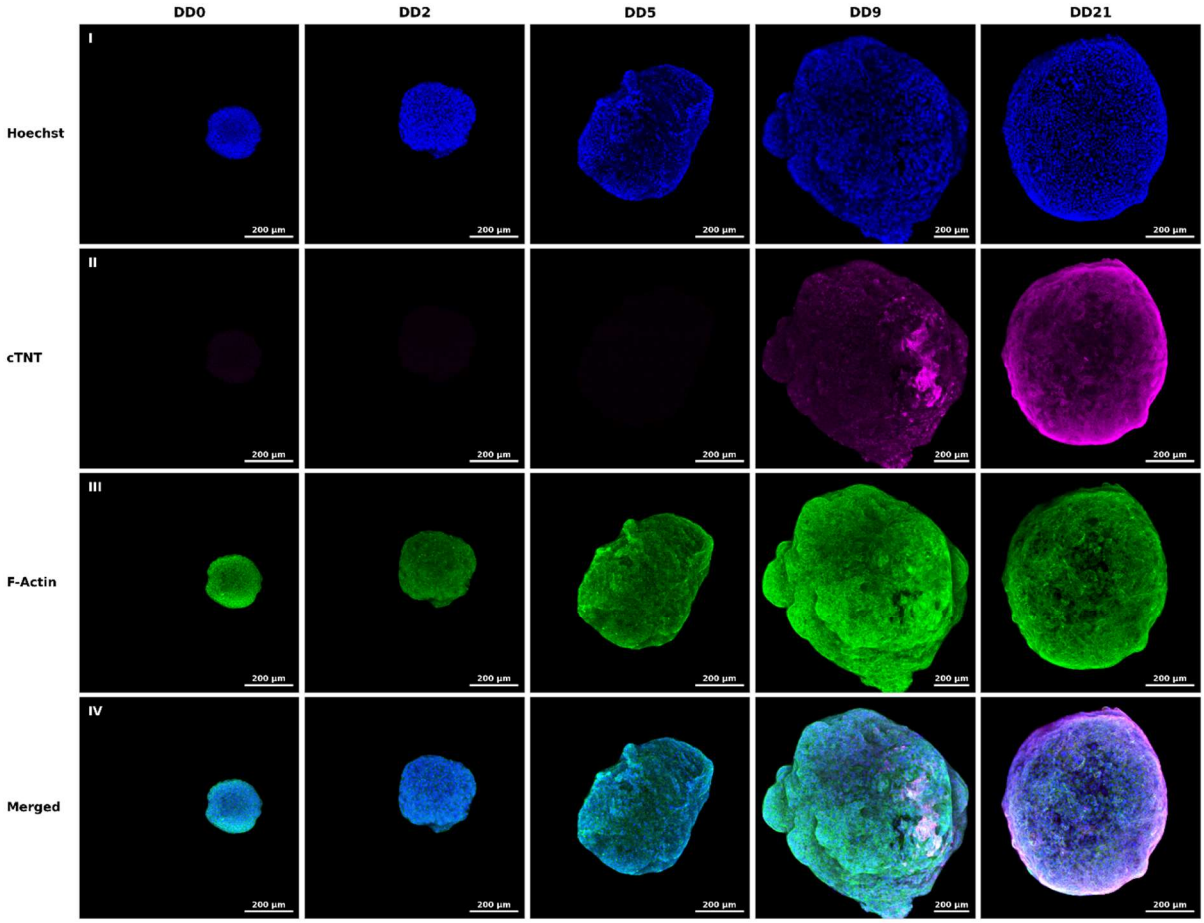

Figure 12: Confocal fluorescence imaging of cardiac spheroid differentiation across five timepoints. Representative maximum intensity projections (MIPs) of WTC11-NGN2 hiPSC-derived cardiac spheroids at differentiation days 0 (DD0), 2 (DD2), 5 (DD5), 9 (DD9), and 21 (DD21). Spheroids were fixed, stained, and imaged by confocal laser scanning microscopy at each timepoint to assess cellular organisation, cardiac troponin T (cTnT) expression, and actin cytoskeleton morphology during directed cardiac differentiation. (I) Nuclear staining with Hoechst 33342 (pseudo-coloured blue; λ_ex: 405 nm). (II) Cardiac troponin T (cTnT; pseudo-coloured green), detected using a mouse monoclonal anti-cTnT primary antibody (Invitrogen, clone 13-11, Cat. No. MA5-12960, Lot: 2504985) and an Alexa Fluor® 647-conjugated goat anti-mouse secondary antibody (Invitrogen, Ref: A21235, Lot: 2306581; λ_ex: 653 nm). cTnT signal was first detectable at DD9 and increased by DD21. (III) Phalloidin-TRITC staining of filamentous actin (F-actin; pseudo-coloured magenta; λ_ex: 561 nm). (IV) Merged composite of all channels (Hoechst, blue; cTnT, green; Phalloidin, magenta). For DD0, DD2, and DD5, the composite includes Hoechst and Phalloidin signals only. Z-stacks were acquired at 1024 × 1024 pixel resolution with a z-step size of 5 µm. Maximum intensity projections were generated. One representative spheroid per timepoint was selected. Images were acquired using a Leica Stellaris 5 confocal laser scanning microscope. Scale bars: 200 µm.

The temporal expression pattern of cTnT is shown in Figure 12. Spheroid morphology changed substantially over the differentiation period. Early-stage spheroids measured approximately 200 µm in diameter and underwent rapid expansion, reaching roughly 800 µm by differentiation day 9, after which overall size remained comparatively stable.

No detectable cTnT signal was observed during early time points (DD0–DD5). Initial cTnT expression became visible at DD9 and increased further by DD21, where signal intensity and distribution were most prominent (Figure 12). At later stages, cTnT-positive cells were distributed throughout the spheroid structure, with increased signal density compared to earlier timepoints.

Cytoskeletal staining revealed progressive structural organization during early development, with increasing filament complexity observed up to DD9. The emergence of structured F-actin patterns is temporally consistent with the onset of detectable cTnT expression.

Together, these findings demonstrate the time-dependent acquisition of cardiomyocyte-associated marker expression during directed differentiation.

3.1.3. Genomic Differentiation Confirmation

To validate the observations obtained from image-based analysis and immunostaining, gene expression profiling was performed using quantitative PCR (qPCR). This approach provided molecular confirmation of differentiation-associated changes that were visually apparent at the cellular level.

RNA was isolated from cardiac spheroids collected at defined stages of differentiation, specifically day 0 (DD0), DD2, DD5, and DD9 and DD21 (5.2.2.1). For each time point, RNA was extracted from entire spheroids to preserve the overall cellular composition and avoid sampling bias introduced by partial dissociation. This strategy ensured that gene expression measurements reflected the integrated state of the three-dimensional construct rather than isolated cell populations (5.2.7).

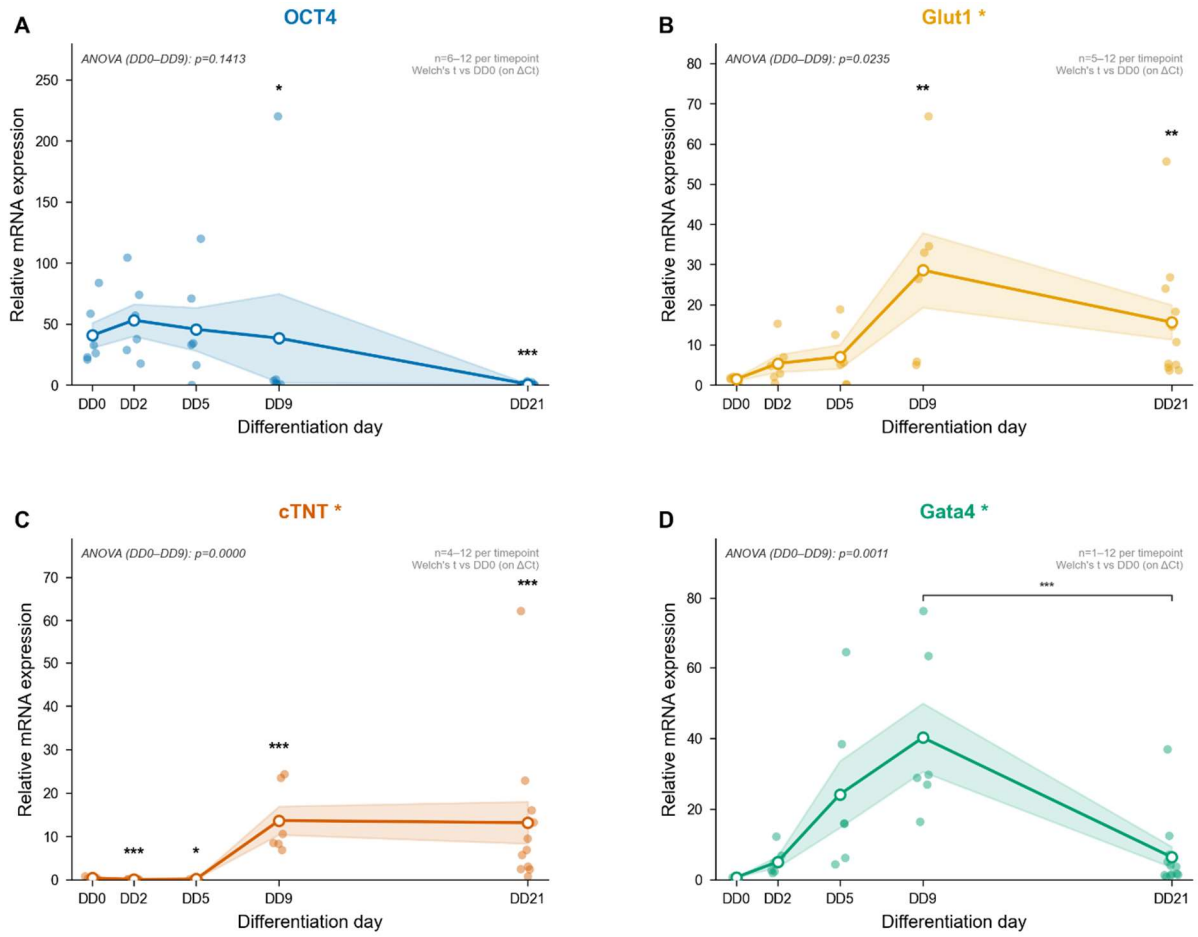

Figure 13: Temporal gene expression dynamics during directed cardiac spheroid differentiation of WTC11 iPSCs. (A-D) Relative mRNA expression of the pluripotency marker OCT4 (A), glucose transporter Glut1 (B), cardiac structural protein cTnT (C), and early cardiac transcription factor GATA4 (D) over the course of 21 days of directed differentiation of WTC11 iPSCs into cardiac spheroids (DD0-DD21). Gene expression was assessed by RT-qPCR and normalised to the housekeeping gene HPRT using the 2^(-dCt) method, which reflects expression relative to the reference gene without calibration to a baseline timepoint. This approach was chosen because three of the four target genes (Glut1, cTnT, GATA4; marked with asterisks) exhibited mean Cq values >= 33 at DD0, indicating expression near the qPCR detection limit; conventional ddCt fold-change normalisation to DD0 would therefore produce unreliable estimates for these genes. Open circles connected by solid lines represent group means; shaded ribbons indicate +/- SEM. Individual biological replicates are shown as semi-transparent scatter points (n = 4-12 per timepoint, pooled across three independent qPCR plates). Statistics: Significance of expression changes relative to DD0 was assessed by Welch's t-test on dCt values (two-tailed, unequal variance): *p < 0.05, **p < 0.01, ***p < 0.001. One-way ANOVA p-values for the DD0-DD9 trend are shown in the upper-left corner of each panel. The bracket in (D) denotes a significant decrease in GATA4 expression between DD9 and DD21 (Welch's t-test, ***p < 0.001), consistent with its role as a transiently expressed early cardiac transcription factor.

qPCR analysis of relative mRNA expression (normalised to HPRT) during directed cardiac spheroid differentiation of WTC11 iPSCs revealed distinct temporal expression profiles for all four genes examined (Figure 13).

cTnT expression remained negligible during early differentiation (DD0–DD5), with Cq values near the detection threshold at these stages. A marked induction was observed at DD9, where mean relative expression reached 13.63 ± 8.02 ($p < 0.001$ vs DD0), and expression levels were maintained at DD21 (13.14 ± 16.79, $p < 0.001$) (Figure 13, C). One-way ANOVA across DD0–DD9 confirmed a highly significant overall trend (F =

131.8, $p < 0.0001$), demonstrating robust activation of the cardiomyocyte-associated marker during mid-to-late differentiation.

Oct4 expression was highest at DD0 (40.71 ± 25.10) and remained elevated through DD5. A decline became apparent from DD9 onward ($p = 0.048$ vs DD0) (Figure 13, A), and by DD21 expression was markedly reduced (0.73 ± 0.95, $p < 0.001$ vs DD0), indicating substantial downregulation of the pluripotency-associated transcript over time.

Glut1 expression increased progressively throughout differentiation. Baseline levels at DD0 were low (1.45 ± 0.77) and peaked at DD9 (28.58 ± 22.80, $p = 0.002$ vs DD0) (Figure 13, B). Although expression decreased slightly by DD21 (15.62 ± 14.95), levels remained significantly elevated compared to DD0 ($p = 0.007$). One-way ANOVA across DD0–DD9 confirmed a significant overall increase ($F = 3.98$, $p = 0.024$).

GATA4 exhibited a transient induction profile. Baseline sampling at DD0 was limited ($n = 1$); therefore, statistical analysis focused on DD2–DD9, where one-way ANOVA demonstrated a significant increase across timepoints ($F = 11.15$, $p = 0.001$), with maximal expression at DD9 (40.19 ± 23.74) (Figure 13, D). Expression declined significantly by DD21 (6.40 ± 10.16; Welch's t-test, $p < 0.0001$).

The combined imaging and gene expression data demonstrate coordinated temporal regulation of pluripotency-associated and cardiomyocyte-specific markers. These findings are discussed below in the context of established molecular mechanisms underlying pluripotency maintenance and cardiac differentiation.

3.1.4. Discussion of Chapter 3.1

3.1.4.1. Molecular Basis of Pluripotency

Pluripotent stem cells are characterized morphologically by compact colonies of cells with high nucleus-to-cytoplasm ratios, prominent nucleoli, and uniform cellular appearance. The WTC11-NGN2 cells analysed in this study displayed these characteristic features, consistent with a maintained pluripotent phenotype.

At the molecular level, pluripotency is governed by a tightly regulated transcriptional network centred around Oct4, Sox2, and Nanog.[192] Oct4 functions as a master regulator of the inner cell mass and is indispensable for maintaining pluripotency. Its expression levels must be precisely controlled, as both upregulation and downregulation can trigger differentiation.[193–195] Nanog, often described as a "gatekeeper" of pluripotency, reinforces the undifferentiated state and prevents spontaneous lineage commitment.

Importantly, Nanog is among the last pluripotency-associated transcription factors to be reactivated during reprogramming and one of the first to be downregulated during differentiation, highlighting its regulatory significance.[196]

3.1.4.2. Importance of Co-Expression Analysis

The confirmation of 100 % co-expression of Oct4 and Nanog in the investigated iPSC population provides strong evidence for maintained pluripotency. During prolonged *in vitro* culture, iPSCs may undergo gradual transcriptional shifts, potentially destabilizing the pluripotency network.[197] Such alterations can lead to heterogeneous populations in which individual markers remain detectable despite functional impairment of the core regulatory circuitry.[198] Therefore, co-expression analysis represents a more reliable assessment of pluripotency than single-marker evaluation.
This distinction is particularly relevant in the context of epigenetic regulation. Promoter methylation or incomplete chromatin remodelling may allow expression of one transcription factor while suppressing another.[199] Furthermore, isolated Oct4 isoform expression has been reported in certain cancer cell lines, contributing to their proliferative capacity without reflecting pluripotency.[200] Simultaneous detection of Oct4 and Nanog thus reduces the likelihood of overlooking partial silencing events. The selection of Oct4 as a central regulator and Nanog as a comparatively sensitive and differentiation-responsive factor provides a robust framework for assessing network integrity.

3.1.4.3. Methodological Considerations

While sufficient for the experimental framework of this study, transcription factor expression alone does not constitute definitive proof of successful reprogramming. Gold-standard validation of pluripotency includes teratoma formation assays or directed trilineage differentiation to demonstrate functional differentiation potential.[201] However, the aim of this thesis was not to re-validate the original reprogramming of the well-established WTC11 cell line, but rather to confirm maintenance of pluripotency during cultivation.[202,203]
Within this context, co-expression of Oct4 and Nanog represents an appropriate and reliable quality control measure. The observed 100 % co-staining of nuclei with both markers indicates that the investigated WTC11-NGN2 population retained pluripotency and differentiation competence at the time of experimental use.

3.1.4.4. Validation of Cardiac Differentiation

Directed differentiation of iPSCs toward a cardiac lineage is a staged process characterized by coordinated transcriptional transitions and progressive structural remodelling.[204] The combined morphological and gene expression analyses performed in this study demonstrate a temporally coherent transition from pluripotency to stable, cardiac spheroids.

Co-expression of Oct4 and Nanog confirmed a homogeneous pluripotent starting population, further supported by characteristic nuclear morphology. Establishing this baseline is critical, as residual pluripotency or partially primed subpopulations can introduce downstream lineage variability.[205] The progressive decline of Oct4 expression, resulting in near-complete suppression by DD21, confirms successful exit from the pluripotent state.[206] Transient Oct4 signal at intermediate stages likely reflects asynchronous differentiation within the 3D construct rather than incomplete lineage commitment.

Complete loss of pluripotency is particularly important for the intended reperfusion model. Undifferentiated cells exhibit fundamentally different metabolic and stress-response behaviour, which could affect injury readouts.[207] The near-complete reduction of Oct4 therefore ensures a cardiomyocyte-dominant population suitable for pathophysiological modelling.

The transcriptional shift away from pluripotency was accompanied by morphological remodelling. Early spheroids displayed compact architecture with nuclei occupying a large proportion of cell volume. Rapid expansion until approximately DD9 match with mesoderm induction and reduction of pluripotency markers, reflecting proliferative activity during early lineage specification.[204,208,209] Stabilization of spheroid size beyond DD9, together with minimal Oct4 expression, suggests a transition from proliferative expansion toward lineage-specific maturation.[210]

Loss of pluripotency was accompanied by upregulation of GATA4, a key cardiac progenitor transcription factor.[188] Its peak expression around DD9 marks active cardiac specification. The subsequent reduction by DD21 does not indicate incomplete differentiation but rather transition from progenitor dominance toward structural cardiomyocyte stabilization.[206] This interpretation is supported by sustained and robust induction of cTnT expression at both transcript and protein levels closely mirroring structural maturation. Transcriptional induction preceded detectable sarcomeric organization, consistent with the temporal delay between mRNA expression and assembly of contractile machinery.[211] Beginning at DD9, cTnT-positive

structures emerged and progressively integrated into increasingly organized F-actin networks. By DD21, widespread cTnT expression and defined cytoskeletal architecture indicate stable cardiomyocyte identity.[212]

The Glut1 expression profile further supports developmental progression. Its peak at DD9 likely reflects high glycolytic demand during early differentiation. The gradual decline toward DD21 is consistent with metabolic maturation and increasing mitochondrial reliance characteristic of cardiomyocytes.[213] Persistent expression may be attributable to the multicellular composition of the spheroids rather than incomplete differentiation, as endothelial and fibroblast populations maintain higher glycolytic activity.[214]

Notably, DD21 spheroids exhibited heterogeneous and occasionally lobed morphology. Such structural variability is inherent to 3D aggregates and reflects diffusion gradients, localized proliferation, and mechanical remodelling within the construct.[215] Rather than indicating inconsistency, this spatial heterogeneity likely enhances physiological relevance by approximating the non-uniform architecture of native myocardium.[216] Importantly, despite morphological variability, gene expression patterns remained consistent across replicates, indicating robust lineage commitment at the population level.

Collectively, the integrated molecular and structural findings demonstrate successful recapitulation of key developmental checkpoints: exit from pluripotency, mesoderm induction, cardiac progenitor formation, and stabilization of cardiomyocyte identity.[217] The resulting DD21 spheroids exhibit organized sarcomeric structure, sustained cardiac marker expression, and metabolic features compatible with mitochondrial dependence.

Establishing this stable and developmentally coherent 3D cardiac construct provides the essential foundation for subsequent hypoxia, reperfusion, and drug-screening experiments. The confirmed absence of pluripotency, structural maturation, and transcriptional stability indicate that the model possesses the biological integrity required for pathophysiological interrogation.

3.1.4.5. Cardiac Differentiation Protocol

Cardiac differentiation was performed using the STEMdiff™ Ventricular Cardiomyocyte Differentiation Kit. Although the exact media composition is not disclosed, the observed transcriptional and structural dynamics align closely with established Wnt-modulated cardiogenesis protocols. Early aggregation (DD−2 to DD0)

relied on ROCK inhibition (Y-27632) to prevent dissociation-induced apoptosis and support stable 3D spheroid formation.[218]

Mesoderm induction at DD0 is consistent with transient activation of canonical Wnt signalling, commonly achieved via GSK3β inhibition. Stabilized β-catenin initiates mesodermal gene expression, establishing the foundation for cardiac lineage commitment.[204] The inclusion of Matrigel at this stage likely enhanced fate stabilization through extracellular matrix support and integrin-mediated signalling, which may be particularly relevant in a 3D environment.[219]

Further mesoderm stabilization and Wnt inhibition are essential to prevent lineage drift and drive cardiac progenitor specification.[220] The observed temporal peak of GATA4 expression around DD9, followed by stable cTnT expression and emergence of spontaneous contractility, is consistent with successful transition from mesoderm to cardiac progenitor and finally to differentiated cardiomyocytes.[221] Reduced retinoic acid signalling likely favoured ventricular specification, aligning with the functional characteristics observed at later stages.[222,223]

Transition to maintenance media with insulin supplementation supports metabolic maturation and survival of beating cardiomyocytes. The progressive structural organization and stabilization of cTnT expression at DD21 suggest completion of lineage commitment and establishment of a functional cardiomyocyte-containing spheroid model.

3.1.4.6. Limitations of Commercial Kit Use

While the use of a commercial differentiation kit limits pathway-specific fine-tuning, this approach enhances reproducibility, a critical requirement for downstream pathophysiological modelling and automated drug screening. The objective of this thesis was not the optimization of cardiomyocyte yield, but the establishment of a stable and scalable 3D cardiac platform. Standardized media minimized media composition variability across differentiation formats (hanging drop and automated 384-well plates (5.2.2)) and ensured that observed downstream effects reflect experimental modulation rather than inconsistencies in differentiation.

3.2. Characterization

3.2.1. Composition of Cardiac Spheroids

In addition to cardiomyocytes, multiple supporting cell populations play essential roles in cardiac structure and pathophysiology. A representative *in vitro* cardiac model should therefore contain endothelial and fibroblast-like cells alongside contractile cardiomyocytes. Endothelial cells constitute a large fraction of cardiac tissue at the cellular level, while fibroblasts, although fewer in number, contribute substantially to tissue organization and mechanical properties.[224] Apart from shear cell volume they also serve crucial parts in pathophysiology and are thus mandatory for disease modelling.[225]

To confirm the presence of these key cell populations, immunostaining was performed on fully differentiated spheroids at day 21. Structural marker proteins were selected to identify major cardiac cell types: VE-cadherin to verify endothelial cells, Alpha-smooth muscle actin (α-SMA) to identify fibroblast-associated structures, and Cardiac troponin T to confirm cardiomyocyte presence.

To assess loss of pluripotency, staining against Oct4 was additionally performed. Oct4 expression is associated with undifferentiated stem cells, therefore, absence of detectable signal supports successful lineage commitment and the lack of residual pluripotent cells.

Spheroids were fixed in 4 % paraformaldehyde and immunochemically stained according to the protocols described in Sections 5.2.5.1, 5.2.5.2, 5.2.5.3, 5.2.5.5. Confocal imaging was conducted using a Leica Stellaris 5 microscope.

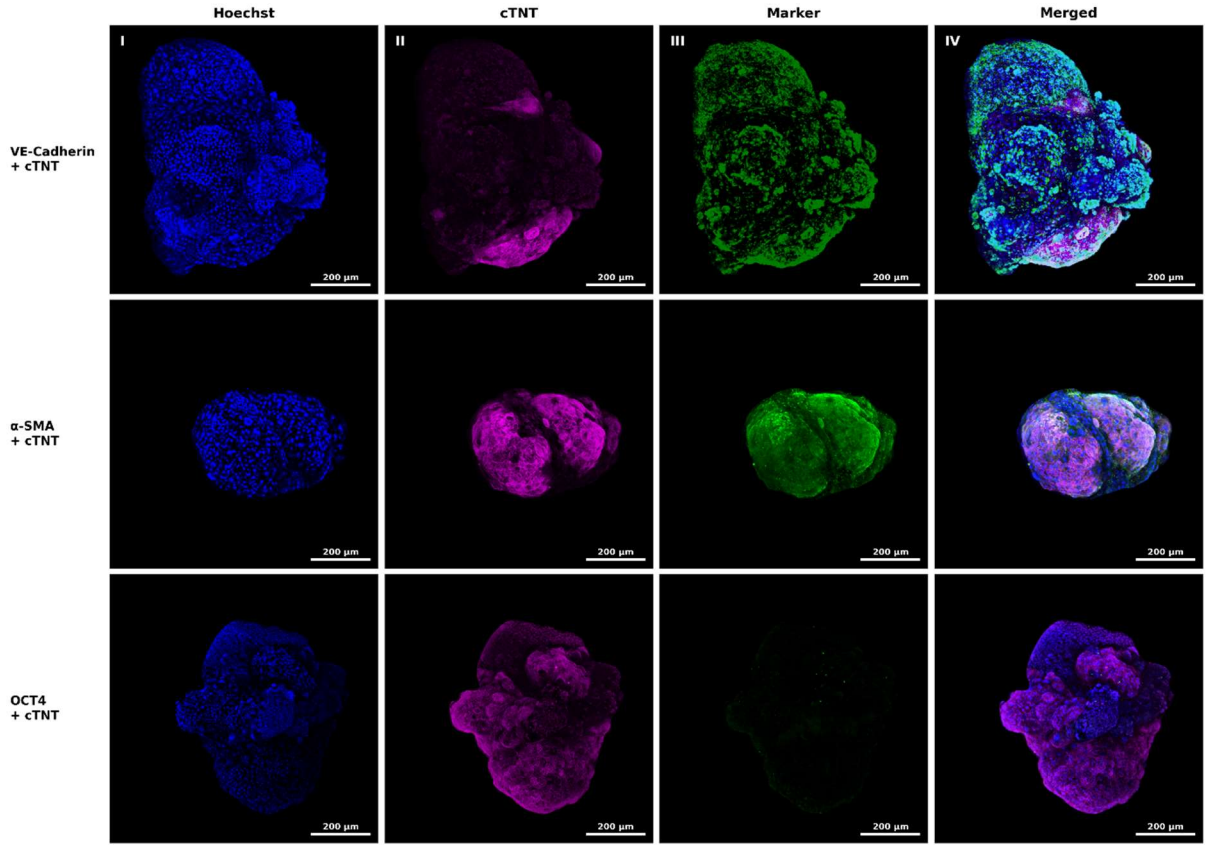

Figure 14: Confocal fluorescence imaging of iPSC-derived cardiac spheroid cell-type composition at differentiation day 21. Representative maximum intensity projections (MIPs) of WTC11-NGN2 hiPSC-derived cardiac spheroids at differentiation day 21 (DD21), showing co-staining of cardiac troponin T (cTnT) with VE-Cadherin (endothelial marker), α-smooth muscle actin (α-SMA; mesenchymal marker), or OCT4 (pluripotency marker). Spheroids were generated in 384-well plates, fixed at DD21, and stained for immunofluorescence analysis. (I) Nuclear staining with Hoechst 33342 (pseudo-coloured blue; λ_ex: 405 nm). (II) Cardiac troponin T (cTnT; pseudo-coloured magenta), detected using a mouse monoclonal anti-cTnT antibody (Invitrogen, clone 13-11, Cat. No. MA5-12960) and either an Alexa Fluor® 488-conjugated goat anti-mouse secondary antibody (Invitrogen, Ref: A11001; λ_ex: 488 nm) or an Alexa Fluor® 647-conjugated goat anti-mouse secondary antibody (Invitrogen, Ref: A21235; λ_ex: 638 nm), depending on marker combination. (III) Group-specific marker (pseudo-coloured green): VE-Cadherin (rabbit anti-VE-Cadherin, Abcam, ab33168), α-SMA (Proteintech), or OCT4 (rabbit monoclonal, Abcam, ab181537). Corresponding secondary antibodies were Alexa Fluor® 647-conjugated goat anti-rabbit (Invitrogen, Ref: A21247; λ_ex: 638 nm) or Alexa Fluor® 488-conjugated chicken anti-goat (λ_ex: 488 nm), applied according to fluorophore configuration. (IV) Merged composite of all three channels. Z-stacks were acquired at 1024 × 1024 pixel resolution with a z-step size of 5 µm using a Leica STELLARIS 5 confocal laser scanning microscope. Maximum intensity projections were generated along the z-axis. One representative spheroid per staining group is shown. Scale bar: 200 µm.

The cellular composition of iPSC-derived cardiac spheroids at differentiation day 21 is shown in Figure 14. Immunofluorescence staining demonstrated robust cTnT expression throughout the spheroids, consistent with the presence of differentiated cardiomyocytes.

VE-cadherin-positive cells were detected in distinct regions within the spheroid, displaying structured staining patterns suggestive of endothelial organisation. Overlay with cTnT revealed adjacent but partially overlapping signal distributions, indicating spatial coexistence of endothelial and cardiomyocyte populations.

α-SMA staining appeared in localized high-intensity clusters. These regions partially overlapped with cTnT-positive areas but were not uniformly distributed, instead forming discrete niche-like structures within the spheroid (Figure 14).
No detectable OCT4 signal above background levels was observed, indicating absence of residual pluripotent cell populations at this stage.

In addition to qualitative characterization by immunofluorescence imaging, functional assessment of contractile activity represents a key feature of cardiac spheroids. Given the importance of rhythmic stability in cardiac physiology and drug safety evaluation, quantitative analysis of beating behaviour and calcium transients was performed.

3.2.2. Beating and Calcium Transient Characterization

Cardiac spheroids were monitored throughout differentiation from differentiation DD11 to DD21 using time-lapse acquisition on an LED microscope to assess changes in spontaneous beating behaviour.
In addition, beating properties at DD21 were compared between two differentiation approaches: the hanging drop method and automated differentiation using the CellXpress.ai platform. CellXpress.ai enables automated spheroid generation and medium exchanges in multiwell plates through robotic liquid handling and integrated incubation, allowing standardized and scalable cardiac differentiation. This automation provides a foundation for future closed-loop optimization strategies aimed at improving differentiation efficiency and reproducibility. (5.2.2). Brightfield time-lapse imaging was performed for both conditions, and beating behaviour was quantified using motion tracking analysis implemented in a MuscleMotion-based Python workflow (Section 5.2.6.1). In this approach, contractile activity is derived from frame-to-frame changes in pixel intensity within the spheroid, allowing contraction peaks and beating frequency to be extracted from the resulting motion trace.

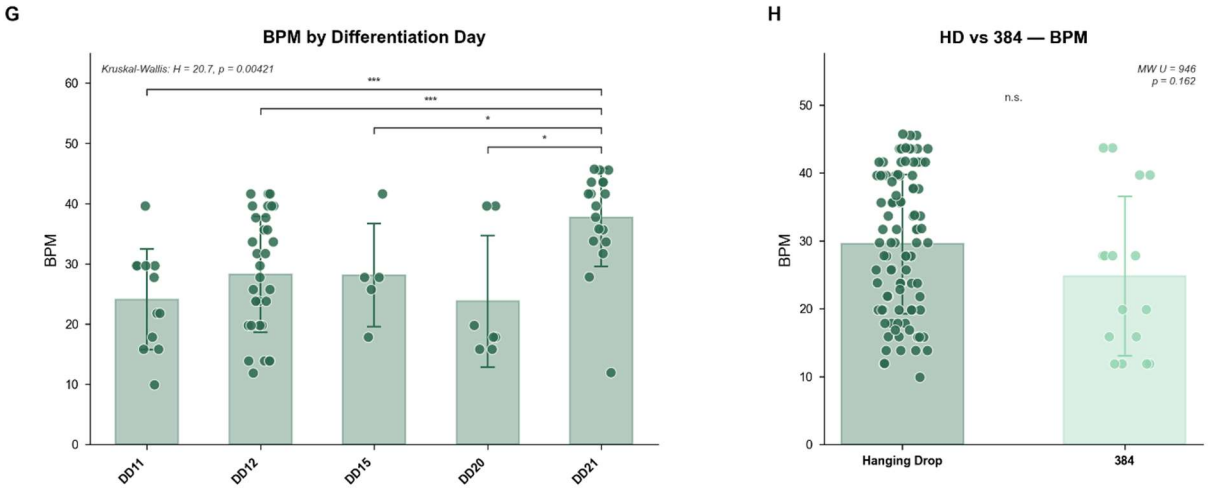

Figure 15: Quantification of spontaneous beating rates during cardiac spheroid differentiation. Beating rates were quantified from contraction signal analysis of cardiac spheroids generated either by hanging drop culture or automated differentiation in 384-well U-bottom plates. Contraction signals were derived from frame-to-frame pixel intensity changes and analysed using prominence-based peak detection. Only spheroids with at least two detected beats were included. (G) Beating rate (beats per minute, BPM) as a function of differentiation day for hanging drop–derived spheroids. Bars represent group means ± standard deviation; individual data points are shown as jittered scatter plots. Only differentiation days included in at least one statistically significant pairwise comparison are displayed. A Kruskal–Wallis H test revealed a significant effect of differentiation day on beating rate ($H = 20.7$, $p = 0.004$). Post hoc Mann–Whitney U tests identified significantly lower beating rates at DD11 and DD12 compared to DD21 (***$p < 0.001$), and at DD15 and DD20 compared to DD21 (*$p < 0.05$). (H) Comparison of beating rates between hanging drop ($n = 97$) and automated 384-well U-bottom plate cultures ($n = 16$). Bars represent group means ± standard deviation with individual data points overlaid. No statistically significant difference was detected between culture methods (Mann–Whitney U test, $U = 946$, $p = 0.162$).

To assess how spontaneous beating activity evolves during cardiac differentiation, beating rates were quantified from contraction signal analysis of hanging drop–derived cardiac spheroids across multiple time points (DD11–DD27). Contraction signals were derived from imaging by measuring the frame-to-frame pixel intensity changes in brightfield recordings, and beats were detected using prominence-based peak detection. Only preparations with at least two detected beats were included ($n = 97$). Due to non-normal distribution and unequal group sizes, non-parametric tests were applied.

A Kruskal–Wallis test demonstrated a significant effect of differentiation day on beating rate ($H = 20.7$, $p = 0.004$; Figure 15, panel G). Post hoc pairwise Mann–Whitney U tests identified significantly lower beating rates at early differentiation time points compared to DD21: both DD11 (24.1 ± 8.4 BPM) and DD12 (28.2 ± 9.6 BPM) were significantly lower than DD21 (37.7 ± 8.1 BPM; $p < 0.001$ for both comparisons). In addition, DD15 (28.1 ± 8.6 BPM) and DD20 (23.8 ± 10.9 BPM) showed lower beating rates relative to DD21 ($p < 0.05$ for both).

Overall, beating rate increased across differentiation time points, with the highest mean rates observed at DD21 (Figure 15, panel G).

To determine whether automated differentiation in a 384-well U-bottom plate format alters spontaneous beating behaviour, beating rates were compared between hanging drop spheroids (n = 97) and 384-well spheroids (n = 16).
No significant difference in beating rate was detected between the two culture methods (hanging drop: 29.6 ± 10.2 BPM; 384-well: 24.8 ± 11.7 BPM; Mann–Whitney U = 946, p = 0.162; Figure 15, panel H).
These findings indicate comparable spontaneous beating rates between spheroids generated using manual hanging drop culture and automated 384-well differentiation under the conditions tested.

To further characterise functional maturation beyond contraction frequency alone, intracellular calcium dynamics were analysed at DD21.
For calcium imaging analysis, spheroids at DD21 were stained with the fluorescent calcium indicator Fluo-4 AM to visualize intracellular calcium transients (Section 5.2.6.2). Spheroids were incubated with Fluo-4 AM, washed to remove excess dye, and allowed to undergo de-esterification prior to imaging. Fluorescence time-lapse recordings of calcium transient–associated beating patterns were then acquired over a 30-second period using a Leica DM IL LED microscope. These recordings were used to assess calcium handling dynamics and contraction synchrony.

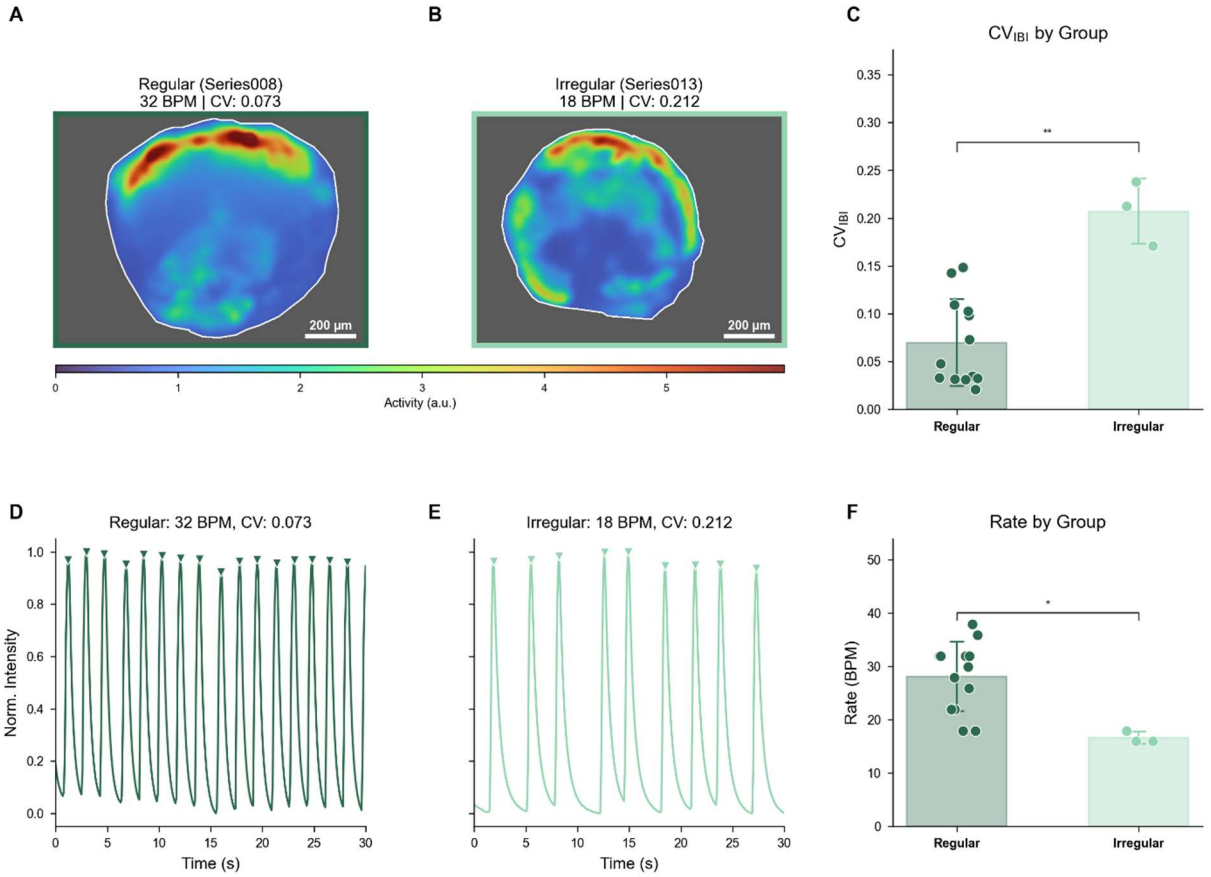

Figure 16: Calcium imaging–based characterization of cardiac spheroid beating patterns. Spontaneous calcium transients were recorded from 16 iPSC-derived cardiac spheroids using fluorescent calcium indicator imaging (10 Hz, 30-second recordings). Spheroids were classified based on the coefficient of variation of inter-beat intervals (CV IBI) into Regular (CV IBI < 0.15, n = 13) and Irregular (CV IBI ≥ 0.15, n = 3) rhythm groups. Representative recordings were selected as those closest to the respective group mean CV IBI. (A, B) Representative calcium activity maps from regular (A) and irregular (B) rhythm spheroids. Images display temporal variance of frame-to-frame fluorescence intensity changes, with warmer colours indicating higher calcium transient activity. Spheroid boundaries were segmented and background masked prior to visualization. Beating rate (BPM) and CV IBI are indicated for each preparation. Scale bars: 200 µm. (C) Comparison of CV IBI between Regular and Irregular groups. Bars represent group means ± standard deviation with individual data points overlaid. CV IBI was significantly higher in the Irregular group (Mann–Whitney U test, **p < 0.01). (D, E) Representative detrended and normalised calcium fluorescence traces from regular (D) and irregular (E) spheroids. Inverted triangles indicate detected calcium transient peaks. (F) Comparison of mean beating rates between rhythm groups. Bars represent group means ± standard deviation with individual data points overlaid. Regular spheroids exhibited significantly higher beating rates compared to irregular spheroids (Mann-Whitney U test, *p < 0.05).

To characterise spontaneous electrophysiological activity of iPSC-derived cardiac spheroids, calcium transients were recorded from 16 preparations using fluorescent calcium indicator imaging (10 Hz, 30-second acquisition windows). Beating rhythm regularity was quantified using the coefficient of variation of inter-beat intervals (CV IBI), a dimensionless measure of temporal variability between successive calcium peaks. The coefficient of variation (CV) is a statistical measure of the relative variability of data. It expresses the standard deviation as a proportion of the mean. Based on a predefined threshold of 0.15, spheroids were classified as regular (CV IBI < 0.15; n = 13) or irregular (CV IBI ≥ 0.15; n = 3). The majority of preparations (81 %) exhibited low beat-to-beat variability consistent with stable rhythmic activity.

Spatial analysis of calcium transient activity revealed distinct activity patterns between groups. Activity maps, calculated as the temporal variance of frame-to-frame fluorescence intensity differences, showed comparatively homogeneous calcium activity in regular spheroids (Figure 16, panel A), whereas Irregular spheroids displayed heterogeneous distributions with focal regions of elevated activity (Figure 16, panel B).

Quantitative comparison confirmed significantly higher CV IBI values in the irregular group (0.207 ± 0.034) compared to the regular group (0.070 ± 0.045; Mann–Whitney U = 0, p = 0.004; Figure 16, panel C). The distributions of CV IBI values did not overlap between groups.

Representative calcium fluorescence traces further illustrate the temporal differences between phenotypes. Regular spheroids exhibited consistent inter-beat intervals throughout the 30-second recording window (32 BPM, CV IBI = 0.073; Figure 16, panel D), whereas irregular spheroids showed variable inter-beat timing (18 BPM, CV IBI = 0.212; Figure 16, panel E).

In addition to rhythm variability, spontaneous beating frequency differed between groups. Regular spheroids displayed higher beating rates (28.1 ± 6.5 BPM) compared to irregular spheroids (16.6 ± 1.2 BPM; Mann-Whitney U = 38, p = 0.014; Figure 16, panel F).

Collectively, these findings define the functional maturation state of the spheroids at DD21, characterised by coordinated calcium transients and quantifiable differences in rhythm stability.

3.2.3. Discussion of Chapter 3.2

The functional and molecular analyses presented in this study demonstrate the successful generation of multicellular cardiac spheroids exhibiting structural organisation, lineage specification, and spontaneous contractile activity. However, the establishment of a representative cardiac tissue model extends beyond the presence of contractile cardiomyocytes alone.

The native myocardium is a multicellular system fundamentally defined by close interactions between cardiomyocytes, endothelial cells, and fibroblasts.[226] Fibroblasts contribute not only to structural organisation and mechanical stability but also play central roles in stress response and tissue remodelling.[227] The immunostaining data confirm the presence of these major cardiac cell populations within the spheroids while simultaneously verifying the absence of residual pluripotent cells (Figure 14).

VE-cadherin–positive structures were detected throughout the entirety of the cardiac spheroid, indicating the presence of endothelial-like populations.[228] Their spatial coexistence with cTnT-positive regions suggests structural integration rather than simple clustering. This feature is essential for recapitulating *in vivo* architecture, where each cardiomyocyte is in close proximity to endothelial cells to ensure efficient oxygen and nutrient delivery and to overcome diffusion limitations beyond approximately 200 µm.[229] In addition to structural and metabolic support, endothelial cells play a decisive role in stress signalling and inflammatory modulation, making their presence indispensable for a representative ischemia–reperfusion model.[230]

Fibroblast-associated regions, visualized through α-SMA staining, appeared as clustered signal domains in-between cTnT-positive areas. *In vivo*, fibroblasts are distributed between cardiomyocytes, where they contribute to tissue stiffness, extracellular matrix organization, and mechanical coupling.[227,231] It is noteworthy that α-SMA primarily marks activated myofibroblasts.[232,233] This activation capacity is particularly relevant for modelling reperfusion injury. Following cardiomyocyte apoptosis *in vivo*, fibroblasts proliferate and produce extracellular matrix components to stabilize damaged regions.[234] The presence of α-SMA–positive cells within the spheroids therefore represents an important prerequisite for recapitulating post-injury remodelling dynamics (Figure 14).

Importantly, no detectable OCT4 signal was observed at this stage. The complete loss of pluripotency is crucial for downstream functional analysis, as pluripotent cells exhibit fundamentally different metabolic and calcium-handling characteristics that could interfere with calcium- or stress-response readouts.[207] The absence of OCT4 confirms stable lineage commitment and supports interpretation of subsequent functional experiments.

The spatial heterogeneity observed in endothelial and α-SMA distribution reflects intrinsic properties of 3D tissue organization. Diffusion gradients, cell–cell interactions, and localized mechanical stress likely contribute to microdomain formation within the spheroid.[235] While such heterogeneity introduces variability, it simultaneously enhances physiological relevance.

Unlike 2D monolayers, 3D aggregates allow for radial oxygen and nutrient gradients, which are central determinants of cardiac stress responses.[236,237] The coexistence of contractile and supporting populations within this architecture establishes a foundation for modelling pathophysiological processes such as fibrosis, ischemia-induced endothelial dysfunction, and remodelling.

Thus, structural heterogeneity should not be interpreted as inconsistency, but rather as a defining feature of the model's tissue-like behaviour

3.2.3.1. Critical Methodological Considerations

While immunostaining provides strong qualitative confirmation of the presence and spatial organization of relevant cell types, it does not allow for precise quantification of population ratios within the spheroids.[238,239] Techniques such as flow cytometry would, in principle, enable more accurate compositional analysis.[240] However, such approaches require complete dissociation into viable single-cell suspensions.

Mature cardiac spheroids displayed substantial structural integrity and extracellular matrix cohesion, rendering enzymatic dissociation inefficient without extensive mechanical disruption. Prolonged enzymatic digestion and mechanical force compromised cellular integrity and phenotype, thereby limiting the reliability of downstream single-cell analyses.[241,242] Given that preservation of three-dimensional architecture is central to the physiological relevance of the model, spatially resolved immunostaining was prioritized over destructive quantification methods.

Consequently, while exact percentage distributions cannot be provided, the combined structural evidence confirms the presence and integration of the principal cardiac cell types required for representative tissue-level modelling.

3.2.3.2. Functional Validation of Maturation, Scalability, and Baseline Clustering

For ischemia–reperfusion modelling and pharmacological screening to be interpretable, the underlying cardiac constructs must exhibit stable and mature excitation–contraction coupling.[243] Structural differentiation alone is insufficient, functional maturation must be demonstrated through coordinated calcium cycling and reproducible rhythmic activity.[244]

3.2.3.3. DD21 as a Functionally Mature Baseline

Between differentiation day 11 and day 21, spheroids exhibited a significant increase in spontaneous beating frequency. DD21 constructs displayed significantly higher and more stable BPM, indicating maturation of excitation–contraction coupling. This acceleration is consistent with improved sarcomeric organization, enhanced electrical coupling, and refinement of calcium handling mechanisms, including more efficient SERCA-mediated reuptake and synchronized RyR2 release.[244,245]

The stabilization of pacing frequency and reduction in early-stage variability at DD21 define this time point as a functionally mature baseline suitable for downstream stress

modelling. Using earlier stages would introduce developmental variability, whereas DD21 provides a reproducible electrophysiological reference state.

3.2.3.4. Automation Preserves Functional Integrity

To enable scalability, spheroids generated using the CellXpressAI, an automated platform capable of handling 384-well U-bottom plates, was compared to hanging drop differentiation derived cardiac spheroids. No significant differences in spontaneous beating frequency were observed between methods (Figure 15). This functional equivalence confirms that automated production does not impair calcium handling or excitation–contraction coupling, thereby validating the use of scalable formats for high-throughput applications.

3.2.3.5. Baseline Rhythm Heterogeneity and Closed-Loop Gating

Despite overall maturation, DD21 spheroids displayed two rhythmic phenotypes: a regular cluster characterized by low beat-to-beat variability and higher pacing rates, and an irregular cluster exhibiting elevated variability and reduced BPM. The irregular group additionally showed increased diastolic calcium levels, suggesting incomplete calcium clearance and impaired coupling efficiency (Figure 16).[246]

Such heterogeneity is an inherent property of three-dimensional multicellular systems, where pacemaker positioning, gap junction distribution, and spatial conduction dynamics produce network variability. Rather than indicating methodological inconsistency, this variability reflects biological complexity analogous to regional conduction heterogeneity in native myocardium.[226,247]

To ensure robustness of subsequent closed-loop concentration optimization, spheroids were excluded based on predefined rhythm stability thresholds derived from baseline BPM and beat-to-beat variability. This functional gating strategy reduced confounding electrophysiological instability while preserving biologically relevant heterogeneity. By implementing electrophysiological quality control prior to pharmacological interrogation, the platform enhances both experimental reproducibility and physiological relevance.

These inclusion criteria were subsequently implemented within the closed-loop optimization workflow (see Section 3.6.4), ensuring that concentration–response analyses were performed exclusively on rhythmically stable, actively contracting spheroids. This step is particularly critical because drug toxicity was assessed using MTT-based metabolic readouts.[248] Although contraction frequency contributes to ATP consumption, cardiomyocyte energy demand is strongly influenced by calcium

cycling efficiency. Elevated diastolic calcium, impaired reuptake, or asynchronous activation can alter mitochondrial workload independent of beat rate, thereby introducing baseline metabolic variability unrelated to pharmacological intervention.[249] Exclusion of irregular and non-beating spheroids therefore minimizes energetic heterogeneity and ensures that changes in metabolic activity more accurately reflect drug-induced effects rather than pre-existing functional instability.

3.2.3.6. Integrative Perspective

Together, these findings establish DD21 as a functionally mature and reproducible stage for experimental manipulation, confirm that automated differentiation is capable of preserving electrophysiological integrity, and justify baseline clustering as a methodological safeguard within the closed-loop framework. The herein established triad of maturation validation, scalability, and controlled heterogeneity provides the functional foundation for the ischemic and pharmacological studies presented in this thesis.

3.3. Pathophysiological Microenvironment

After establishing the functional maturity of the cardiac spheroid model, the focus shifted toward recreating key elements of the ischemic microenvironment in a controlled *in vitro* setting. Because ischemia includes simultaneous alterations in oxygen availability, metabolic support, mechanical load, and extracellular composition, no single manipulation is sufficient to reproduce its complexity. Therefore, several distinct strategies were evaluated, including hydrogel-mediated stiffness modulation, atmospheric oxygen control using a microscope gas chamber, diffusion limitation via mineral oil overlay and nitrogen flux, and modification of extracellular ionic conditions with adjusted Tyrode's solution. The following sections outline the experimental outcomes associated with each method.

3.3.1. Hydrogels as Disease Model

Hydrogels are widely used in tissue engineering to enhance cell viability by providing a three-dimensional microenvironment that increases structural complexity and cell–matrix interactions.[250,251] Beyond supporting survival, hydrogels offer tuneable mechanical properties that allow *in vitro* reconstruction of tissue-level biomechanical changes associated with pathological conditions.[252,253] In the context of cardiac ischemia–reperfusion injury, regional tissue remodelling leads to increased stiffness

and impaired contractility, which in turn alters the mechanical load experienced by surrounding viable cardiomyocytes.[254]

Following ischemic damage, affected regions contribute minimally to contractile force while exhibiting increased stiffness. Neighbouring cardiomyocytes must compensate for this mechanical imbalance to maintain overall tissue function, resulting in elevated workload and altered stress distribution.[255] Replicating these biomechanical features *in vitro* provides an opportunity to study how cardiac tissue responds to localized stiffness and injury-related mechanical constraints.

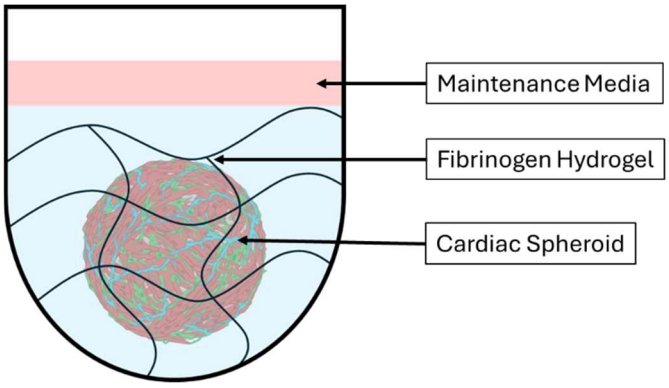

Figure 17: Experimental visualization hydrogel embedment. The cardiac spheroid is completely embedded in a fibrinogen hydrogel, with maintenance media added after gelation to support cardiac function. Gas composition unaltered.

To model this environment, cardiac spheroids were embedded within fibrinogen-based hydrogels, enabling controlled mechanical confinement while preserving cellular organization. Spheroids were placed in a fibrinogen solution and gelation was initiated by addition of thrombin, resulting in rapid polymerization of a fibrin matrix surrounding the spheroid. (5.2.4) (Figure 17). This configuration was designed to approximate stiffness-associated effects observed in reperfusion injury and to evaluate their influence on spheroid contractile behaviour.

Embedded spheroids, alongside normoxic controls, were monitored using the ImageXpress HT.ai live-cell imaging system. Contractile activity was quantified through repeated stream acquisitions, in which continuous image sequences were recorded at 12.38 frames per second (fps). This acquisition mode records consecutive frames with the camera running continuously rather than capturing discrete time-lapse images, allowing high-temporal-resolution measurement of spheroid contractions during repeated 12.5-second recordings over a 6-hour observation period. This approach allowed assessment of beating dynamics by comparing fibrin hydrogel–embedded spheroids with non-embedded control spheroids, providing insight into how hydrogel-mediated mechanical confinement influences functional cardiac behaviour.

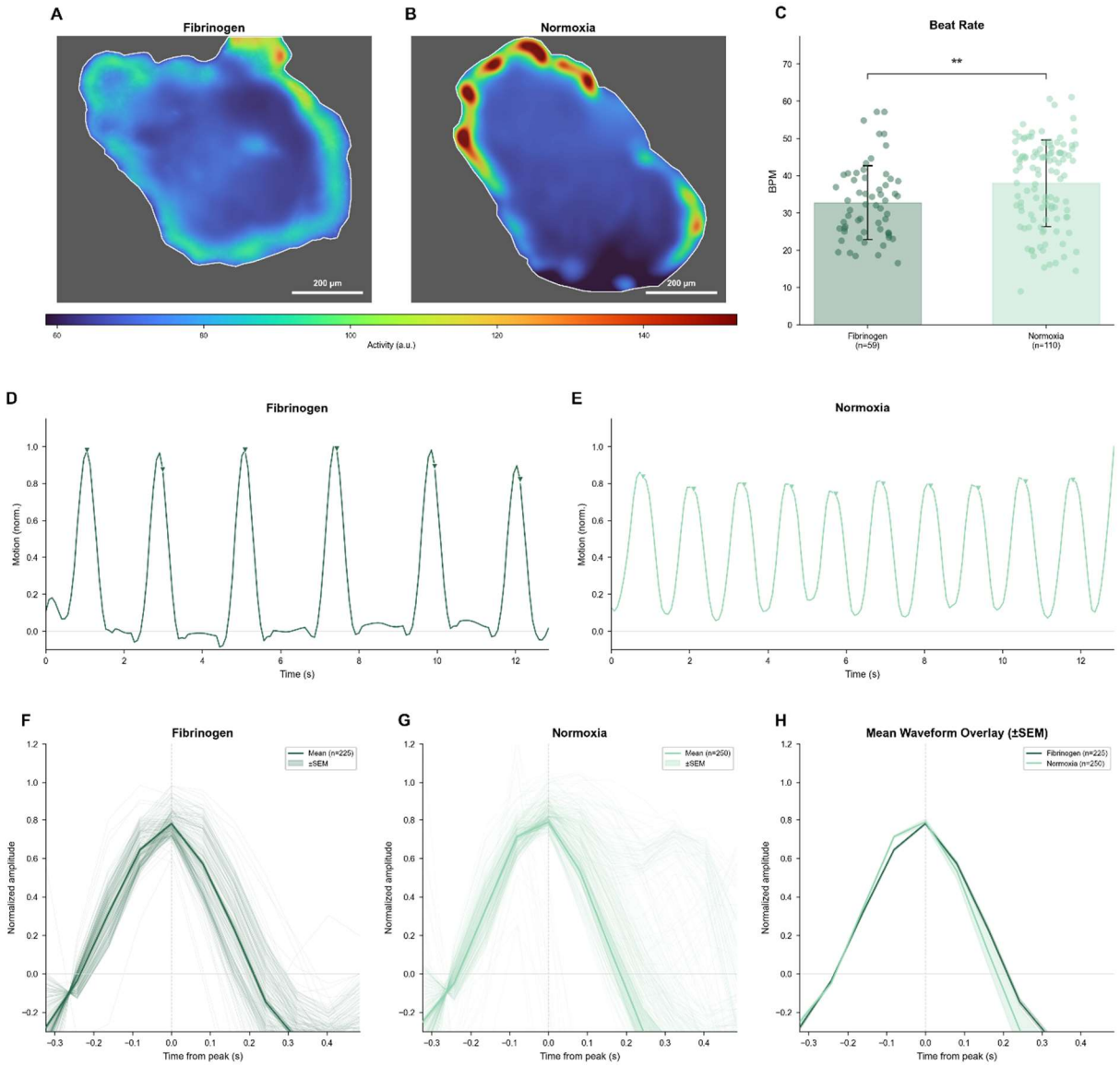

Figure 18: Contractile characterisation of fibrinogen-embedded versus normoxic cardiac spheroids. Fluorescence-based motion analysis was performed to compare spontaneous contractile behaviour between fibrinogen-embedded spheroids and spheroids cultured under normoxic conditions. Contractile motion was quantified from time-lapse recordings acquired at 488 nm excitation. (A, B) Spatial activity maps of representative fibrinogen-embedded (A) and normoxic (B) spheroids. Activity was calculated as the pixel-wise standard deviation of absolute frame-to-frame intensity differences and displayed using a pseudo-colour scale. The grey underlay represents the temporal mean image, and white contours indicate manually defined spheroid boundaries. Scale bars: 200 µm. (C) Quantification of spontaneous beating rate (beats per minute, BPM). Bars represent mean ± standard deviation with individual data points overlaid. Fibrinogen-embedded spheroids exhibited lower beating rates compared to normoxic controls (fibrinogen: 32.7 ± 9.9 BPM, n = 59; normoxia: 37.9 ± 11.6 BPM, n = 110; Mann–Whitney U = 2298, $p = 1.79 \times 10^{-3}$). The normoxia group comprises pooled normoxic and untreated control spheroids. (D, E) Representative motion traces from individual fibrinogen-embedded (D) and normoxic (E) spheroids over approximately 12 seconds of recording. Inverted triangles indicate detected contraction peaks. (F, G) Normalised contraction waveforms aligned to peak amplitude for fibrinogen (F; 225 beats from 40 spheroids) and normoxia (G; 250 beats from 40 spheroids). Semi-transparent traces represent individual beats; bold lines indicate group means ± SEM. (H) Overlay of mean contraction waveforms (± SEM) for both conditions, enabling direct comparison of contraction and relaxation dynamics. Time-lapse recordings were acquired at 12.38 fps and analysed using frame-to-frame intensity difference–based motion quantification with adaptive peak detection. Statistical comparison was performed using a two-sided Mann–Whitney U test. Significance levels: *p < 0.05, **p < 0.01, ***p < 0.001.

To assess whether encapsulation in fibrinogen hydrogel affects the contractile properties of hiPSC-derived cardiac spheroids, time-lapse recordings acquired at 488

nm excitation (12.38 fps) were analysed for spontaneous beating activity. A total of 59 fibrinogen-embedded and 110 normoxic control spheroids were evaluated.

Among contractile spheroids, spontaneous beat rate differed between conditions (Figure 18, C). Fibrinogen-embedded spheroids exhibited a mean beat rate of 32.7 ± 9.9 BPM (median: 32.0 BPM; IQR: 24.9–39.0; range: 16.5–57.1; n = 59), whereas normoxic controls showed a higher mean beat rate of 37.9 ± 11.6 BPM (median: 41.3 BPM; IQR: 29.0–46.1; range: 8.9–61.1; n = 110). This difference was statistically significant (Mann–Whitney U = 2298, $p = 1.79 \times 10^{-3}$).

Representative activity maps were generated to visualise the spatial distribution of contractile motion within individual spheroids (Figure 18, A–B). Activity was calculated as the pixel-wise standard deviation of absolute frame-to-frame intensity differences across the recording and subsequently smoothed. In both conditions, contractile activity was predominantly localised to central regions of the spheroid, with higher activity observed in areas of dense tissue. Fibrinogen-embedded and normoxic spheroids displayed qualitatively similar spatial activity distributions.

To further characterise contraction dynamics, peak-aligned waveforms were extracted from a subset of 40 spheroids per condition (Figure 18, F–H). A total of 225 beats (fibrinogen) and 250 beats (normoxia) were aligned to peak amplitude, normalised, and averaged. Both groups exhibited a rapid contraction phase followed by a slower relaxation phase. Representative motion traces (Figure 18, D–E) illustrate the beating patterns observed under each condition, and overlay of mean waveforms (Figure 18, H) enables comparison of contraction and relaxation kinetics between groups, revealing a modest prolongation of the relaxation phase in fibrinogen-embedded spheroids.

While fibrinogen encapsulation altered contraction kinetics, it did not directly manipulate oxygen availability.

3.3.2. Hypoxia

To directly investigate oxygen-dependent stress mechanisms, experimental hypoxia was subsequently introduced as a defined and controllable ischemic stimulus.

Accurate *in vitro* modelling of reperfusion injury requires the establishment of a pronounced hypoxic state prior to reoxygenation. Oxygen deprivation, together with associated metabolic and ionic alterations, represents a central component of ischemic pathophysiology. Achieving reliable hypoxia in three-dimensional cultures is therefore essential for reproducing key aspects of ischemic stress responses.

Several approaches to oxygen deprivation were evaluated, including microscopy chambers with adjustable oxygen atmospheres, diffusion-limiting mineral oil overlays, and nitrogen-based displacement of dissolved oxygen. Among these, continuous nitrogen flux provided rapid and reproducible oxygen removal while allowing real-time imaging of cellular activity, making it suitable for dynamic functional assessment.

3.3.2.1. Hypoxic Chamber

To evaluate the performance of the hypoxic chamber integrated into the ImageXpress HT.ai system, cardiac spheroids were subjected to controlled atmospheric modulation while contractile behaviour was monitored in real time. The goal of this experiment was to confirm that chamber-based oxygen reduction produces measurable functional responses consistent with hypoxic stress.

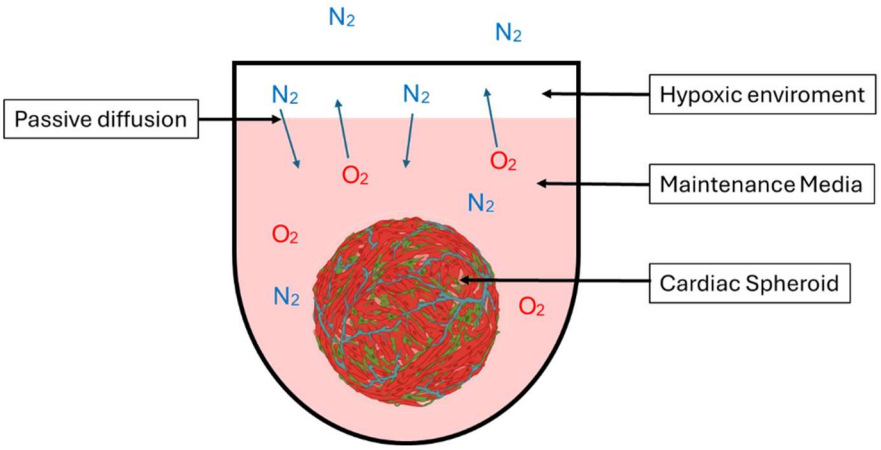

Figure 19: Experimental setup for Hypoxia simulation with an Imaging gas chamber. Cardiac spheroids are exposed to altered gas compositions in the imaging chamber. Passive diffusion is the driving force of gas exchange.

Experimentally spheroids were equilibrated inside the imaging system for 4 hours at 37 °C under normoxic gas conditions to establish stable baseline activity. Hypoxia was then induced by reducing chamber oxygen content, and spheroids were monitored for an additional 6-hour period (5.2.3.1) (Figure 19). Contractile behaviour was recorded through 12-second stream acquisitions collected every 10 minutes.

A matched control experiment was performed under identical thermal and imaging conditions, except that normoxic gas composition was maintained throughout the full 6-hour observation period. This design allowed separation of hypoxia-driven effects from imaging or environmental artifacts (5.2.3.1).

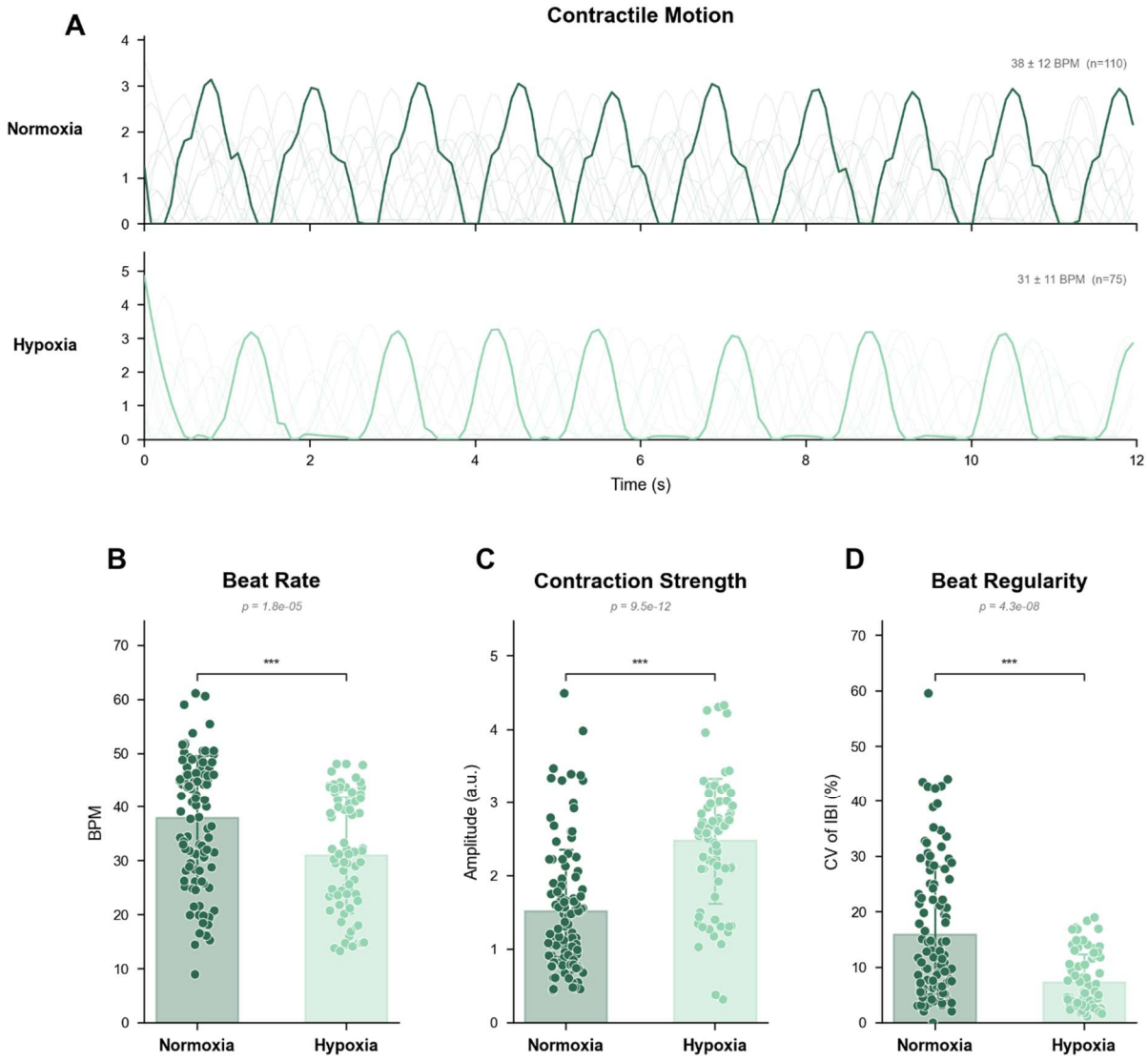

Figure 20: Contractile characterisation of cardiac spheroids under hypoxic versus normoxic conditions. Spontaneous contractile behaviour of hiPSC-derived ventricular cardiac spheroids was analysed under normoxic and hypoxic conditions using time-lapse imaging (12.38 fps). Motion signals were quantified from frame-to-frame pixel intensity differences and processed for peak detection. (A) Representative contractile motion traces recorded over 12 seconds. For each condition, traces from 10 individual contractile spheroids are displayed as semi-transparent lines, with one representative spheroid highlighted. Normoxic spheroids exhibited higher mean beating rates (38 ± 12 BPM, n = 110) compared to hypoxic spheroids (31 ± 11 BPM, n = 75). (B) Spontaneous beat rate (beats per minute). Hypoxic spheroids displayed significantly lower beating rates than normoxic controls (Mann–Whitney U = 5657, $p = 1.84 \times 10^{-5}$). Bars represent mean ± standard deviation with individual data points overlaid. (C) Contraction strength, defined as the mean peak amplitude of the motion signal per spheroid (arbitrary units). Hypoxic spheroids exhibited higher contraction amplitudes compared to normoxic controls (Mann–Whitney U = 1688, $p = 9.51 \times 10^{-12}$). (D) Beat-to-beat regularity expressed as the coefficient of variation (CV) of inter-beat intervals. Hypoxic spheroids showed lower CV values compared to normoxic spheroids (Mann–Whitney U = 6084, $p = 4.29 \times 10^{-8}$). Only spheroids classified as contractile were included in the analysis (Hypoxia: 75 of 116, 64.7 %; Normoxia: 110 of 215, 51.2 %). Statistical comparisons were performed using two-sided Mann–Whitney U tests. Significance levels: *p < 0.05, **p < 0.01, ***p < 0.001.

To assess the functional impact of reduced oxygen availability on cardiac spheroid contractility, time-lapse recordings were acquired from human iPSC-derived ventricular spheroids cultured under normoxic or hypoxic (1 % O_2) conditions.

Representative motion traces illustrate differences in contraction dynamics between conditions (Figure 20, A). Normoxic spheroids displayed faster oscillatory motion, whereas hypoxic spheroids exhibited lower beat frequency with higher peak amplitudes.

Quantitative analysis confirmed significant differences across all measured contractile parameters. Hypoxic spheroids exhibited a lower spontaneous beating rate compared to normoxic controls (31.0 ± 10.8 vs. 37.9 ± 11.6 BPM; Mann–Whitney U = 5657, $p = 1.84 \times 10^{-5}$; Figure 20, B).

Contraction amplitude, defined as the mean peak height of the baseline-corrected motion signal per spheroid, was significantly higher under hypoxia (2.48 ± 0.86 vs. 1.51 ± 0.84 arbitrary units; Mann–Whitney U = 1688, $p = 9.51 \times 10^{-12}$; Figure 20, C).

Beat-to-beat regularity, expressed as the coefficient of variation (CV) of inter-beat intervals, was significantly lower in hypoxia-exposed spheroids compared to normoxic controls (7.25 ± 5.04 % vs. 15.9 ± 12.3 %; Mann–Whitney U = 6084, $p = 4.29 \times 10^{-8}$; Figure 20, D).

Together, these findings demonstrate that hypoxic exposure is associated with reduced beating frequency, increased contraction amplitude, and decreased beat-to-beat variability in hiPSC-derived cardiac spheroids.

A second evaluation of the hypoxic capabilities of the imaging chamber focused on hypoxic preconditioning and its influence on subsequent oxygen deprivation responses. In contrast to the previous experiment, spheroids were not equilibrated under normoxic conditions. Instead, recordings began immediately under hypoxia, allowing calcium transient dynamics to be tracked throughout the full sequence of hypoxia, recovery, and rehypoxia.

Following the initial hypoxic phase, spheroids were returned to normoxic conditions to observe recovery of contractile behaviour. A second hypoxic interval was then applied to assess whether prior exposure altered functional responses. Calcium activity was recorded continuously using 30-second acquisitions at a frame rate of 1 frame per second, resulting in clearly resolved transient profiles. Imaging was performed using the ImageXpress HT.ai platform.

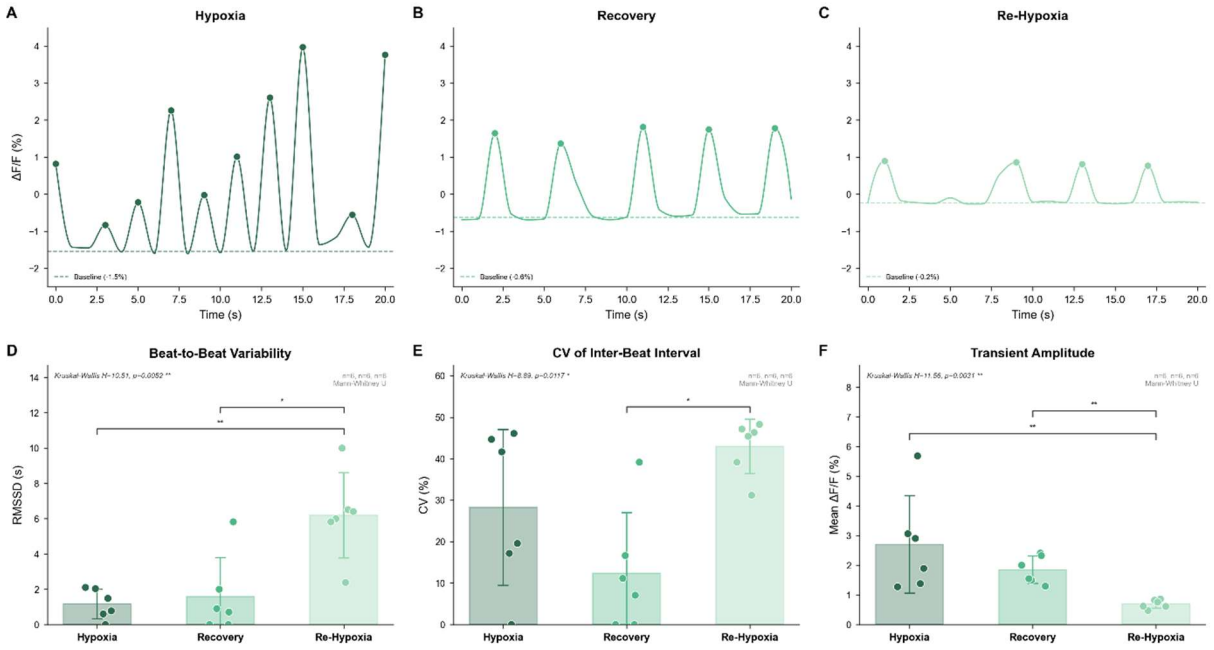

Figure 21: Calcium transient dynamics across sequential hypoxia–recovery–re-hypoxia exposure. Calcium transient activity was recorded from cardiac spheroids during sequential hypoxia (1 % O_2), recovery (return to normoxia), and re-hypoxia (1 % O_2 following a 5-minute recovery interval). (A–C) Representative calcium fluorescence traces (ΔF/F, %) recorded over 20 seconds under Hypoxia (A), Recovery (B), and Re-Hypoxia (C) conditions. Filled circles indicate detected transient peaks. All panels share a common y-axis scale to enable direct comparison of transient amplitude. (D) Beat-to-beat variability quantified as the root mean square of successive differences (RMSSD) of inter-beat intervals. RMSSD differed significantly across conditions (Kruskal–Wallis H = 10.51, p = 0.0052). Re-Hypoxia exhibited higher RMSSD compared to Hypoxia (Mann–Whitney U = 0.0, p = 0.0022) and Recovery (Mann–Whitney U = 1.5, p = 0.010). (E) Coefficient of variation (CV) of inter-beat intervals. A significant overall difference was detected (Kruskal–Wallis H = 8.89, p = 0.012), with higher CV values observed under Re-Hypoxia compared to Recovery (Mann–Whitney U = 1.5, p = 0.010). (F) Mean transient amplitude (ΔF/F, %) per recording. Amplitude differed significantly across conditions (Kruskal–Wallis H = 11.56, p = 0.0031), with lower amplitudes detected during Re-Hypoxia compared to Hypoxia (Mann–Whitney U = 36.0, p = 0.0022) and Recovery (Mann–Whitney U = 36.0, p = 0.0022). For quantitative analyses (D–F), recordings with ≥3 detected beats were included (n = 6 per condition). Bars represent mean ± standard deviation with individual data points overlaid. Statistical comparisons were performed using Kruskal–Wallis tests followed by pairwise two-sided Mann–Whitney U tests. Significance levels: *p < 0.05, **p < 0.01, ***p < 0.001.

Figure 21 illustrates the functional effects of hypoxic preconditioning on calcium transient behaviour in cardiac spheroids. Representative calcium traces illustrate distinct transient patterns across conditions (Figure 21, A–C). During initial hypoxia, spheroids exhibited regularly spaced calcium transients with peak ΔF/F values of approximately 4 % (Figure 21, A). Following recovery under normoxia, transient amplitude was moderately reduced while rhythmic activity was maintained (Figure 21, B). Upon re-exposure to hypoxia, transient amplitude decreased further and inter-beat intervals became more variable (Figure 21, C).

Quantitative analysis of beat-to-beat timing variability supported these observations. The root mean square of successive differences (RMSSD) of inter-beat intervals differed significantly across conditions (Kruskal–Wallis H = 10.51, p = 0.0052; Figure 21, D). RMSSD values were significantly higher under re-hypoxia compared to both initial hypoxia (Mann–Whitney U = 0.0, p = 0.0022) and recovery (Mann–Whitney U = 1.5, p = 0.010), whereas initial hypoxia and recovery did not differ significantly.

The coefficient of variation (CV) of inter-beat intervals showed a similar pattern. A significant overall difference was detected (Kruskal–Wallis H = 8.89, p = 0.012; Figure 21, E), with higher CV values under re-hypoxia compared to recovery (Mann–Whitney U = 1.5, p = 0.010).

Calcium transient amplitude was also significantly affected by condition. Mean ΔF/F amplitude per recording differed across groups (Kruskal–Wallis H = 11.56, p = 0.0031; Figure 21, F). Amplitude was significantly reduced under re-hypoxia compared to both initial hypoxia (Mann–Whitney U = 36.0, p = 0.0022) and recovery (Mann–Whitney U = 36.0, p = 0.0022), whereas no significant difference was observed between initial hypoxia and recovery (Mann–Whitney U = 22.0, p = 0.59).

Together, these results demonstrate preserved calcium transient amplitude and rhythm stability during initial hypoxia and recovery, followed by reduced amplitude and increased beat-to-beat variability upon re-exposure to hypoxia.

3.3.2.2. Mineral Oil as Oxygen Diffusion Regulator

In addition to atmospheric oxygen control, diffusion-mediated oxygen restriction was evaluated as an alternative method to modulate oxygen availability in the culture system.

Oxygen transport in aqueous systems follows Fick's law of diffusion, where flux is proportional to the concentration gradient and inversely related to diffusion path length (Equation 1). Increasing the diffusion distance therefore slows oxygen replenishment, promoting localized hypoxic conditions.[256] In addition to geometric effects, barrier materials with lower oxygen permeability further restrict exchange.

Equation 1

$$J = -D\frac{\partial C}{\partial x}$$

Fick's First Law of Diffusion

Mineral oil was selected as a diffusion-limiting overlay due to its low oxygen solubility relative to aqueous media and its ability to suppress convective mixing at the liquid surface.[257] The overlay increases the effective diffusion path length while reducing surface-tension-driven convection, meaning oxygen transport becomes dominated by passive molecular diffusion. Together, these effects substantially slow oxygen equilibration, creating a controlled hypoxic microenvironment without active gas displacement.

3.3.2.2.1. Impact of Mineral Oil Inflicted Hypoxia on Beating Patterns

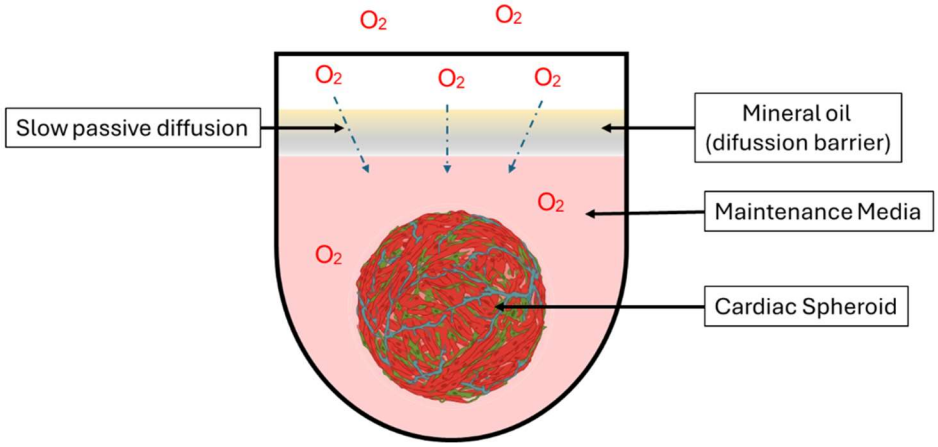

Figure 22: Experimental setup for hypoxia induction via mineral oil overlay. The cardiac spheroids are cultivated in MM. For hypoxia induction a Mineral oil overlay is applied. Increasing the diffusion coefficient, increasing the distance and limiting convective mixing resulting in slow passive diffusion guided gas exchange and constantly decreasing oxygen availability.

For experimental evaluation, cardiac spheroids cultured in 384-well U-bottom plates were used at differentiation day 21 (DD21). Prior to treatment, plates containing control and treatment cardiac spheroids were equilibrated in the imaging system for 4 hours under standard culture conditions (37 °C, 5 % CO_2, saturated humidity) to minimize baseline variability associated with transfer into the system. Hypoxic conditions were induced by overlaying treatment wells with 20 µL of mineral oil, forming an approximately 2 mm barrier layer (5.2.3.2) (Figure 22). Control wells remained untreated.

Contractile behaviour of the spheroids was monitored using the ImageXpress HT.ai imaging platform. Beating activity was recorded at 20-minute intervals using 30-second stream acquisitions (12.38 fps) over a total observation period of 20 hours. This setup allowed continuous assessment of functional changes associated with diffusion-limited oxygen availability.

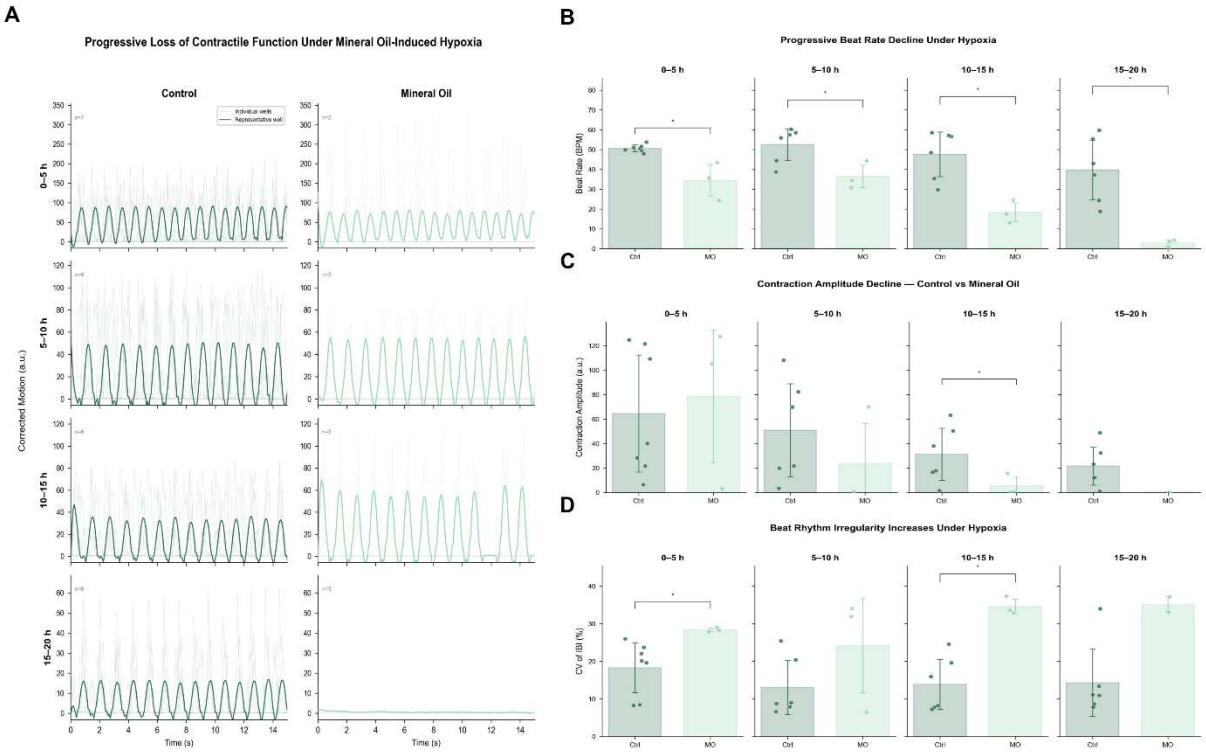

Figure 23: Contractile behaviour of cardiac spheroids under mineral oil–induced hypoxia. (A) Representative contractile motion traces recorded over a 20-hour time course, comparing control spheroids (dark green, n = 7 wells) and mineral oil–treated spheroids (light green, n = 3 wells). Traces are displayed for four consecutive 5-hour intervals (0–5 h, 5–10 h, 10–15 h, 15–20 h). Faded lines represent individual wells; bold lines indicate representative examples. (B) Beat rate (BPM) across time intervals. Control spheroids maintained measurable beating throughout the 20-hour recording period (0–5 h: 50.6 ± 1.8 BPM; 15–20 h: 39.7 ± 16.3 BPM). Mineral oil–treated spheroids exhibited lower baseline beating rates (34.5 ± 9.7 BPM at 0–5 h; U = 21.0, p = 0.017) and progressive reduction over time (15–20 h: 2.9 ± 1.9 BPM; U = 18.0, p = 0.024). Beat rate was significantly reduced in the mineral oil group at all four time bins (two-sided Mann–Whitney U test, *p < 0.05). (C) Contraction amplitude (arbitrary units) across time intervals. Both groups demonstrated declining amplitude over the 20-hour period. The reduction was more pronounced in mineral oil–treated spheroids. Differences reached statistical significance at the 10–15 h interval (U = 17.0, p = 0.048). At 15–20 h, analysis was limited by reduced mineral oil sample size (n = 2). (D) Beat rhythm variability quantified as the coefficient of variation (CV) of inter-beat intervals. Mineral oil–treated spheroids exhibited higher CV values compared to controls. Significant differences were detected at the 0–5 h (U = 0.0, p = 0.017) and 10–15 h (U = 0.0, p = 0.024) intervals. Cardiac spheroids were cultured in 384-well U-bottom plates. Contractile motion was quantified from time-lapse recordings (12.38 fps) using frame-to-frame intensity difference analysis with baseline correction. Data are presented as mean ± standard deviation. Statistical comparisons were performed using two-sided Mann–Whitney U tests.

Figure 23 summarizes the functional effects of diffusion-limited hypoxia induced by mineral oil overlay. Representative motion traces across four consecutive 5-hour intervals (0–5 h, 5–10 h, 10–15 h, 15–20 h) revealed sustained rhythmic contractions in control spheroids (n = 7) throughout the recording period (Figure 23, A). In contrast, mineral oil–treated spheroids (n = 3) exhibited a progressive reduction in contractile activity over time, with marked alteration of signal amplitude in later intervals.

Beat rate was quantified as beats per minute (BPM) within each time interval (Figure 23, B). Control spheroids maintained measurable beating throughout the experiment, declining from 50.6 ± 1.8 BPM (0–5 h) to 39.7 ± 16.3 BPM (15–20 h). Mineral oil–treated spheroids exhibited a lower baseline beat rate (34.5 ± 9.7 BPM at 0–5 h; U = 21.0, p = 0.017) and a progressive decline across subsequent intervals (5–10 h: 36.5 ± 7.0 BPM;

10–15 h: 18.4 ± 5.8 BPM; 15–20 h: 2.9 ± 1.9 BPM) (Figure 23, B). Differences between groups were statistically significant at all time intervals (two-sided Mann–Whitney U test, $p < 0.05$).

Contraction amplitude, defined as the mean peak height of the baseline-corrected motion signal per recording, decreased over time in both groups (Figure 23, C). Control spheroids showed a reduction from 64.5 ± 51.6 arbitrary units (0–5 h) to 21.7 ± 17.1 arbitrary units (15–20 h). Mineral oil–treated spheroids demonstrated a more pronounced decline from 78.7 ± 66.2 arbitrary units (0–5 h) to 0.5 ± 0.1 arbitrary units (15–20 h). Baseline amplitude did not differ significantly between groups ($U = 10.0$, $p = 1.000$). A significant difference emerged at 10–15 h ($U = 17.0$, $p = 0.048$). At 15–20 h, analysis was limited by reduced sample size in the mineral oil group ($n = 2$).

Beat rhythm regularity was assessed using the coefficient of variation (CV) of inter-beat intervals (Figure 23, D). Mineral oil–treated spheroids exhibited higher CV values compared to controls across time intervals. Significant differences were observed at 0–5 h ($U = 0.0$, $p = 0.017$) and 10–15 h ($U = 0.0$, $p = 0.024$). At later intervals, statistics were limited by reduced sample size in the mineral oil group.

Together, these findings demonstrate a time-dependent reduction in beat rate and contraction amplitude, accompanied by increased beat-to-beat variability, in cardiac spheroids cultured under mineral oil overlay compared to controls.

3.3.2.2.2. Morphological Changes Induced by Mineral Oil Inflicted Hypoxia

To determine whether the mineral oil–induced hypoxia model reproduces cardio pathophysiological characteristics associated with severe stress, particularly fibrotic remodelling following cardiomyocyte injury, collagen deposition was assessed after recovery.

Cardiac spheroids were subjected to mineral oil–induced hypoxia and retrieved at two defined injury stages: 3 hours (moderate stress) and 20 hours (severe stress). Corresponding untreated control spheroids were maintained in parallel. After removal of the mineral oil overlay, spheroids were cultured under normoxic conditions for 7 days to allow potential remodelling processes to develop.

Following the recovery period, spheroids were fixed and stained with an anti-collagen antibody to visualize extracellular matrix deposition. Hoechst staining was applied to visualize nuclei (5.2.5.1-5.2.5.3). MitoTracker™ Green (5.2.6.6) was retained from the

hypoxic phase to provide additional context regarding mitochondrial organization. Confocal images were acquired using the Leica Stellaris 5.

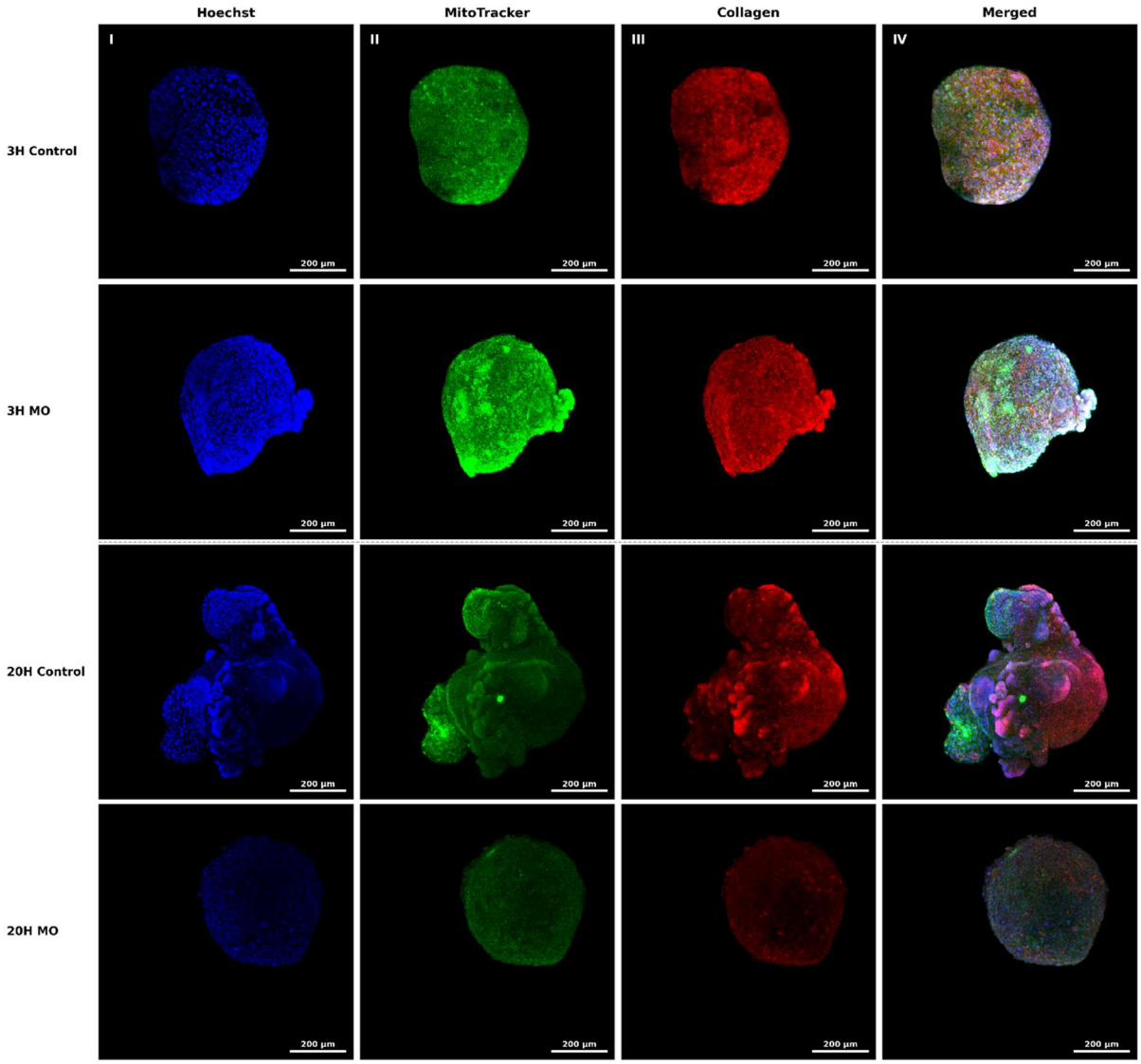

Figure 24: Confocal fluorescence imaging of Collagen I and MitoTracker™ Green expression in iPSC-derived cardiac spheroids following mineral oil–induced hypoxia. iPSC-derived cardiac spheroids were generated in 384-well U-bottom plates and analysed at differentiation day 21 (DD21). Hypoxia was induced by mineral oil (MO) overlay for 3 hours (3H) or 20 hours (20H), each with corresponding untreated controls. Following treatment, mineral oil was removed and spheroids were returned to standard culture conditions. Spheroids were fixed and stained 7 days after treatment. Prior to fixation, spheroids were incubated with MitoTracker™ Green FM (200 nM, 30 min; Invitrogen, M7514, lot 1948108) to label mitochondria. Nuclei were stained with Hoechst 33342 (1:5000, 60 min). Collagen I was detected using a rabbit anti-Collagen I primary antibody (Proteintech, 14695-1-AP) followed by an Alexa Fluor 647–conjugated goat anti-rabbit secondary antibody (Invitrogen, A21247, lot 2186088). Images were acquired using a Leica STELLARIS 5 confocal microscope (DMI8-CS inverted platform) with an HC PL APO CS2 10x/0.40 DRY objective. Z-stacks were collected at 0.88 µm/pixel lateral resolution with a 5 µm z-step size. Columns (I–IV) display individual channels: (I) Hoechst (blue), (II) MitoTracker™ Green (green), (III) Collagen I (red), and (IV) merged composite. Images represent mean intensity z-projections. A spheroid mask was applied to remove extracellular background. Within the 3H group, MO-treated spheroids showed comparable fluorescence intensity to controls across all channels. In contrast, 20H MO-treated spheroids exhibited reduced MitoTracker™ Green and Collagen I signal relative to corresponding controls. Representative images from one spheroid per condition are shown. Scale bars: 200 µm.

Figure 24 displays collagen expression patterns in control and mineral oil–treated spheroids following 7 days of recovery. In the 3H group, MO-treated spheroids

displayed comparable MitoTracker™ Green and Collagen I fluorescence intensity relative to untreated controls (Figure 24, rows 1–2, columns II–III). Nuclear staining appeared preserved in both conditions (Figure 24, column I), and no severe morphological differences were observed between treated and control spheroids.
In contrast, the 20H group showed clear differences between control and MO-treated spheroids (Figure 24, rows 3–4). Control spheroids exhibited strong MitoTracker™ Green and Collagen I fluorescence throughout the spheroid body (Figure 24, row 3, columns II–III). MO-treated spheroids subjected to 20 hours of mineral oil overlay displayed reduced fluorescence intensity in both the MitoTracker™ Green and Collagen I channels (Figure 24, row 4). Hoechst staining remained detectable but appeared less intense and more diffuse compared to the corresponding control.

Together, these observations indicate a duration-dependent effect of mineral oil–induced hypoxia on mitochondrial and collagen-associated fluorescence signals in cardiac spheroids. While 3 hours of treatment did not result in marked differences compared to control, 20 hours of mineral oil overlay was associated with reduced fluorescence intensity across multiple channels.

3.3.2.2.3. Gene Expression Changes Caused by Mineral Oil Induced Hypoxia

To further assess the suitability of the mineral oil overlay as a hypoxia-inducing strategy, transcriptional responses were evaluated using RT-qPCR (5.2.7). The experimental setup followed the conditions described in Section 3.3.2.2.1. After a 4-hour normoxic preconditioning phase, the mineral oil layer was applied to induce diffusion-limited oxygen deprivation.
Samples were harvested at 1, 3, and 6 hours after hypoxia initiation, with control spheroids collected at matching time points. An additional 20-hour time point was planned; however, RNA isolation from mineral oil–treated spheroids was unsuccessful due to extensive loss of viability, preventing downstream analysis.

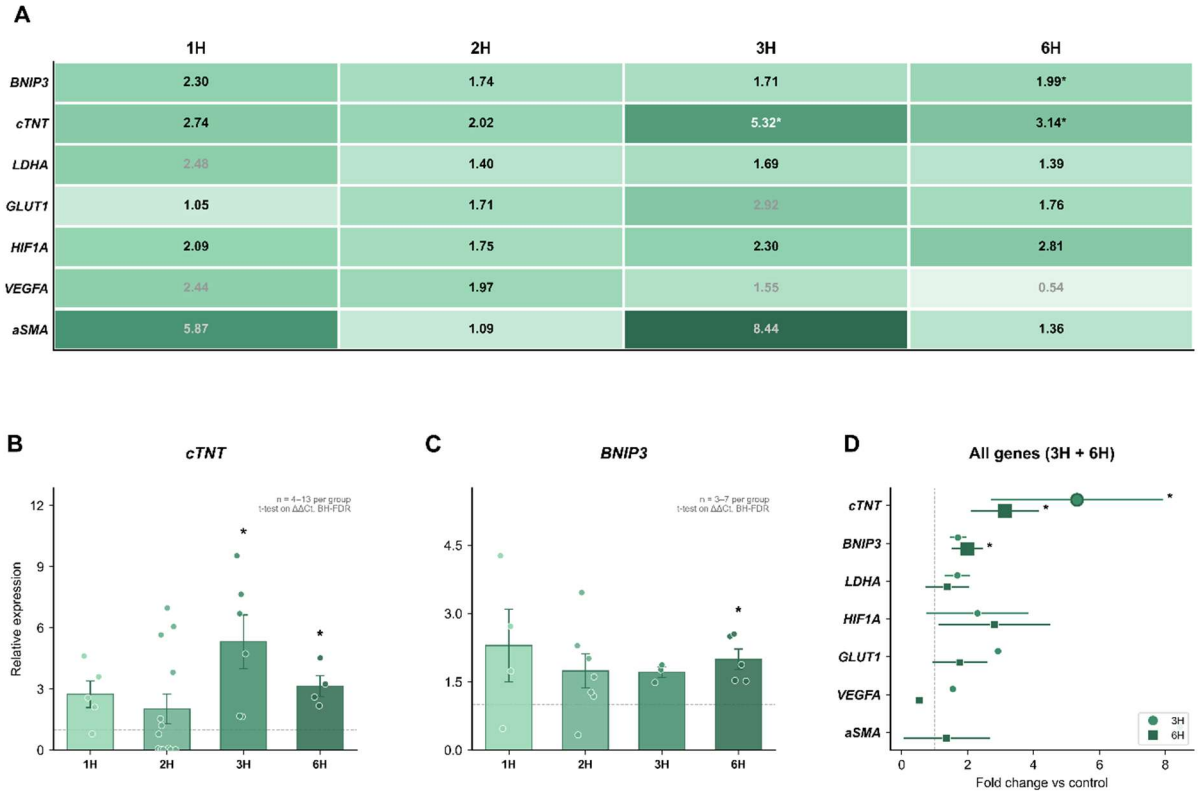

Figure 25: Gene expression profiling of hypoxia-responsive markers following mineral oil–induced oxygen deprivation. (A) Heatmap showing mean relative gene expression (fold change vs. untreated control) of seven target genes at four timepoints (1 h, 2 h, 3 h, 6 h) following mineral oil–induced hypoxia. Expression levels were quantified by RT-qPCR and normalised to HPRT. Fold change values are indicated within each cell. Asterisks denote statistically significant differences from control after false discovery rate (FDR) correction (*p_adj < 0.05). Grey labels indicate groups with insufficient sample size for statistical testing (n < 3). Colour intensity reflects relative fold change (white: no change; dark green: upregulation). (B, C) Relative expression of cTnT (B) and BNIP3 (C), the two genes exhibiting significant upregulation after FDR correction. Bars represent mean fold change at each timepoint with error bars indicating standard error of the mean (SEM). Individual biological replicates are shown. The dashed horizontal line indicates control baseline (fold change = 1). (D) Forest plot summarising mean fold change and 95 % confidence intervals for all target genes at 3 h and 6 h. The vertical dashed line represents baseline expression (fold change = 1). Filled symbols indicate statistically significant changes after FDR correction; grey symbols denote groups not included in statistical testing (n < 3). Statistical analysis was performed on ΔΔCt values using one-sample t-tests against a theoretical mean of 0 (no change vs. control), followed by Benjamini–Hochberg correction for multiple testing (FDR < 0.05). Only groups with n ≥ 3 biological replicates were included in statistical testing. Data represent independent biological replicates derived from separate experiments (n = 3–13 per condition).

To characterize early transcriptional responses to mineral oil–induced hypoxia, a panel of hypoxia- and cardiac-related genes was analysed by RT-qPCR across the selected timepoints. An overview of relative expression changes across all seven principal target genes is presented as a heatmap in Figure 25 A. Mean fold changes above baseline were observed for multiple genes and timepoints. However, after correction for multiple comparisons, only two genes, cTnT and BNIP3, showed statistically significant upregulation.

cTnT exhibited the strongest and most consistent increase in expression (Figure 25 B). Mean relative expression was elevated at all four timepoints, increasing from 2.74-fold at 1 h (n = 5; p_adj = 0.15) to 5.32-fold at 3 h (n = 6; p_adj = 0.044), followed by 3.14-fold

at 6 h (n = 4; p_adj = 0.044). The 3 h and 6 h timepoints reached statistical significance after false discovery rate (FDR) correction, which controls for multiple testing.

BNIP3 showed moderate upregulation across the time course (Figure 25 C), with fold changes ranging from 1.71 at 3 h (n = 3; p_adj = 0.085) to 1.99 at 6 h (n = 5; p_adj = 0.044). Statistical significance after FDR correction was observed at 6 h only.

Several additional genes representing hypoxia-responsive pathways, metabolic adaptation, and lineage markers were also analysed but did not remain significant after correction for multiple testing (Figure 25 D). LDHA was elevated at 3 h (1.69-fold; n = 4; uncorrected p = 0.019; p_adj = 0.085). HIF-1α showed approximately two-fold mean elevation across timepoints (range: 1.75–2.81-fold), accompanied by substantial inter-replicate variability. Glut1 and VEGFA exhibited elevated mean expression at individual timepoints but were limited by low replicate numbers (n = 2), precluding statistical testing. Expression of α-SMA, KDR, NKX2.5, and OCT4 could not be reliably assessed at several timepoints due to limited sample size.

Collectively, these results identify cTnT and BNIP3 as the most consistently upregulated transcripts in response to mineral oil–induced oxygen deprivation within the analysed time window (1–6 h), with peak expression observed between 3 and 6 hours.

3.3.2.3. Direct Nitrogen Flux

While mineral oil overlay restricts oxygen diffusion gradually, direct nitrogen flux provides a rapid and externally controllable method for reducing oxygen availability. By displacing dissolved oxygen through continuous nitrogen perfusion, this approach enables acute hypoxic exposure without introducing a physical diffusion barrier. In contrast to mineral oil–induced hypoxia, nitrogen flux allows real-time monitoring of immediate functional responses during oxygen withdrawal and subsequent reoxygenation.

The following section evaluates the acute effects of nitrogen-induced hypoxia on calcium transient dynamics in cardiac spheroids.

3.3.2.3.1. Influence of Nitrogen Flux Inflicted Hypoxia on Calcium Transients

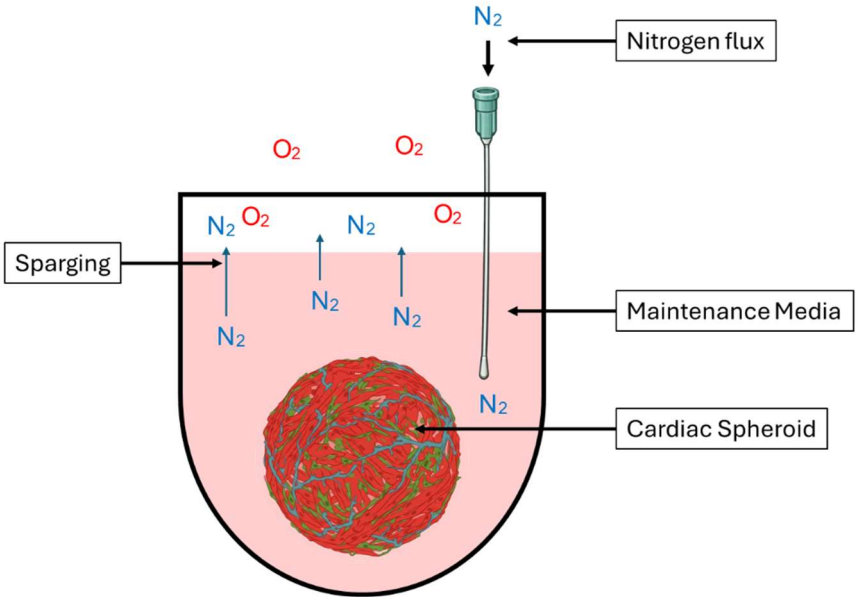

Figure 26: Experimental setup for active oxygen removal via nitrogen sparging. A syringe needle connected to a nitrogen regulator was used to deliver a controlled nitrogen flow into the culture medium containing the cardiac spheroid. The gas line included sterile tubing and a syringe filter to maintain sterility during the gas transfer. Nitrogen was introduced directly into the maintenance medium through the needle, creating a continuous stream of bubbles that displaced dissolved oxygen from the medium.

For experimental analysis, cardiac spheroids at differentiation day 21 (DD21) were used to ensure stable cardiomyocyte maturation. Baseline calcium imaging was performed as described in Section 5.2.6.2 to establish pre-treatment activity patterns. Spheroids were then exposed to controlled nitrogen flux while calcium transients were continuously recorded using a Leica LED imaging system (Figure 26). Measurements were obtained before, during, and after hypoxic exposure to capture acute functional responses to oxygen deprivation and subsequent recovery. This approach enabled real-time assessment of calcium handling dynamics under hypoxic stress conditions.

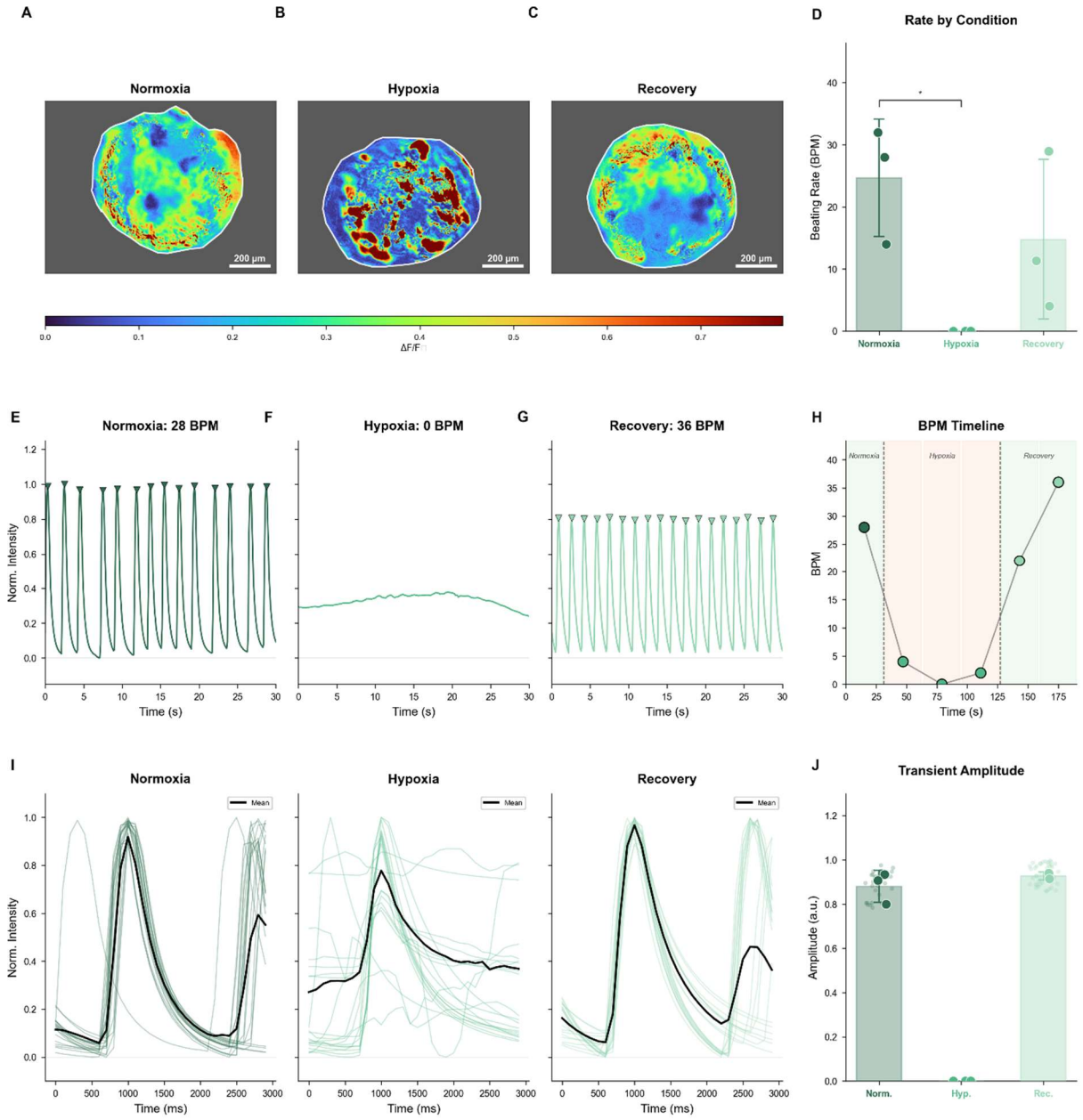

Figure 27: Acute hypoxia reversibly modulates spontaneous calcium activity in human iPSC-derived cardiac spheroids. (A–C) Maximum $\Delta F/F_0$ projection maps from a representative cardiac spheroid (Spheroid 1) during normoxia (A), acute hypoxia (B), and recovery after reoxygenation (C). Heatmaps are displayed using a shared pseudo-colour scale. Spheroid boundaries are indicated by white contours; regions outside the spheroid are masked. Scale bars: 200 µm. (D) Spontaneous beating rate (beats per minute, BPM) across experimental phases (Spheroids 1, 4, and 5; n = 3 biological replicates). For normoxia, the baseline recording per spheroid was used. For hypoxia, the recording with the lowest BPM per spheroid was selected to represent established hypoxic suppression. For recovery, per-spheroid means were calculated by averaging across all recovery recordings. Bars represent mean ± standard deviation; individual points correspond to per-spheroid values. During hypoxia, all spheroids exhibited cessation of detectable beating (0.0 ± 0.0 BPM), significantly reduced compared to normoxia (24.7 ± 9.5 BPM; paired t-test, *p < 0.05). Partial recovery of beating rate was observed following reoxygenation. (E–G) Representative 30-second calcium fluorescence traces from Spheroid 1 during normoxia (E), hypoxia (F), and recovery (G). Traces were linearly detrended and normalised to the normoxia-phase amplitude range. Inverted triangles indicate detected transient peaks. (H) Temporal progression of beating rate across six sequential 30-second recordings from Spheroid 1. Background shading indicates experimental phases; vertical dashed lines mark phase transitions. (I) Overlay of individual calcium transient waveforms aligned to peak onset, pooled across all spheroids (normoxia: n = 34; hypoxia: n = 26; recovery: n = 45 transients). Individual traces are shown with the ensemble mean overlaid. (J) Quantification of calcium transient peak amplitude (arbitrary units) using the same per-spheroid aggregation strategy as in panel D. Bars represent mean ± standard deviation (n = 3 spheroids); large data points indicate per-spheroid values, and small faded points represent individual transient amplitudes. During hypoxia, selected recordings contained no detectable transients (0.0 a.u.). Normoxia amplitude was 0.88 ± 0.07 a.u.; recovery amplitude was 0.93 ± 0.02 a.u. (n = 2; one spheroid excluded due to technical artefact). Calcium

fluorescence was recorded at 10 Hz (100 ms frame interval) using a LED microscope (Leica). Pixel size: 0.933 µm. Each recording epoch comprised 30 seconds. One spheroid was excluded due to technical artefacts.

Figure 27 illustrates the effects of oxygen deprivation on intracellular calcium dynamics and contractile behaviour in cardiac spheroids. Maximum $\Delta F/F_0$ projection maps were generated to visualise the spatial distribution of calcium activity. $\Delta F/F_0$ projection maps are commonly used in functional fluorescence imaging, such as calcium imaging or voltage-sensitive dye imaging, to visualize spatial patterns of biological activity. The parameter $\Delta F/F_0$ represents the normalized change in fluorescence intensity relative to a baseline level and is calculated as $(F - F_0)/F_0$, where F is the fluorescence intensity at a given time point and F_0 is the baseline fluorescence, typically determined as the average signal during a resting or pre-stimulation period. This normalization allows comparison of signal changes across different regions of a sample by accounting for variations in baseline intensity. At baseline prior to hypoxia induction (ambient laboratory conditions: room air and room temperature), the representative spheroid (Spheroid 1) exhibited spatially distributed regions of elevated $\Delta F/F_0$ signal (Figure 27 A). During hypoxia, these regions were markedly reduced (Figure 27 B). Upon reoxygenation, $\Delta F/F_0$ signal reappeared across the spheroid (Figure 27 C).

Spontaneous beating rate was quantified using a per-spheroid aggregation approach to avoid pseudoreplication. For normoxia, the baseline recording per spheroid was used; for hypoxia, the recording with the lowest BPM per spheroid was selected to represent established suppression; for recovery, per-spheroid means were calculated by averaging across recovery recordings. This yielded n = 3 biological replicates per condition. Under normoxic conditions, spheroids exhibited beating rates of 28, 32, and 14 BPM (mean 24.7 ± 9.5 BPM). During hypoxia, no detectable spontaneous activity was observed in any spheroid (0.0 ± 0.0 BPM), representing a significant reduction compared to normoxia (paired t-test, $p < 0.05$; Figure 27 D). Following reoxygenation, beating resumed in all spheroids, although recovery magnitude varied between samples.

Temporal progression of activity was examined in Spheroid 1 across six sequential recordings (Figure 27 H). Beating rate declined during hypoxia and increased following reoxygenation. Representative 30-second fluorescence traces illustrate this pattern (Figure 27 E–G). Normoxic recordings showed regular calcium oscillations. During hypoxia, no discrete transients were detected and the fluorescence trace displayed an elevated and slowly drifting baseline relative to normoxic recordings.

Upon reoxygenation, rhythmic oscillations reappeared together with a return of baseline fluorescence toward pre-hypoxic levels.

To assess waveform characteristics, individual calcium transients were extracted, aligned to peak onset, and overlaid (Figure 27 I). Normoxic (n = 34) and recovery (n = 45) transients exhibited similar waveform morphology. During hypoxia (n = 26), detected events were less frequent and showed greater variability.

Peak transient amplitude was quantified using the same per-spheroid aggregation strategy (Figure 27 J). During hypoxia, selected recordings contained no detectable transients (0.0 a.u.). Normoxic amplitude was 0.88 ± 0.07 a.u. Recovery amplitude was 0.93 ± 0.02 a.u. (n = 2; one spheroid excluded due to technical artefact).

Together, these findings demonstrate reversible suppression of spontaneous calcium transient activity during acute hypoxia, characterised by cessation of detectable beating, elevation of baseline fluorescence, and reduction of transient amplitude, followed by reappearance of activity upon reoxygenation.

3.3.3. The Effects of Tyrode Solution

Recreating ischemic preconditioning *in vitro* requires not only oxygen deprivation but also restriction of nutrient availability. This combined stress is necessary to approximate the metabolic imbalance that contributes to reperfusion-associated damage in cardiomyocytes. To model nutrient deprivation, Tyrode solution was selected due to its widespread use as a controlled buffer system in cardiac research.

Before incorporating Tyrode treatment into the ischemia–reperfusion workflow, its isolated effects on cardiac spheroid function were evaluated. The goal was to determine whether exposure alone altered beating behaviour or viability in a way that could affect later experiments.

Cardiac spheroids were monitored continuously during three defined phases: a baseline period, a Tyrode treatment phase, and a recovery phase. For baseline and recovery recordings, spheroids were maintained in standard culture medium. During treatment, spheroids were exposed to Tyrode solution adjusted to pH 7.2 to approximate ischemic buffering conditions. The baseline phase lasted 1 hour to establish stable reference activity. Tyrode exposure was extended to 2.5 hours, exceeding the intended ischemic preconditioning duration to rule out delayed buffer-specific effects. Recovery was tracked for 17 hours following reintroduction of maintenance medium. Functional activity was recorded throughout using the ImageXpress HT.ai imaging system.

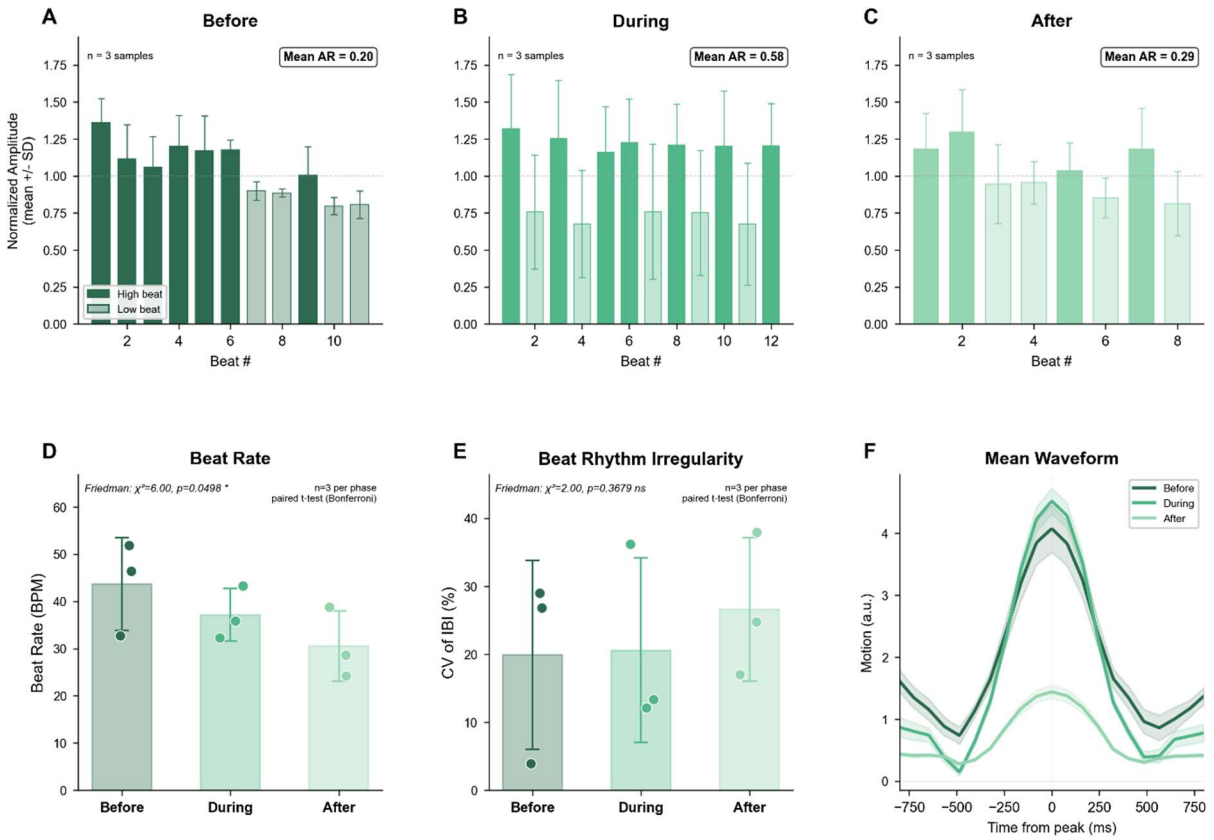

Figure 28: Contractile dynamics before, during, and after Tyrode solution exchange. (A–C) Normalised beat amplitude plotted as a function of beat sequence for the Before (A), During (B), and After (C) phases. Amplitudes were normalised to the recording-wise mean after exclusion of the first detected beat. Dark bars indicate beats at or above the mean (≥ 1.0), light bars indicate beats below the mean. The mean alternans ratio (AR), calculated as the average of consecutive pairwise amplitude differences divided by their local mean, is shown for each phase. Higher AR values indicate greater beat-to-beat amplitude alternation. Data represent n = 3 biological replicates per phase. (D) Spontaneous beating rate (BPM) across treatment phases. Mean BPM decreased from 43.6 ± 9.8 (Before) to 37.1 ± 5.6 (During) and 30.6 ± 7.5 (After). A Friedman test indicated a borderline overall effect ($\chi^2 = 6.00$, $p = 0.050$). Pairwise comparisons did not reach significance after Bonferroni correction (paired t-tests; all adjusted $p > 0.05$). (E) Beat rhythm irregularity quantified as the coefficient of variation (CV) of inter-beat intervals. CV values were comparable across phases (Before: 19.9 ± 13.9 %; During: 20.6 ± 13.6 %; After: 26.6 ± 10.6 %), with no significant omnibus effect (Friedman $\chi^2 = 2.00$, $p = 0.368$). (F) Mean contraction waveform aligned to peak amplitude. Solid lines represent the grand mean; shaded areas indicate ± SEM. While overall waveform morphology remained comparable between phases, the After condition exhibited reduced absolute contraction amplitude relative to Before and During. Bars in (D) and (E) represent group means ± SD. Individual data points (n = 3 per phase) correspond to per-sample means. Statistical analysis used the Friedman test for repeated-measures comparisons followed by Bonferroni-corrected paired t-tests. Contractile motion was derived from frame-to-frame absolute intensity differences in time-lapse recordings (12.38 fps) with minimum-filter baseline correction and Savitzky–Golay smoothing.

Figure 28 summarizes the functional effects of Tyrode exposure on cardiac spheroids. Beat-to-beat amplitude patterns were examined by normalising peak amplitudes within each recording to their respective mean (Figure 28, A–C). Before treatment, contraction amplitudes were relatively uniform across successive beats, with a low mean alternans ratio (AR = 0.20 ± 0.13) (Figure 28, A). The mean alternans ratio (AR), calculated as the average of consecutive pairwise amplitude differences divided by their local mean, is shown for each phase. During Tyrode perfusion, beat-to-beat amplitude variability increased (AR = 0.58 ± 0.87), largely driven by one sample exhibiting pronounced alternans (AR = 1.59). Following washout, the alternans ratio

returned toward baseline levels (AR = 0.29 ± 0.35). Given the high inter-sample variability, particularly during perfusion, no formal statistical comparison of alternans ratios was performed.

Beat rate showed a progressive decline across phases, decreasing from 43.6 ± 9.8 BPM (Before) to 37.1 ± 5.6 BPM (During) and 30.6 ± 7.5 BPM (After) (Figure 28, D). A Friedman test indicated a borderline overall effect ($\chi^2(2) = 6.00$, $p = 0.050$). However, pairwise comparisons did not reach significance after Bonferroni correction (paired t-tests; all adjusted $p > 0.05$). Although the trajectory suggests a gradual reduction in spontaneous beating frequency, the small sample size limits statistical sensitivity.

The coefficient of variation (CV) of inter-beat intervals remained comparable across phases (Before: 19.9 ± 13.9 %; During: 20.6 ± 13.6 %; After: 26.6 ± 10.6 %; Figure 28, E). No significant omnibus effect was detected (Friedman $\chi^2(2) = 2.00$, $p = 0.368$), and no pairwise comparison reached significance. These findings indicate that temporal rhythm regularity was largely preserved despite changes in beat rate.

Alignment of individual contraction waveforms to their peak revealed a marked reduction in absolute contraction amplitude in the After phase (Figure 28, F). Mean peak amplitude was similar between the Before (4.18 ± 2.57 a.u.) and During (4.64 ± 1.35 a.u.) phases but decreased substantially following washout (1.30 ± 0.87 a.u.). Despite the reduction in amplitude, waveform morphology remained comparable across phases, and rhythmic contractions persisted.

Overall, Tyrode solution exchange was associated with a reduction in contraction amplitude and a gradual decline in beat rate, while beat-to-beat timing regularity was maintained. Given the limited number of biological replicates, these findings should be interpreted as indicative trends.

3.3.4. Discussion of Chapter 3.3

Following validation of a structurally and molecularly stable cardiac spheroid model, the next critical objective was the establishment of a controllable and physiologically meaningful pathophysiological environment capable of recapitulating the essential features of ischemia–reperfusion injury. Unlike isolated cytotoxic paradigms, reperfusion injury represents a complex, multifactorial phenomenon driven by the interplay of oxygen deprivation, nutrient limitation, ionic imbalance, metabolic rewiring, calcium dysregulation, and mechanical stress.[43]

Successfully reproducing ischemia must hence satisfy several criteria. Hypoxia induction must be reproducible and tuneable, targeted nutrient deprivation must be

possible and fast reoxygenation and nutrient supply must be guaranteed to replicate the devastating damage done by reperfusion. Mechanistically the model must capture the cardiac arrest as well as elevated calcium baseline and general calcium dysfunction and finally the environment must show sufficient reversibility of the conditions to display reperfusion instead of terminal collapse.
This chapter systemically evaluates multiple strategies to recreate distinct components of this pathophysiology and assess suitability for the integration into a reproducible ischemia reperfusion-workflow.

3.3.4.1. Mechanical Confinement as a Secondary Ischemia Inducer

An initial strategy aimed to induce secondary ischemia in the cardiac spheroids through mechanical modulation of encapsulation properties. *In vivo* myocardial infarction triggers regional stiffening through ECM remodelling, an enhanced force the remaining contractile cardiomyocytes must overcome to keep up blood flow.[258,259] This effect gets severely worsened by the stiffed region additionally loosing contractile capacity hence the viable myocardium does not only need to overcome the stiffening but essentially must move the dead weight of the cardiomyocytes.[260,261] This heavily increased wall tension leads to severe stress for the remaining cardiomyocytes, to facilitate the increased work metabolic demand rises drastically.[262] *In vivo* this can lead to so called secondary ischemia, where the neighbouring cardiomyocytes become insufficiently supplied through the increased workload and begin showing ischemia symptoms.[263,264]
The embedment of cardiac spheroids into fibrinogen-based hydrogels aimed to inflict these stiffness-associated mechanical constraints *in vitro*. The hydrogels should serve a dual purpose, firstly the increased mechanical burden should elevate metabolic demand and secondly, the hydrogel should limit the effectiveness of passive diffusion.[265,266] Thus, the increased metabolic demand would be harder to meet, effectively recapitulating the two major problems of secondary ischemia, increased stiffness combined with too little blood vessels to sophistically supply the nutrients needed to sustain contractility.[267,268]
Functionally the embedded spheroids exhibited significant reduction in beating frequency while maintaining comparable contraction amplitude relative to normoxic controls. This pattern suggests an adaptive downregulation of pacing to manage resource availability while maintaining beating properties under the increased mechanical stress. Cardiomyocytes characteristically adapt their spontaneous beating

rate in response to energetic stress. This energy dependent shutdown is directly mediated through specific K_{ATP} channels, which under sufficient nutrient supply are repressed through ATP binding.[269] During metabolic stress or nutrient deprivation, the declining ATP levels promote channel opening, increasing the outward current of K^+, which causes membrane hyperpolarization and shortening of action potential duration.[270] This hyperpolarization severely impairs the spontaneous AP generation, effectively decreasing automaticity.[271] In this context the reduced pacing can be interpreted as a metabolic conservation strategy rather than primary contractile dysfunction.

The additional waveform analysis revealed prolonged relaxation kinetics, alterations that can be attributed to modified mechanical boundary conditions rather than intrinsic contractile dysfunction. In the hydrogel-embedded configuration, the surrounding matrix constrains spheroid deformation and thereby imposes an external mechanical load. During contraction the cardiac spheroid displaces the surrounding Hydrogel matrix, which in this phase functions as an external mechanical load comparable to afterload.[272] This load is the resistance the cardiac spheroid has to overcome to generate contractile shortening of the tissue. During relaxation cardiomyocytes must first reestablish intracellular calcium homeostasis primarily via ATP dependent reuptake of Ca^{2+} into the sarcoplasmic reticulum through sarcoplasmic reticulum Ca^{2+} ATPase (SERCA) combined with Ca^{2+} extrusion via the Na^+/Ca^{2+} exchanger.[273] The drop in intracellular calcium terminates the actin-myosin cross-bridge cycling, enabling sarcomeric relaxation. The mechanical return to resting length is achieved through the elastic recoil properties of titin.[274] In the case of the hydrogel embedded spheroid this elastic rebound is constrained by the viscoelastic nature of the surrounding matrix, particularly recoil kinetics can delay structural recovery by resisting tissue re-expansion.[275] This bidirectional mechanical interaction alters apparent contraction dynamics even if sarcomeric force generation remains stable.

Despite these meaningful mechanical effects, hydrogel-embedding failed to reproduce hallmark ischemic features such as severe arrhythmia or progressive beating arrest.[276] The gained insights render Hydrogels theoretically interesting, while achieving the stiffness threshold sufficient to drive metabolic collapse without inhibiting contractile activity form the start would demand precise rheological tuning. Apart from the rheological challenges hydrogel-based models possess an even more excluding limitation for reperfusion studies, reversibility. Reperfusion requires rapid restoration of oxygen and nutrient supply, a feat that in the hydrogel system could only be

achieved through rapid degradation of the hydrogel matrix, inflicting additional unintended stress on the cardiac spheroid.[277] Given these constraints, hydrogel embedding was categorized as a valuable model for mechanical stress modulation but was not further continued as ischemic priming strategy.

3.3.4.2. Direct Hypoxia Induction Strategies

After deeming secondary ischemia unsuited for the reperfusion model. Three distinct strategies for the direct hypoxia induction were evaluated. Firstly, the chamber-based oxygen reduction, secondly diffusion-limited hypoxia via mineral oil overlay, and lastly active oxygen displacement through nitrogen flux. Each method produced distinct functional signatures, highlighting that "hypoxia" is not a uniform condition but strongly dependent on induction kinetics and diffusion characteristics.

3.3.4.3. Hypoxic Imaging Chamber: Partial Oxygen Depletion

The chamber-integrated hypoxia system allowed controlled reduction of atmospheric oxygen during live imaging. Functionally, hypoxia reduced beating rate compared to normoxic controls, consistent with diminished ATP availability due to impaired mitochondrial oxidative phosphorylation and increased reliance on glycolysis. As oxygen serves as the terminal electron acceptor of the electron transport chain, its reduction limits ATP production efficiency, thereby lowering intracellular ATP levels.[278] The resulting energetic deficit may trigger the previously described K_{ATP}-mediated modulation of membrane excitability, leading to reduced spontaneous contraction frequency.[279]

Interestingly, contraction amplitude increased while the coefficient of variation of inter-beat intervals (CV IBI) decreased, indicating more stereotyped beat timing despite apparent visual irregularity. Given that data acquisition was performed over an extended period of 6 h, the high variability observed in normoxic controls likely reflects physiological adaptability of healthy cardiac tissue to subtle fluctuations in pH, temperature, gas composition, metabolic byproducts, and nutrient availability.[280] In contrast, prolonged but regular interbeat intervals in the hypoxic group may reflect constrained electrophysiological flexibility, a feature often associated with pathological stress responses.[281,282]

Importantly, no sustained elevation of baseline intracellular calcium or progressive contractile collapse was observed. Under hypoxic conditions, ATP depletion commonly impairs calcium homeostasis through reduced SERCA activity and

diminished Na^+/K^+-ATPase function.[283] This can lead to secondary Na^+ accumulation, altered Na^+/Ca^{2+} exchanger activity, and cytosolic Ca^{2+} overload.[283,284] Sustained calcium elevation is a hallmark of ischemic injury and precedes contractile failure and cell death.[285]

These findings indicate that chamber hypoxia induced moderate metabolic stress but likely did not achieve near-zero oxygen levels. Residual dissolved oxygen in the media, incomplete sealing of the system, and diffusion through plate lids likely buffered the system. For ischemia–reperfusion modelling, this level of hypoxia appears insufficient, as it fails to produce the profound electrophysiological and calcium-handling disturbances characteristic of severe ischemia.

3.3.4.4. Mineral Oil Overlay: Diffusion-Limited Progressive Hypoxia

Mineral oil overlay introduced a diffusion barrier at the medium–air interface, not merely increasing diffusion distance and thus, according to Fick's First Law, reducing diffusion flux, but also, more importantly suppressing convective mixing.[256,257] By reducing convective contribution, oxygen transport becomes heavily dependent on passive diffusion.[286] In highly metabolically active systems such as contractile cardiac spheroids, oxygen consumption rates are substantial due to continuous ATP demand for cross-bridge cycling, calcium reuptake via SERCA, and maintenance of ion gradients.[287–289] Under these conditions, passive diffusion alone is insufficient to maintain metabolic demand, over a prolonged period resulting in the establishment of steep oxygen gradients.[290]

Functionally, this approach generated pronounced ischemia-like phenotypes, including early reductions in beat rate, increased arrhythmicity, progressive amplitude decline, and complete arrest following prolonged exposure. Unlike controlled chamber hypoxia, which induces a relatively stable reduction in oxygen availability, mineral oil overlay created a cumulative stress environment characterized by progressive intracellular ATP depletion, impaired ion homeostasis, and increasing metabolic acidosis due to anaerobic glycolysis and lactate accumulation.[291]

CV IBI increased significantly, reflecting rising arrhythmicity and progressive destabilization of electrical pacing.[292] In several specimens, beating ultimately progressed to complete contraction arrest, indicating severe electrophysiological and metabolic failure. Mechanistically, profound oxygen deprivation compromises ATP-dependent ion pumps, including Na^+/K^+-ATPase and SERCA, leading to membrane depolarization instability, disrupted calcium cycling, and increased susceptibility to

afterdepolarizations.[293,294] These functional changes strongly support effective and progressively worsening oxygen deprivation.

Transcriptionally, mineral oil treatment triggered upregulation of BNIP3 (Figure 25), consistent with hypoxia-induced mitochondrial stress and metabolic reprogramming toward glycolysis.[295,296] BNIP3 induction reflects activation of hypoxia-responsive pathways, including HIF-dependent signalling, and is associated with mitochondrial dysfunction, mitophagy initiation, and pro-apoptotic signalling under severe stress.[297] Increased collagen deposition observed after 3 hours of hypoxia followed by 3 days of incubation suggests early stress-induced extracellular matrix remodelling, potentially mediated by hypoxia-driven fibroblast activation and TGF-β–associated profibrotic signalling.[298,299] Such remodelling may represent an attempt to stabilize tissue structure under stress but can simultaneously increase mechanical stiffness and further impair diffusion.

However, prolonged (20-hour) exposure, which functionally culminated in complete beating impairment, led to severe structural deterioration and failure of RNA extraction, consistent with extensive necrosis and/or apoptosis.[300] At this stage, sustained ATP depletion likely disrupts ion homeostasis through failure of ATP-dependent pumps, promoting calcium overload, mitochondrial permeability transition pore opening, and excessive reactive oxygen species accumulation.[301] These processes collectively drive irreversible cellular injury, marking the transition from an initially adaptive hypoxic response to overt ischemic damage.[302]

While mineral oil effectively induces severe hypoxia and key ischemic responses, it presents substantial practical limitations for reperfusion modelling. Its diffusion-dependent onset and inherently slow kinetics limit temporal precision. Even minor variations in oil layer thickness or energy consumption of the cardiac spheroids can markedly alter incubation times, leading to premature or delayed hypoxic onset and thereby missing the critical window required to model reperfusion injury.[256,303]

Moreover, simultaneous nutrient and oxygen deprivation is required to replicate ischemic conditions.[304] In this model, nutrient restriction necessitates the addition of buffer solution prior to the introduction of the mineral oil layer, resulting in cells that are already metabolically compromised by the time hypoxia is established. This pre-existing starvation may confound the onset kinetics and alter cellular contractile activity, further complicating interpretation.

Reperfusion injury modelling requires tightly defined ischemic durations and rapid, well-controlled reoxygenation.[305] The mineral oil approach lacks this level of temporal

controllability and was therefore not selected as the primary strategy for ischemic induction.

3.3.4.5. Nitrogen Flux: Rapid, Tuneable, and Mechanistically Aligned

Nitrogen flux directly displaces dissolved oxygen from the extracellular medium, enabling rapid and reproducible induction of hypoxia.[306] In contrast to diffusion-based approaches, this method achieves near-immediate oxygen depletion, minimizing transitional variability and allowing sharp definition of ischemic onset. Functionally, nitrogen flux produced the most pronounced acute hypoxic phenotype, characterized by rapid suppression of spontaneous beating, marked elevation of diastolic (baseline) intracellular calcium, reduced calcium transient amplitude, and robust recovery following reoxygenation.

The elevation of baseline cytosolic calcium represents a central mechanistic hallmark of early ischemic injury.[307] Oxygen deprivation impairs mitochondrial oxidative phosphorylation, resulting in ATP depletion and a subsequent reduction in ATP-dependent ion transport.[308] Decreased Na^+/K^+-ATPase activity promotes membrane depolarization and intracellular sodium accumulation, which in turn reduces the driving force for forward-mode Na^+/Ca^{2+} exchange (NCX) and may even favour reverse-mode operation (1.10).[309] Simultaneously, ATP depletion limits SERCA-mediated sarcoplasmic reticulum calcium reuptake, further contributing to cytosolic calcium accumulation.[310] Elevated intracellular calcium not only suppresses coordinated contractility but also promotes mitochondrial calcium loading, which increases the likelihood of mitochondrial permeability transition pore (mPTP) sensitization, and primes cells for amplified injury upon reperfusion.[311] Thus, the observed calcium elevation is not merely a functional readout but reflects activation of core ischemic injury pathways.

Importantly, nitrogen flux provides precise temporal control over hypoxic duration. Even brief exposures (e.g., 60 seconds) were sufficient to induce transient beating arrest, closely resembling early ischemic contractile suppression observed *in vivo*.[312] The rapid reversibility upon reoxygenation confirms that injury severity can be modulated within defined temporal windows, enabling discrimination between adaptive suppression and irreversible damage. This degree of temporal resolution is critical for modelling reperfusion injury, where both ischemic duration and reoxygenation kinetics determine downstream outcomes such as calcium overload, oxidative stress generation, and mitochondrial dysfunction.[313]

Among the tested strategies, nitrogen flux therefore offered the optimal balance of severity, reproducibility and temporal precision. Its ability to induce rapid, mechanistically relevant hypoxic responses while maintaining controlled reversibility makes it particularly well suited for reperfusion injury modelling.[314]

3.3.4.6. Nutrient Deprivation and Ionic Control

Ischemia is not defined solely by oxygen deprivation. *In vivo*, occlusion of coronary vessels eliminates not only oxygen but also glucose and fatty acid supply.[315] Anaerobic glycolysis temporarily compensates but leads to lactate accumulation and intracellular acidosis.[94] Ionic imbalances arise due to ATP-dependent pump failure, contributing to calcium overload and arrhythmia.[316]

To model nutrient deprivation while maintaining defined ionic composition, Tyrode solution was selected. Tyrode is widely used in cardiac electrophysiology due to its precisely defined Na^+, K^+, Ca^{2+}, Mg^{2+}, and bicarbonate composition.[317] The pH was adjusted to 7.2 to successfully mimic the extracellular pre ischemia environment.[318,319] It supports short-term cardiomyocyte survival while lacking metabolic substrates required for sustained ATP production.

Standalone Tyrode exposure induced mechanical alternans-like behaviour, characterized by alternating strong and weak contractions. Mechanical alternans is closely associated with instability in intracellular calcium cycling and represents a recognized pro-arrhythmic phenotype under metabolic stress conditions.[320,321] The emergence of alternans therefore indicates functional stress at the level of excitation–contraction coupling rather than structural damage.

Importantly, alternans was partially reversible upon washout, suggesting that Tyrode exposure induces a metabolically stressed yet viable state without immediate irreversible injury. The absence of sustained dysfunction can likely be attributed to preserved mitochondrial oxidative phosphorylation and the availability of endogenous energy reserves.[322] Cardiomyocytes possess substantial metabolic flexibility and maintain intracellular glycogen stores, phosphocreatine buffering capacity, and ongoing fatty acid oxidation under normoxic conditions.[323] As long as oxidative phosphorylation remains intact and ATP levels do not fall below critical thresholds, ion homeostasis and calcium handling can be sufficiently supported to prevent irreversible injury.[284,324]

Under these conditions, metabolic stress is primarily reflected in alternans rather than bioenergetic collapse. SERCA activity and sarcolemma ion pumps may operate at

reduced efficiency, increasing susceptibility to beat-to-beat variability, yet remain functional enough to avoid sustained calcium overload or membrane destabilization.[310,325] Thus, the observed phenotype reflects reversible energetic strain rather than structural or mitochondrial failure.

Collectively, these findings indicate that Tyrode exposure induces a controlled metabolic challenge that stresses calcium handling dynamics without exceeding the threshold for irreversible ischemic injury. This reversibility is essential in the context of reperfusion modelling. Ischemia–reperfusion is not defined by isolated oxygen or nutrient deprivation, but by their combined restriction followed by reintroduction.[302] Each component must therefore produce a stress response that remains within a recoverable range when applied independently.

Within this framework, Tyrode solution fulfils the role of controlled nutrient deprivation. It removes exogenous metabolic substrates while preserving short-term cellular viability, thereby sensitizing cardiomyocytes without inducing terminal injury. This property makes it suitable as the nutrient deprivation component in a combined ischemia–reperfusion model.

3.3.4.7. Integrative Interpretation and Method Selection

The comparative evaluation highlights that the tested methods capture distinct components of the ischemic phenotype, with limitations when applied as a standalone reperfusion model. Mechanical confinement effectively models stiffness-associated load but lacks reversibility. Chamber hypoxia induces moderate metabolic stress without pronounced calcium dysregulation. Mineral oil overlay produces severe hypoxia but lacks temporal precision and compatibility with rapid reperfusion transitions.

In contrast, nitrogen flux enables rapid and tuneable oxygen deprivation with reproducible disturbances in calcium handling and well-defined reversibility, while Tyrode solution complements this by imposing metabolic substrate deprivation and ionic stress without precipitating immediate catastrophic failure. Combined, these approaches allow precise control of ischemic duration, reproducible induction of functional impairment, such as beating arrest and baseline calcium elevation and a defined transition into reoxygenation through media restoration. This strategy establishes a mechanistically grounded and experimentally reproducible framework for modelling reperfusion injury.

3.4. Reperfusion

Reperfusion following prolonged ischemia represents a critical determinant of cardiac cell survival in ischemic pathophysiology. Cells primed by oxygen and nutrient deprivation respond sensitively to the rapid reintroduction of oxygen and metabolic substrates, which can trigger secondary injury mechanisms.[302]

3.4.1. Metabolic Activity Assessment Under Reperfusion

The first block addresses the biological foundation of the model. Following directed cardiac differentiation, spheroids were structurally and functionally characterized to confirm cardiomyocyte identity and baseline properties. This was followed by the establishment of a temporally controlled ischemia–reperfusion protocol combining rapid oxygen deprivation with defined metabolic restriction using cardiac spheroids.

Ischemic conditions were mimicked by incubating spheroids in Tyrode solution adjusted to pH 7.2 while applying a continuous nitrogen stream to remove dissolved oxygen (degassed Tyrode solution). This setup enabled rapid and reproducible modulation of oxygen availability while simultaneously limiting nutrient supply. After a 30-minute ischemic interval, the Tyrode solution was removed and replaced with oxygenated maintenance medium, and nitrogen flow was discontinued to simulate reperfusion.

To evaluate the individual contributions of mechanical handling, oxygen deprivation, and nutrient deprivation, three control conditions were included. A media-exchange control underwent the same solution replacement steps as the experimental condition but without oxygen deprivation, controlling for potential mechanical stress associated with medium exchange. A deoxygenated medium control was exposed to nitrogen-degassed culture medium while maintaining nutrient-rich conditions, thereby isolating the effects of oxygen deprivation in the absence of nutrient limitation. Finally, a Tyrode control exposed spheroids to nitrogen-degassed, pH-adjusted Tyrode solution for 30 minutes without additional nitrogen treatment, allowing evaluation of nutrient deprivation and altered buffering conditions independent of active oxygen displacement.

Cellular metabolic activity following reperfusion was quantified using an MTT assay (5.2.6.3) at multiple recovery intervals. Measurements were performed immediately after reperfusion (T0), as well as 24 hours (T1), 72 hours (T3), and 7 days (T7) post-treatment. For each time point, MTT reagent was added directly after the designated

recovery period and incubated for 3 hours prior to analysis, enabling assessment of short- and long-term effects on spheroid viability and metabolic function.

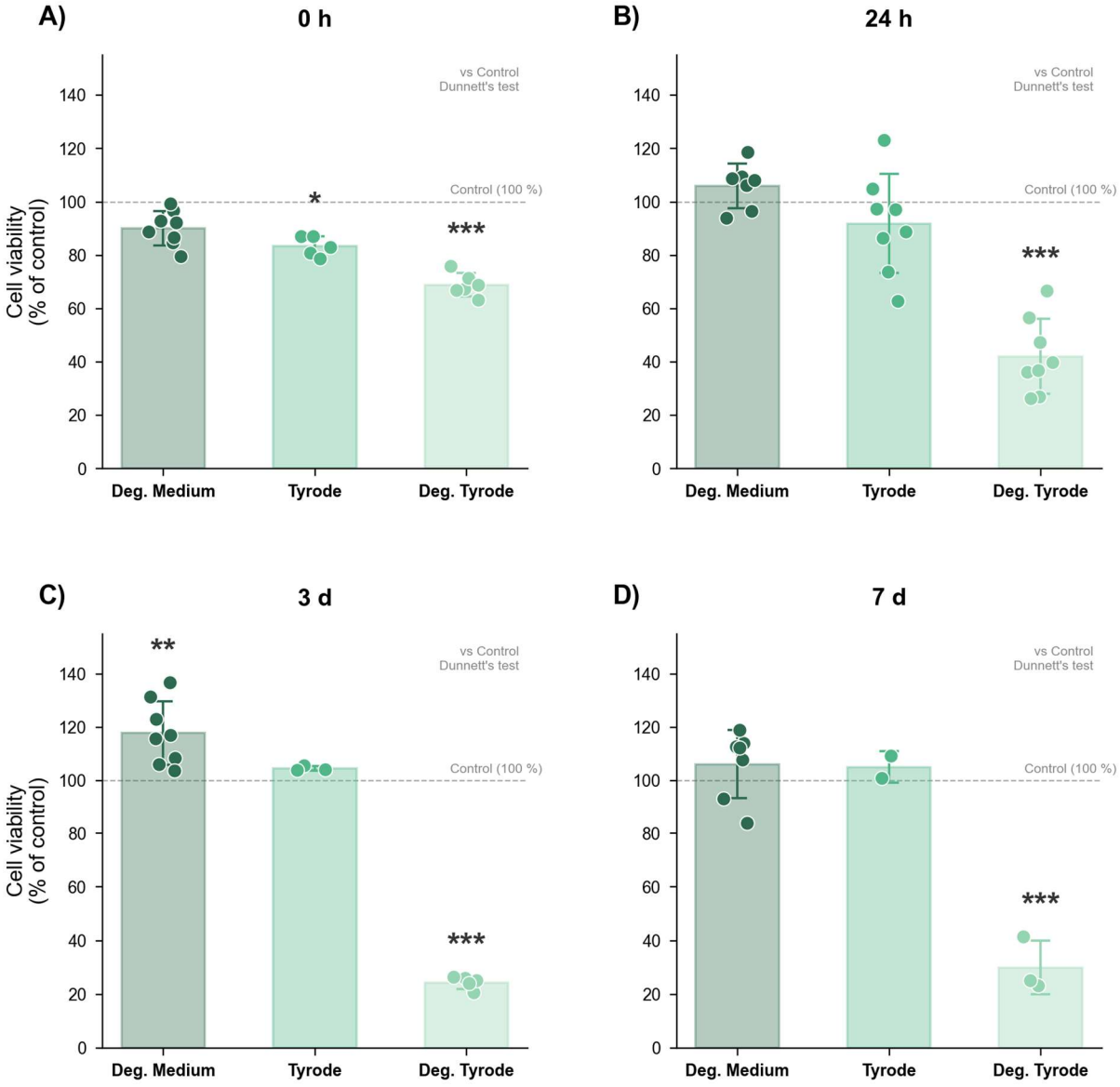

Figure 29: Effect of degassed solutions on cardiomyocyte viability over time. Cell viability was assessed by MTT assay at 0 h (A), 24 h (B), 3 days (C), and 7 days (D) following treatment with Degassed Medium, Tyrode solution, or Degassed Tyrode solution. Absorbance values were normalised to the Control group mean at the corresponding timepoint (dashed line, 100 %). Bars represent group means; error bars indicate ± SD; individual data points are overlaid. Statistical comparisons versus Control were performed independently at each timepoint using Dunnett's multiple comparison test (*p < 0.05; **p < 0.01; ***p < 0.001). Degassed Tyrode reduced viability at all analysed timepoints, with mean values decreasing from 68.9 ± 4.4 % at 0 h to 24.2 ± 2.2 % at 3 days (p < 0.001 at indicated timepoints). Tyrode solution alone produced a reduction at 0 h (83.3 ± 3.8 %, p = 0.021), which was not observed at later timepoints. Degassed Medium showed a transient increase in viability at 3 days (117.8 ± 11.9 %, p = 0.007). Sample sizes ranged from n = 2 to n = 8 per group per timepoint. Outliers were excluded prior to analysis using the 1.5 × IQR method.

Figure 29 illustrates the effects of simulated reperfusion on spheroid metabolic activity normalized to time-matched control groups.

Degassed Tyrode solution was associated with reduced viability at all examined timepoints compared to Control. Viability decreased to 68.9 ± 4.4 % at 0 h (p < 0.001, Dunnett's test), 42.0 ± 14.1 % at 24 h (p < 0.001), and 24.2 ± 2.2 % at 3 days (p < 0.001),

with values remaining low at 7 days (29.9 ± 10.1%, $p < 0.001$). The most pronounced reduction occurred within the first 24 hours, followed by persistently reduced viability at later timepoints (Figure 29).

Tyrode solution alone produced a reduction in viability at 0 h (83.3 ± 3.8 %, $p = 0.021$) (Figure 29, A), which was not observed at subsequent timepoints. No significant differences from Control were detected at 24 h, 3 days, or 7 days (Figure 29).

Degassed Medium did not reduce viability at any timepoint. At 3 days, viability was increased relative to Control (117.8 ± 11.9 %, $p = 0.007$) (Figure 29, C), whereas no difference was observed at 7 days (106.1 ± 12.7 %, $p = 0.687$).

Overall, these findings indicate that the combination of Tyrode solution and degassing was associated with a sustained reduction in cardiomyocyte viability, whereas Tyrode alone and Degassed Medium did not produce comparable effects under the conditions tested.

3.4.2 Morphological Changes Caused by Reperfusion injury

Reperfusion injury especially affects cardiomyocytes due to their high mitochondrial density and energy demands necessary for contractile function.[326] Ischemic preconditioning can exacerbate structural stress in these cells, leading to contraction arrest and rigor-like states.[302]

Given the marked reduction in viability observed under certain treatment conditions, it was important to determine whether this effect reflected selective cardiomyocyte injury or a more generalized loss of spheroid integrity. To address this, immunostaining was performed to assess cytoskeletal organisation and mitochondrial distribution, two structural features commonly altered during ischemia–reperfusion-associated cellular damage.[327]

Experimentally cardiac spheroids at differentiation day 21 were separated into four treatment groups: control, deoxygenated medium, Tyrode solution (pH 7.2), and deoxygenated Tyrode solution, thereby isolating the effects of oxygen and nutrient deprivation individually and in combination. Spheroids were treated as described in Section 3.4.1. For immunostaining, three spheroids per group were harvested at four time points: immediately post-treatment (T0), 24 hours (T1), 3 days (T3), and 7 days (T7).

Following fixation with 4 % PFA (after Mito Tracker™ staining (5.2.6.6)), spheroids were stained with anti-cTnT antibodies to visualize cardiomyocyte structure. Hoechst

staining was applied prior to imaging, and confocal image acquisitions were performed using the Leica Stellaris 5 (5.2.5).

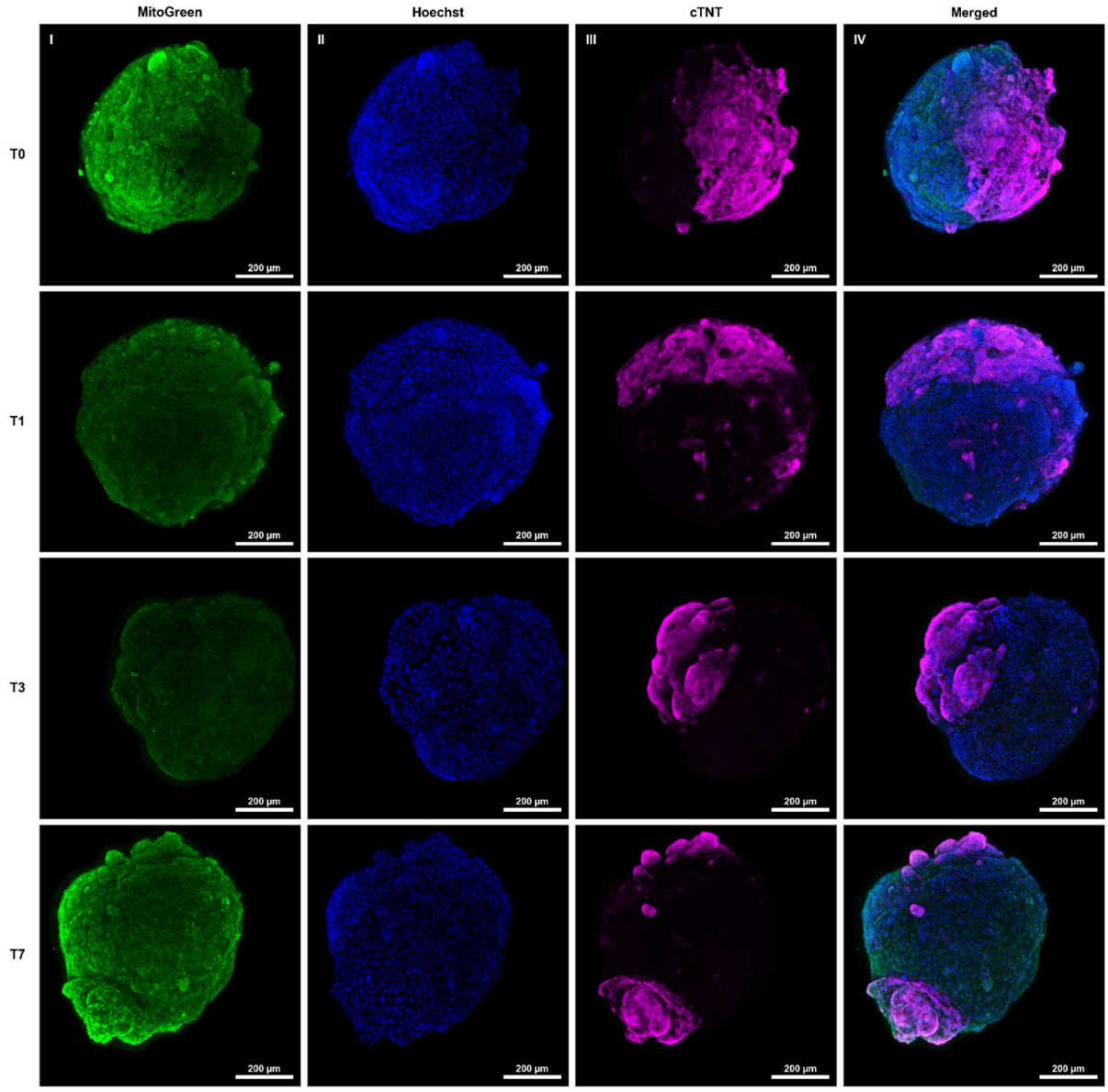

Figure 30: Confocal fluorescence imaging of mitochondrial activity and cardiomyocyte marker expression in iPSC-derived cardiac spheroids over time under control conditions. iPSC-derived cardiac spheroids were generated in 384-well plates and analysed at differentiation day 21 (DD21). Spheroids were maintained under standard culture conditions (37 °C, 5 % CO_2) without experimental treatment. Four timepoints were assessed: T0 (baseline), T1 (1 day), T3 (3 days), and T7 (7 days). Prior to fixation at each timepoint, spheroids were stained with MitoTracker Green FM (200 nM, 30 min; Invitrogen, M7514, Lot 1948108) to assess mitochondrial membrane potential. Following fixation, nuclei were labelled with Hoechst 33342 (1:5000, 60 min; Thermo Fisher, 62249). Cardiomyocytes were identified by immunostaining for cardiac troponin T (cTnT; mouse monoclonal, clone 13-11, 1:400; Invitrogen, MA5-12960, Lot 2504985) followed by Alexa Fluor 647–conjugated goat anti-mouse secondary antibody (1:500; Invitrogen, A21235, Lot 2186088). Images were acquired using a Leica STELLARIS 5 confocal laser scanning microscope (DMI8-CS inverted platform) with an HC PL APO CS2 10×/0.40 DRY objective, bidirectional scanning, 4× frame averaging, and pinhole set to 1 Airy unit. Z-stacks were collected at 0.88 µm/pixel lateral resolution and displayed as mean intensity projections. Columns (I–IV) show (I) MitoTracker Green (green), (II) Hoechst (blue), (III) cTnT (magenta), and (IV) the merged composite. A spheroid mask was generated from the combined Hoechst and cTnT channels using Otsu thresholding followed by morphological refinement to exclude background signal. Contrast was normalised per channel across all four timepoints using percentile-based scaling of spheroid pixels (p1.5–p99.5) to enable direct temporal comparison. For the T3 MitoTracker channel, a blended contrast normalisation (30 % per-sample, 70 % global scaling) was applied to account for reduced staining intensity at this timepoint. Representative images from one spheroid per timepoint are shown. Scale bars: 200 µm.

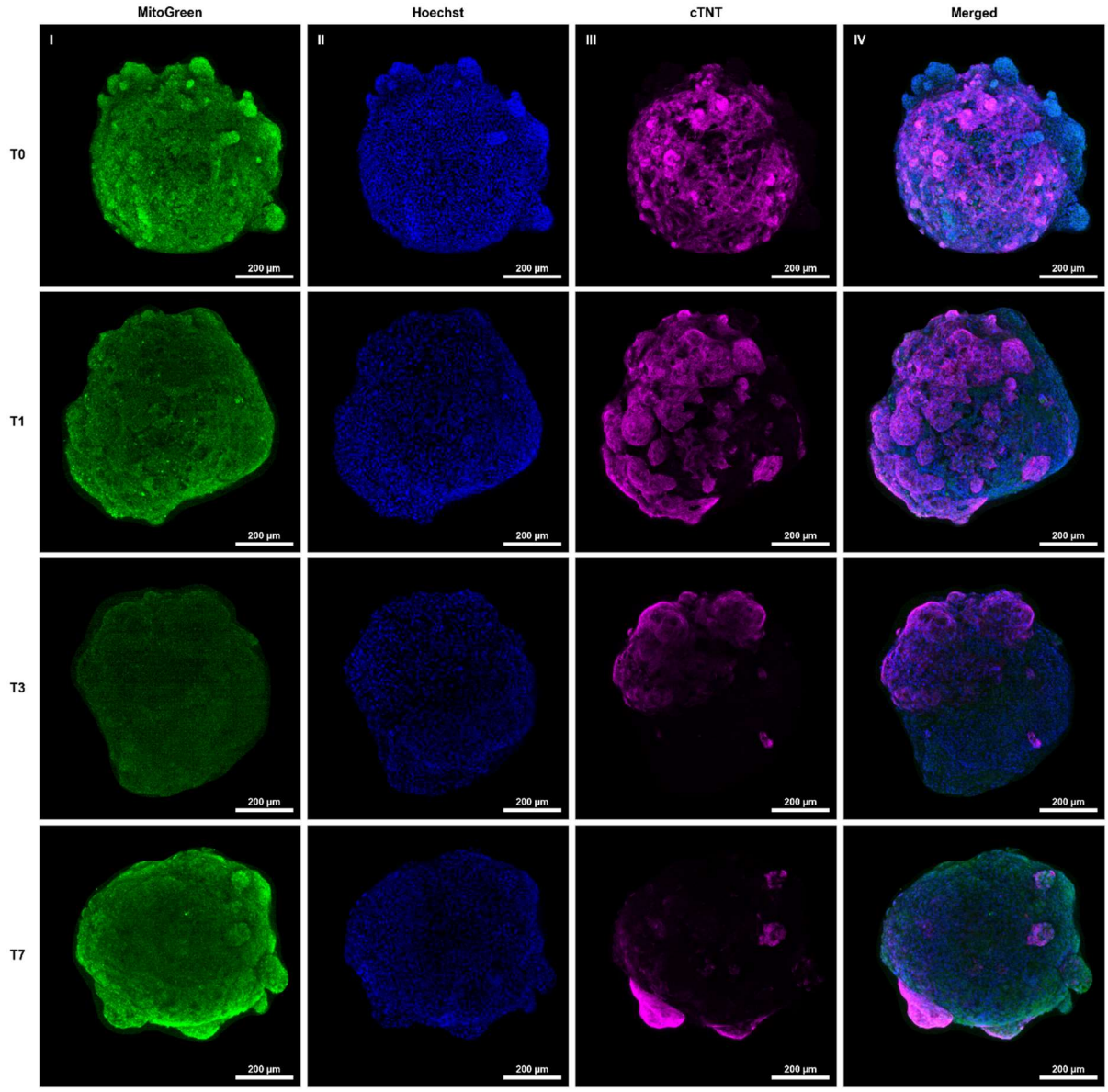

Figure 31: Confocal fluorescence imaging of mitochondrial activity and cardiomyocyte marker expression following incubation in deoxygenated culture medium. iPSC-derived cardiac spheroids were incubated in deoxygenated cell culture medium to model oxygen deprivation. At defined timepoints following treatment, spheroids were stained with MitoTracker Green to assess mitochondrial membrane potential, Hoechst 33342 for nuclear visualisation, and immunostained for cTnT to identify cardiomyocytes. Imaging was performed using confocal laser scanning microscopy as described in Figure X. Z-stacks were acquired and displayed as mean intensity projections. Contrast was normalised per fluorescence channel across all four timepoints within this condition. Representative images from one spheroid per timepoint are shown. Experimental design, staining, and image processing were performed as described in Figure X. Scale bars: 200 µm.

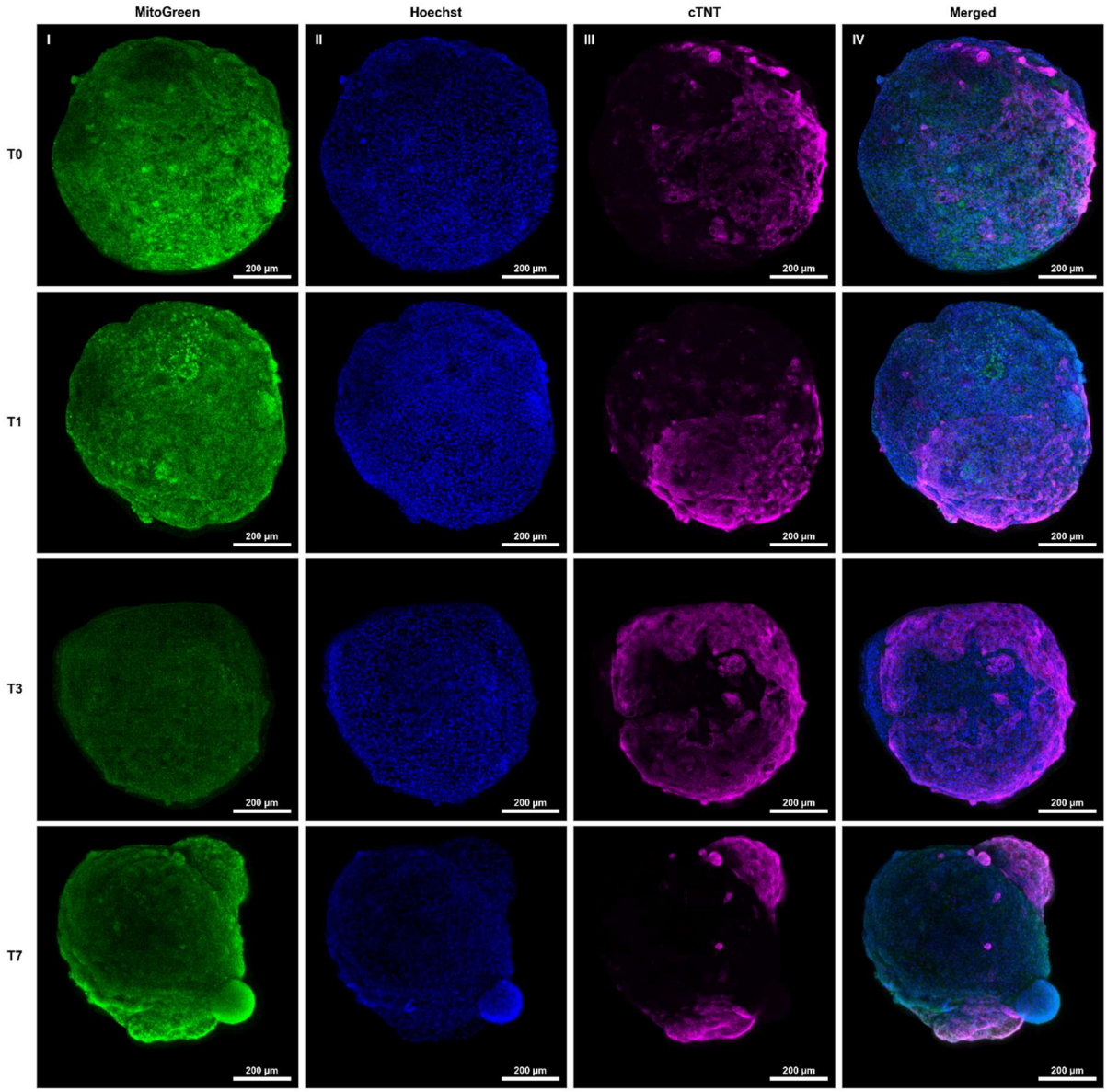

Figure 32: Confocal fluorescence imaging of mitochondrial activity and cardiomyocyte marker expression following incubation in Tyrode solution. iPSC-derived cardiac spheroids were incubated in Tyrode solution as an isotonic, nutrient-free control condition. At defined timepoints, spheroids were stained with MitoTracker Green, Hoechst 33342, and immunolabelled for cTnT. Image acquisition and processing were performed as described in Figure X. Z-stacks are displayed as mean intensity projections. Contrast was normalised per channel across all four timepoints within this condition. Representative images from one spheroid per timepoint are shown. Experimental design, staining, and image processing were performed as described in Figure X. Scale bars: 200 µm.

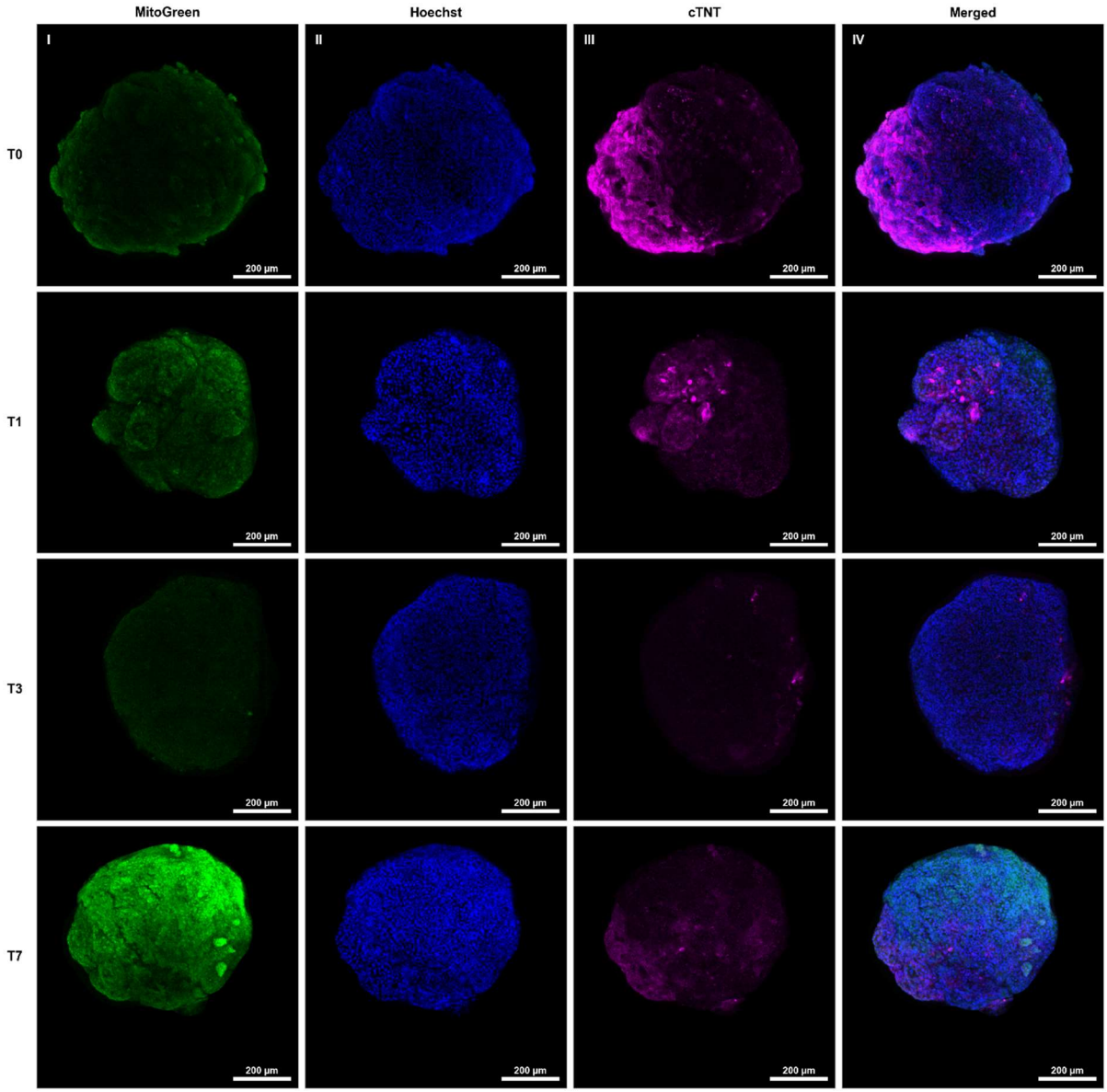

Figure 33: Confocal fluorescence imaging of mitochondrial activity and cardiomyocyte marker expression following incubation in deoxygenated Tyrode solution. iPSC-derived cardiac spheroids were incubated in deoxygenated Tyrode solution, combining oxygen deprivation and nutrient withdrawal. At defined timepoints, spheroids were stained with MitoTracker Green, Hoechst 33342, and immunolabelled for cTnT. Image acquisition and processing were performed as described in Figure X. Z-stacks are displayed as mean intensity projections. Contrast was normalised per channel across all four timepoints within this condition. Representative images from one spheroid per timepoint are shown. Experimental design, staining, and image processing were performed as described in Figure X. Scale bars: 200 µm.

Cardiac spheroids of the control group maintained stable morphology and fluorescence signal distribution across all timepoints (Figure 30). MitoTracker Green signal remained uniformly distributed from T0 to T7, indicating preserved mitochondrial activity. Hoechst staining showed consistent nuclear density and morphology, and cTnT signal exhibited the expected heterogeneous distribution characteristic of cardiomyocyte-enriched regions. No progressive structural alterations were observed over the 7-day period.

Spheroids exposed to deoxygenated culture medium displayed a comparable temporal pattern (Figure 31). MitoTracker Green, Hoechst, and cTnT signals remained largely preserved across all assessed timepoints. A transient reduction in MitoTracker signal intensity was observed at T3; however, this was also present in the control condition and corresponded to a technical variation in staining duration at this timepoint. No consistent evidence of progressive structural disruption was detected under deoxygenated medium alone within the analysed time frame.

Similary, incubation in Tyrode solution did not exhibit pronounced structural alterations over the 7-day period (Figure 32). MitoTracker Green signal remained largely preserved across timepoints, with a transient reduction at T3 that was also observed in the control and deoxygenated medium conditions and corresponded to a technical variation in staining duration. Hoechst staining remained well defined, with no evident loss of nuclear density. cTnT signal was maintained throughout the time course, retaining its characteristic heterogeneous distribution and organised sarcomeric pattern. Overall, Tyrode solution alone did not produce clear evidence of progressive structural disruption under the conditions tested.

The most pronounced structural changes were observed in spheroids treated with deoxygenated Tyrode solution (Figure 33). MitoTracker Green signal decreased substantially between T0 and T3 and remained low at T7, with altered spatial distribution compared to baseline. Hoechst staining persisted across timepoints but appeared increasingly diffuse at later stages. cTnT signal intensity declined markedly between T0 and T3. At T7, cTnT staining was detectable but exhibited a diffuse pattern lacking the organised sarcomeric appearance observed at earlier timepoints.

Collectively, these findings demonstrate a graded response across treatment conditions. Deoxygenated medium as well as Tyrode solution alone produced minimal structural alteration over the 7-day period. The combination of oxygen deprivation and nutrient removal resulted in the most substantial reduction and disruption of mitochondrial- and cardiomyocyte-associated signal intensity and structure. These data indicate that combined metabolic and oxygen stress exerts a greater impact on spheroid structural integrity than either deprivation alone under the conditions tested.

3.4.2. Gene Expression During Reperfusion

To further characterize the molecular effects of simulated ischemia–reperfusion injury, gene expression analysis was performed using RT-q-PCR. Experimental conditions

mirrored those described for the functional reperfusion timeline 3.4.1, enabling direct comparison between metabolic activity and transcriptional responses.

Spheroids were collected at defined recovery intervals corresponding to 24 hours (T1), 73 hours (T3), and 7 days (T7) post-treatment. At each time point, RNA was extracted from intact spheroids to capture global transcriptional changes across the three-dimensional construct and to minimize bias that could arise from region-specific sampling. Expression of selected cardiac, mesenchymal, and hypoxia-associated markers (cTnT, α-SMA, Glut1, and HIF-1α) was subsequently quantified by RT-qPCR (5.2.7).

It should be noted that no T3 sample was available for the reperfusion condition due to experimental limitations. Consequently, molecular analysis for this group was restricted to T1 and T7, while all other treatment conditions were evaluated across the full time course.

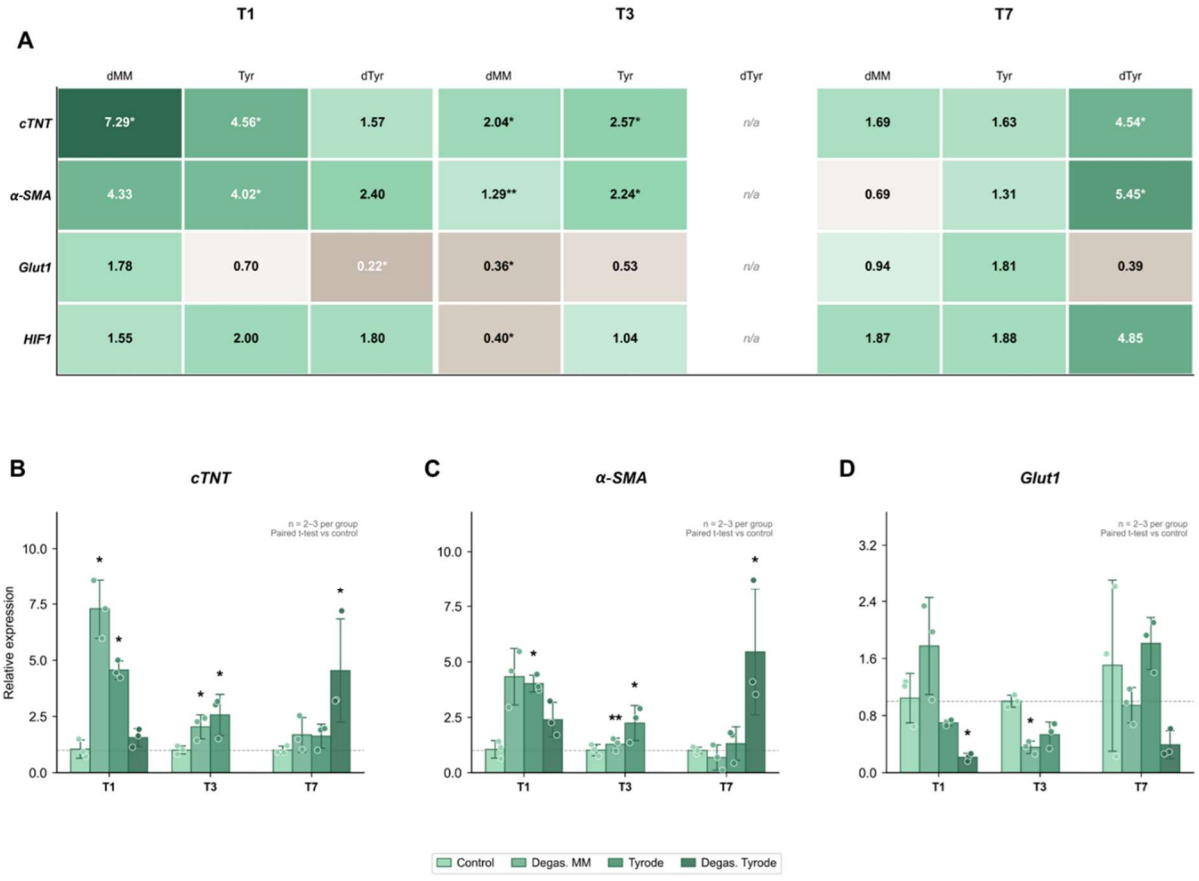

Figure 34: Gene expression analysis of reperfusion-associated markers following simulated ischaemia–reperfusion injury in cardiac spheroids. (A) Heatmap showing mean relative expression (fold change vs. time-matched untreated control) of four target genes (cTnT, α-SMA, Glut1, HIF-1α) across three reperfusion timepoints (T1, T3, T7) under three experimental conditions: degassed maintenance medium (dMM), Tyrode solution (Tyr), and degassed Tyrode solution (dTyr). Gene expression was quantified by RT-qPCR and normalised to the housekeeping gene HPRT using the 2^(-ΔΔCt) method (Livak and Schmittgen, 2001). Untreated control samples at each respective timepoint served as the reference (fold change = 1). Fold change values are annotated within each cell. Asterisks indicate significant differences relative to the time-matched control (* $p < 0.05$, ** $p < 0.01$; paired t-test on ΔCt values). Colour intensity reflects relative expression level (white: no change; dark green: upregulation; brown-grey: downregulation). The degassed Tyrode condition at T3 is indicated as n/a due to failed

RNA extraction (HPRT not detected). (B–D) Bar plots showing relative expression of cTnT (B), α-SMA (C), and Glut1 (D) across conditions and timepoints. Bars represent mean fold change; error bars indicate ± SD. Individual biological replicates are shown as data points. The dashed horizontal line denotes baseline expression of the time-matched untreated control (fold change = 1). Statistical significance relative to control is indicated by asterisks (* $p < 0.05$, ** $p < 0.01$; paired t-test). Statistical analysis was performed on ΔCt values using paired t-tests comparing each treatment condition to its corresponding time-matched untreated control within the same biological replicate. Only groups with $n \geq 2$ biological replicates were included in statistical testing. HIF-1α expression data are limited to $n = 2$ per group and should therefore be interpreted cautiously. All data represent independent biological replicates derived from separate pooled spheroid batches ($n = 2–3$ per condition).

An overview of expression changes for the target genes is shown in Figure 34 A. The most prominent transcriptional changes occurred at the earliest reperfusion timepoint (T1), particularly for cTnT and α-SMA under the degassed Maintenance Media (dMM) and Tyrode solution conditions. In contrast, Glut1 exhibited reduced expression under degassed Tyrode at T1.

cTnT displayed the most consistent upregulation across conditions (Figure 34 B). At T1, expression was significantly elevated under degassed maintenance medium (7.29-fold; $n = 3$; $p = 0.026$) and Tyrode solution (4.56-fold; $n = 3$; $p = 0.014$), whereas degassed Tyrode showed a non-significant increase (1.57-fold; $p = 0.28$). At T3, cTnT remained significantly elevated under dMM (2.04-fold; $p = 0.018$) and Tyrode solution (2.57-fold; $p = 0.026$). By T7, expression under dMM and Tyrode had returned toward baseline, while degassed Tyrode solution exhibited significant upregulation (4.54-fold; $p = 0.047$) with greater inter-replicate variability.

α-SMA also demonstrated time-dependent changes (Figure 34 C). At T1, Tyrode solution treatment produced significant upregulation (4.02-fold; $n = 3$; $p = 0.024$), while dMM showed a similar magnitude of increase that did not reach significance (4.33-fold; $p = 0.061$). At T3, both dMM (1.29-fold; $p = 0.010$) and Tyrode (2.24-fold; $p = 0.012$) were significantly elevated. At T7, degassed Tyrode solution showed significant upregulation (5.45-fold; $p = 0.044$), whereas other conditions were not significantly different from control.

Glut1 exhibited a distinct pattern characterised primarily by reduced expression (Figure 34 D). Under degassed Tyrode solution at T1, Glut1 was significantly decreased (0.22-fold; $n = 3$; $p = 0.046$). At T3, dMM also showed significant downregulation (0.36-fold; $p = 0.013$), while Tyrode demonstrated a reduction that did not reach statistical significance (0.53-fold; $p = 0.055$). By T7, Glut1 expression under dMM and Tyrode solution returned toward baseline levels. Degassed Tyrode solution remained reduced (0.39-fold; $p = 0.30$), though not significantly.

HIF-1α expression is presented in the heatmap overview but is limited by small sample size ($n = 2$ per group). Expression remained near baseline at T1, showed reduced expression under dMM at T3 (0.40-fold; $p = 0.012$), and increased under degassed

Tyrode solution at T7 (4.85-fold; p = 0.21). Given the limited replication, these findings should be interpreted cautiously.

Overall, the data demonstrates condition- and time-dependent transcriptional responses following simulated ischaemia–reperfusion injury. Early upregulation of cTnT and α-SMA was observed under degassed maintenance medium and Tyrode solution conditions at T1 and T3, while degassed Tyrode solution exhibited a delayed pattern of significant upregulation at T7. Glut1 expression showed early suppression under degassed Tyrode solution and dMM. These findings indicate distinct temporal response profiles across treatment conditions.

3.4.3. ROS Production Under Reperfusion Injury

A central hallmark of ischemia–reperfusion injury is excessive production of reactive oxygen species (ROS), which contributes to intracellular damage and ultimately apoptosis. During ischemia, accumulation of mitochondrial metabolites such as succinate primes the electron transport chain for abrupt reactivation upon oxygen reintroduction. This sudden metabolic flux overloads the respiratory chain and promotes ROS overproduction.

To evaluate whether the reperfusion model reproduces this characteristic feature of injury, ROS generation was assessed following treatment.

Cardiac spheroids at differentiation day 21 were divided into three groups: control (media exchange only), deoxygenated medium, and deoxygenated Tyrode solution (pH 7.2). Spheroids were subjected to 30 minutes of treatment before being transferred to fresh maintenance medium supplemented with 2′,7′-Dichlorfluorescein-Diacetat (DCFDA) for ROS detection (5.2.7.4). For microscopy, Hoechst was additionally included to visualize nuclei (5.2.5.3).

The control group underwent identical media exchange without hypoxic exposure to account for mechanical stress effects. ROS staining was performed for 45 minutes in complete darkness prior to analysis (5.2.7.4). ROS abundance was quantified using a SpectraMax 3000 plate reader and spatial distribution was assessed by confocal imaging using a Leica Stellaris 5 microscope.

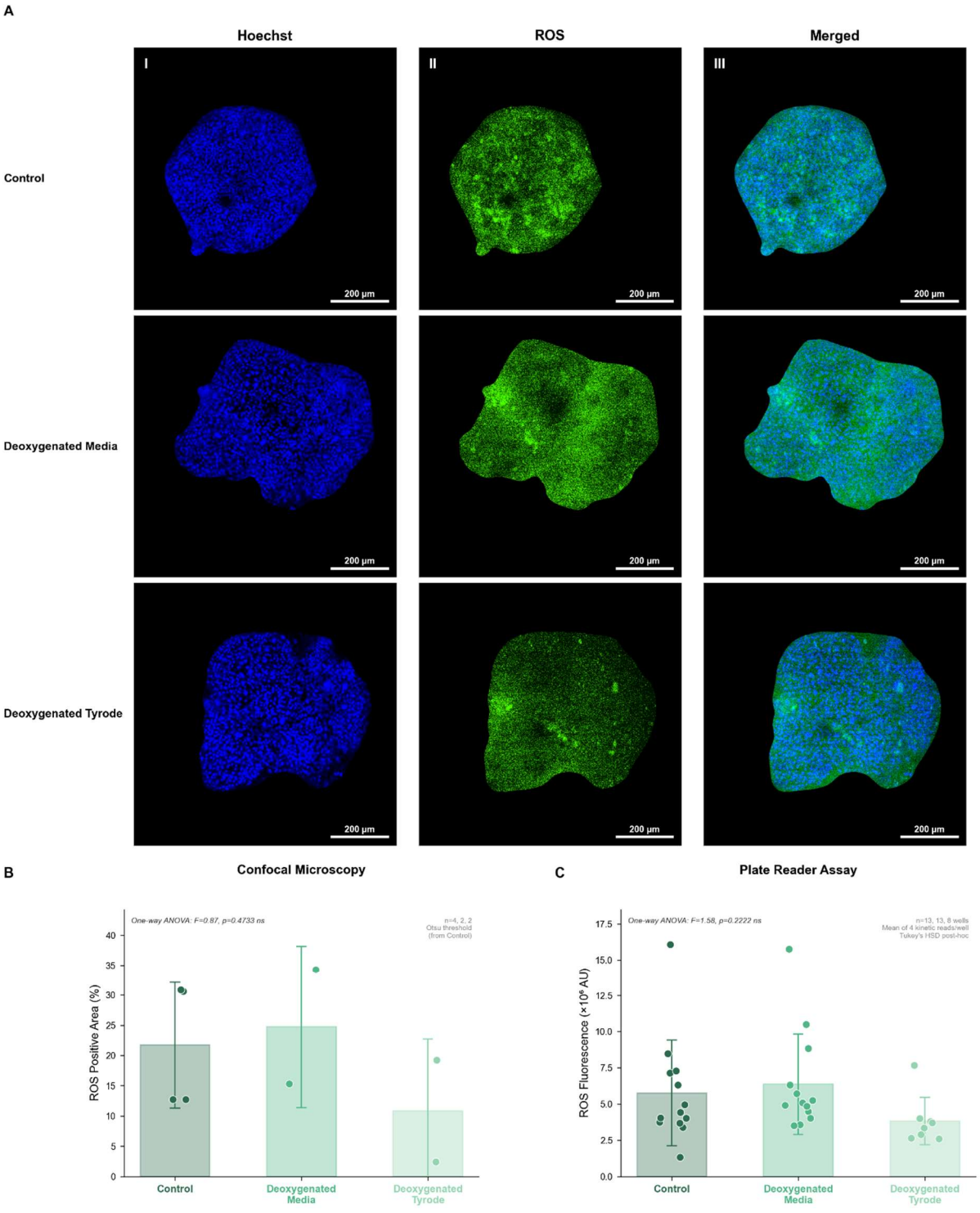

Figure 35: Reactive oxygen species (ROS) detection in iPSC-derived cardiac spheroids following simulated ischaemia–reperfusion injury. (A) Confocal fluorescence imaging of intracellular ROS under three conditions: Control (maintenance media exchange without deoxygenation), Deoxygenated Media (maintenance media deoxygenated by constant nitrogen flux for 30 minutes), and Deoxygenated Tyrode (Tyrode solution deoxygenated by constant nitrogen flux for 30 minutes). The ischaemia–reperfusion protocol was performed as described in Section 3.4.1. At the onset of reperfusion, spheroids were incubated with DCFDA Green (25 µM, 45 min; Sigma-Aldrich) and Hoechst 33342 (1:5000, 45 min; Thermo Fisher, 62249) added directly to the reperfusion medium. Images were acquired using a Leica STELLARIS 5 confocal microscope with an HC PL APO CS2 10x/0.40 DRY objective, bidirectional scanning, 4× frame averaging, and pinhole set to 1 Airy unit. Z-stacks were acquired at 5 µm/pixel lateral resolution and displayed as mean intensity projections. Columns show (I) Hoechst (blue), (II) ROS (green; Otsu-thresholded overlay with bright green indicating ROS-positive pixels), and (III) merged composite. A spheroid mask was applied to exclude extracellular background. Contrast was normalised per channel across conditions using percentile-based scaling of masked spheroid pixels to allow direct visual comparison. Representative images from one spheroid per condition are shown. Scale bars: 200 µm. (B) Quantification of ROS-

positive area from confocal images. An Otsu-derived intensity threshold defined from the Control condition was applied uniformly across all groups. The percentage of spheroid area exceeding this threshold was calculated per sample. Individual data points represent independent spheroids (Control: n = 4; Deoxygenated Media: n = 2; Deoxygenated Tyrode: n = 2). Bars indicate mean ± SD. Overall group differences were assessed by one-way ANOVA. (C) Plate reader-based quantification of ROS fluorescence. Spheroids were treated as in (A), and DCFDA fluorescence was measured following reperfusion without nuclear counterstaining. Fluorescence was recorded across four sequential kinetic reads per well and averaged to obtain one value per well (Control: n = 13; Deoxygenated Media: n = 13; Deoxygenated Tyrode: n = 8). Bars show mean ± SD; individual data points represent per-well means. Statistical analysis was performed using one-way ANOVA followed by Tukey's HSD post-hoc test. Significance levels: * $p < 0.05$, ** $p < 0.01$, *** $p < 0.001$.

The spatial distribution of ROS one hour after reperfusion is shown in Figure 35. Confocal imaging demonstrated heterogeneous intracellular ROS distribution across all conditions (Figure 35 A). Quantification of ROS-positive area using a uniform Otsu-derived threshold revealed 21.7 ± 10.6 % ROS-positive area in the Control group (n = 4). The Otsu method is a widely used technique in image processing for automatic thresholding. It automatically finds the threshold that separates pixels into two classes: foreground and background. It can automatically decide the intensity cutoff to distinguish bright cells from the dark background, without manually picking a threshold. The deoxygenated media condition showed a comparable proportion of ROS-positive area (24.8 ± 13.4 %; n = 2). In contrast, the deoxygenated Tyrode group exhibited a lower mean ROS-positive area (10.9 ± 12.0 %; n = 2). One-way ANOVA did not detect a statistically significant difference between groups ($F = 0.87$, $p = 0.48$; Figure 35 B).

Bulk fluorescence quantification using a plate reader yielded a similar pattern (Figure 35 C). Mean fluorescence intensity was 5.77 ± 3.78 × 10^6 AU in Control (n = 13 wells), 6.37 ± 3.43 × 10^6 AU in Deoxygenated Media (n = 13), and 3.84 ± 1.60 × 10^6 AU in Deoxygenated Tyrode (n = 8). One-way ANOVA revealed no significant group effect ($F = 1.58$, $p = 0.52$), and post-hoc comparisons did not identify significant pairwise differences.

Across both analytical approaches, ROS levels in the deoxygenated media condition were comparable to control, whereas the deoxygenated Tyrode condition consistently exhibited lower fluorescence values. Although these differences did not reach statistical significance, the directionality of the effect was consistent between confocal and plate reader measurements.

3.4.4. Reperfusion Based Calcium Disruption

Proper regulation of intracellular calcium is essential for healthy cardiomyocyte function. Efficient contraction–relaxation cycles depend on the rapid clearance of cytosolic calcium following each beat. When calcium levels fail to return below

baseline, cardiomyocytes cannot effectively detach troponin from the sarcomere, resulting in prolonged contraction and impaired relaxation. Sustained calcium elevation therefore represents a critical threat to cellular viability.

Disruption of calcium homeostasis is a hallmark of reperfusion injury. Beyond mechanical dysfunction, calcium overload contributes directly to apoptotic signalling by promoting opening of the mitochondrial permeability transition pore (mPTP). This mitochondrial destabilization leads to swelling, membrane rupture, and eventual loss of mitochondrial integrity. A physiologically relevant reperfusion model should therefore reproduce both the transient calcium overload and the subsequent collapse of calcium dynamics associated with cellular injury.

To assess whether the experimental reperfusion setup captures these calcium-related mechanisms, intracellular calcium dynamics were examined using the previously described nitrogen flux model. Cardiac spheroids were calcium-stained according to section 5.2.6.2 and thoroughly washed prior to treatment. The experimental group underwent media exchange to Tyrode solution adjusted to pH 7.2 and was exposed to continuous nitrogen flow for 30 minutes to induce hypoxia. Control spheroids received a parallel media exchange but were maintained under normoxic conditions.

Following the incubation period, both groups were returned to maintenance medium to simulate reperfusion. Calcium activity was recorded immediately after this exchange using 30-second time-lapse acquisitions with 488 nm excitation on the Leica LED system. After imaging, spheroids were returned to incubation for one hour, followed by a second calcium assessment to evaluate short-term recovery or progression of injury (Figure 36).

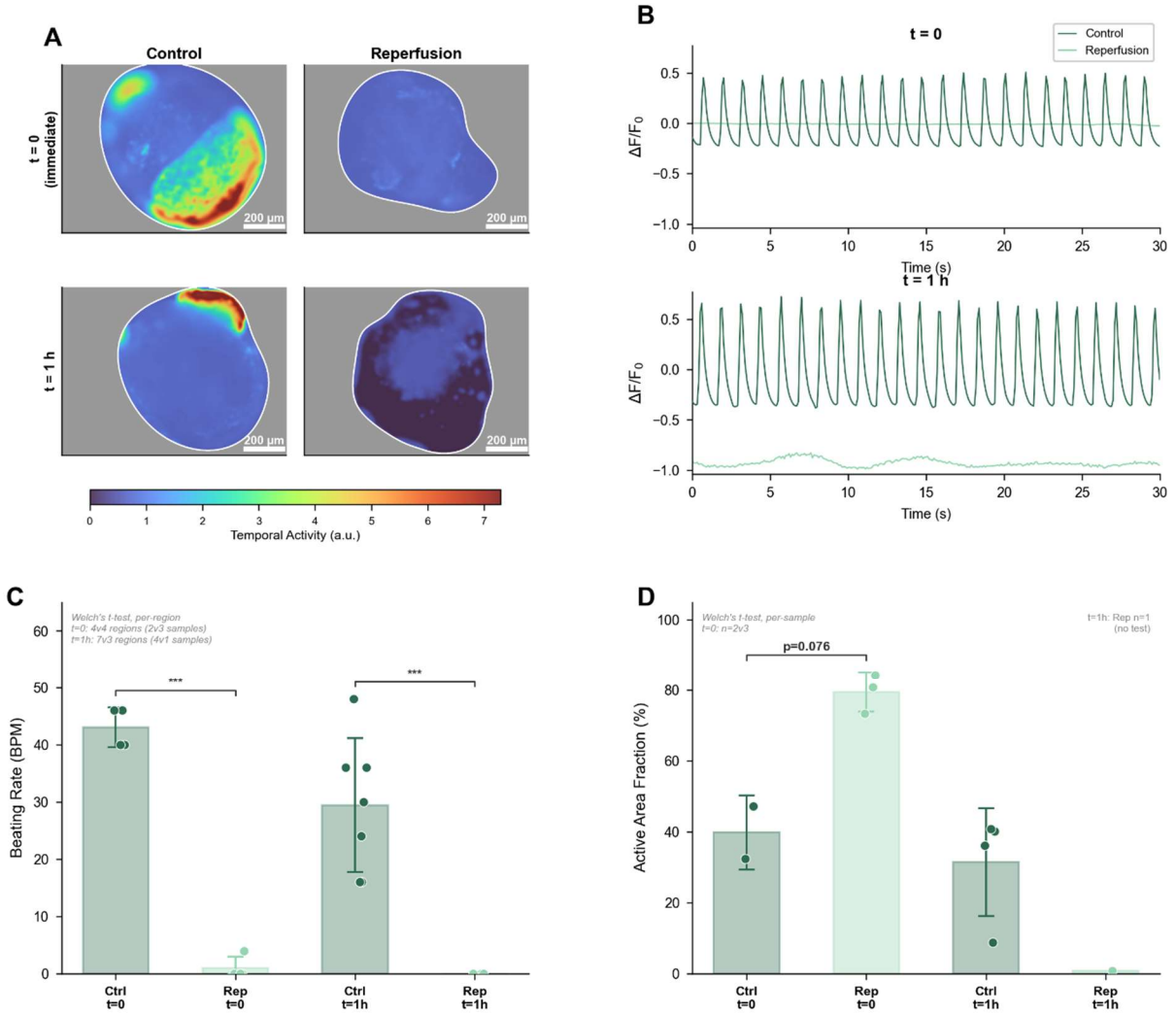

Figure 36: Calcium handling is severely disrupted in cardiac spheroids following ischaemia–reperfusion injury. (A) Spatial activity heatmaps of representative cardiac spheroids immediately after reperfusion (t = 0; top row) and one hour post-reperfusion (t = 1 h; bottom row). Activity maps display pixel-wise temporal variability of calcium fluorescence (turbo colourmap), calculated as the Gaussian-smoothed (σ = 8 px) standard deviation of frame-to-frame intensity differences across 301 frames (30 s recording at ~10 fps). A global colour scale normalised to the 99.5th percentile across all samples was applied to allow direct visual comparison. Control spheroids exhibited spatially confined regions of high calcium activity. Reperfusion spheroids at t = 0 displayed diffuse, low-amplitude activity across the tissue. At t = 1 h, reperfusion spheroids showed near-complete absence of detectable calcium activity. Scale bars: 200 µm. White outlines indicate manually defined spheroid boundaries. (B) Representative regional $\Delta F/F_0$ calcium traces from the same samples shown in (A). At t = 0, Control regions displayed regular, high-amplitude calcium transients ($\Delta F/F_0$ range: −0.23 to 0.51), whereas Reperfusion regions showed minimal fluctuation around baseline ($\Delta F/F_0$ range: −0.03 to 0.00). At t = 1 h, Control regions maintained rhythmic transients ($\Delta F/F_0$ range: −0.38 to 0.72), while Reperfusion traces remained flat with markedly reduced baseline fluorescence. Y-axes are shared across time points for direct comparison. (C) Calcium transient frequency quantified per independently active sub-region. Spatially distinct regions within a spheroid were analysed individually; both regional and sample-level n are reported. At t = 0, Control regions exhibited a mean frequency of 43.0 ± 3.5 min^{-1} compared with 1.0 ± 2.0 min^{-1} in Reperfusion regions (Welch's t-test, $p = 6.6 \times 10^{-6}$; n = 4 vs. 4 regions from 2 and 3 samples, respectively). At t = 1 h, Control regions maintained a mean frequency of 29.4 ± 11.7 min^{-1}, whereas all Reperfusion regions exhibited zero detectable transients (Welch's t-test, $p = 5.6 \times 10^{-4}$; n = 7 vs. 3 regions from 4 and 1 samples, respectively). Bars represent mean ± SD; individual data points are shown. (D) Active area fraction per sample, defined as the proportion of spheroid area covered by detected calcium-active sub-regions. At t = 0, Reperfusion spheroids showed a higher active area fraction (79.5 ± 5.7 %) than Control (39.9 ± 10.5 %), though this difference did not reach statistical significance at the sample level (Welch's t-test, p = 0.076; n = 2 vs. 3 samples). At t = 1 h, Reperfusion spheroids exhibited minimal active area (0.8 %; n = 1), whereas Control spheroids maintained 31.5 ± 15.2 % (n = 4). Bars represent mean ± SD; individual data points are shown. All statistical comparisons were performed using Welch's t-test. Values are reported as mean ± SD.

Spatial activity heatmaps revealed marked differences between control and reperfusion spheroids (Figure 36 A). Control spheroids displayed, high-intensity regions of calcium activity at both time points. In contrast, reperfusion spheroids at t = 0 exhibited diffuse, low-amplitude activity distributed across the tissue. At t = 1 h, Reperfusion spheroids showed near-complete absence of calcium activity.

Representative regional calcium traces reflected these spatial patterns (Figure 36 B). Control regions exhibited regular, high-amplitude calcium transients at both time points. Reperfusion regions at t = 0 showed a persistently elevated baseline fluorescence with minimal oscillatory activity, resulting in a largely flat trace lacking discrete transients. At t = 1 h, traces from reperfusion spheroids remained flat and displayed markedly reduced baseline fluorescence relative to Control.

Quantification of calcium transient frequency confirmed these observations (Figure 36 C). At t = 0, controls exhibited a mean frequency of 43.0 ± 3.5 min^{-1}, whereas reperfusion samples showed markedly reduced activity (1.0 ± 2.0 min^{-1}; Welch's t-test, $p = 6.6 \times 10^{-6}$; n = 4 vs. 4 regions from 2 and 3 samples, respectively). At t = 1 h, controls maintained spontaneous activity (29.4 ± 11.7 min^{-1}), while all reperfusion samples exhibited zero detectable transients (Welch's t-test, $p = 5.6 \times 10^{-4}$; n = 7 vs. 3 regions from 4 and 1 samples, respectively). Regional analysis was performed at the level of independently active sub-regions; both regional and sample-level n are reported.

The fraction of spheroid area occupied by calcium-active sub-regions was also quantified (Figure 36 D). At t = 0, Reperfusion spheroids exhibited a higher active area fraction (79.5 ± 5.7 %) compared with Control (39.9 ± 10.5 %), though this difference did not reach statistical significance at the sample level (Welch's t-test, p = 0.076; n = 2 vs. 3 samples). By t = 1 h, Reperfusion spheroids exhibited minimal active area (0.8%; n = 1), whereas Control spheroids maintained 31.5 ± 15.2 % (n = 4).

Collectively, these findings demonstrate a rapid and profound disruption of calcium transient activity following ischaemia–reperfusion. Immediately after reperfusion, rhythmic calcium activity was markedly reduced despite widespread fluorescence variability. One hour later, calcium transients were completely absent in reperfusion spheroids, whereas control spheroids maintained organised activity throughout the observation period.

3.4.5. Discussion of Chapter 3.4

Reperfusion injury represents one of the most paradoxical phenomena in cardiovascular pathophysiology. The restoration of oxygen supply, which is essential

for survival, triggers a second wave of cellular damage that frequently exceeds the primary ischemic damage.[124] The present model was designed to recapitulate this biphasic stress response in a controlled three-dimensional cardiac system.

By combining nitrogen-induced oxygen deprivation with Tyrode-mediated nutrient restriction, followed by rapid reoxygenation and metabolic restoration, the experimental setup successfully reproduced several core hallmarks of ischemia–reperfusion injury at functional, structural, metabolic, and molecular levels.

3.4.5.1. Metabolic Viability and Delayed Collapse After Reoxygenation

The MTT assay revealed a pattern characteristic of reperfusion-associated injury rather than simple ischemic toxicity. Immediately after treatment (T0), all stress groups exhibited reduced metabolic activity, reflecting acute energetic suppression. However, the reperfusion condition (deoxygenated Tyrode) demonstrated a progressive decline in viability over 72 hours, reaching approximately 30 % before partial stabilization at day 7.

This delayed deterioration is mechanistically consistent with reperfusion injury.[328–330] During ischemia, impaired oxidative phosphorylation leads to ATP depletion, reduced ion pump activity, membrane depolarization, and a metabolic shift toward glycolysis.[331] Simultaneously, mitochondrial succinate accumulates as a consequence of altered TCA-cycle flux and reversal of succinate dehydrogenase activity under hypoxic conditions.[332]

Upon reoxygenation, rapid restoration of electron transport chain activity drives accelerated oxidation of accumulated succinate via Complex II (succinate dehydrogenase).[333] This produces a highly reduced ubiquinone pool and a steep proton motive force across the inner mitochondrial membrane. Under these conditions, reverse electron transport (RET) at Complex I is favoured, resulting in excessive superoxide generation.[334] This ROS burst represents a central driver of reperfusion-associated mitochondrial damage.[335]

Additionally, ischemia-induced ATP depletion compromises SERCA and Na^+/Ca^{2+} exchanger activity, leading to intracellular calcium accumulation.[336,337] During ischemia, intracellular acidosis caused by lactate accumulation partially inhibits mPTP opening, as low pH reduces calcium sensitivity of the pore. Upon reperfusion, rapid pH normalization removes this protective effect while cytosolic and mitochondrial calcium levels remain elevated.[338,339] The combination of calcium overload and ROS promotes mPTP opening, loss of mitochondrial membrane potential, and release of

pro-apoptotic factors such as cytochrome c, thereby initiating secondary cell death pathways.[340,341]

The initial moderate reduction in viability followed by a more pronounced decline over 24–72 hours, supports activation of delayed mitochondrial and apoptotic mechanisms rather than exclusive acute necrosis (figure 29).

In contrast, degassed medium alone induced a transient increase in metabolic activity at 72 hours (~120 %), potentially reflecting compensatory metabolic upregulation following reversible hypoxic stress.[342–344] Tyrode alone produced temporary suppression with full recovery, confirming that nutrient deprivation in isolation is insufficient to induce sustained injury.

Collectively, these findings indicate that combined oxygen and substrate deprivation is required to initiate the mitochondrial and calcium-dependent cascades that drive progressive reperfusion-specific damage.

3.4.5.2. Structural Disintegration and Selective Cardiomyocyte Collapse

Confocal imaging of cTnT and mitochondrial organization provided spatial resolution of structural injury. Control spheroids preserved well-defined sarcomeric alignment and homogeneous mitochondrial distribution over seven days, confirming that the mechanical stress induced through media handling alone does not induce structural disruption.

Exposure to deoxygenated medium or Tyrode solution individually resulted in transient sarcomeric disorganization at T0, followed by full structural recovery by T1. This reversible disruption is consistent with acute energetic suppression affecting excitation–contraction coupling without irreversible myofibrillar degradation.[345,346]

In contrast, combined deoxygenated Tyrode treatment produced severe structural alterations. At T0, mitochondrial staining was markedly reduced, consistent with acute mitochondrial depolarization and fragmentation following abrupt reoxygenation stress.[347] Loss of mitochondrial signal at this early stage likely reflects transient collapse of membrane potential and structural remodelling rather than immediate organelle loss.[327,348,349]

Concurrently, cTnT organization was disrupted, with progressive sarcomeric collapse evident at T1 and T3. Reduction in cTnT signal intensity and loss of alignment are mechanistically compatible with calcium-dependent proteolysis.[350] Elevated cytosolic Ca^{2+} activates calpains, a family of calcium-sensitive cysteine proteases known to

cleave key contractile proteins, including cTnT and cTnI.[351–353] Such proteolytic processing directly compromises sarcomeric integrity and contractile stability.

This structural destabilization is further amplified by oxidative stress during reperfusion.[354] Reverse electron transport–driven superoxide production at Complex I generates reactive oxygen species that can oxidize cysteine thiol groups within sarcomeric proteins.[355] Reversible modifications such as *S*-nitrosylation and *S*-glutathionylation can transiently alter protein conformation and function and are typically restored by antioxidant systems including thioredoxin and glutaredoxin.[356–359] However, sustained oxidative stress may promote irreversible thiol overoxidation to sulfonic acid, resulting in permanent structural alteration and loss of contractile protein function.[355,360–362]

Accordingly, the transient structural disorganization observed with deoxygenated medium or Tyrode alone may reflect reversible thiol oxidation and mild energetic suppression. In contrast, the progressive loss of cTnT integrity following combined oxygen and substrate deprivation is consistent with the coherent effects of calcium overload, calpain activation, and sustained oxidative modification, ultimately driving irreversible sarcomeric damage.[363,364]

Notably, overall spheroid size and coarse morphology remained largely preserved despite extensive cardiomyocyte-specific structural loss. This suggests that injury primarily affects contractile cardiomyocytes rather than causing global tissue dissolution. Such selective vulnerability aligns with *in vivo* ischemia–reperfusion pathology, where cardiomyocytes undergo apoptosis or necrosis while non-contractile cells, especially fibroblasts, may remain viable.[365–367]

This differential susceptibility is largely attributable to differences in metabolic demand and bioenergetic flexibility. Cardiomyocytes rely heavily on continuous mitochondrial oxidative phosphorylation to sustain ATP-dependent processes such as ion homeostasis, sarcomeric cycling, and calcium reuptake.[368,369] Even short interruptions in oxygen supply therefore lead to rapid ATP depletion, impaired SERCA and Na^+/K^+-ATPase activity, calcium overload, and structural destabilization.[294,370,371] In contrast, fibroblasts exhibit greater metabolic adaptability and can shift more efficiently toward glycolytic ATP production under hypoxic conditions.[372] Their lower contractile and electrophysiological energy demands allow maintenance of basic ion homeostasis during transient metabolic stress, rendering them comparatively resistant to ischemia–reperfusion injury.[365]

Thus, the preservation of overall spheroid architecture despite marked sarcomeric loss reflects cell type–specific metabolic vulnerability rather than uniform tissue degradation.

By T7, partial restoration of mitochondrial signal was observed without corresponding recovery of organized sarcomeric architecture. This pattern suggests metabolic stabilization of surviving cells or mitochondrial repopulation through biogenesis, yet irreversible loss of contractile integrity.[373] The incoherence between mitochondrial reappearance and myofibrillar structure loss is consistent with post-reperfusion remodelling rather than uniform cell death, supporting the presence of delayed, structurally specific injury mechanisms.[374,375]

3.4.5.3. Transcriptional Reprogramming and Delayed Remodelling Signature

Gene expression analysis further supports a biphasic injury pattern characterized by early stress responses followed by delayed structural remodeling.[376]

Transient upregulation of cTnT at T1 in the degassed and Tyrode groups likely reflects acute stress-induced transcriptional activation.[377–379] In contrast, the reperfusion group exhibited delayed cTnT upregulation at T7, consistent with activation of post-injury remodelling programs in surviving cardiomyocytes.[378–381] Following ischemia–reperfusion injury *in vivo*, compensatory modulation of contractile gene expression occurs during the early remodelling phase which occurs days after injury.[381] However, restoration of sarcomeric organization often remains incomplete due to prior proteolytic damage, persistent calcium dysregulation, and mitochondrial dysfunction.[382,383] The contrast between increased cTnT transcript levels and continued structural disruption in the present model therefore likely reflects an attempted but incomplete remodelling response rather than functional recovery. This mismatch is consistent with post-transcriptional and assembly-level constraints, where elevated gene expression does not necessarily translate into effective sarcomere reconstruction under conditions of sustained metabolic stress.[382,384]

The most pronounced transcriptional alteration was the strong induction of α-SMA at T7 exclusively in the reperfusion group. As α-SMA marks activated myofibroblasts, its delayed upregulation suggests secondary fibroblast activation following cardiomyocyte injury.[385] The absence of early α-SMA elevation indicates that fibrotic signalling represents a remodelling response rather than an immediate consequence of acute ischemic stress. This pattern aligns with replacement fibrosis mechanisms observed *in vivo* after ischemia–reperfusion injury.[386]

In parallel, Glut1 expression was suppressed at T1 in the reperfusion group. Under isolated hypoxic conditions, Glut1 is typically upregulated to enhance glucose uptake and support glycolytic ATP production.[387–389] Its downregulation therefore suggests impaired metabolic adaptation rather than a coordinated glycolytic shift. This finding is consistent with reperfusion-associated mitochondrial dysfunction limiting effective metabolic reprogramming.[390]

Collectively, these transcriptional changes indicate that the combined oxygen and substrate deprivation model induces not only acute cellular stress but also delayed remodelling processes characteristic of reperfusion injury,[376] reinforcing the temporal progression observed in metabolic, structural, and functional analyses.

3.4.5.4. ROS Production is Not Simply Elevated, but Dynamically Altered

Interestingly, global ROS levels did not exhibit a marked increase in the reperfusion group compared to controls at the time of measurement. This does not exclude a role for oxidative stress in injury progression. Reperfusion-associated ROS generation is typically characterized by a rapid and transient burst immediately upon reoxygenation, largely driven by reverse electron transport (RET) at Complex I.[391] ROS measurements in the present study were performed approximately one hour after reperfusion. As the oxidative burst occurs within minutes of reoxygenation,[392] this temporal window may not capture the initial peak in ROS production. The observed signal therefore likely reflects residual or sustained oxidative activity rather than the early transient phase.

In addition, endogenous antioxidant systems, including superoxide dismutase, catalase, and glutathione-dependent pathways, can neglect detectable ROS signals despite prior oxidative events.[393] Reduced metabolic activity, as indicated by MTT decline, may further limit sustained mitochondrial ROS production at later time points, since steady-state ROS generation depends on ongoing electron transport chain flux.

Importantly, severe mitochondrial depolarization observed in the combined deprivation group may itself constrain continued ROS generation. RET requires a highly reduced ubiquinone pool and a strong proton motive force. The collapse of mitochondrial membrane potential diminishes this driving force and limits further ROS amplification.[394,395] Thus, extensive mitochondrial dysfunction may paradoxically reduce measurable ROS at later stages despite having been initiated by an early oxidative burst.

The reduced ROS area coverage in deoxygenated Tyrode samples despite pronounced structural damage therefore suggests that ROS production in this model is temporally restricted rather than constantly elevated. Oxidative stress likely acts as an early trigger that synergizes with calcium overload and mitochondrial destabilization to initiate injury cascades. The continuous structural disintegration in the absence of sustained global ROS elevation supports a model in which transient oxidative events are sufficient to drive delayed, structurally specific reperfusion injury.

3.4.5.5. Calcium Dysregulation and the Central Mechanistic Driver

The most compelling validation of the model emerges from calcium imaging. Immediately following reperfusion, cardiomyocytes exhibited a marked elevation in baseline intracellular calcium, loss of coordinated calcium transients, and near-complete suppression of spontaneous beating. One hour later, calcium signalling had collapsed entirely, with no detectable coordinated activity, indicating sustained functional arrest.

This temporal progression closely reflects the established *in vivo* sequence of ischemia–reperfusion injury. During ischemia, ATP depletion impairs SERCA function and disrupts Na^+/K^+-ATPase activity, promoting intracellular sodium accumulation and reversal of the Na^+/Ca^{2+} exchanger.[285,337] The resulting calcium overload primes mitochondria for instability. Upon reoxygenation, rapid mitochondrial reactivation generates a transient ROS burst, likely occurring within minutes, as discussed above. Together with elevated calcium, this promotes mitochondrial permeability transition pore (mPTP) opening.[396] The combined effects of oxidative stress and calcium overload drive contractile dysfunction, hyper contracture, and initiation of apoptotic pathways.[397]

The paradoxical increase in spatially "active" area observed immediately after reperfusion likely reflects diffuse and uncoordinated calcium elevation rather than synchronized excitation–contraction coupling. This pattern is consistent with global calcium dysregulation rather than functional recovery.[398] The subsequent complete collapse of calcium signalling at one hour supports irreversible contractile failure and aligns temporally with progressive structural deterioration observed in confocal imaging.

Taken together, this calcium signature provides the most direct functional evidence that the model reproduces reperfusion-specific injury mechanisms rather than isolated

hypoxic stress. The rapid transition from dysregulated calcium overload to complete signalling collapse mirrors the pathological sequence observed *in vivo*.[302]

3.4.5.6. Integrated Interpretation: Does the Model Recapitulate Reperfusion Injury?

A valid reperfusion model should reproduce the defining features of ischemia–reperfusion injury, including acute functional suppression, intracellular calcium overload, delayed metabolic deterioration, progressive structural disintegration of cardiomyocytes, secondary fibrotic activation, and partial tissue survival rather than uniform necrosis.[376]

The combined nitrogen flux and Tyrode deprivation system fulfils these criteria. Immediately following reperfusion, the model demonstrates calcium overload, loss of coordinated transients, and functional arrest. This is followed by delayed metabolic decline over 24–72 hours, progressive sarcomeric collapse, and late transcriptional activation of remodelling markers, including α-SMA upregulation indicative of fibroblast activation. Importantly, overall spheroid architecture remains preserved, reflecting partial tissue survival and selective cardiomyocyte vulnerability rather than global tissue dissolution.

In contrast, isolated hypoxia or isolated nutrient deprivation fail to reproduce the full injury cascade. While each induces transient stress responses, neither alone generates the delayed viability decline, sustained structural deterioration, fibroblast activation, and persistent loss of calcium dynamics observed under combined oxygen and substrate deprivation. The requirement for dual stress exposure underscores the multifactorial nature of reperfusion injury and supports the physiological relevance of the integrated model.

Collectively, these findings demonstrate that the system recapitulates the temporal and mechanistic complexity of reperfusion injury rather than modelling simple hypoxic toxicity.

3.4.5.7. Strengths and Limitations

The principal strength of this model lies in its precise temporal control of ischemic induction and reperfusion transition. Nitrogen flux enables rapid and tuneable oxygen deprivation, while Tyrode solution imposes defined metabolic substrate restriction, together allowing reproducible simulation of combined ischemic stress. Multi-level validation across functional (calcium dynamics), metabolic (MTT), structural (confocal imaging), and transcriptional (qPCR) analyses provides convergent evidence

supporting the model's biological relevance. Furthermore, the use of a three-dimensional multicellular spheroid system enhances physiological complexity compared to monolayer cultures by preserving cell–cell interactions and differential cell-type susceptibility. The static culture format permits experimental scalability and parallelization, enabling controlled replication and higher-throughput assessment compared to perfused ex vivo systems.[399] In addition, the defined induction and recovery steps are compatible with automated liquid handling and imaging platforms, suggesting potential for standardized, automated screening applications in future implementations.

Compared to diffusion-based hypoxia systems or static chamber models, the present approach offers sharper temporal control over ischemic onset and reoxygenation. In contrast to conventional 2D monolayer cultures, the 3D spheroid architecture permits cell type–specific vulnerability and remodelling dynamics to emerge.[168,399] However, unlike perfused ex vivo heart preparations, the system lacks hemodynamic flow and circulating inflammatory components.

Several limitations should be acknowledged. Direct assessment of mitochondrial permeability transition pore opening was not performed, and ROS measurements may not capture the immediate oxidative burst occurring within minutes of reoxygenation. Loss of RNA samples at T3 limits complete temporal resolution of transcriptional dynamics. Additionally, the absence of a perfusion flow component restricts simulation of shear stress, inflammatory recruitment, and systemic interactions present *in vivo*.[400]

Nevertheless, within the constraints of a static 3D culture system, the model robustly reproduces central mechanistic features of ischemia–reperfusion injury and provides a controlled platform for examining reperfusion-associated cellular responses.

Collectively, the combined nitrogen–Tyrode system reproduces key mechanistic features of reperfusion injury, with calcium overload and oxidative stress emerging as central components of the observed phenotype. To further interrogate the functional relevance of these pathways, pharmacological modulation was employed as a mechanistic probe. Rather than assuming therapeutic efficacy, this approach enables assessment of how selective interference with calcium influx or reactive oxygen species influences injury progression within the established model. Accordingly, the following section evaluates the effects of L-type calcium channel blockade using verapamil and ROS scavenging via ascorbic acid on functional, metabolic, and structural outcomes following simulated reperfusion.

3.5. Potential Reperfusion Drugs

Following the pronounced structural and metabolic disruption observed after reperfusion, potential pharmacological strategies to mitigate injury were investigated. Two mechanistically distinct candidates were selected: Ascorbic acid and verapamil.

Ascorbic acid functions as a reactive oxygen species scavenger, aiming to neutralize excess ROS generated during reperfusion and thereby limit oxidative damage. In contrast, verapamil targets calcium homeostasis by blocking L-type calcium channels, reducing intracellular calcium influx. Through stabilization of calcium dynamics, verapamil may help prevent mitochondrial permeability transition pore (mPTP) opening and subsequent apoptotic signalling.

3.5.1. Characterizing Safe Dosage

Before evaluating protective efficacy under reperfusion conditions, a safe concentration range for both compounds was determined. Maintaining drug exposure within the maximal physiological range (MPR) is essential to support recovery without inducing additional toxicity.

Cardiac spheroids were exposed to a broad concentration spectrum based on reported *in vitro* physiological ranges: 1–500 µM for verapamil[401] and 40–1000 µM for ascorbic acid.[402] Metabolic activity was assessed using the MTT assay as described in Section 5.2.6.3.

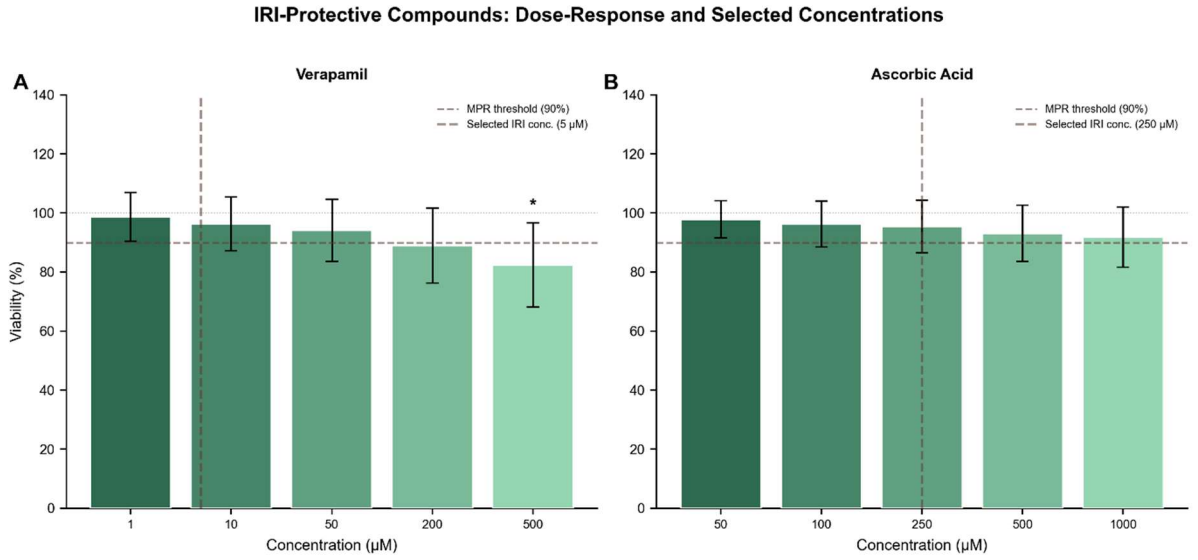

Figure 37: Dose–response characterisation of candidate IRI-protective compounds in cardiac spheroids. (A) Verapamil dose–response (1–500 µM; Round 3). Bars represent mean viability (% of untreated control) with error bars indicating ± SD. Viability remained above 88 % across concentrations from 1 to 200 µM (1 µM: 98.7 ± 8.2 %, n = 16; 10 µM: 96.3 ± 9.1 %, n = 9; 50 µM: 94.1 ± 10.5 %, n = 10; 200 µM: 88.9 ± 12.7 %, n = 8), with no

significant difference from untreated control (Welch's t-test with Holm–Bonferroni correction; all p_adj > 0.08). The highest concentration (500 µM; 82.4 ± 14.2 %, n = 11) resulted in a significant reduction in viability (p_adj = 0.032). A significant negative linear trend across concentrations was detected (z = −3.66, p < 0.001). The concentration selected for IRI experiments (5 µM; indicated by vertical dashed line) lies between the 1 and 10 µM tested doses and corresponds to an interpolated viability of approximately 97%. (B) Ascorbic acid dose–response (50–1000 µM; Round 3). All concentrations maintained viability above 90 % of untreated control (50 µM: 97.8 ± 6.3 %, n = 9; 250 µM: 95.4 ± 8.9 %, n = 14; 500 µM and 1000 µM: ≥ 91.8 %, n = 9–16). No concentration differed significantly from control after Holm–Bonferroni correction (all p_adj > 0.49). A marginal negative linear trend was observed (z = −2.02, p = 0.044). The selected concentration for IRI experiments (250 µM; vertical dashed line) was directly tested and did not significantly affect viability. Bars are coloured according to increasing concentration (dark to light green). The dotted grey line indicates 100% control reference; the horizontal dashed line marks the 90 % viability threshold. Statistical comparisons were performed using Welch's t-test against the shared untreated control group (n = 19, SD = 17.8 %), with Holm–Bonferroni correction for five comparisons per compound. WTC11 Round 3 data; n = 8–16 valid wells per concentration following quality-based exclusion from a 384-well plate.

Dose–response relationships for verapamil and ascorbic acid are presented in Figure 37. To confirm that pharmacologically active concentrations fall within a non-cytotoxic window, both compounds were evaluated across a defined concentration range in cardiac spheroids using MTT-based viability assessment.

Verapamil was tested at concentrations ranging from 1 to 500 µM. Viability remained close to control levels between 1 and 200 µM, with no statistically significant reduction detected within this range (Figure 37, A). Only the highest concentration (500 µM) resulted in a significant decrease in viability (p_adj = 0.032). A significant negative linear trend was observed across the concentration series ($p < 0.001$), indicating a concentration-dependent decline at higher doses.

Ascorbic acid was tested across 50–1000 µM. Viability remained above 90 % of control at all concentrations, and no individual dose differed significantly from untreated control after correction for multiple comparisons (Figure 37, B). A shallow negative trend across concentrations was detected ($p = 0.044$), though no single concentration reached statistical significance.

On the basis of these findings, and in the absence of any statistically significant viability reduction at low-to-intermediate concentrations, literature-supported working concentrations were selected for subsequent IRI experiments: 5 µM verapamil and 250 µM ascorbic acid.

3.5.2. Testing Protective Abilities

To evaluate potential protective effects of verapamil and ascorbic acid during simulated ischemia–reperfusion injury, the experimental protocol described in 3.4.1 was repeated with pharmacological supplementation. The core ischemia–reperfusion procedure remained unchanged to allow direct comparison with untreated conditions. Prior to ischemic incubation, spheroids assigned to treatment groups were preconditioned with maintenance medium supplemented with either verapamil or

ascorbic acid. For each experimental condition, three parallel groups were established: an untreated control, a verapamil-treated group, and an ascorbic acid–treated group. This design enabled assessment of drug-specific effects under identical mechanical and metabolic stress conditions.

Following the reperfusion phase, treated spheroids continued to receive drug-supplemented maintenance medium for the duration of the recovery period to maintain pharmacological exposure. Metabolic activity was assessed 72 hours after reperfusion using an MTT assay (5.2.6.3). At this time point, MTT reagent was applied and incubated for 3 hours prior to analysis, providing a quantitative measure of post-injury cellular viability and recovery in response to pharmacological intervention.

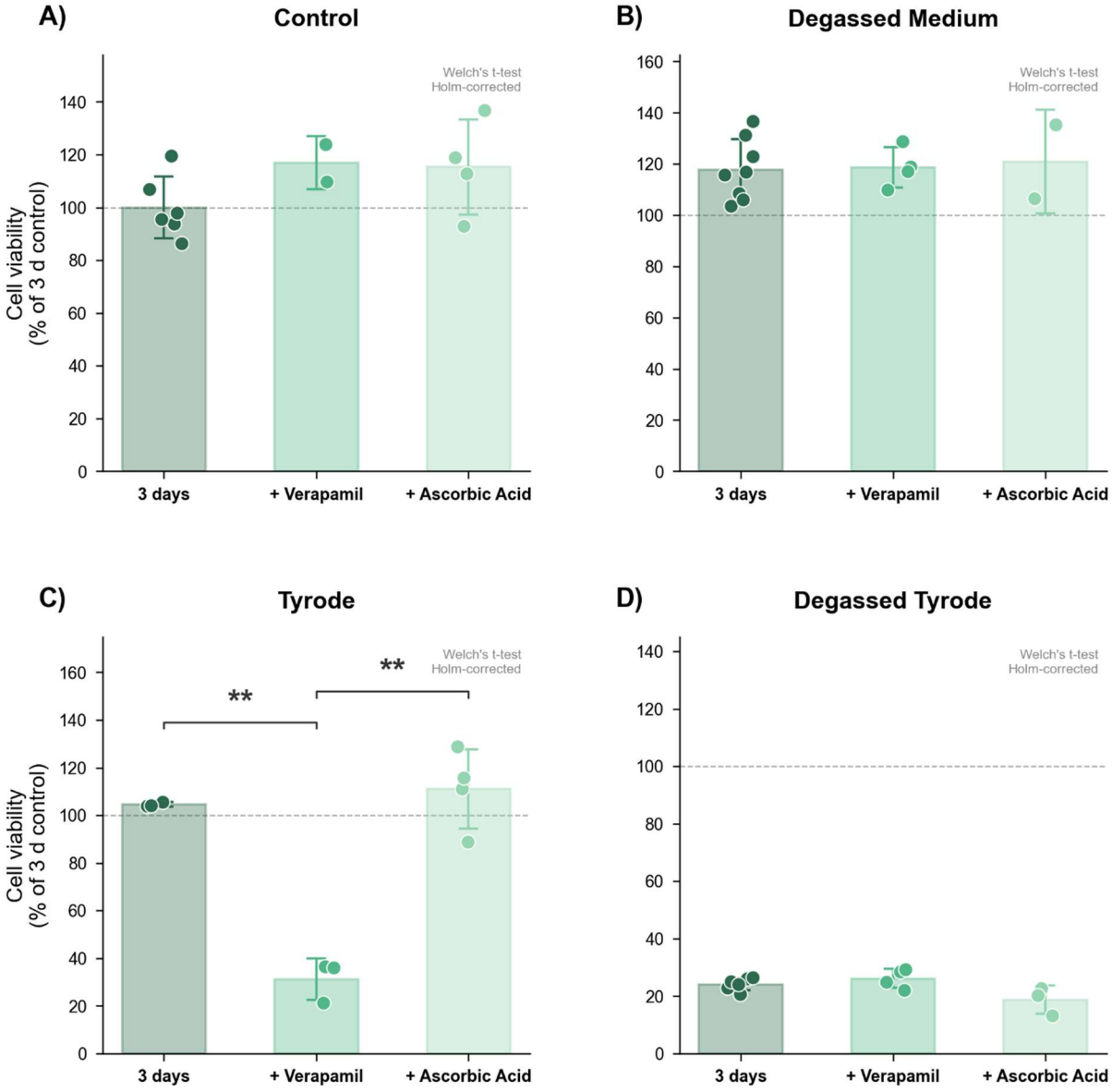

Figure 38: Effect of verapamil and ascorbic acid supplementation on cardiomyocyte viability at 3 days post-treatment. Cell viability was assessed by MTT assay at 3 days under three supplementation conditions, untreated (3 days), verapamil, or ascorbic acid, across four treatment groups: (A) Control, (B) degassed medium, (C) Tyrode, and (D) degassed Tyrode. Absorbance values were normalised to the mean of the 3-day control group (dashed line, 100 %). Bars represent mean ± SD; individual data points are shown. Pairwise comparisons within each treatment panel were performed using Welch's t-test with Holm–Bonferroni correction for multiple comparisons. In

the Tyrode group (C), Verapamil significantly reduced viability (31.3 ± 8.8 %) relative to the untreated 3-day condition (104.6 ± 0.9 %; p = 0.009), whereas ascorbic acid supplementation did not significantly alter viability (111.2 ± 16.6 %; p = 0.485). Viability differed significantly between verapamil and ascorbic acid conditions within the Tyrode group (p = 0.002). No significant differences were detected between supplementation conditions in the control, degassed Medium, or degassed Tyrode groups. Sample sizes ranged from n = 2 to n = 8 per condition. Significance threshold: **p < 0.01.

Figure 38 summarizes the effects of verapamil and ascorbic acid across the four experimental reperfusion conditions, with all values normalized to the untreated maintenance media control. In the Tyrode group (Figure 38, panel C), verapamil reduced viability from 104.6 ± 0.9 % to 31.3 ± 8.8 % (Welch's t-test with Holm correction, p = 0.009). Ascorbic Acid supplementation maintained viability at 111.2 ± 16.6 %, which did not differ significantly from the untreated Tyrode solution condition (p = 0.485). The difference between verapamil and ascorbic acid within the Tyrode solution group was statistically significant (p = 0.002).

In the control (Figure 38, panel A) and degassed medium (Figure 38, panel B) groups, neither verapamil nor ascorbic acid produced statistically significant changes in viability relative to their respective untreated conditions.

In the degassed Tyrode solution group (Figure 38, panel D), baseline viability was 24.2 ± 2.2 %. Verapamil (26.2 ± 3.3 %) and ascorbic acid (18.7 ± 4.9 %) did not significantly differ from the untreated degassed Tyrode solution condition (both p = 0.374).

Overall, verapamil only significantly reduced viability in the Tyrode solution group, whereas ascorbic acid did not significantly alter viability in any treatment condition.

3.5.3. Morphological Protection

Following evaluation of the protective effects of verapamil and ascorbic acid on reperfusion-induced metabolic decline, morphological preservation of cardiomyocytes was assessed.

Cardiac spheroids at differentiation day 21 were divided into four treatment conditions: maintenance medium control, deoxygenated medium, Tyrode solution (pH 7.2), and deoxygenated Tyrode solution to simulate reperfusion injury. Each condition was further subdivided into three treatment groups: untreated control, verapamil supplementation, and ascorbic acid supplementation.

Treatment exposure lasted 30 minutes, after which all spheroids underwent media exchange to fresh maintenance medium to model reperfusion and to control for mechanical stress associated with handling. Both the initial treatment solutions and the reperfusion media for the drug groups were supplemented with the respective compounds to maintain protective exposure.

Spheroids were fixed in paraformaldehyde 72 h (T3) after reperfusion treatment and stained for cTnT to assess structural integrity and for mitochondrial labelling to visualize metabolic organization (Section 5.2.5). Imaging was performed using a Leica Stellaris 5 confocal fluorescence microscope.

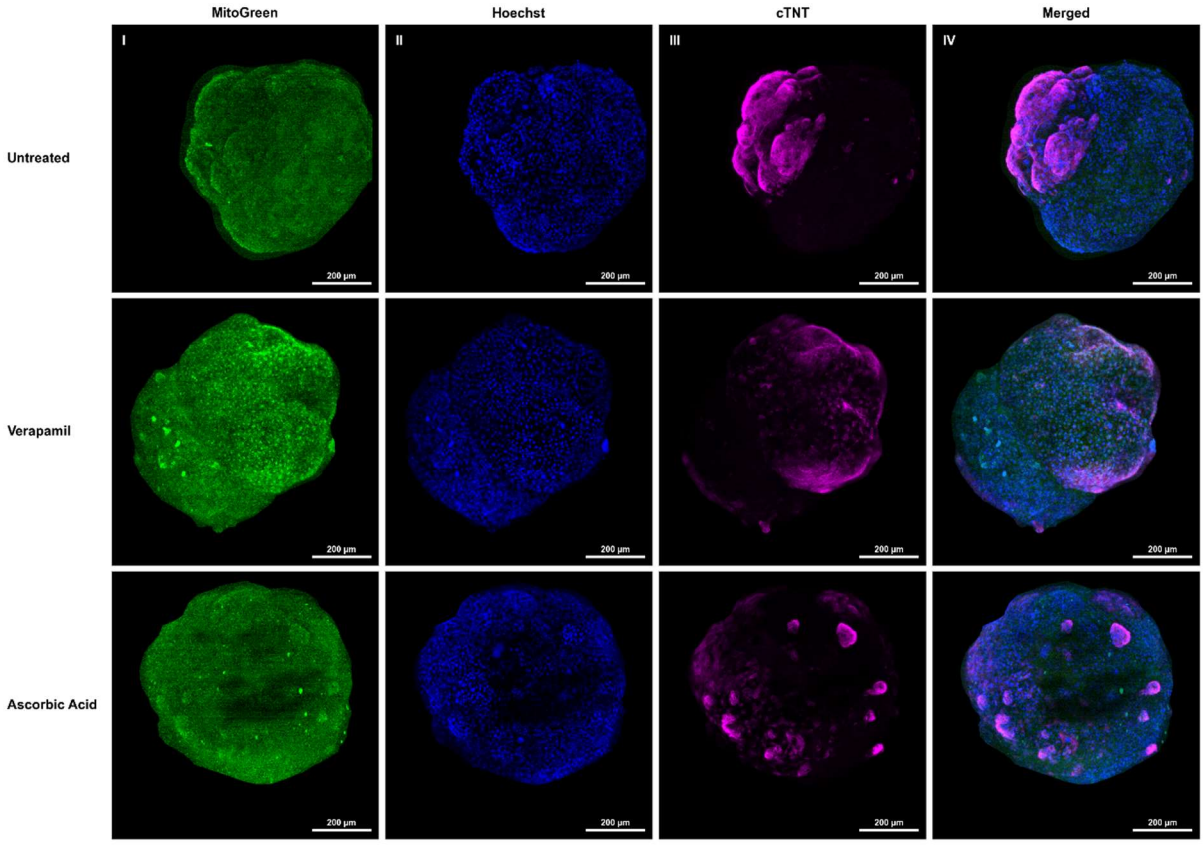

Figure 39: Confocal fluorescence imaging of iPSC-derived cardiac spheroids under control conditions at day 3 post-treatment, comparing untreated, verapamil-treated, and Ascorbic Acid-treated spheroids. iPSC-derived cardiac spheroids (DD21) were generated in 384-well plates. During the 30-minute treatment period, spheroids were co-treated with verapamil (L-type calcium channel blocker) or Ascorbic Acid (antioxidant). In the control condition, maintenance medium was exchanged without deoxygenation. At T3 (day 3 post-treatment), spheroids were stained with MitoTracker™ Green FM (200 nM, 30 min; Thermo Fisher, M7514) prior to fixation (4 % paraformaldehyde). Nuclei were labelled with Hoechst 33342 (1:5000, 60 min; Thermo Fisher, 62249). Cardiac troponin T (cTnT) was detected using mouse anti-cTnT (1:200, overnight; Invitrogen, MA5-12960, clone 13-11) followed by Alexa Fluor 647 goat anti-mouse secondary antibody (1:500, overnight; Thermo Fisher, A-21235). Images were acquired on a Leica STELLARIS 5 confocal microscope (DMI8-CS inverted platform) using a 10×/0.40 objective. Z-stacks (0.88 µm/pixel lateral resolution) were recorded with bidirectional scanning, 4× frame averaging, and a 1 Airy unit pinhole. Columns (I–IV) display MitoTracker™ Green (green), Hoechst (blue), cTnT (magenta), and the merged composite. Images represent mean-intensity z-projections. MitoTracker™ Green and Hoechst contrast were normalised per channel across treatment groups within each condition using percentile-based scaling (p1.5–p99.5) of masked spheroid pixels. cTnT contrast was normalised to a fixed intensity range derived from the Control condition (p1.5–p99.5 of masked Control spheroid pixels) and applied uniformly across all four treatment conditions (Figures X–X+3), enabling direct comparison of cTnT signal intensity across injury severities. Representative images from one spheroid per treatment group are shown. Scale bars: 200 µm.

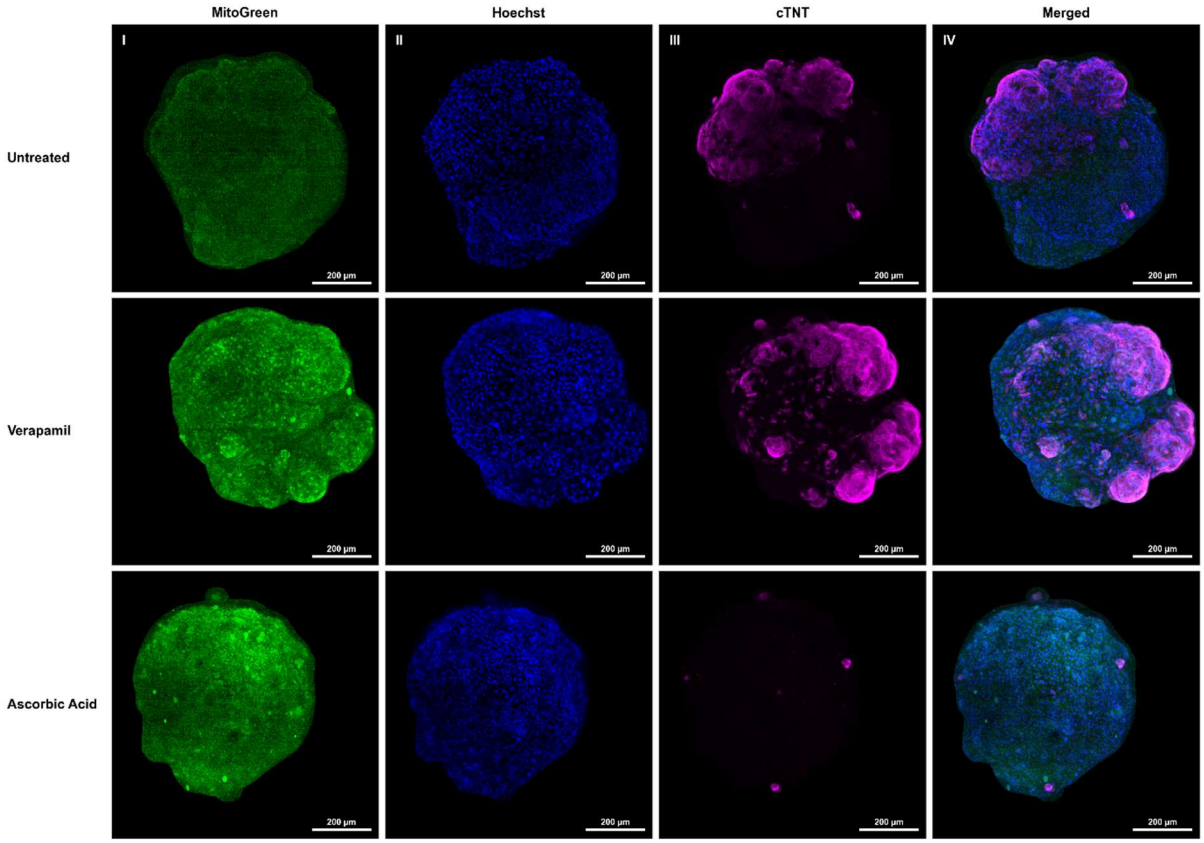

Figure 40: Confocal fluorescence imaging following treatment with deoxygenated maintenance medium. Spheroids were exposed to maintenance medium deoxygenated by constant nitrogen flux for 30 minutes. Verapamil or Ascorbic Acid was co-administered during treatment. Imaging, masking, and processing were performed as described in Figure X. MitoTracker™ Green and Hoechst contrast were normalised across treatment groups within this condition; cTnT contrast uses the shared Control-derived intensity range described in Figure X. Representative images from one spheroid per treatment group are shown. Scale bars: 200 µm.

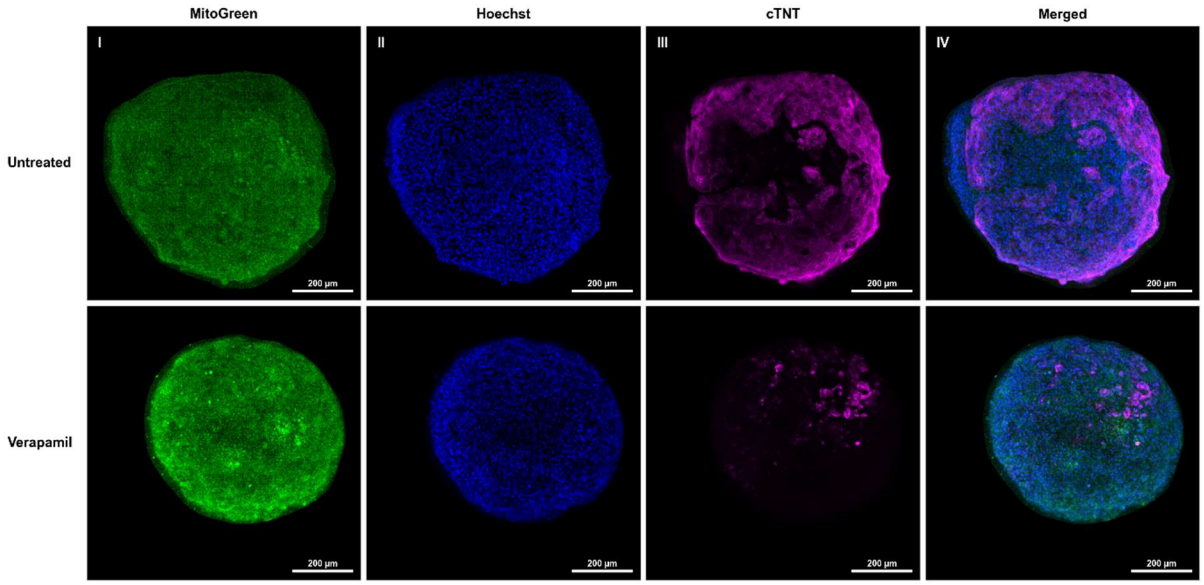

Figure 41: Confocal fluorescence imaging following treatment with Tyrode's solution. Spheroids were incubated in Tyrode's solution (pH 7.2) for 30 minutes without deoxygenation. Verapamil was co-administered during treatment. Ascorbic Acid was not included in this condition. Imaging and processing were performed as described in Figure X. MitoTracker™ Green and Hoechst contrast were normalised across treatment groups within this condition; cTnT contrast uses the shared Control-derived range. Representative images from one spheroid per treatment group are shown. Scale bars: 200 µm.

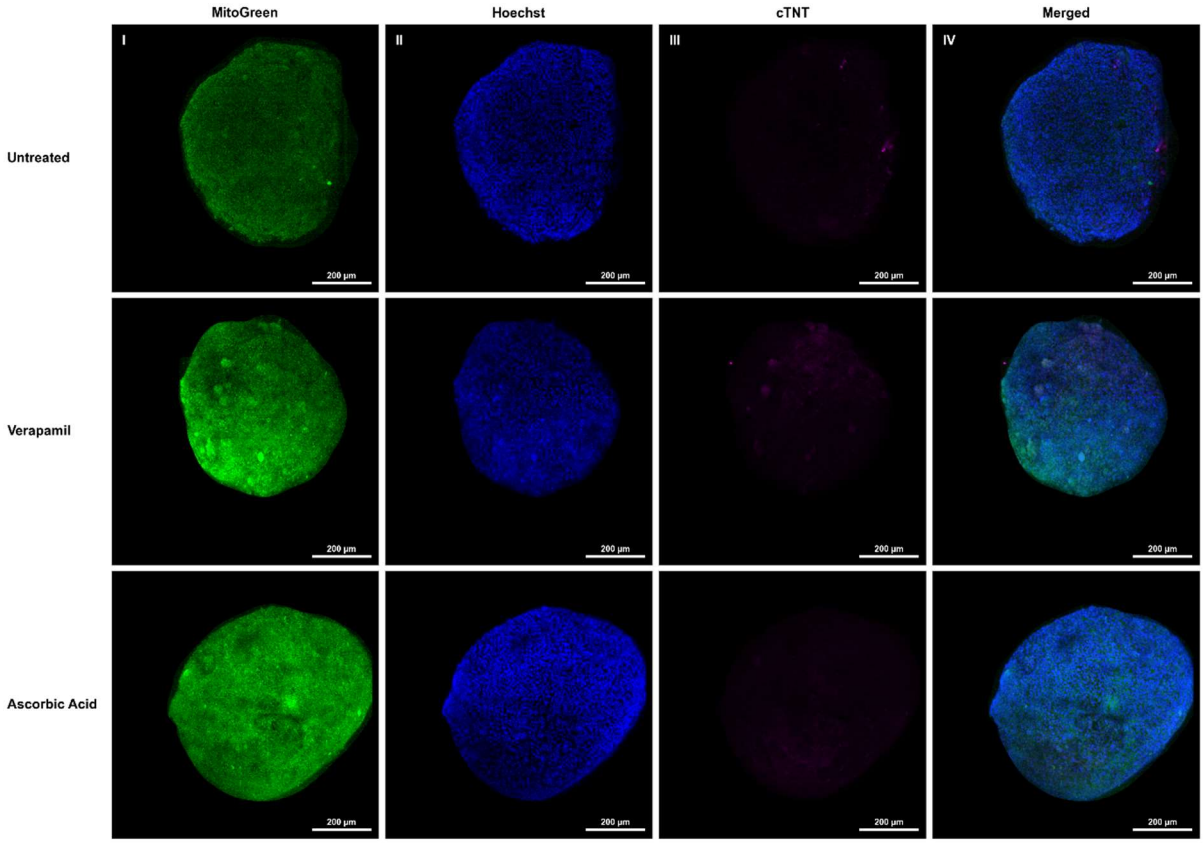

Figure 42: Confocal fluorescence imaging following treatment with deoxygenated Tyrode's solution. Spheroids were incubated in Tyrode's solution (pH 7.2) deoxygenated by nitrogen flux for 30 minutes, followed by replacement with fresh maintenance medium to model reperfusion. Verapamil or Ascorbic Acid was co-administered during treatment. Imaging and processing were performed as described in Figure X. MitoTracker™ Green and Hoechst contrast were normalised across treatment groups within this condition; cTnT contrast uses the shared Control-derived intensity range described in Figure X, enabling direct visual comparison of cTnT signal reduction relative to non-injured conditions. Representative images from one spheroid per treatment group are shown. Scale bars: 200 µm.

Under control conditions, untreated, verapamil-treated, and ascorbic acid-treated spheroids all exhibited strong MitoTracker™ Green signal and uniform nuclear density, indicating preserved mitochondrial membrane potential and structural integrity as displayed in Figure 39. Untreated and verapamil-treated spheroids showed broadly distributed cTnT expression throughout the spheroid body. In contrast, ascorbic acid-treated spheroids displayed a more heterogeneous cTnT distribution, with signal concentrated in discrete regions rather than uniformly distributed, despite preserved overall morphology and viability markers.

Following treatment with deoxygenated maintenance medium, MitoTracker™ Green and Hoechst signals remained comparable across all groups. Untreated spheroids showed mildly heterogeneous cTnT expression relative to control. Verapamil-treated spheroids retained strong cTnT signal comparable to non-injured conditions (Figure 40). ascorbic acid-treated spheroids exhibited visibly reduced cTnT intensity compared to both untreated and verapamil-treated groups.

In the Tyrode condition, assessed for untreated and verapamil-treated spheroids, both groups maintained strong MitoTracker™ Green and Hoechst staining. Untreated spheroids displayed robust cTnT expression (Figure 41). Verapamil-treated spheroids showed preserved mitochondrial and nuclear staining but a moderately reduced and more fragmented cTnT distribution relative to untreated spheroids.

The most pronounced structural disruption was observed following deoxygenated Tyrode treatment. In untreated spheroids, MitoTracker™ Green signal remained detectable, and nuclei were preserved; however, cTnT expression was markedly reduced compared to non-injured conditions. Verapamil- and Ascorbic Acid-treated spheroids displayed similar patterns, with preserved mitochondrial and nuclear staining but minimal residual cTnT signal (Figure 42). As cTnT contrast was normalised to the control intensity range across all figures, the near absence of cTnT signal in the treated spheroids indicates substantial sarcomeric protein loss relative to non-injured controls.

Across injury conditions, neither verapamil nor ascorbic acid restored cTnT expression under severe ischemic challenge at T3. MitoTracker™ Green and Hoechst staining remained detectable in all treatment groups, indicating preserved cellular structure despite loss of sarcomeric marker expression in the most severe condition.

3.5.4. Discussion of Chapter 3.5

Collectively, the combined nitrogen–Tyrode system reproduces key mechanistic features of reperfusion injury, with calcium overload and oxidative stress emerging as central components of the observed phenotype. To further investigate the mechanistic drivers of injury within the established ischemia–reperfusion model, two pathway-targeted pharmacological modulators were evaluated: the L-type calcium channel blocker verapamil[403] and the antioxidant ascorbic acid.[404] These compounds were selected based on their mechanistically defined intervention rather than their clinical validated reperfusion therapy.[405]

Both calcium overload and ROS generation represent central components of canonical reperfusion pathophysiology.[406] However, clinical and experimental attempts to mitigate ischemia–reperfusion injury through isolated targeting of these pathways have yielded mixed and often limited success.[407–411] Within this framework, pharmacological modulation in the present study serves as an exploratory validation of pathway relevancy rather than expectation of complete therapeutic rescue.

3.5.4.1. Context-Dependent Effects of Verapamil

Despite continuous administration before ischemia and throughout reperfusion, verapamil did not significantly improve metabolic recovery under full reperfusion conditions. Viability at 72 hours remained reduced and comparable to untreated controls. This suggests that L-type calcium influx alone does not represent the dominant irreversible injury driver in this model.

Under isolated nutrient deprivation (Tyrode condition), verapamil significantly reduced viability. This apparent paradox can be mechanistically explained by the physiological role of calcium in mitochondrial metabolic regulation.[411] Rhythmic cytosolic Ca^{2+} elevations stimulate mitochondrial dehydrogenases within the tricarboxylic acid cycle.[412] This supports NADH production and oxidative phosphorylation. Under nutrient deprivation, this calcium-dependent metabolic stimulation may become critical for maintaining ATP output.[413] Pharmacological blockade of L-type calcium channels in this context likely suppresses mitochondrial activation.[414,415] This results in energetic adaptation impairment rather than protection. In contrast, under normoxic and isolated hypoxic conditions, verapamil exerted either neutral or mildly stabilizing effects. Reduced calcium influx lowers contractile workload and ATP demand, potentially stabilizing mitochondrial membrane potential and limiting redox stress.[416] These findings underscore the dual and context-dependent role of calcium signalling in cardiomyocytes. Excessive calcium promotes injury, physiological calcium oscillations are required for metabolic support.[417]

Collectively, these observations indicate that reperfusion-associated calcium dysregulation in the model is unlikely to be driven solely by L-type calcium entry. Instead, downstream mechanisms, including Na^{+}/Ca^{2+} exchanger reversal, sarcoplasmic reticulum leak, ATP-dependent pump failure, and mitochondrial permeability transition, likely play dominant roles in mediating irreversible structural damage.[284,418,419]

3.5.4.2. Ascorbic Acid and the Limits of ROS Scavenging

Ascorbic acid supplementation likewise failed to produce substantial protection under full reperfusion conditions. Although well tolerated across the tested concentration range, antioxidant treatment did not restore metabolic viability and in some instances modestly reduced it.

This outcome is consistent with the temporal dynamics of reperfusion-associated oxidative stress. ROS generation during reoxygenation occurs rapidly and transiently,

largely driven by RET at mitochondrial Complex I.[420] Even with continuous addition, antioxidant supplementation may not effectively intercept localized mitochondrial ROS production at the moment of burst initiation. Once oxidative damage has triggered mitochondrial depolarization, calcium overload, and proteolytic cascades, scavenging is unlikely to reverse downstream injury progression.[341]

Furthermore, physiological redox signalling plays essential roles in cellular adaptation.[421] Broad ROS scavenging may interfere with these processes, potentially contributing to the absence of protective benefit.[422] The limited morphological rescue observed despite preserved mitochondrial staining further supports the interpretation that oxidative stress acts as an early initiating factor rather than a sustained, independently sufficient driver of structural collapse.

3.5.4.3. Implications for Model Validity and Translational Relevance

Importantly, the modest and context-dependent pharmacological effects observed for both verapamil and ascorbic acid are consistent with the limited success of single-target interventions in experimental and clinical ischemia–reperfusion settings.[423] Although calcium overload and oxidative stress are central components of reperfusion pathology, attempts to mitigate injury through isolated modulation of these pathways have repeatedly yielded variable or incomplete protection *in vivo*.[424]

The parallel lack of robust rescue in the present model therefore supports its biological realism. Rather than reflecting a simplified hypoxic toxicity model, the injury cascade reproduced here appears multifactorial and resistant to single-pathway intervention. This mirrors the translational challenge of ischemia–reperfusion therapy, where combinatorial or temporally optimized strategies are likely required.[424]

Taken together, the pharmacological interrogation strengthens the mechanistic interpretation of the system. The data indicate that calcium dysregulation and oxidative stress contribute to injury progression, yet irreversible structural collapse emerges from their integration with mitochondrial destabilization and proteolytic degradation. The model therefore captures not only the hallmarks of reperfusion injury but also its therapeutic complexity.[425]

The combined nitrogen–Tyrode model reproduces the temporal progression of ischemia–reperfusion injury, from acute calcium dysregulation and mitochondrial destabilization to delayed metabolic decline, structural disintegration, and fibrotic activation. The limited efficacy of targeted L-type calcium channel blockade and antioxidant supplementation underscores the multifactorial nature of the injury

cascade. Rather than being readily reversible through single-axis modulation, the observed phenotype reflects a tightly coupled network of metabolic, redox, and calcium-dependent mechanisms. This complexity, together with the model's scalability and experimental controllability, supports its utility as a physiologically relevant platform for mechanistic examination and future combinatorial therapeutic exploration.

3.6. Integrated Closed-Loop Platform

3.6.1. System Overview

The fully integrated closed-loop platform combines five autonomous subsystems into a single, unattended workflow for dose-response characterization of iPSC-derived ventricular cardiomyocyte spheroids (Figure 44). The platform was designed to address a critical bottleneck in patient-specific cardiac drug screening: the need to determine accurate IC_{50} and maximal physiological range (MPR) values for compounds of interest prior to their evaluation in ischemic reperfusion injury models, where incorrect dosing can obscure therapeutic effects or induce artefactual toxicity.

Spheroids and organoids represent powerful three-dimensional biological model systems, but their production and experimental use remain notoriously difficult to standardize with conventional laboratory protocols. Variability in cell aggregation, growth conditions, and handling steps often leads to significant differences between experiments, limiting reproducibility and the systematic exploration of complex experimental parameters. To move beyond the current state of the art, autonomous and AI-based experimental platforms are therefore required that can precisely control experimental conditions, perform large numbers of experiments in parallel, and iteratively optimize protocols through data-driven feedback. This paradigm is realized in self-driving laboratories (SDLs), in which robotic experimentation, automated instrumentation, and artificial intelligence are integrated into a closed experimental loop. In such systems, algorithms analyse experimental outcomes, determine the most informative next experiment, and automatically trigger the required laboratory processes. This creates an iterative design–make–measure–learn cycle, enabling efficient exploration of large experimental spaces while generating standardized, machine-readable datasets.

Within the HELMHOLTZ Acceleration Alliance (HELMA), a self-driving laboratory initiative headed by the Karlsruhe Institute of Technology, this concept is implemented through interconnected automated laboratory platforms that combine robotics, AI-driven analysis, and digital infrastructure. A central component of this ecosystem is the Bio.MAT and Bio.Lab self-driving lab platform, which provides autonomous capabilities for the generation and functional analysis of complex 3D biological models such as spheroids and organoids. At the core of this platform is a CellXpress.ai Automated Cell Culture System, one of only three such systems worldwide capable of fully autonomous spheroid and organoid production (Figure 43). This highly specialized robotic cell culture platform enables standardized, large-scale generation of 3D tissue models in 384-well U-bottom plates without manual intervention, providing a crucial technological basis for reproducible high-throughput biological experimentation within HELMA. The Bio.MAT/ Bio.LAB self-driving lab integrates this system with an ImageXpress HT.ai High-Content Imaging System for automated brightfield stream acquisition to quantify contractile activity prior to treatment. Liquid handling tasks, including serial dilutions and compound dispensing, are carried out using an Opentrons Flex platform, while endpoint metabolic activity is measured via MTT absorbance at 570 nm using a SpectraMax Microplate Reader (figure 43).

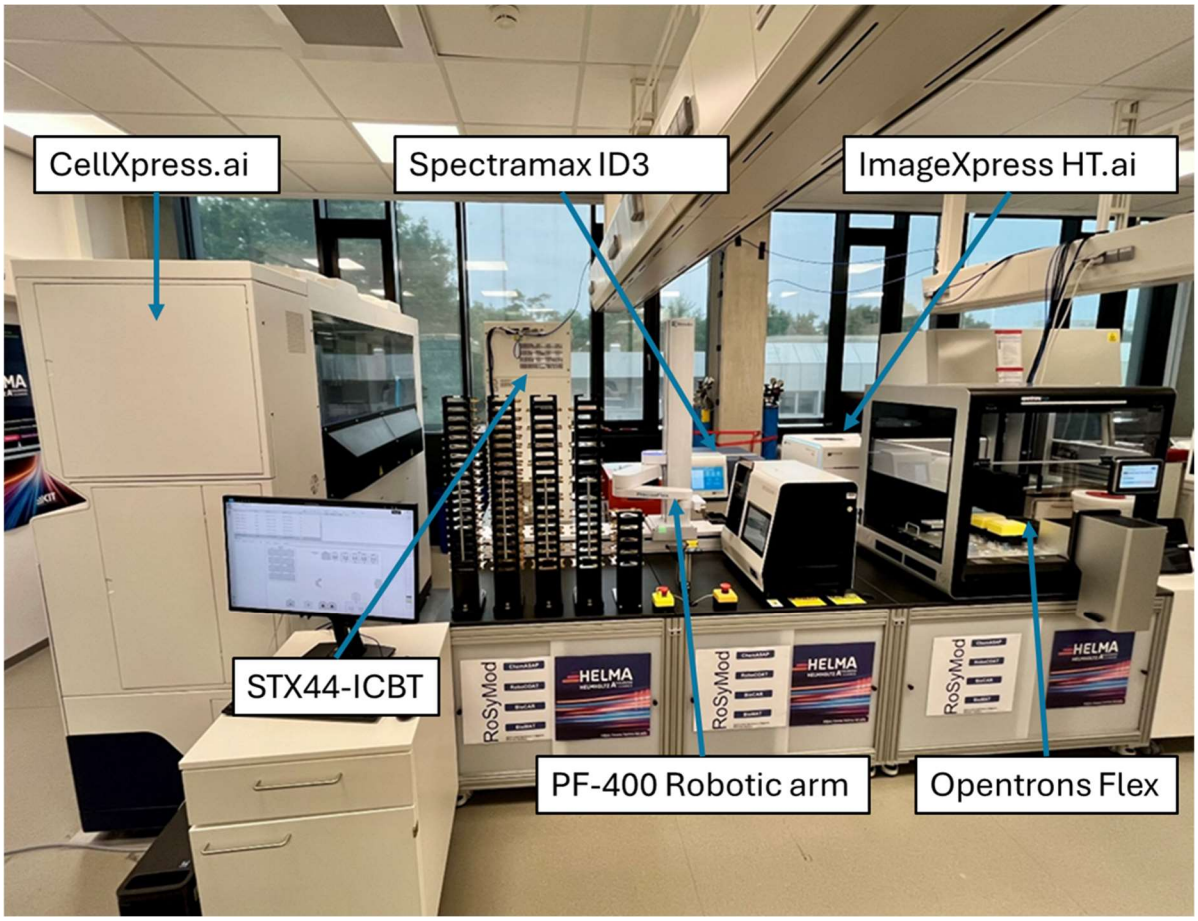

Figure 43: Bio.MAT/Bio.LAB self-driving laboratory (SDL) platform. The automated system integrates a CellXpress.ai for automated spheroid and organoid generation, a STX44-ICBT Liconic benchtop incubator for controlled assay incubation, and a PF400 robotic arm for automated plate transfer between devices. Liquid handling is performed using an Opentrons Flex workstation. Endpoint measurements are conducted with a SpectraMax iD3 plate reader, while high-throughput fluorescence imaging is carried out using an ImageXpress HT.ai system.

Experimental orchestration across all instruments is coordinated through the Retisoft Genera 6.8.6 Laboratory Execution System, which manages instrument access, scheduling, plate transport, and automated error recovery. A dedicated analysis workstation orchestrates the AI-driven closed-loop logic of the platform. It runs Bayesian optimization algorithms that determine subsequent experimental conditions, triggers Genera processes, and automatically retrieves instrument output files over the local network (Figure 44). By linking automated experiment execution with real-time analysis and algorithmic decision making, the Bio.MAT/Bio.LAB embodies the HELMA vision of a self-driving laboratory, enabling autonomous experimentation and the generation of standardized datasets for predictive modelling and digital twin approaches in advanced biomedical research.

Each 384-well plate accommodates up to four test substances simultaneously. Columns 1–4 serve as untreated controls (64 wells), while columns 5–24 are divided into four substance blocks of five columns each. Each concentration is represented by

16 technical replicates (rows A–P), providing sufficient statistical power for robust mean viability estimation while enabling identification and exclusion of outlier wells.

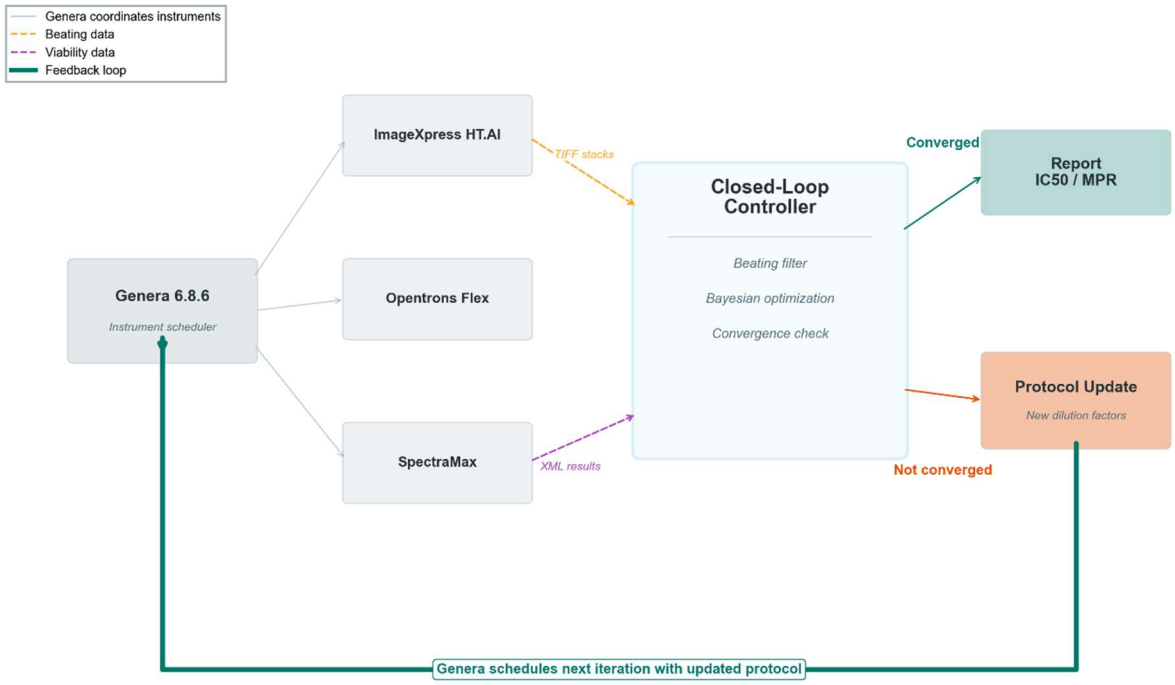

Figure 44: Architecture of the closed-loop drug screening platform. Genera 6.8.6 serves as the instrument scheduler, coordinating the ImageXpress HT.ai (stream acquisition), the Opentrons Flex (liquid handling), and the SpectraMax plate reader (absorbance measurement). Dashed lines indicate data transfer: TIFF stacks from the imager and XML result files from the reader feed into the closed-loop controller, which performs beating-based well filtering, Bayesian dose-response optimization, and convergence evaluation. When convergence criteria are met, IC_{50} and MPR estimates are reported (top right). Otherwise, the controller generates an updated dilution protocol that is returned to Genera (bottom arc), which schedules the next experimental iteration.

3.6.2. Pre-Treatment Beating Assessment

3.6.2.1. Rationale for Baseline Beating Assessment

In this thesis, cardiac spheroids were generated and differentiated in a high-throughput automated workflow using the CellXpress.ai platform, which standardized cell seeding, reagent dispensing, medium exchanges, and plate handling across all wells (5.2.2.2). However, while this workflow ensured process consistency, it did not eliminate biological variability in differentiation outcome between individual spheroids. Therefore, a baseline assessment of spontaneous beating was required as a functional quality-control step to identify wells containing successfully differentiated and metabolically comparable cardiac spheroids prior to viability analysis (3.2.2).

Spontaneous contractile activity represents a hallmark of mature iPSC-derived cardiomyocyte spheroids, reflecting the functional state of the underlying cardiomyocytes. Cardiac contraction constitutes the dominant energy-consuming

process in cardiomyocytes, accounting for approximately 60–70 % of total cellular ATP turnover.[426] In the MTT assay, the reduction of tetrazolium salt to formazan is directly proportional to mitochondrial metabolic activity. Consequently, non-beating spheroids, which lack the energetic demand of active contraction, exhibit a fundamentally different metabolic baseline than their beating counterparts: non-beating spheroids are metabolically less active overall, producing lower MTT absorbance.

Including non-beating wells in viability statistics introduces two systematic errors. First, non-beating wells yield reduced absorbance values, deflating mean viability and making compounds appear more cytotoxic than they are, particularly at sub-IC_{50} concentrations, where the contrast between beating and non-beating metabolic baselines is most pronounced. Second, the coexistence of beating and non-beating wells within the same concentration group increases the coefficient of variation, reducing the statistical power to detect dose-dependent viability changes and delaying convergence of the Bayesian optimization framework used in this thesis to iteratively select experimental conditions and compounds (3.6.3).

The beating pre-screen was therefore introduced as a data quality assurance step: prior to compound addition, each well is assessed for contractile activity, and wells falling below a minimum beating threshold are flagged for exclusion from the downstream viability analysis. Critically, no data is discarded, all absorbance measurements are recorded and stored, the exclusion affects only the aggregated statistics provided to the optimizer (3.6.3).

3.6.2.2. Contraction Signal Extraction

The contraction signal is computed from each TIFF stack using a MuscleMotion-style algorithm, which quantifies frame-to-frame pixel intensity changes as a proxy for contractile displacement (Figure 45, panels A–B).[427] Each frame is first convolved with a Gaussian kernel (sigma = 10 pixels) to suppress acquisition noise while preserving the spatial extent of the contractile motion. From the resulting blurred stack, a temporal median frame is computed and the reference frame is selected as the frame exhibiting the smallest mean absolute deviation from this median, representing the closest approximation to the resting diastolic state. The contraction amplitude for each frame t is then calculated as the mean absolute pixel-wise difference between the current frame and the reference frame (Equation 2):

Equation 2

$$S(t) = \frac{1}{N_{pixels}} \sum_{x,\,y} |I_\sigma(x, y, t) - I_\sigma(x, y, t_{ref})|$$

where I_σ denotes the Gaussian-blurred intensity and t_{ref} is the reference frame index. The resulting one-dimensional signal S(t) exhibits peaks corresponding to maximal contraction (systole) and valleys corresponding to relaxation (diastole).

3.6.2.3. Signal Preprocessing and Beat Detection

Prior to peak detection, the raw contraction signal undergoes baseline correction and amplitude normalization. A rolling 5th-percentile filter with a window of 30 frames (~3 s) estimates the slowly-varying baseline, which is subtracted from the signal. The 5th percentile was chosen to track the signal floor without being influenced by the contraction peaks themselves, and negative values after subtraction are clamped to zero. The baseline-corrected signal is then divided by its 95th percentile value, mapping it to an approximate [0, 1] range. This normalization renders the subsequent peak detection thresholds invariant to absolute pixel intensity, image magnification, and spheroid size, critical properties for consistent analysis across the heterogeneous population inherent to iPSC-derived spheroids.

Contraction peaks are identified using scipy.signal.find_peaks with adaptive, signal-relative thresholds: a prominence threshold of 20 % of the dynamic range above the median, a height threshold of 10 % of the signal maximum, and a minimum inter-beat distance of 1 second (10 frames) reflecting the physiological refractory period of iPSC-derived ventricular cardiomyocytes. Each well is then classified as either active or excluded based on the number of detected beats (Equation 3, Figure 45 panel C, D, E):

Equation 3

$$\text{Well status}: \quad \textbf{Active} \ \text{if} \ n_{beats} \geq 2 \qquad \textbf{Excluded} \ \text{if} \ n_{beats} < 2$$

The threshold of two beats ensures that at least one complete contraction cycle (peak-to-peak) is present, which is the minimum required to confirm rhythmic contractile activity rather than a single, potentially artefactual displacement event.

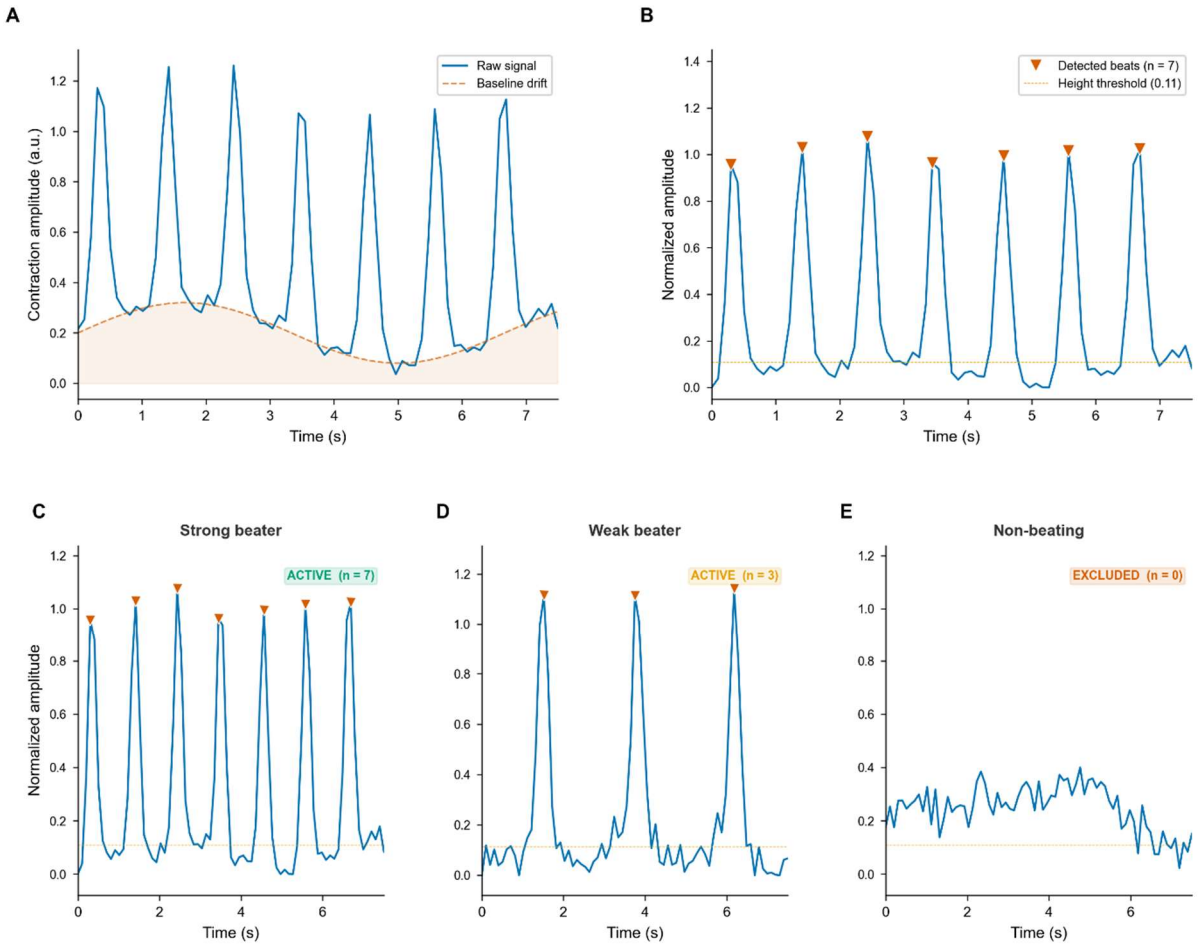

Figure 45: Contraction signal analysis for pre-treatment beating assessment. (A) Raw MuscleMotion-style contraction signal from an actively beating iPSC-CM spheroid, showing periodic systolic peaks superimposed on a slowly varying baseline drift (dashed, shaded region). (B) Signal after rolling 5th-percentile baseline correction and 95th-percentile amplitude normalization; detected beat peaks are marked by inverted triangles and the adaptive height threshold is indicated (dashed line). (C–E) Gallery of representative well classifications on a shared amplitude scale. (C) Strong beater with seven detected contractions (ACTIVE). (D) Weak beater with three detected contractions at lower amplitude, still exceeding the minimum beat count of two (ACTIVE). (E) Non-beating well exhibiting aperiodic noise that remains below the detection threshold throughout the recording window (EXCLUDED, n = 0).

3.6.2.4. Integration with the Closed-Loop Workflow

The beating analysis is integrated into the Genera wait phase of each optimization iteration. Since the ImageXpress HT.ai acquisition occurs at the beginning of the Genera workflow, before compound addition, the imaging data typically becomes available within the first 1–2 hours of the approximately 42-hour process. The closed-loop-controller monitors the imaging output directory at regular intervals and, upon detecting new data, processes all TIFF stacks sequentially, parsing well identifiers from filenames and recording the beat count for each well. Wells with fewer than two detected beats are added to the exclusion set. If no imaging data appears within 36 hours, the system proceeds without exclusions, ensuring the optimization loop is not blocked by a non-critical subsystem failure.

When plate reader results arrive, viability statistics are computed twice: first with all wells for archival completeness, then with excluded wells masked before aggregation. Only the filtered statistics are passed to the Bayesian optimizer. The exclusion mechanism operates at the per-well level and affects both control and substance wells. Non-beating control wells are removed from the reference absorbance calculation, preventing them from deflating the control mean and artificially inflating all viability percentages. Non-beating substance wells are masked from the per-concentration viability matrix before computing mean and standard deviation, reducing the influence of low-absorbance outliers on the statistics reported to the optimizer.

3.6.3. Bayesian Optimization-Guided Dose-Response Characterization

Bayesian optimization was employed to efficiently characterize dose–response relationships while minimizing the number of experimental measurements required. Bayesian optimization is an iterative experimental design strategy that uses a probabilistic surrogate model to approximate the relationship between input variables and measured responses, and an acquisition function to determine the most informative next experiments. In the present workflow, cell viability measurements obtained from the MTT assay were used to iteratively update a dose–response model, enabling adaptive selection of drug concentrations that maximize information gain for pharmacological parameter estimation. Within this framework, the four-parameter logistic model serves as the surrogate model describing the dose–response relationship.

3.6.3.1. Four-Parameter Logistic Model

The dose-response relationship between drug concentration and cell viability is modelled using a four-parameter logistic (4PL) function (Equation 4, Figure 46 panel A):

Equation 4

$$V(C) = V_{bottom} + \frac{V_{top} - V_{bottom}}{1 + \left(\frac{C}{IC_{50}}\right)^{H}}$$

where V_{bottom} and V_{top} represent the lower and upper asymptotes (minimum and maximum viability), IC_{50} is the concentration producing 50 % of the maximal effect, and H is the Hill coefficient describing the steepness of the transition. This is widely

applied to describe sigmoidal biological responses such as drug efficacy, toxicity, or receptor activation. The model captures the sigmoidal shape characteristic of dose-response curves across the full concentration range.

Two key pharmacological parameters are derived from the fitted curve. The IC_{50} is the concentration at which viability drops to 50 %, read directly from the inflection point and indicating the potency of the cytotoxic effect. The MPR (maximal physiological range) is defined as the highest concentration at which viability remains above 90 % of the untreated control, representing the maximum safe dosing concentration for downstream applications such as ischemic reperfusion injury models.

3.6.3.2. Initial Exploration and Adaptive Concentration Selection

The first iteration of each optimization run employs a logarithmically-spaced concentration series spanning the testable range (Equation 5), providing broad coverage of the dose-response curve without prior knowledge of the compound's potency:

Equation 5

$$C_i = C_{min} \cdot \left(\frac{C_{max}}{C_{min}}\right)^{\frac{i-1}{M-1}}, \quad i = 1, \ldots, M$$

where M = 5 is the number of available concentration slots per substance. For a typical stock concentration of 10 mM, the default range spans from 1 nM to 1 mM, covering four orders of magnitude with approximately equal resolution per decade to maximize the probability of capturing the transition region in a single exploratory iteration.

From the second iteration onward, the Bayesian optimizer selects concentrations using the fitted 4PL model as an informed surrogate and acquisition functions tailored to the optimization objective. For the IC50 objective, concentrations are selected to minimize IC50 uncertainty by prioritizing the transition region of the dose-response curve (40–60 % viability) where sensitivity to the IC50 parameter is greatest (Figure 46, panels A–B). The acquisition function balances exploitation, placing points near the current IC50 estimate, with exploration of regions exhibiting high prediction uncertainty (Figure 46, panel C).

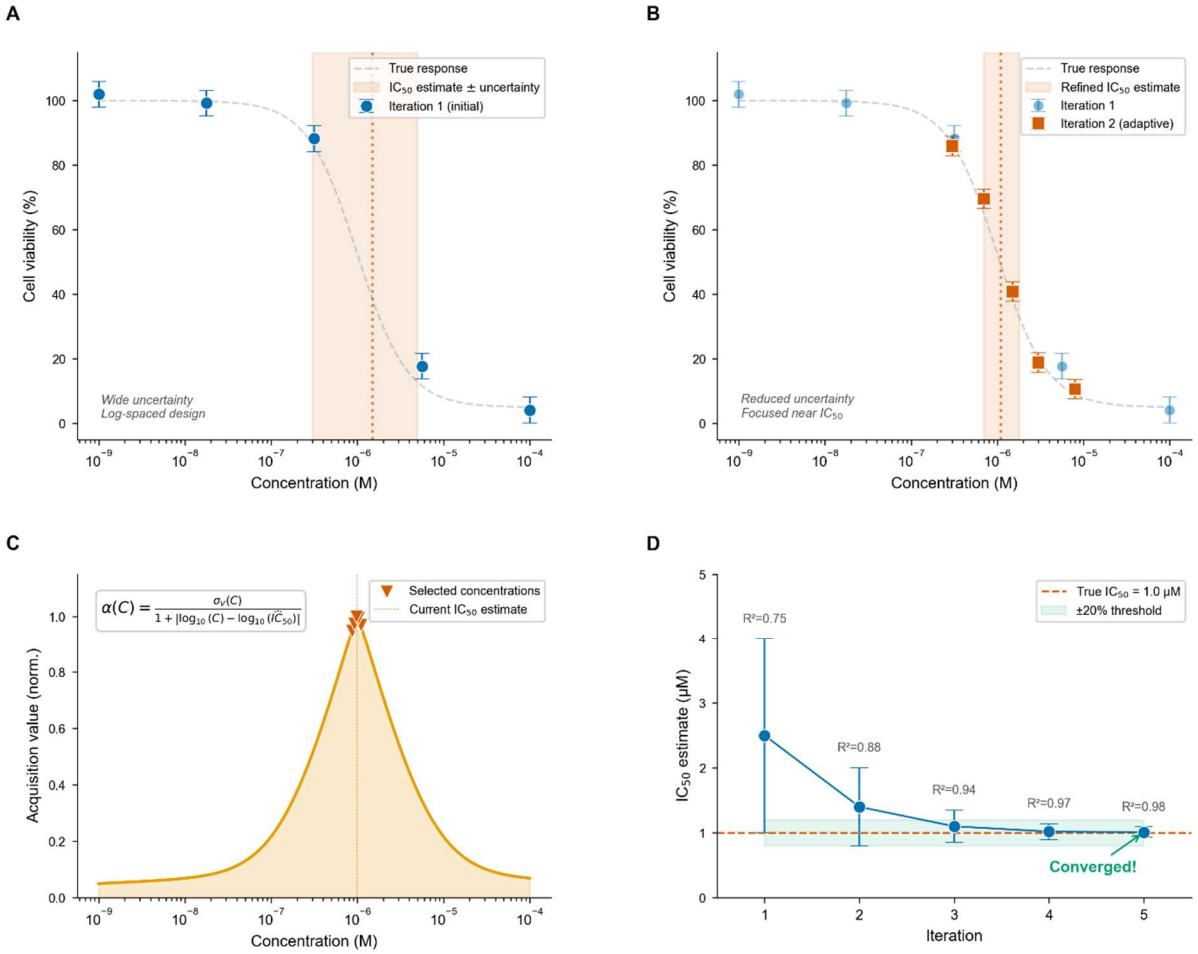

Figure 46: Bayesian optimization of IC_{50} estimation. (A) Iteration 1, five logarithmically spaced concentrations provide initial coverage of the dose-response curve; the shaded band indicates the wide IC_{50} uncertainty region estimated from the preliminary four-parameter logistic fit. (B) Iteration 2, five adaptively selected concentrations (squares) cluster around the transition zone, narrowing the IC_{50} estimate (reduced shaded band) while iteration 1 data circles, faded) are retained in the pooled fit. (C) Acquisition function used for concentration selection, defined as the ratio of predictive uncertainty to distance from the current IC_{50} estimate on a log-concentration scale; inverted triangles mark the five concentrations with highest acquisition value. (D) IC_{50} convergence across five iterations, showing progressive narrowing of the 95 % confidence interval toward the true IC_{50} (dashed line, 1.0 µM); R^2 values annotate model goodness-of-fit at each iteration.

Data from successive iterations is pooled, so when the same concentration appears in multiple iterations, the replicate count increases and the combined standard error decreases, progressively tightening the confidence interval (Figure 46, panel D). For the MPR objective, concentrations are placed to bracket the 90 % viability threshold from above and below, with preference for higher concentrations and regions of high uncertainty (Figure 47, panels A–B). The MPR acquisition function jointly weights concentration magnitude, predictive uncertainty, and the probability that viability exceeds the safety threshold (Figure 47, panel C), efficiently narrowing the confidence interval around the maximum safe concentration across successive iterations (Figure 47, panel D).

3.6.3.3. Convergence Criteria

Optimization terminates when objective-specific convergence criteria are satisfied or the maximum iteration count (k_max = 5) is reached.

IC_{50} convergence requires simultaneous satisfaction of three conditions (Figure 46, panel D): the 95 % confidence interval width must be less than 30 % of the IC_{50} estimate, the coefficient of determination R^2 must exceed 0.85, and at least two data points must fall within the 40–60 % viability transition zone. These criteria ensure that the IC_{50} estimate is not only precise but also well-supported by data in the most informative region of the curve, while the R^2 threshold guards against accepting a numerically precise but poorly-fitting model.

MPR convergence requires a confidence metric of at least 80 %, computed as (Equation 6):

Equation 6

$$\text{Confidence}_{MPR} = \left(1 + \frac{\sigma_V}{10}\right)^{-1}$$

where σ_v is the viability uncertainty at the estimated maximum safe concentration. To quantify differences between experimental conditions, two complementary metrics were used: the bracket gap ratio and the fold-difference. These measures provide intuitive ways to describe the magnitude of change between two values or conditions. The bracket gap ratio is defined as the fold-difference between the highest tested concentration that maintains viability above the 90 % threshold and the lowest concentration at which viability falls below this threshold. For convergence, this ratio must not exceed 2.0× (Figure 47, panel D). This criterion ensures that the MPR is tightly bounded from both sides with sufficient precision for pharmacological applications.

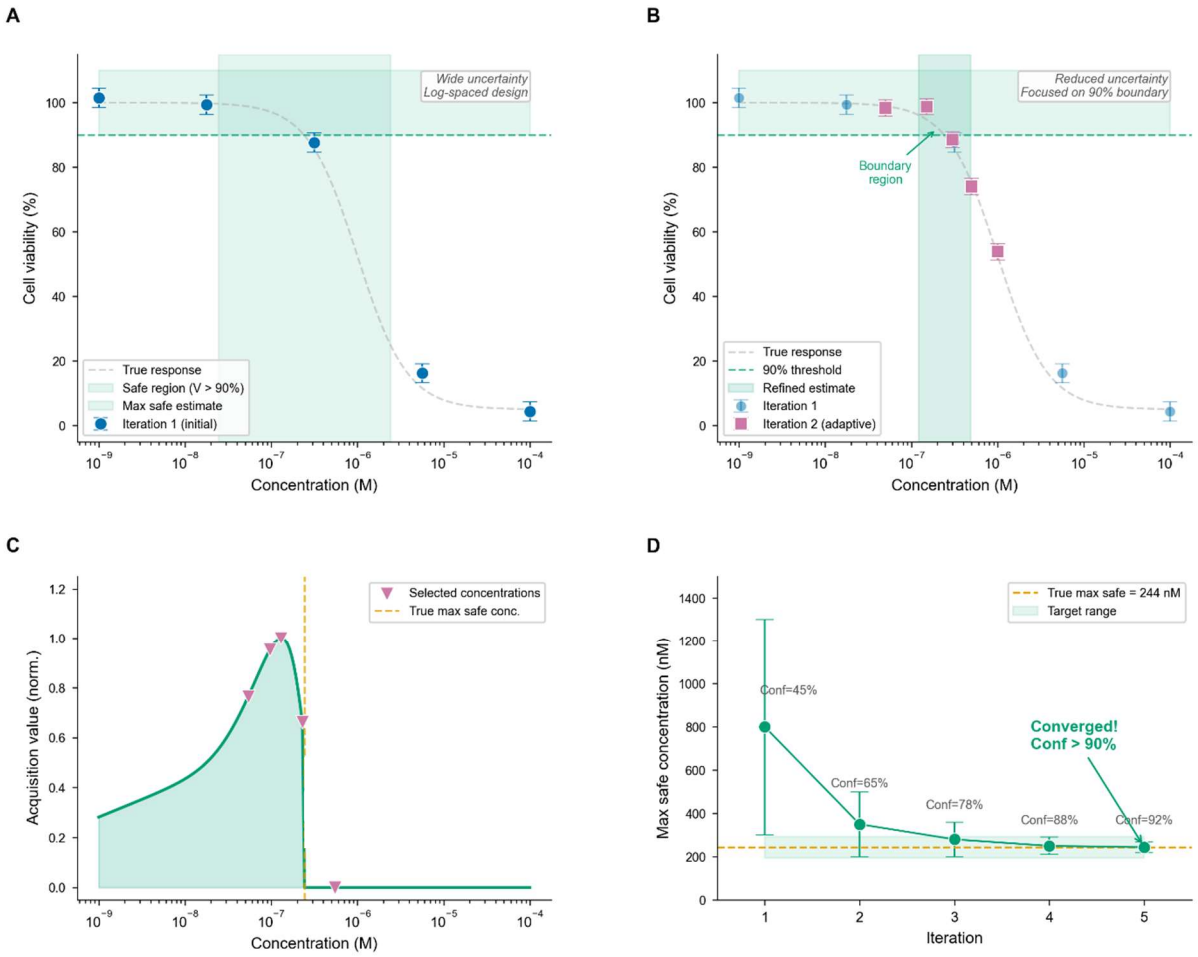

Figure 47: Figure 4: Bayesian optimization of the maximal physiological range (MPR). (A) Iteration 1, initial log-spaced exploration with the 90 % viability threshold (dashed horizontal line) and estimated safe region (shaded); the broad shaded vertical band reflects high uncertainty in the maximum safe concentration. (B) Iteration 2, adaptively selected concentrations (squares) bracket the 90 % viability boundary, reducing the safe concentration estimate to a narrower band. (C) MPR acquisition function, which weights concentration by the joint probability of safety and predictive uncertainty; inverted triangles mark selected concentrations, and the dashed vertical line indicates the true maximum safe concentration. (D) Convergence of the maximum safe concentration estimate (nM) across iterations, with confidence annotations increasing from 45 % to 92 %; the system terminates at iteration 5 upon exceeding the 90 % confidence threshold.

3.6.3.4. Adaptive Range Escalation and Non-Standard Profiles

In automated dose–response experiments, the initially selected concentration range may not always capture the full biological response. To address this limitation, an adaptive range escalation strategy was implemented. If the measured responses did not reach the expected lower or upper plateau of the dose–response curve, the experimental concentration range was automatically extended in subsequent iterations. This adaptive adjustment ensures that the relevant response window is sufficiently covered to enable reliable model fitting and accurate parameter estimation. In detail, the system implements an escalation mechanism for compounds whose IC_{50} lies above the initial testable range. When viability at the highest tested concentration exceeds 50 %, the system infers that the IC_{50} has not been reached and escalates to

undiluted or minimally diluted stock concentrations (dilution series 1:1, 1:2, 1:3, 1:5, 1:10), dedicating all five concentration slots to the previously untested high-concentration region in a single iteration. Subsequent iterations then employ standard Bayesian optimization to refine the estimate within the expanded range.

Not all compounds produce a classical sigmoidal dose-response. When all tested concentrations yield viability above the upper threshold, the system classifies the compound as stimulatory, producing enhanced rather than reduced metabolic activity and terminates optimization, reporting the MPR as unbounded. Conversely, when viability remains above 50 % even after range escalation, the compound is reported as non-cytotoxic within the testable range after the maximum number of iterations preventing an endless loop.

3.6.4. Impact of Beating-Based Well Exclusion on Viability Statistic

3.6.4.1. Expected Effect on Data Quality

The beating pre-screen is expected to improve viability data quality in two measurable ways (Figure 48). By removing wells with artificially depressed absorbance, reflecting basal metabolism only, without the energetic expenditure of active contraction, the filtered mean viability more accurately represents the drug's effect on functionally active cardiomyocytes, correcting the negative bias that non-beating wells introduce (Figure 48, panel A). Simultaneously, the exclusion reduces the coefficient of variation at each concentration by removing the low-absorbance non-beating outlier population, with the effect being most pronounced in the sub-IC_{50} range where the contrast between beating and non-beating metabolic baselines is greatest (Figure 48, panel B).

3.6.4.2. Quantitative Impact Model

The magnitude of the exclusion effect quantifies the extent to which a specific condition leads to the omission of a subset of measurements from downstream analysis. In biological and high-throughput experiments, such exclusions typically occur when data points fail predefined quality-control criteria or fall outside acceptable experimental ranges. In the present study, exclusion arises from wells containing non-beating spheroids, which are removed from viability statistics to avoid systematic metabolic bias.

The magnitude of the exclusion effect depends on the fraction of non-beating wells and the metabolic differential between beating and non-beating states. Let f_{nb} denote

the fraction of non-beating wells and ΔA the average absorbance deficit of non-beating wells relative to beating wells at the same drug concentration. The bias introduced by including non-beating wells in the viability calculation is (Equation 7):

Equation 7

$$\text{Bias}(\bar{V}) \approx f_{nb} \cdot \frac{\Delta A}{\bar{A}_{control}} \times 100\%$$

For a representative scenario where 10 % of wells are non-beating and non-beating wells exhibit 30% lower absorbance than beating wells at the same concentration, the expected viability bias is approximately 3 percentage points, sufficient to shift the apparent IC_{50} downward by 10–20 % on a logarithmic concentration scale (Figure 48, C).

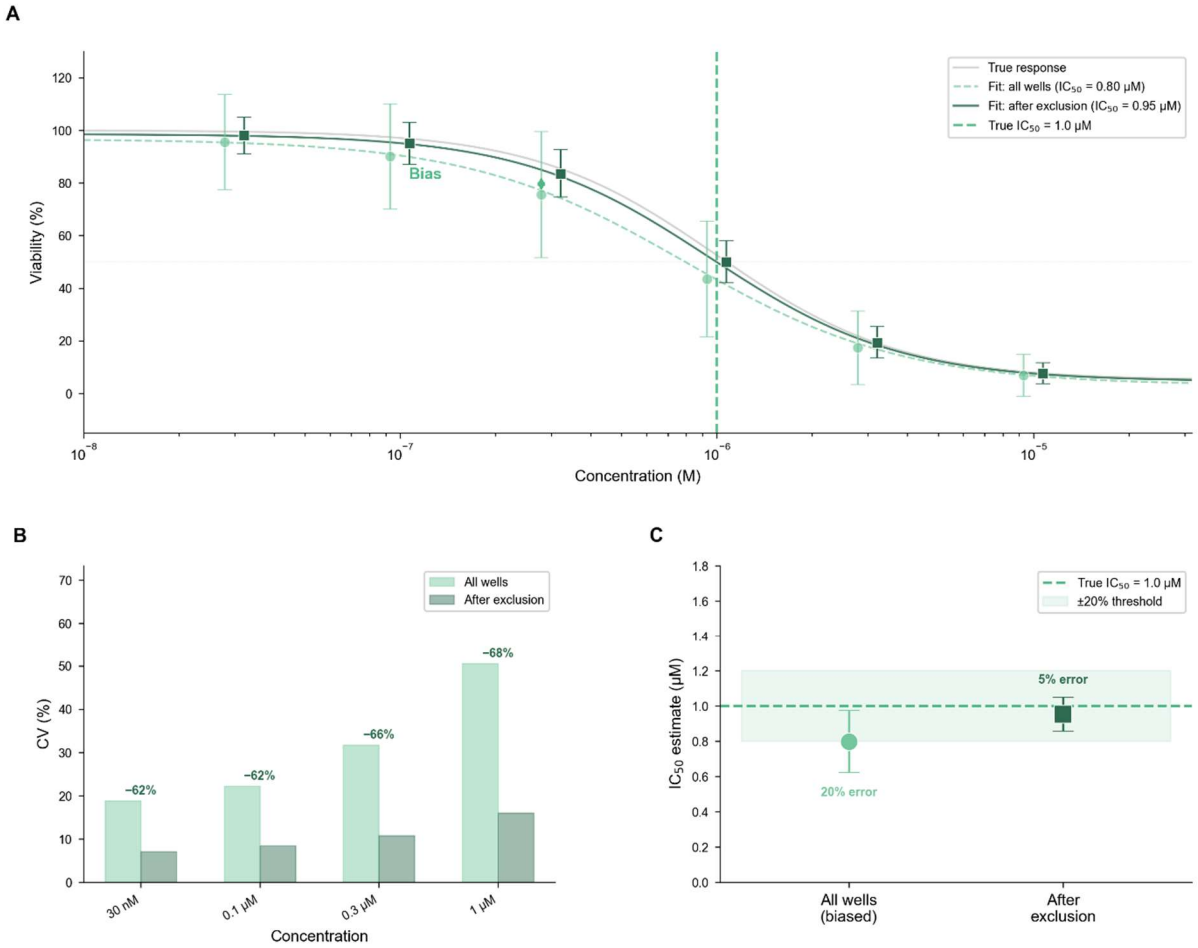

Figure 48: Projected impact of beating-based well exclusion on viability statistics. (A) Dose-response curves fitted to data computed with all wells (amber, dashed) versus after excluding non-beating wells (blue, solid). Non-beating wells exhibit reduced MTT absorbance due to lower metabolic activity, deflating the group mean and shifting the apparent IC_{50} to 0.80 µM, a 20 % underestimate relative to the true value of 1.0 µM. After exclusion, the IC_{50} estimate recovers to 0.95 µM (5 % error). Error bars represent standard deviation across replicate wells; the vertical dashed line marks the true IC_{50}. (B) Coefficient of variation at four sub-IC_{50} concentrations, showing 62–68 % reduction after exclusion of non-beating wells. (C) IC_{50} point estimates with 95 % confidence intervals before and after exclusion; the shaded band denotes the ±20 % acceptance threshold around the true IC_{50}.

3.6.4.3. Effect on Optimizer Convergence

In autonomous experimental workflows, the convergence behaviour of the optimizer is an important indicator of how efficiently optimal experimental conditions can be identified. In Bayesian optimization, convergence is reached when additional experimental iterations yield only marginal improvements in the objective function and parameter estimates stabilize within predefined confidence bounds. Experimental factors such as measurement noise, incomplete coverage of the dose–response range, or systematic data exclusion can influence both the speed and reliability of convergence.

The improved precision afforded by beating-based exclusion has a direct impact on convergence speed. Reduced variance in viability estimates propagates to narrower confidence intervals on the IC_{50} and MPR parameters via the parameter covariance matrix of the 4PL fit. Lower prediction uncertainty at previously tested concentrations shifts the acquisition function's exploration-exploitation balance toward regions that genuinely require additional data, improving the information gain per iteration. The combination of reduced bias and reduced variance is expected to decrease the average number of iterations to convergence, particularly for the IC_{50} objective where the 30 % CI width criterion is sensitive to measurement noise.

3.6.5. Summary of Closed-Loop-Platform

The integrated closed-loop platform described in this chapter combines Bayesian optimization-guided dose-response characterization with automated beating pre-screening for iPSC-derived cardiac spheroids. Each 384-well plate screens up to four substances in parallel, with five adaptively selected concentrations and 16 replicates per concentration. A pre-treatment beating assessment (10 FPS, 7.5 s per well, 75 frames) classifies wells as active or excluded based on a minimum threshold of two detected beats, and the exclusion is applied analytically to the viability statistics without discarding raw data. The Bayesian optimizer fits a four-parameter logistic model after each iteration and selects new concentrations to minimize uncertainty around IC_{50} or MPR, with convergence typically achieved within 2–3 iterations. The platform operates without manual intervention from the initiation of the first iteration to the final convergence report, providing the optimizer with viability statistics that more accurately reflect the drug response of functionally active cardiomyocytes.

3.6.6. Discussion of Chapter 3.6

3.6.6.1. Adaptive Optimization as a Design Strategy

The implementation of Bayesian optimization in this work replaces the traditional fixed dilution series with an adaptive, data-driven design. Instead of sampling concentrations based on investigator intuition, each experimental iteration updates a structured surrogate model of the dose-response curve and selects the next concentrations based on parameter uncertainty

The efficiency of this approach becomes clear when considering the structure of sigmoidal dose-response curves. Most information about IC_{50} is confined to the transition region, while plateau regions contribute little to parameter refinement. A fixed design must distribute points broadly without knowing where this region lies. The adaptive approach localizes the transition in the exploratory phase and subsequently concentrates sampling where it is most informative.

Importantly, the surrogate model used here is not a generic statistical approximation but a pharmacologically interpretable four-parameter logistic model. This allows objective-specific acquisition strategies for IC_{50} determination and maximal physiological range (MPR) estimation. The domain-informed modelling framework was central to the convergence observed across compounds.

3.6.6.2. IC_{50} and MPR as Distinct Optimization Targets

An important practical insight from implementation is that IC_{50} and MPR converge under different statistical constraints.

IC_{50} estimation benefits from high sensitivity of the 4PL model in the transition zone. Once this region is identified, relatively few well-placed data points substantially reduce uncertainty.

MPR estimation, however, depends on precise definition of the 90 % viability threshold, typically located in a flatter, high-viability region with greater biological variability. In this context, the beating-based well exclusion improved performance by removing systematically depressed signals from non-contractile spheroids. The reduction in deviation allowed more accurate threshold bracketing and accelerated convergence.

This distinction becomes particularly relevant for cardiac applications. In reperfusion injury modelling, identifying a safe upper concentration limit (MPR) is often more

clinically relevant than defining IC_{50}.[428] Therefore, precision in the high-viability region directly impacts translational utility.

3.6.6.3. MTT as Both Limitation and Advantage

The exclusive reliance on MTT as a readout imposes interpretative constraints, yet it also provides mechanistic relevance within cardiac pathophysiology.

MTT measures mitochondrial dehydrogenase activity rather than cell number alone.[429] In many systems this is considered a limitation; however, in cardiomyocytes, mitochondrial function is tightly coupled to contractility and survival. Ischemia and reperfusion injury primarily disrupt oxidative metabolism before complete structural loss occurs. Therefore, a decline in MTT signal reflects early metabolic dysfunction, not merely terminal cell death. Furthermore, myocardial contractility accounts for the majority (≈80–90 %) of cardiac ATP consumption under physiological conditions. Since excitation–contraction coupling is highly ATP-dependent, MTT provides a metabolically sensitive readout that more closely reflects early contractile impairment than assays focused exclusively on proliferation or late-stage viability.[182,430]

The epinephrine results illustrate both sides of this property. Increased MTT conversion under β-adrenergic stimulation reflects enhanced metabolic activity rather than proliferation. While this prevents strict interpretation as "viability," it accurately captures functional metabolic stimulation, a relevant physiological response.

Nonetheless, MTT cannot distinguish metabolic activation from cytotoxicity in all contexts, nor can it resolve structural alterations independent of mitochondrial activity. Orthogonal endpoints such as ATP luminescence, LDH release, or high-content imaging would strengthen mechanistic resolution.[429] The closed-loop framework is technically prepared to integrate such multi-objective readouts without redesigning the core control logic.

3.6.6.4. Scalability and Translational Perspective

The platform's efficiency is primarily biology-limited rather than hardware-limited, enabling throughput increases through interleaved scheduling. Reconfiguration toward multi-line testing is straightforward and would allow systematic comparison of donor-specific drug sensitivity.

This scalability directly leads to the next question addressed in this thesis: whether genotype-dependent variability can be detected within this automated framework.

The closed-loop system establishes reliable, reproducible concentration-response characterization. However, its translational value ultimately depends on its ability to discriminate biological differences between patient-derived lines. Chapter 6 therefore builds on the optimized platform to evaluate inter-line variability in drug response and to test whether adaptive screening can reveal genotype-specific pharmacodynamic behaviour in iPSC-derived cardiac spheroids.

3.7. Drug Evaluation

3.7.1. Effects of Lidocaine

Lidocaine is an amino-amide compound consisting of a lipophilic aromatic group connected via an amide linkage to a hydrophilic amine moiety (Figure 49). Functionally, lidocaine acts as a Class IB antiarrhythmic agent primarily targeting fast voltage-gated sodium channels. Its binding preference for the inactivated channel state results in use-dependent inhibition, meaning channels are preferentially blocked immediately following depolarization.

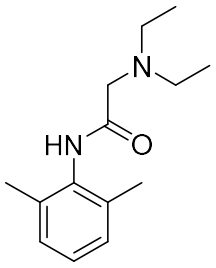

Figure 49: Chemical structure of Lidocaine drawn in ACS 1997 ChemDraw style. Lidocaine is an amino-amide consisting of a lipophilic aromatic ring connected via an amide linkage to a tertiary amine moiety. This structural organization underlies its membrane permeability and selective interaction with voltage-gated sodium channels.

Under physiological conditions, long diastolic intervals allow lidocaine to dissociate from the channel, resulting in minimal interference with normal cardiac rhythm. In ischemic or partially depolarized tissue, however, sodium channels spend extended periods in the inactivated state. This prolongs lidocaine binding, suppressing aberrant electrical activity and reducing the likelihood of premature action potentials by shortening the effective refractory period.

To determine the maximal physiological range (MPR) of Lidocaine, Bayesian optimization within the closed-loop platform was employed. Initial concentrations were selected based on published *in vitro* lidocaine data. Subsequent escalation and refinement concentrations were algorithmically proposed by the closed-loop controller.

Three optimization iterations were performed to achieve convergence on the MPR. The metabolic assay was conducted as described in Section 5.2.8 using cardiac spheroids at differentiation day 21.

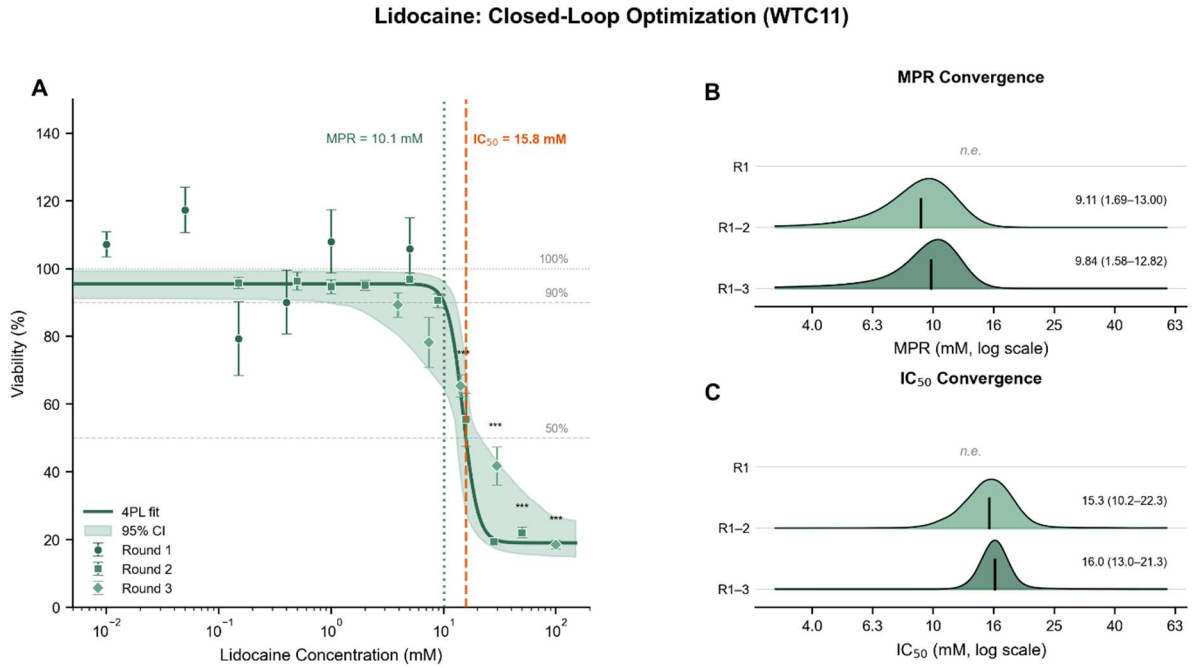

Figure 50: Closed-loop Bayesian optimisation of lidocaine cytotoxicity in cardiac spheroids. (A) Combined dose–response relationship across three sequential optimisation rounds. Lidocaine concentrations (mM, log scale) are plotted against cell viability (%, mean ± SEM). Round 1 (circles, dark green; 0.01–5 mM; n = 6–16 per concentration) explored sub-therapeutic concentrations and detected no significant toxicity. Round 2 (squares, medium green; 0.15–50 mM; n = 8 per concentration) extended the range into the cytotoxic regime, revealing significant reductions in viability at 15.81 mM and higher. Round 3 (diamonds, light green; 3.9–100 mM; n = 4–16 per concentration) refined the transition region. A four-parameter logistic (4PL) model fitted to the combined dataset (solid green line; shaded 95 % confidence interval) yielded an IC_{50} of 15.8 mM (orange dashed line) and a maximum permissible response (MPR) threshold of 10.1 mM at 90% viability (dark green dotted line). Horizontal reference lines indicate 100 %, 90 %, and 50 % viability. Significance markers denote Bonferroni-corrected one-sample t-tests versus 100 % viability (21 tests total; *p < 0.05, **p < 0.01, ***p < 0.001). (B) Convergence of the MPR estimate across cumulative optimisation rounds. Ridgeline density plots represent Monte Carlo–sampled posterior distributions (8,000 draws from parameter covariance) for the 4PL model fitted to Round 1 alone (R1), R1–2, and R1–3 cumulative datasets. The MPR was not estimable from R1 data alone. Vertical ticks indicate posterior medians; annotations show median and 95 % credible intervals. Panels B and C share a common x-axis scale. (C) Convergence of the IC_{50} estimate across cumulative optimisation rounds, displayed as in Panel B. The IC_{50} was not estimable from R1 data alone. Incorporation of Round 2 enabled initial estimation (median 15.3 mM; 95 % CI: 10.2–22.3 mM), which was further refined after Round 3 (median 16.0 mM; 95 % CI: 13.0–21.3 mM). Statistical comparisons were performed using one-sample t-tests versus 100 % viability with Bonferroni correction for 21 comparisons.

As shown in Figure 50, closed-loop Bayesian optimisation required three sequential rounds to characterise the cytotoxic profile of lidocaine in WTC11 hiPSC-derived cardiac spheroids.

In Round 1 (0.01–5 mM; n = 6–16 per concentration), all tested concentrations yielded viability values within the non-toxic range (79.3–117.3 %), and none differed significantly from the 100 % control after Bonferroni correction. No concentration-dependent trend was observed, indicating that the entire explored range lay below the toxicity threshold.

Round 2 expanded the range to 0.15–50 mM. This round identified the transition zone from minimal to pronounced toxicity. Concentrations up to 8.89 mM maintained viability near or above 90 %, whereas marked reductions were observed at 15.81 mM and higher. Significant decreases in viability were detected at 15.81 mM and above, with progressively severe reductions at 28.12 mM and 50 mM. The abrupt transition between 8.89 mM and 28.12 mM suggested a steep dose–response relationship (Figure 50, A).

Round 3 (3.9–100 mM) refined this transition region. Viability declined progressively across the tested range, with significant reductions confirmed at 14.2 mM and higher concentrations. Lower concentrations within this round (3.9 and 7.4 mM) remained near the non-toxic plateau, consistent with proximity to the upper boundary of the permissible range.

A four-parameter logistic (4PL) model fitted to the combined dataset across all three rounds yielded an estimated IC_{50} of 15.8 mM and a maximum permissible response (MPR) threshold of 10.1 mM at 90 % viability. The fitted Hill coefficient (6.6) indicated a narrow concentration window between minimal and maximal toxicity, consistent with the sharp transition observed experimentally.

Convergence analysis demonstrated that Round 1 alone was insufficient to estimate either IC_{50} or MPR. Incorporation of Round 2 enabled initial parameter estimation, while Round 3 reduced uncertainty and stabilised the IC_{50} estimate (median 16.0 mM; 95 % CI: 13.0–21.3 mM) (Figure 50, B, C). The MPR estimate remained comparatively broader, reflecting its position on the upper shoulder of the dose–response curve, where small changes in slope produce larger concentration shifts.

Across all 21 tested concentrations, significant reductions in viability were confined to the mid- and high-millimolar range, while sub-5 mM concentrations were consistently non-toxic. The estimated IC_{50} of 15.8 mM lies well above clinically relevant plasma concentrations of lidocaine (6–25 μM for antiarrhythmic use), indicating a wide safety margin under therapeutic conditions. The steep dose–response profile observed here is consistent with previously reported variability in lidocaine IC_{50} estimation across platforms, particularly when the transition region is sparsely sampled.[431]

Taken together, these results demonstrate that the closed-loop framework successfully identified the cytotoxic transition region for lidocaine, progressively refined parameter uncertainty across rounds, and converged on stable pharmacological estimates of IC_{50} and MPR.

To evaluate the functional effects of lidocaine on cardiac spheroids, intracellular calcium dynamics were monitored using Fluo-4 AM staining as described in Section 5.2.6.2. After staining, spheroids were transferred to fresh maintenance medium and allowed to equilibrate for one hour to minimize mechanical preconditioning effects.
Baseline recordings were obtained using 30-second time-lapse acquisitions with 488 nm excitation on the Leica LED imaging system. Following baseline measurement, spheroids in the treatment group were exposed to lidocaine dissolved in maintenance medium (9.8 mM) and incubated for one hour. Subsequent recordings were collected at 1, 2, and 3 hours post treatment.
Due to dye washout over extended incubation, calcium imaging at 20 and 72 hours was not feasible. At these later time points, contractile activity was assessed via brightfield imaging using identical acquisition settings.

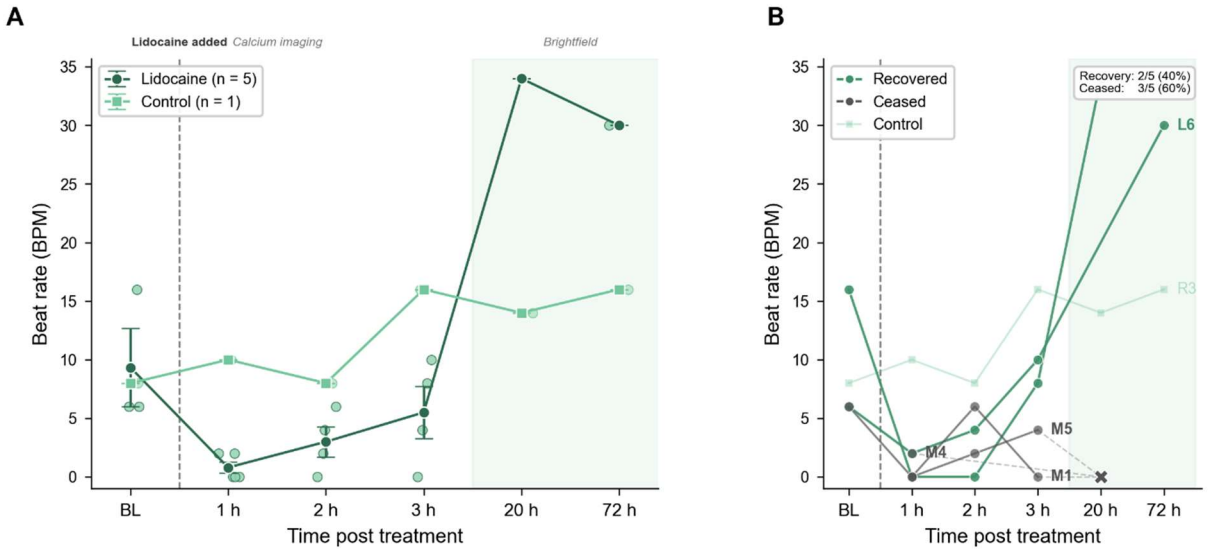

Figure 51: Effect of 9.8 mM lidocaine on cardiac spheroid beat rate over 72 hours. (A) Group-level beat rate trajectory following administration of 9.8 mM lidocaine. Data are shown as mean ± SEM for the lidocaine-treated group (n = 5 wells at baseline; individual wells overlaid as jittered points) and as individual measurements for the untreated control well (n = 1). The dashed vertical line indicates the time of lidocaine addition. Beat rate was quantified by calcium imaging from baseline to 3 h post-treatment and by brightfield video analysis at 20 h and 72 h (shaded region). (B) Individual well trajectories for the five lidocaine-treated wells, coloured by outcome: recovered (wells that resumed spontaneous beating by 20–72 h post-treatment; green) and ceased (wells with no detectable beating at subsequent time points; grey). Dashed lines terminating with an "X" symbol indicate extrapolated cessation of beating activity. The untreated control well (R3) is shown as a semi-transparent reference trace. Inset text summarises the observed outcomes (2/5 recovered, 40 %; 3/5 ceased, 60 %).

The effect of lidocaine on cardiac spheroid contractility is shown in Figure 51. At baseline, three of five treated wells exhibited spontaneous beating, with a mean beat rate of 9.3 ± 3.3 BPM (mean ± SEM). The control well beat at 8.0 BPM. Within 1 hour of lidocaine administration, beating activity was markedly suppressed in the treated group, declining to a mean of 0.8 ± 0.5 BPM (n = 5 wells). Three treated wells (M1, M4, M5) showed no detectable beating at this timepoint, while two wells (L1 and L6)

exhibited minimal residual activity (2.0 BPM each). The control well maintained stable activity (10.0 BPM at 1 h).

Partial recovery was observed over the subsequent hours. At 2 h post-treatment, the group mean increased to 3.0 ± 1.3 BPM (n = 4 wells with detectable beating), and at 3 h to 5.5 ± 2.2 BPM (n = 4). Wells L1 and L6 showed the most pronounced recovery (8.0 and 10.0 BPM at 3 h, respectively). Well M1 exhibited transient activity at 2 h (6.0 BPM) but ceased beating again by 3 h.

At 20 h post-treatment, assessed by brightfield video analysis, well L1 demonstrated robust beating at 34.0 BPM, exceeding both its baseline rate (16.0 BPM) and the concurrent control rate (14.0 BPM). At 72 h, well L6 exhibited sustained recovery at 30.0 BPM, above its baseline value of 6.0 BPM. The remaining three treated wells (M1, M4, M5) showed no detectable beating beyond 3 h and were classified as ceased (Figure 51, B). The control well maintained stable activity across all timepoints (range: 8.0–16.0 BPM).

Overall, 2 of 5 lidocaine-treated wells (40 %) recovered spontaneous beating within 20–72 hours, whereas 3 of 5 wells (60 %) exhibited persistent cessation of contractile activity. Given the limited sample size (n = 5 treated wells; n = 1 control), results are presented descriptively without formal statistical testing.

3.7.2. Effects of Epinephrine

Epinephrine (adrenaline) is a catecholamine characterized by a catechol ring linked to an ethanolamine side chain with N-methyl substitution, distinguishing it structurally from norepinephrine. It naturally occurs as the L-isomer, which exhibits substantially higher biological potency than its D-enantiomer (Figure 52). [432]

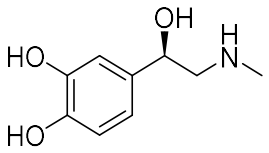

Figure 52: Molecular structure of epinephrine (L-isomer) rendered in ACS 1997 ChemDraw format, highlighting the catechol ring, ethanolamine side chain, and N-methylated amine.

Epinepehrine is commonly used in cardiac treatment, to counter cardiac arrest or generally boost contractility. Epinephrine acts as a non-selective agonist binding to α, as well as β adrenergic receptors. Its effects varied based on effector binding, after binding the α-recpetor vasoconstriction happens constricting peripheral vessels and thus raising the coronary perfusion presure.[433]

Pharmacologically, epinephrine acts as a non-selective agonist at α- and β-adrenergic receptors. Activation of α-receptors induces peripheral vasoconstriction, thereby increasing coronary perfusion pressure. β-receptor stimulation enhances sinoatrial node activity (positive chronotropy), increases contractile force via augmented Ca^{2+} influx (positive inotropy), and accelerates atrioventricular conduction (positive dromotropy). While these effects can restore spontaneous circulation during cardiac arrest, the associated increase in energy demand may exacerbate injury in metabolically compromised tissue, such as during ischemia.[434–436]

To determine a stimulatory yet physiologically tolerable concentration range in cardiac spheroids, a dose-response experiment was conducted. Cardiac spheroids at differentiation day 21 were treated with increasing concentrations of epinephrine and incubated for 24 hours prior to MTT analysis (5.2.8). When the initial concentration screen did not yield a clearly stimulatory response, a closed-loop Bayesian optimization tool (5.2.8.5) was employed to propose refined concentration ranges for a second iteration.

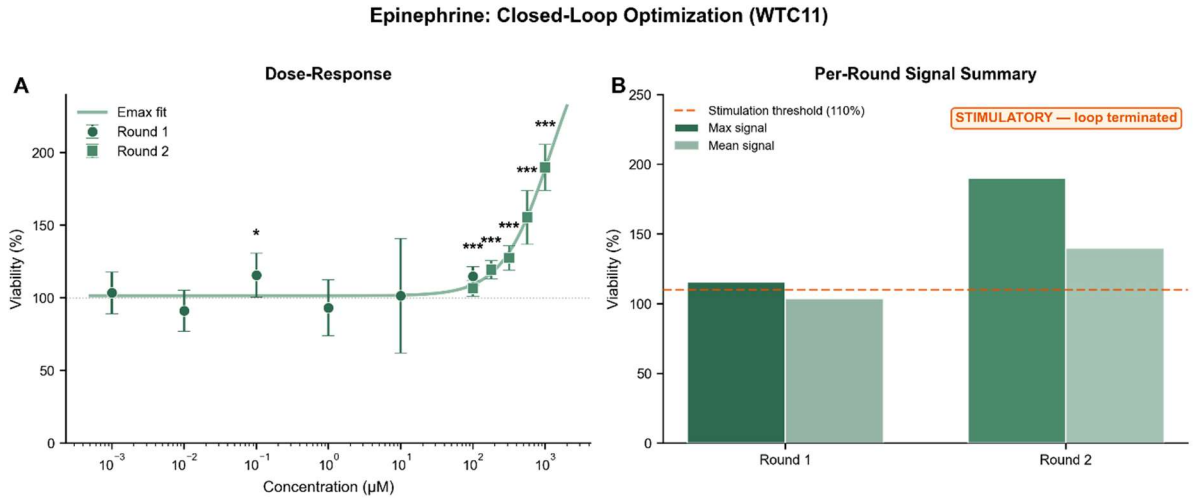

Figure 53: Closed-loop Bayesian optimisation of epinephrine concentration in WTC11 hiPSC-derived cardiac spheroids assessed by MTT viability assay. (A) Dose–response curve across two sequential optimisation rounds. Cardiac spheroids were exposed to epinephrine at concentrations spanning 0.001–1000 µM. Round 1 concentrations (0.001–100 µM; n = 8–13 per concentration) are shown as circles (dark green), and Round 2 concentrations (100–1000 µM; n = 16 per concentration) as squares (medium green). The solid curve represents a sigmoidal Emax model fit (E_0 = 101.5 %, Emax = 300.0 %, EC_{50} = 1200.7 µM, Hill coefficient n = 1.29). Significance markers indicate one-sample t-tests versus 100 % control with Bonferroni correction across 11 tested concentrations (* p < 0.05, ** p < 0.01, *** p < 0.001). At the overlapping 100 µM concentration, the marker reflects the stronger statistical result. Error bars represent ± SD. (B) Per-round signal summary. Dark bars indicate the maximum MTT signal observed within each round, and lighter bars (α = 0.5) indicate the mean signal across all concentrations within that round. The dashed orange line marks the predefined stimulation threshold (110 %). In Round 1, the maximum signal reached 115.7 % (mean: 103.3 %), with 2 of 6 concentrations exceeding the threshold. In Round 2, the maximum signal increased to 189.9 % (mean: 139.8 %), with 4 of 5 concentrations exceeding the threshold. Based on these results, the optimisation algorithm classified the response as stimulatory and terminated the loop after Round 2. Data are presented as mean ± SD. Statistical comparisons were performed using one-sample t-tests versus 100% with Bonferroni correction (11 tests total).

As shown in Figure 53, epinephrine did not induce cytotoxicity in WTC11 hiPSC-derived cardiac spheroids across the tested concentration range but instead produced a concentration-dependent increase in metabolic activity as measured by MTT assay.
In round 1, epinephrine was tested across 0.001–100 μM (n = 8–13 per concentration). Viability values fluctuated around the 100% control baseline (range: 91.2–115.7 %; mean: 103.3 %), with no evidence of concentration-dependent inhibition. Two concentrations (0.1 μM and 100 μM) showed statistically significant elevations above 100 % following Bonferroni correction; however, these deviations reflected increased MTT signal rather than reduced viability.
Given the elevated signal observed at 100 μM, round 2 explored a higher concentration range (100–1000 μM; n = 16 per concentration). Across this range, MTT signal increased progressively, reaching 189.9 ± 15.8 % at 1000 μM. All round 2 concentrations were significantly elevated above the 100 % control baseline after correction for multiple testing (Figure 53, A). The overall response was well described by a sigmoidal Emax model (maximum achievable effect) (E_0 = 101.5 %, Emax = 300.0 %, EC_{50} = 1200.7 μM, Hill coefficient = 1.29), although a plateau was not reached within the tested range.
Across both rounds, 7 of 11 tested concentrations were significantly elevated relative to control. At no concentration was a reduction below baseline observed (Figure 53, B). The response pattern was therefore classified as stimulatory by the optimisation algorithm, and the loop was terminated after round 2.
Taken together, these results demonstrate that epinephrine induces robust metabolic stimulation without evidence of cytotoxicity in cardiac spheroids across the tested concentration range. The closed-loop system appropriately identified this non-cytotoxic, stimulatory response profile and terminated optimisation once the pattern was confirmed.
Following confirmation of a stimulatory metabolic effect, the functional impact of Epinephrine on the cardiac contraction cycle was evaluated.
Cardiac spheroids at differentiation day 21 were first recorded under baseline conditions using 30-second time-lapse acquisitions at 10 frames per second to confirm stable spontaneous beating. Spheroids were then divided into two groups: a treatment group receiving epinephrine at the previously determined stimulatory concentration 1000 μM, and a control group receiving fresh maintenance medium.
Contractile activity was recorded over a 20-minute period, with 30-second time-lapse acquisitions obtained every 5 minutes. Imaging was performed in brightfield mode

using the Leica LED microscope. Beating dynamics were quantified via pixel-based motion tracking analysis (5.2.7.1).

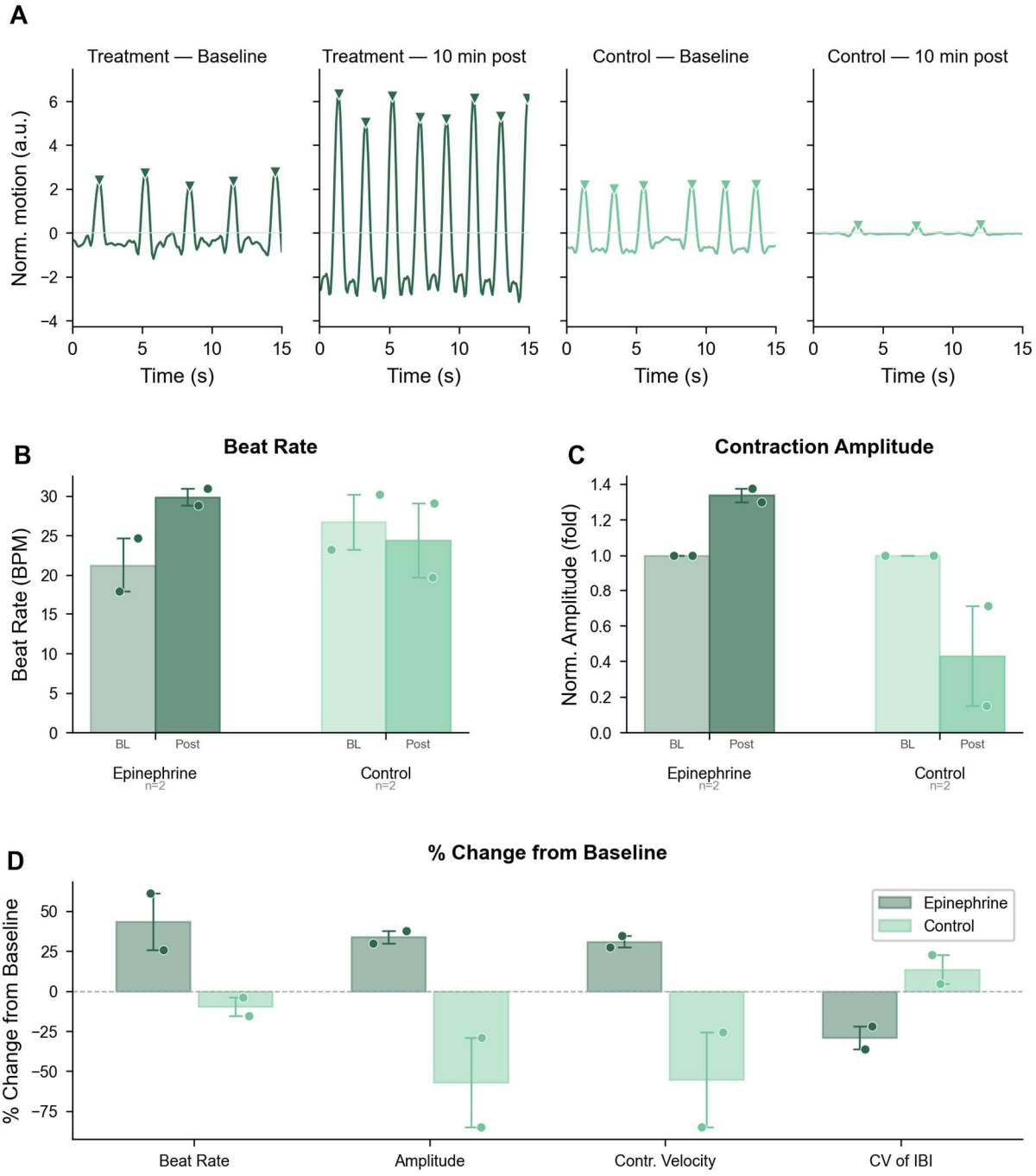

Figure 54: Effects of epinephrine on contractile function in cardiac spheroids. (A) Representative motion index traces derived from brightfield video recordings of one epinephrine-treated spheroid (1000 µM epinephrine) and one vehicle control spheroid at baseline and 10 minutes post-treatment. Motion signals were bandpass-filtered and Savitzky–Golay smoothed prior to peak detection. Inverted triangles indicate detected contraction peaks. Traces are normalised to the baseline standard deviation of each spheroid to facilitate comparison of relative amplitude changes within each sample. (B) Beat rate (beats per minute) at baseline (BL) and 10 minutes post-treatment (Post) for epinephrine-treated (n = 2) and control (n = 2) spheroids. Bars represent group means; error bars indicate ± SEM; individual spheroid values are overlaid. (C) Contraction amplitude normalised to each spheroid's own baseline (fold-change), displayed as in (B). (D) Percentage change from baseline for four contractile parameters: beat rate, contraction amplitude, contraction velocity, and coefficient of variation of the inter-beat interval (CV IBI). Bars represent group means ± SEM with individual data points overlaid.

Representative motion index traces demonstrate increased beat frequency and contraction amplitude in the epinephrine-treated spheroid, whereas the control spheroid showed minimal change over the same period (Figure 54, A).
Quantitative analysis revealed a mean beat rate increase of +43.3 % from baseline in the treatment group, compared with a −9.5 % change in controls (Figure 54 B, D). Contraction amplitude (normalised to each spheroid's own baseline) increased by +33.8% in treated spheroids and decreased by −57.0 % in controls (Figure 54 C, D). Contraction velocity showed a similar pattern, increasing by +31.0 % in treated spheroids and decreasing by −55.2 % in controls. Beat-to-beat variability, quantified as the coefficient of variation of the inter-beat interval (CV IBI), decreased by −29.1 % in the treatment group and increased by +13.6 % in controls.
Across all four contractile parameters, effect sizes (Hedges' g) were large ($|g| > 1.5$), consistently favouring the epinephrine-treated group. However, due to the small sample size (n = 2 per group), no statistically significant differences were detected following permutation testing with correction for multiple comparisons.

Overall, epinephrine exposure was associated with increased beat rate, enhanced contraction amplitude and velocity, and reduced beat-to-beat variability relative to vehicle-treated controls in this pilot experiment.

3.7.3. Patient Specific Drug Response

Cardiac pharmacotherapy is characterized by a narrow physiological safety window, while interindividual variability in ion channel composition and genetic background strongly influences drug response. This variability makes individualized dose verification critical for maximizing therapeutic benefit while minimizing adverse effects.
A robust *in vitro* cardiac disease model should therefore be capable of reflecting genotype-dependent drug sensitivity. To evaluate this, drug response testing was performed on cardiac spheroids derived from two genetically distinct iPSC lines: WTC11, originating from a healthy 30-year-old male donor, and HD11.
Both lines underwent identical cardiac differentiation and were used for testing after confirmation of stable spontaneous beating at differentiation day 21. Drug response experiments were conducted using the automated closed-loop Bio.MAT/Bio.LAB screening platform with a single optimization iteration.
Three pharmacological agents were evaluated. Concentrations previously identified as functionally relevant in WTC11 derived cardiac spheroids were applied to HD11

derived cardiac spheroids to determine whether comparable effects could be reproduced. The tested compounds included lidocaine, epinephrine, and verapamil.

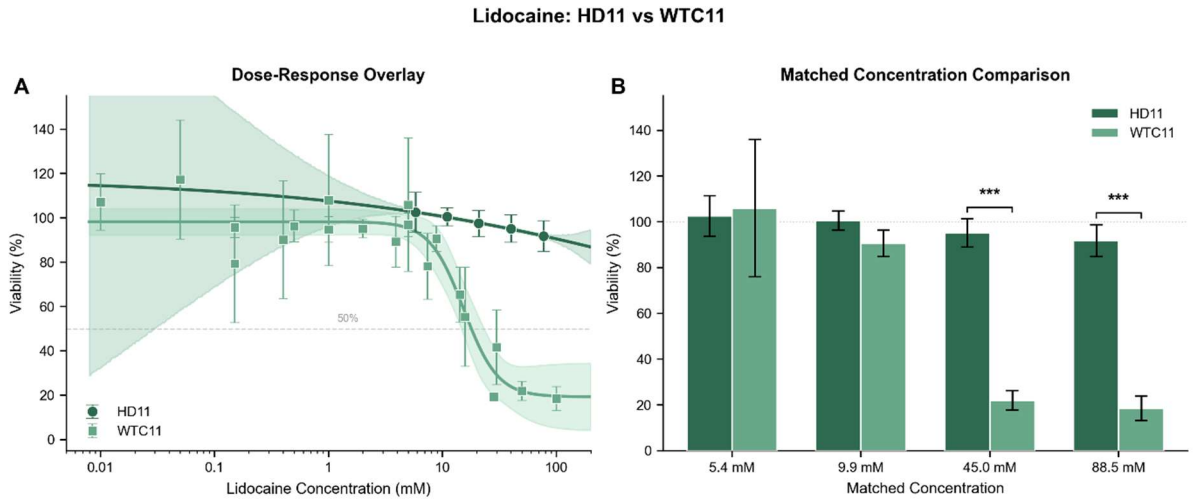

Figure 55: Lidocaine dose–response comparison between HD11 and WTC11 hiPSC-derived cardiac spheroids. (A) Overlay of lidocaine dose–response curves for HD11 (dark green circles) and WTC11 (light green squares) cardiomyocytes. Cell viability (%) is plotted against lidocaine concentration (mM, log scale). Solid lines represent four-parameter logistic (4PL) model fits; shaded regions indicate 95 % confidence intervals. HD11 cardiac spheroids maintained viability above 91 % across the tested range (5.8–76.9 mM), exhibiting a flat dose–response profile with no estimable IC_{50} within this range. In contrast, WTC11 cardiac spheroids displayed a sigmoidal dose–response curve with an estimated IC_{50} of approximately 15.4 mM (Hill coefficient = 2.91). The dashed horizontal line indicates 50 % viability. HD11 data derive from a single experimental iteration (n = 2–8 wells per concentration), whereas WTC11 data are pooled from three optimisation rounds (n = 4–16 wells per concentration). (B) Matched-concentration comparison between HD11 (dark green) and WTC11 (light green) at four approximate overlapping concentration points. Bars represent mean ± SD. Statistical significance was assessed using Welch's two-tailed t-test with Bonferroni correction for four comparisons. At higher concentrations (45.0 mM and 88.5 mM), HD11 cardiac spheroids retained >91 % viability, whereas WTC11 derived cardiac viability fell below 23% (***p_bonf < 0.001). No significant difference between cell lines was detected at the two lower matched concentrations (5.4 mM and 9.9 mM; p_bonf > 0.05). Data are presented as mean ± SD.

As shown in Figure 55, lidocaine produced distinct dose–response profiles in HD11 and WTC11 hiPSC-derived cardiac spheroids.

HD11 cardiac spheroids maintained viability above 90 % across the entire tested concentration range (5.8–76.9 mM), with the lowest observed viability of 91.8 ± 7.0 % at 76.9 mM. The dose–response profile was flat, and no IC_{50} could be estimated within the experimental range.

In contrast, WTC11 cardiac spheroids exhibited a sigmoidal dose–response curve. Viability remained above 90 % up to approximately 5 mM and declined steeply at higher concentrations, with an estimated IC_{50} of 15.4 mM. At concentrations above 28 mM, viability reached a lower plateau of approximately 18–22 % (Figure 55).

Comparison at four matched concentrations confirmed concentration-dependent divergence between cell lines. At 5.4 mM and 9.9 mM, no statistically significant inter-line difference was detected after Bonferroni correction. At 45.0 mM, HD11 viability was 95.1 ± 6.2 %, whereas WTC11 viability was 22.0 ± 4.3 % (p_bonf < 0.001). At 88.5

mM, HD11 viability was 91.8 ± 7.0 % compared with 18.5 ± 5.4% for WTC11 (p_bonf < 0.001) (Figure 55, B).

These data demonstrate a marked difference in lidocaine-induced cytotoxicity between HD11 and WTC11 cardiac spheroids, with HD11 derived spheroids maintaining high viability across concentrations that produced pronounced toxicity in WTC11 derived spheroids.

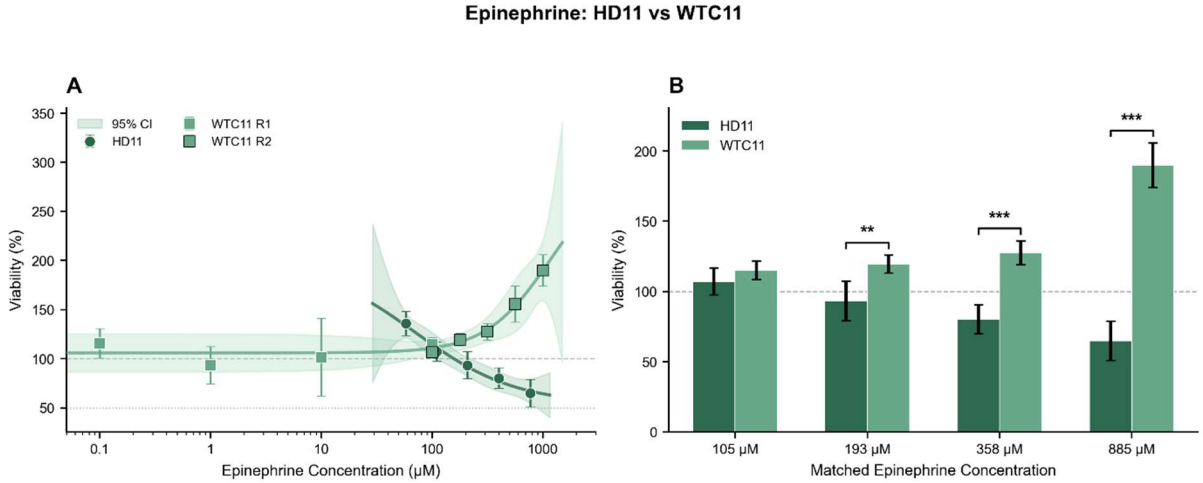

Figure 56: Divergent epinephrine dose–response profiles in HD11 and WTC11 iPSC-derived cardiac spheroids. (A) Dose–response curves for HD11 cardiac spheroids (dark green circles) and WTC11 cardiac spheroids (light green squares) showing cell viability (%) as a function of epinephrine concentration (0.1–1000 µM, log scale). Solid lines represent four-parameter logistic (4PL) fits; shaded regions indicate 95 % confidence intervals. HD11 cardiac spheroids exhibited a monotonic decrease in viability with increasing concentration, whereas WTC11 cardiac spheroids displayed a progressive increase across the tested range, resulting in opposing response trajectories. WTC11 cardiac spheroids data derive from two independent experimental runs (R1 and R2); only concentrations ≥ 0.1 µM are shown to match the HD11 cardiac spheroids domain. The dashed horizontal line indicates 100 % (vehicle control), and the dotted line indicates 50 % viability. Error bars represent ± SD. (B) Matched-concentration comparison at four overlapping concentrations (105, 193, 358, and 885 µM). Bars represent mean ± SD for HD11 (dark green) and WTC11 (light green). Statistical significance was assessed using Welch's t-test with Bonferroni correction for four comparisons (**p < 0.01, ***p < 0.001). The 105 µM comparison was not significant. HD11 data derive from a single experimental iteration (n = 7–8 per concentration). WTC11 data are pooled from two independent runs (n = 8–16 per concentration).

As shown in Figure 56, epinephrine produced opposing dose–response profiles in HD11 and WTC11 iPSC-derived cardiac spheroids.

In HD11 cardiac spheroids, viability decreased progressively with increasing epinephrine concentration, declining from 135.9 % at 58 µM to 64.9 % at 885 µM (Figure 56, A). The fitted four-parameter logistic (4PL) model displayed a descending sigmoidal trajectory across the tested range.

In contrast, WTC11 cardiac spheroids exhibited a concentration-dependent increase in MTT signal, rising from near-baseline values (103.5 % at low nanomolar concentration) to 189.9 % at 1000 µM (Figure 56, A). The 4PL fit demonstrated an ascending sigmoidal profile across the shared concentration range.

Direct comparison at four matched concentrations confirmed progressive divergence between cell lines. At 105 µM, no statistically significant difference was detected after

Bonferroni correction (p_adj = 0.263). At 193 µM, the difference reached statistical significance (p_adj = 0.0085). At 358 µM and 885 µM, inter-line differences were highly significant (p_adj = 5.02×10^{-7} and 7.39×10^{-12}, respectively). The magnitude of separation increased monotonically with concentration, reaching a 125 percentage-point difference at 885 µM (Figure 56, B).

Across all matched concentrations, HD11 cardiac spheroid viability was lower than WTC11 cardiac spheroid viability, with the direction and magnitude of divergence becoming more pronounced at higher concentrations.

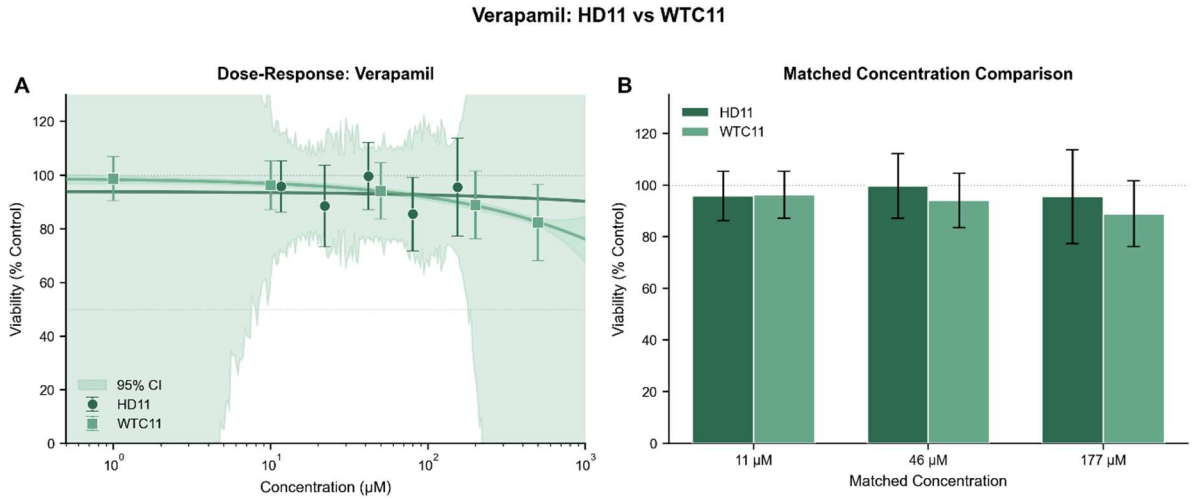

Figure 57: Verapamil dose–response comparison between HD11 and WTC11 iPSC-derived cardiac spheroids. (A) Overlay of verapamil dose–response curves for HD11 (dark green circles) and WTC11 (light green squares) cardiac spheroids. Cell viability (%) is plotted against verapamil concentration (µM, log scale). Solid lines represent four-parameter logistic (4PL) fits; shaded regions indicate 95% confidence intervals. Neither cell line reached an IC_{50} within the tested range and both were classified as BEYOND_RANGE. HD11 cardiac spheroid viability ranged from 85.5–99.7 % across 11.6–153.8 µM, while WTC11 cardiac spheroid viability ranged from 82.4–98.7 % across 1–500 µM. Dashed horizontal lines indicate 100 % and 50 % viability reference levels. (B) Matched-concentration comparison between HD11 and WTC11 cardiac spheroids at three overlapping concentrations (11, 46, and 177 µM). Bars represent mean ± SD. No statistically significant differences were detected between cell lines at any matched concentration following Bonferroni correction for three comparisons (all p_adj ≥ 0.986; Welch's t-test). HD11 data derive from a single experimental iteration (n = 5–8 spheroids per concentration). WTC11 data correspond to Round 3 of the optimisation protocol (n = 8–16 spheroids per concentration).

As shown in Figure 57, verapamil did not induce marked cytotoxicity in either HD11 or WTC11 iPSC-derived cardiac spheroids within the tested concentration ranges.

HD11 cardiac spheroid viability ranged from 85.5 % to 99.7 % across 11.6–153.8 µM (n = 5–8 per concentration) (Figure 57, A). WTC11 cardiac spheroid viability ranged from 82.4 % to 98.7 % across 1–500 µM (n = 8–16 per concentration). In both cell lines, no IC_{50} could be estimated within the tested range, and both were classified as BEYOND_RANGE.

Comparison at three matched concentrations (11, 46, and 177 µM) revealed no statistically significant differences between HD11 and WTC11 following Bonferroni correction (Figure 57, B). At 11 µM, HD11 viability was 95.8 ± 9.5 % (n = 7) compared

with 96.3 ± 9.1 % for WTC11 (n = 9; p_adj = 1.000). At 46 µM, HD11 viability was 99.7 ± 12.5 % (n = 8) compared with 94.1 ± 10.5 % for WTC11 (n = 10; p_adj = 0.986). At 177 µM, HD11 viability was 95.5 ± 18.2 % (n = 7) compared with 88.9 ± 12.7 % for WTC11 (n = 8; p_adj = 1.000).
Across all matched concentrations, viability values remained above 85 % in both cell lines, and no concentration-dependent inter-line divergence was observed.

3.7.4. Discussion of Chapter 3.7

Cardiac pharmacotherapy operates within a narrow therapeutic window, and interindividual variability in ion channel expression, receptor signalling, and metabolic regulation substantially influences drug response.[437,438] A physiologically relevant *in vitro* cardiac model should therefore not only reproduce general electrophysiological and metabolic phenotypes but also reflect genotype-dependent pharmacodynamic variability.
To enable direct genotype comparison, concentration ranges previously identified as functionally relevant in WTC11-derived cardiac spheroids were applied to HD11-derived cardiac spheroids. This strategy prioritized cross-line comparability over independent dose-range optimization and was designed to evaluate whether pharmacological responses established in one genetic background would translate to another. Although this approach does not include full optimization of the HD11 therapeutic window, it allows assessment of genotype-dependent differences under standardized dosing conditions.
Notably, the two iPSC lines originate from donors of different biological sex, introducing an additional layer of biological variability that may influence ion channel composition, adrenergic signalling, and electrophysiological properties.[439] While the present study does not isolate sex-specific mechanisms, the observed differences highlight the importance of incorporating genetic and sex diversity into cardiac *in vitro* modelling frameworks.

3.7.4.1. Lidocaine: Differential Sodium Channel Sensitivity

The most striking genotype-dependent divergence was observed in response to Lidocaine. WTC11 cardiac spheroids displayed a clear dose-dependent reduction in metabolic viability, enabling IC_{50} estimation and identification of a defined maximal physiological range. In contrast, HD11 cardiac spheroids remained largely resistant

across the tested concentration range, with viability remaining near baseline even at concentrations that were strongly inhibitory in WTC11.

This separation suggests fundamental differences in sodium channel sensitivity, channel expression levels, or membrane excitability between the two lines. Lidocaine preferentially binds to inactivated Nav1.5 channels in a use-dependent manner.[440] Differences in resting membrane potential, action potential duration, sodium channel density, or channel inactivation kinetics could therefore significantly alter pharmacological response.[441] The flat response profile in HD11 indicates reduced functional sensitivity rather than experimental variability.

Importantly, this difference was not subtle, with high-dose lidocaine reducing WTC11 viability to approximately 20 % while HD11 retained near-baseline metabolic activity. Such magnitude differences are unlikely to reflect random biological noise and instead suggest genotype-dependent electrophysiological properties. The platform therefore demonstrates the capacity to detect robust inter-line pharmacodynamic heterogeneity.

3.7.4.2. Epinephrine: Divergent Adrenergic Signalling

Epinephrine exposure revealed an equal divergence in the opposite direction. While WTC11 spheroids exhibited strong metabolic stimulation at higher concentrations, consistent with β-adrenergic enhancement of mitochondrial activity, HD11 spheroids displayed a biphasic response, with stimulation at lower concentrations followed by dose-dependent decline at higher doses.[442]

This pattern may reflect differential β_1 versus β_2 adrenergic receptor signalling balance.[443] β-adrenergic receptor subtype expression and downstream coupling efficiency are known to vary across iPSC-CM line.[444,445] High-dose β_1-dominant signalling is associated with pro-apoptotic calcium-dependent pathways, whereas β_2-associated signalling may promote metabolic activation and survival signalling.[446–448] Although receptor subtype expression was not directly measured, the concentration-dependent divergence observed here suggests differential adrenergic signalling dynamics between the two genetic backgrounds.

3.7.4.3. Verapamil: Conserved Calcium Channel Sensitivity

Both lines exhibited comparable responses to verapamil across the tested concentration range. L-type calcium channels are essential for excitation–contraction coupling and are robustly expressed across cardiomyocyte differentiation stages.[174,449,450] The absence of significant inter-line differences for this target suggests

that CaV1.2-mediated pharmacology is relatively conserved in these spheroids. Importantly, this conserved response serves as an internal control, indicating that the differential sensitivity observed for lidocaine and epinephrine is target-specific rather than reflective of global differences in spheroid viability or assay performance.

3.7.4.4. Implications for Precision Cardiac Modelling

The differential responses to Lidocaine and Epinephrine, accompanied by the conserved response to verapamil, indicate that the model reveals drug-specific genotype-dependent sensitivity patterns rather than general variability.

These findings carry important implications. Firstly, they support the biological robustness of the system, as pharmacodynamic differences emerge selectively in a target-specific manner rather than appearing as random variability. Secondly, they demonstrate that the closed-loop screening platform can detect concentration-dependent divergence between genotypes without requiring prior assumptions about expected behaviour. Thirdly, they highlight the potential of this framework for personalized pharmacological profiling within a controlled *in vitro* setting.

While extrapolation to clinical prediction must remain cautious, the ability to detect profound inter-line differences in sodium channel and adrenergic responsiveness underscores the translational relevance of patient-specific iPSC-derived cardiac spheroids. These findings position the platform not only as a mechanistic research tool but also as a potential framework for individualized cardiac drug sensitivity assessment.

Across ischemia–reperfusion modelling, pharmacological interrogation, and genotype-dependent drug response testing, the presented system demonstrates controlled mechanistic induction, multi-level phenotypic validation, and reproducible pharmacodynamic differentiation. The ability to capture both conserved and divergent drug responses across genetic backgrounds reinforces its biological fidelity and experimental robustness. Within the constraints of static 3D culture, the platform integrates temporal precision, functional readouts, and adaptive concentration optimization to provide a scalable framework for mechanistic cardiotoxicity testing and exploratory precision pharmacology.

4. Final Discussion

4.1. Addressing the Central Challenge

Ischemia–reperfusion injury (IRI) remains one of the most complex and therapeutically resistant pathologies in cardiovascular medicine.[451] Despite decades of investigation, clinical strategies targeting single molecular pathways have repeatedly failed to prevent reperfusion-associated damage.[452] A central reason lies in the multifactorial and temporally dynamic nature of IRI, where oxygen deprivation, metabolic collapse, calcium dysregulation, mitochondrial destabilization, and structural remodelling occur in tightly coupled sequence rather than isolation.[124]

Additionally, many *in vitro* systems lack either temporal precision, multicellular complexity, or scalability for systematic pharmacological interrogation.[399,452,453] This thesis therefore aimed to establish a temporally controlled, mechanistically integrated, and scalable *in vitro* model capable of reconstructing key sequential phases of reperfusion injury while enabling adaptive drug evaluation and genotype-dependent analysis.

4.2. Core Contribution I – Mechanistic Reconstruction of the Reperfusion Cascade

A central contribution of this work is the establishment of a temporally tuneable three-dimensional IRI model that reconstructs the sequential cascade of ischemic priming, acute reperfusion collapse, and delayed remodelling.[454]

Rather than modelling hypoxia as a prolonged static condition, rapid oxygen deprivation was achieved via direct nitrogen flux, enabling precise control over ischemic onset and immediate reoxygenation. This temporal accuracy is critical, as *in vivo* ischemic injury often develops within minutes rather than extended incubation periods.[455] The addition of Tyrode solution allowed synchronized nutrient deprivation and defined metabolic restoration upon reperfusion, thereby modelling complete ischemia rather than isolated hypoxia. Controlled media exchange further introduced a reproducible mechanical shear-stress imitating flow re-entry.

Importantly, the system does not merely induce hypoxic stress, it reproduces the injury cascade. During ischemic priming, elevated intracellular calcium baseline levels were observed, consistent with ATP depletion and impaired calcium pump function.[456] Upon reperfusion, calcium homeostasis collapsed rapidly, with loss of coordinated transients and functional arrest. This acute calcium signature closely mirrors *in vivo*

reperfusion pathology, where mitochondrial reactivation, ROS generation, and mPTP opening combine to drive calcium overload.[457,458]

Beyond acute functional collapse, the model captured the delayed metabolic collapse characteristic of reperfusion-specific injury.[459] Combined oxygen and nutrient deprivation resulted in progressive viability decline reaching a low point at 72 hours, followed by partial stabilization, a pattern distinct from isolated hypoxia. Structural analysis further demonstrated selective disintegration of cTnT-defined sarcomeric organization while overall spheroid morphology remained grossly preserved. This selective vulnerability of cardiomyocytes, alongside preserved non-contractile populations, reflects *in vivo* tissue behaviour.[230,460]

The observed late-stage α-SMA upregulation indicates activation of early remodelling programs,[461] reinforcing the system capability to model post-injury progression rather than acute necrosis alone. Collectively, the model reconstructs the multifactorial and temporally ordered nature of IRI rather than representing a simplified oxygen withdrawal paradigm.

The limited efficacy of isolated pharmacological interventions within this system further supports its mechanistic integrity. Targeting individual pathways failed to restore structural or metabolic stability, consistent with the interconnected architecture of reperfusion injury and mirroring clinical challenges in single-node intervention strategies.[462]

4.3. Core Contribution II – Adaptive Closed-Loop Optimization in 3D Cardiac Systems

Beyond disease modelling, this work introduces an adaptive closed-loop Bayesian optimization framework for automated dose refinement directly within three-dimensional cardiac spheroids.

The platform demonstrated iterative convergence behaviour, dynamic exploration–exploitation balancing, and automated safety threshold detection. By identifying maximal physiological ranges and refining dose–response curves without predefined assumptions, the system enables efficient pharmacological profiling in complex 3D tissues.

Importantly, electrophysiological baseline gating was integrated into the workflow. Spheroids exhibiting irregular or absent beating were excluded prior to optimization, minimizing intrinsic metabolic variability that could falsify MTT-based toxicity assessment.[463] This integration of functional quality control into algorithmic

concentration selection enhances reproducibility and establishes a generalizable framework for phenotypic screening in multicellular cardiac constructs.
The scalability of automated spheroid generation in 384-well format further supports future high-throughput applications without compromising excitation–contraction coupling integrity.

4.4. Core Contribution III – Genotype-Dependent Pharmacodynamic Sensitivity

A translational extension of the platform was demonstrated through genotype-specific drug response analysis.
Comparative testing across two genetically distinct iPSC-derived cardiac lines revealed drug-specific divergence patterns. Lidocaine exposure produced significant differential sensitivity, while adrenergic stimulation triggered qualitatively distinct metabolic responses. In contrast, verapamil response remained conserved across lines. These findings indicate selective pharmacodynamic heterogeneity rather than global assay variability. While not implying clinical predictability, this proof-of-principle demonstrates that the platform can resolve target-specific genotype-dependent differences under standardized experimental conditions. Such capability is essential for future precision-oriented cardiac pharmacology.

4.5. Limitations and Opportunities for Refinement

Despite its strengths, the system remains a simplified representation of *in vivo* physiology.
The absence of controlled perfusion limits simulation of shear stress and dynamic metabolite clearance. Incorporation of flow-based platforms could enhance translational accuracy, particularly during the remodelling phase.[463,464] While the multicellular composition represents a substantial advancement over monocellular systems, the lack of immune components restricts modelling of inflammatory amplification and resolution dynamics.[400]
Although functional maturation was validated through calcium transient stability and beating behaviour, further metabolic characterization, particularly direct assessment of mitochondrial respiration and mPTP opening, would strengthen mechanistic confirmation.[465] Similarly, ROS detection protocols with higher temporal resolution could capture the immediate oxidative burst upon reperfusion more precisely.[466]

Finally, expansion of genotype analysis and increased sample sizes would enhance statistical power for inter-line comparisons. These refinements represent logical extensions rather than corrections and highlight the adaptability of the platform.

4.6. Conceptual Integration

Taken together, this thesis demonstrates that IRI is a temporally precise and inherently multifactorial process that cannot be adequately modelled through isolated hypoxic exposure. Effective *in vitro* reconstruction requires coordinated modulation of oxygen availability, metabolic substrate supply, calcium dynamics, and multicellular architecture.

By integrating mechanistic injury reconstruction with adaptive experimental design and genotype-sensitive pharmacological interrogation, this work advances toward a systems-level framework for cardiac *in vitro* modelling. The findings underscore that single-axis interventions are insufficient within interconnected injury networks and that adaptive, data-driven approaches enhance both resolution and translational relevance.

4.7. Future Directions

Future development of the platform could include automated integration of nitrogen flux delivery via plate-based lid systems to further refine temporal precision and reproducibility. Coupling the established automated differentiation pipeline with the closed-loop pharmacological screening would enable continuous high-throughput experimentation.

Implementation of dynamic perfusion modules, combinatorial drug testing strategies, and multi-omics profiling would expand mechanistic depth. Single-cell transcriptomic analysis could further verify cell-type–specific responses within the multicellular spheroid architecture. Expansion to additional patient-derived iPSC lines would strengthen evaluation of genotype-dependent variability and enhance precision-oriented applications.

4.8. Final Perspective

By integrating temporally controlled ischemia–reperfusion modelling with adaptive closed-loop experimentation and genotype-specific pharmacological interrogation, this work establishes a scalable and mechanistically grounded framework for

advanced cardiac *in vitro* research. The findings highlight both the complexity of reperfusion injury and the necessity of integrative, systems-oriented strategies to dissect it. Rather than simplifying pathology to isolated pathways, the presented approach embraces its interconnected architecture, providing a controlled yet physiologically relevant platform for future translational investigation.

5. Material and Methods

5.1. Material

5.1.1. Cell Lines

iPSC-Line HD11	Human induced pluripotent stem cells (iPSCs), provided by Prof. Dr. med. Jochen Utikal, DKFZ Heidelberg.
iPSC-Line WTC11-NGN2	Human induced pluripotent stem cells (iPSCs) with a doxycycline-inducible promoter for the expression of NGN2, provided by Prof. Dr. Peter St George-Hyslop, University of Cambridge, England, passage 27–50.

5.1.2. Devices

Confocal microscope	Leica STELLARIS 5 8119637
Analytical balances	VWR
CO2-Incubator	C170 Binder
NanoDrop™ Lite	Thermo Scientific™
Pipettes	Eppendorf Research Plus 0,5-10 / 2-20 / 1-100 / 20-200 / 100-1000 µl
Multichannel pipettes	1-10 µl / 20-200 µl VWR® International
Microcentrifuge	Micro Star 17R VWR® International
Pipette aid	accuJET pro VWR® International
Thermocycler peqSTAR	VWR® International
plate centrifuge	Laborfuge 400R Heraeus
Thermomixer	5436, Eppendorf
Microplate reader	SpectraMax® iD3 Molecular Devices
Widefield microscope	DMiL LED Leica Microsystems GmbH
Liquid nitrogen tank	Biosafe MD Chronos 100 Messer Industriegase
Opentrons Flex Magnetic Bead Protein Purification Workstation	OT-991-00185 I&L Biosystems
Standalone Benchtop Incubator	STX44-ICBT Liconic

Robotic Arm	PF400 Brooks Automation
CellXpressAI	Molecular Devices
pH meter	VWR® International
ImageXpress Confocal HT.ai High-Content Imaging system	Molecular Devices

5.1.3. Consumables

Cryogenic tubes 2 ml	VWR® International
Hemocytometer cover glasses	VWR® International
Nalgene® square media bottle, PETG, 125 ml	VWR® International
Nalgene® square media bottle, PETG, 250 ml	VWR® International
Mr. FrostyTM Freezing Container	Thermo Scientific™
Multiwell plate 96- / 48- / 24- / 12- / 6-Well	VWR® International
Parafilm M, 4 in. X 125 ft. roll	Carl-Roth
Pasteur pipettes	Brand GmbH
Pipette tips 0,5-20 / 1-200 / 100-1000 µl	VWR® International
Pipette tips 300/ 1000 µl	
Petri dishes, PS, 10 cm	Greiner Bio-One GmbH
Black reaction tubes, 1,5 ml	Eppendorf SE
Colourless reaction tubes, 1,5 / 2 ml	Eppendorf SE
Reservoir 50 ml	VWR® International
Serological pipettes 5 / 10 / 25 ml	VWR® International
Sterile filters, Aerodisc syringe filters	PALL life sciences
Neubauer counting chamber	VWR® International
Centrifuge tubes with a conical bottom, 15 / 50 mL	VWR® International
µ-Slide 8 Well ibiTreat	ibidi® GmbH
µ-Slide 18 Well ibiTreat	ibidi® GmbH
PCR-Strips	Brand GmbH
qPCR Plates	Bio-Rad Laboratories GmbH
384 well round Bottom ULA Plate	Corning®
Sterican® 30 G x ½ "	B. Braun SE
Sterican® 27 G x ½ "	B. Braun SE

Sterican® 26 G x ½ "	B. Braun SE
Sterican® 25 G x 5/8 "	B. Braun SE
Syringe filter 0,22 µm	Lab Logistic Groups GmbH

5.1.4. Chemicals

DMSO, Dimethylsulfoxid (A994.2)	Carl-Roth
Ethanol absolut (20821.296)	VWR® International
Lidocaine hydrochloride monohydrate, 98 % (J63035.06)	Thermo Fisher Scientific
MTT, 3-(4,5-Dimethylthiazol-2-yl)2,5-diphenyltetrazoliumbromid (G4100)	Promega GmbH
PFA, Paraformaldehyd (818715)	Carl-Roth
Solubilization Solution Stop Mix (G4100)	Promega GmbH
Triton X-100 (T-9284)	Sigma-Aldrich
(-)-Epinephrine (E4250-1G)	Sigma-Aldrich
BSA 10 %	Macs®
TRIzol (15596018)	Thermo Fisher Scientific
Ethidiumbromidlösung (10 mg/ml) (2140840)	Carl Roth
Nuclease Free Water (P119E)	Promega GmbH
Random Primer (C1181)	Promega GmbH
RNase AWAY® (732-2271)	VWR® International
RQ1 DNase Stop Solution (M6101)	Promega GmbH
M-MLV Reverse Transcriptase (M3683)	Promega GmbH
Isopropanol (6752.1)	Carl-Roth
GoTaq® Polymerase (M7845)	Promega GmbH
GoTaq® MasterMix (A6001)	Promega GmbH
6x Loading Dye (B7021S)	New England Biolabs®
5x Green GoTaq Reactionbuffer (M7911)	Promega GmbH
10x RQ1 DNase buffer (M6101)	Promega GmbH
dNTP Solution Mix (N0447S)	Promega GmbH
Verapamil hydrochloride (676777)	Sigma-Aldrich
L-Ascorbic acid (APO456787373)	Sigma Aldrich
Mineral oil (330760)	Sigma Aldrich

5.1.5. Cell Media

Cardiomyocyte Maintenance Kit (05020)	Stemcell™ Technologies
Corning® Matrigel®, hESC qualified (354277)	Corning Inc.
DMEM/F12, Dulbecco's Modified Eagle Medium Nutrient Mixture F12 (11320033)	Gibco® life Technologies
DPBS-/-, Dulbecco's Phosphate Buffered Saline-/- (14190 094)	Gibco® Life Technologies
DPBS+/+, Dulbecco's Phosphate Buffered Saline+/+ (14190 094)	Gibco® Life Technologies
FCS, Fetal calf serum (10500064)	Gibco® life Technologies
KnockOut™ DMEM (10829018)	Gibco® Life Technologies
mTeSR™Plus Kit (100-0276)	Stemcell™ Technologies
STEMdiff™ Cardiomyocyte Dissociation Kit (05025)	Stemcell™ Technologies
STEMdiff™ Ventricular Cardiomyocyte Differentiation Kit (05010)	Stemcell™ Technologies
Doxycyclin-hyclat (D9891-1G)	Sigma Aldrich® Merck KGaA
Pen/Strep (Penicillin/Streptomycin) (15140122)	Gibco® Life Technologies
StemPro™ Accutase™ Cell dissociation reagent (A1110501)	Gibco® Life Technologies
Y-27632 Dihydrochlorid (ROCK- Inhibitor, 1293823)	PeproTech

5.1.6. Antibodies

5.1.6.1. Primary Antibodies

Anti-Nanog produced in mouse	ab62734, abcam, Lot: GR3209024-8
Anti-Oct-4 produced in rabbit	ab181537, abcam Lot: GR3209024-8
Anti-cTnT produced in mouse	MA5-12960, Invitrogen™ Lot: 2504985
Anti VE-Cadherin produced in rabbit	ab33168, abcam Lot: n/a
Anti α-SMA produced in rabbit	177524, Proteintech Lot: 00177524
Anti Collagen I produced in rabbit	14695-1-AP, Proteintech Lot: n/a

5.1.6.2. Secondary Antibodies

Alexa Fluor® 647 Goat Anti-Mouse	A21235, Invitrogen™, Lot: 2306581
Alexa Fluor® 488 Goat Anti-Mouse	A11001, Invitrogen™, Lot: 3148303
Alexa Fluor® 647 Goat Anti-Rabbit	A21247, Invitrogen™, Lot: 2186088
Alexa Fluor® 647 Chicken Anti-Rabbit	A21443, invitrogen™, Lot: 3188340

5.1.7. Fluorescence Dyes

Fluo-4-AM, membrane-permeable	(F14201) Thermo Fisher Scientific
Hoechst33342 Trihydrochlorid	(H3570) Sigma-Aldrich
Phalloidin-TRITC	(P1951) Sigma-Aldrich
MitoTracker Green FM	(M7514) Invitrogen
DCFDA	Sigma Aldrich

5.1.8. Primer

Oct4 FW	CCTGAAGCAGAAGAGGATCACC
Oct4 RV	AAAGCGGCAGATGGTCGTTTGG
GATA4 FW	GCGGTGCTTCCAGCAACTCCA
GATA4 RV	GACATCGCACTGACTGAGAACG
cTnT FW	AAGAGGCAGACTGAGCGGGAAA
cTnT RV	AGATGCTCTGCCACAGCTCCTT
HIF-1α FW	TATGAGCCAGAAGAACTTTTAGGC
HIF-1α RV	CACCTCTTTTGGCAAGCATCCTG
BNIP3 FW	TCAGCATGAGGAACACGAGCGT
BNIP3 RV	GAGGTTGTCAGACGCCTTCCAA
Glut1 FW	TTGCAGGCTTCTCCAACTGGAC
Glut1 RV	CAGAACCAGGAGCACAGTGAAG
VEGF FW	TTGCCTTGCTGCTCTACCTCCA
VEGF RV	GATGGCAGTAGCTGCGCTGATA
α-SMA FW	CTATGCCTCTGGACGCACAACT
α-SMA RV	CAGATCCAGACGCATGATGGCA
LDHA FW	GGATCTCCAACATGGCAGCCTT
LDHA RV	AGACGGCTTTCTCCCTCTTGCT
HPRT FW	CATTATGCTGAGGATTTGGAAAGG

HPRT RV	CTTGAGCACACAGAGGGCTACA

5.1.9. Software

All data analysis, statistical testing, and signal processing were performed using Python (version 3.13; Python Software Foundation). The following libraries were used: NumPy (Harris et al., 2020) for numerical computation, SciPy (Virtanen et al., 2020) for statistical analysis and signal processing, Pandas (McKinney, 2010) for data handling, and Matplotlib (Hunter, 2007) for data visualization.[467–470] Contractile motion analysis was implemented following the MuscleMotion framework (Sala et al., 2018).[427] The adaptive Bayesian closed-loop optimization framework was implemented as a custom Python-based pipeline.

Laboratory automation was coordinated using the Retisoft Genera 6.8.6 laboratory execution system. Confocal images were acquired using Leica Application Suite X (LAS X; Leica Microsystems). Live-cell imaging and brightfield stream acquisition were performed using the MetaXpress software (Molecular Devices). Endpoint absorbance measurements were recorded using a SpectraMax plate reader (Molecular Devices). Citations and references were managed using Citavi (Swiss Academic Software).

Generative AI tools were used during the preparation of this thesis. Claude (Anthropic) assisted in the development and refinement of Python-based analysis scripts, including components of the adaptive Bayesian closed-loop optimization pipeline and statistical workflows. All generated code was critically reviewed, independently tested, and validated prior to application. ChatGPT 5.2 (OpenAI) was used for language editing, including spelling correction and text refinement. Gemini (Google; Banana Pro model) and FigureLabs were used to assist in the creation and refinement of schematic figures and conceptual visualizations in the introduction. The conception of experiments, data analysis decisions, interpretation of results, and all scientific conclusions were made by the author. Generative AI tools were used exclusively as supportive tools during code development, visualization design, and language editing.

5.2. Methods

5.2.1. Cell Culture

5.2.1.1. Matrigel Coating

Culture wells for the iPSC lines HD11 and WTC11-NGN2 were coated with hESC-qualified Matrigel™ (Corning, Lot: 09424002) at a 1:100 dilution prepared in DMEM/F12 or KnockOut™ DMEM, respectively. Matrigel™ was thawed on ice and diluted under cold conditions to prevent premature gelation. For coating, 1 mL of diluted Matrigel™ solution was added per well of a 6-well plate and incubated at room temperature for 1 hour. The coating solution was reused for a total of six plates. Coated plates were stored at 4 °C for up to two weeks. Prior to cell seeding, wells were washed once with DPBS without calcium and magnesium (DPBS−/−).

5.2.1.2. iPSC Culture

Cells used in this study were maintained in their respective culture medium (mTeSR™ Plus, STEMCELL Technologies). Cells were incubated at 37 °C, 5 % CO_2, and saturated humidity. Medium was exchanged every second day. Unless otherwise specified, passaging was performed at 80–90 % confluency, and the passage number was increased by one. All cell culture procedures were conducted under sterile conditions in a biological safety cabinet.

5.2.1.3. Freezing and Thawing

For long-term storage, iPSCs were cryopreserved in liquid nitrogen (−196 °C). Cell suspensions were adjusted to 1×10^6 cells per vial, centrifuged, and resuspended in 1 mL of freezing medium. The suspension was transferred into cryovials and placed in a Nalgene™ Mr. Frosty™ freezing container to ensure controlled-rate cooling to −80 °C. After 24 h at −80 °C, vials were transferred to liquid nitrogen for long-term storage. For thawing, cryovials were briefly handled under sterile conditions to remove residual liquid nitrogen and then rapidly thawed in a 37 °C water bath. Immediately after thawing, 1 mL of mTeSR™ Plus medium was added dropwise to the cryovial to minimize osmotic shock. The cell suspension was then transferred into a pre-coated 6-well plate containing culture medium supplemented with 10 μM ROCK inhibitor (Y-27632). Cells were incubated at 37 °C and 5 % CO_2 for 6 h to allow attachment, after which the medium was replaced to remove DMSO. The passage number was increased by one following thawing.

5.2.1.4. Passaging

For routine passaging, culture medium was aspirated and cells were washed once with DPBS (-/-). Subsequently, 1 mL Accutase was added per well, and cells were incubated at 37 °C, 5 % CO_2, and saturated humidity for 10 minutes to allow enzymatic detachment. After incubation, 1 mL maintenance medium (MM) was added to stop enzymatic activity. Cells were detached from the culture surface by gentle pipetting. The resulting cell suspension was transferred to a 15 mL conical tube and centrifuged at 300 × g for 3 minutes. The supernatant was carefully removed, and the cell pellet was resuspended in 1 mL mTeSR medium supplemented with 10 µM ROCK inhibitor. Cell numbers were determined using a Neubauer counting chamber by loading 10 µL of the cell suspension. Cells were either used directly for downstream experiments or reseeded at a density of 1×10^5 cells per well.

5.2.2. Differentiation

5.2.2.1. Hanging Drop

For hanging drop-based cardiac differentiation, a cell suspension containing 1,000 cells per 10 µL was prepared on differentiation day −2 (DD−2). A 10 µL droplet of the cell suspension, supplemented with 10 µM ROCK inhibitor and 1:100 hESC-qualified Matrigel™ (Corning, Lot: 09424002), was carefully placed in the center of each well of a 48-well plate lid. The corresponding plate bottom was filled with DPBS to prevent evaporation and osmolarity changes within the droplets. The lid was then repositioned onto the plate and incubated for 2 days at 37 °C, 5 % CO_2, and saturated humidity to allow spheroid formation. On differentiation day 0 (DD0), 10 µL of 2× Medium A (STEMCELL Technologies Ventricular Cardiomyocyte Differentiation Kit) supplemented with 1:100 hESC-qualified Matrigel™ (Corning, Lot: 09424002) was added directly to each droplet, resulting in a final 1× concentration. The plate was returned to the incubator and maintained under standard conditions (37 °C, 5 % CO_2, saturated humidity) for 2 days. On differentiation day 4 (DD4), 20 µL Medium B was pre-dispensed onto a new 48-well plate lid. Spheroids were carefully transferred using a 200 µL pipette tip. The lid was placed onto a DPBS-filled plate bottom and incubated until DD5 under standard conditions. On differentiation day 5 (DD5), Medium C was pre-dispensed onto a new lid, and spheroids were transferred accordingly. Spheroids were maintained in Medium C for 2 days. On differentiation day 9 (DD9), spheroids were transferred into maintenance medium (MM). Subsequently, medium exchanges

were performed every 2 days by transferring spheroids into fresh MM on new lids. On differentiation day 21 (DD21), spheroids were considered functionally mature and ready for downstream applications.

5.2.2.2. CellXpressAI

Automated cardiac differentiation was performed using the CellXpress.ai system. A starting cell suspension containing 1,000 cells per 20 µL was prepared and supplemented with 10 µM ROCK inhibitor and 1:100 hESC-qualified Matrigel™ (Corning, Lot: 09424002). The CellXpress.ai platform automatically dispensed the cell suspension into 384-well U-bottom plates and transferred the plates to a humidified incubator (37 °C, 5 % CO_2). On differentiation day 0 (DD0), 20 µL of 2× Medium A (STEMCELL Technologies Ventricular Cardiomyocyte Differentiation Kit) supplemented with 1:100 hESC-qualified Matrigel™ (Corning, Lot: 09424002) was added to each well, resulting in a final 1× concentration. Plates were incubated under standard conditions (37 °C, 5 % CO_2, saturated humidity). On differentiation day 2 (DD2), 30 µL of medium was aspirated, and 20 µL Medium B was added. Plates were returned to the incubator and maintained for an additional 2 days under standard conditions. On differentiation day 5 (DD5), 30 µL of medium was aspirated at a height of 3 mm using the lowest flow rate to prevent disturbance or aspiration of the spheroids. Subsequently, 20 µL Medium C was dispensed. The same medium exchange procedure was performed on differentiation day 7 (DD7). On differentiation day 9 (DD9), the culture medium was switched to maintenance medium (MM). From this time point onward, medium exchange was performed every second day under standard incubation conditions. On differentiation day 21 (DD21), spheroids were considered functionally mature and ready for downstream applications.

5.2.3. Hypoxia

5.2.3.1. Hypoxic Imaging Chamber

For hypoxia simulation using the ImaxeXpress HT.ai imaging chamber, cardiac spheroids were either differentiated directly in a 384-well plate or transferred into a 384-well plate prior to the experiment. The plate was subsequently placed into the imaging system, and the oxygen concentration was adjusted using the integrated gas regulation system to achieve the desired oxygen level.

5.2.3.2. Mineral Oil Overlay

For hypoxia simulation using a mineral oil overlay, the culture medium of cardiac spheroids cultured in a 384-well U-bottom plate was removed and replaced with 20 µL of fresh medium. Subsequently, the plate was preconditioned for 3 h at 37 °C, 5 % CO_2, and saturated humidity. After the preconditioning phase, experimental wells were overlaid with 20 µL of mineral oil. The plate was then incubated at 37 °C and 5 % CO_2 under saturated humidity. Incubation times varied depending on the desired severity of hypoxic exposure.

5.2.3.3. Nitrogen Flux

For the establishment of a constant nitrogen flow, a silicone tubing system was connected to a syringe filter, which was attached to a 27 G needle. Nitrogen flow was initiated and adjusted to overcome the initial valve opening pressure. The pressure was calibrated using a dummy well containing 50 µL of liquid until slow and intermittent bubble formation was observed. After calibration, cardiac spheroids generated using the CellXpressAI system were exposed to a continuous nitrogen flux for 30 min. Alternatively, cardiac spheroids were pooled in 2 mL reaction tubes. Following pressure adjustment using a dummy tube, the pooled samples were degassed under nitrogen flow for 30 min. After completion of the degassing period, nitrogen flow was stopped and an immediate medium exchange was performed.

5.2.4. Hydrogels

For the preparation of fibrin hydrogels, 10 mg fibrinogen were dissolved in 1 mL DPBS (-/-) by heating and vortexing until complete dissolution was achieved. Thrombin was thawed on ice prior to use. On ice, 20 µL of the fibrinogen solution were mixed with 15 µL DPBS (-/-). The reaction mixture was dispensed into a 384-well plate, and a cardiac spheroid was transferred into the respective well. Subsequently, 5 µL of thrombin were added to initiate polymerization. For gelation, the plate was incubated for 30 min at 37 °C, 5 % CO_2, and saturated humidity. After gelation, 30 µL of MM medium were added to each well. Experiments were performed 24 h after gel formation.

5.2.5. Microscopy

Microscopy was performed using three imaging platforms depending on the experimental application: a Leica STELLARIS 5 confocal microscope for fluorescence

imaging of fixed and stained samples, a Leica widefield microscope for brightfield and live-cell imaging, and an ImageXpress HT.ai high-content imaging system for automated plate-based acquisition.

5.2.5.1. Leica Stellaris 5

Confocal fluorescence imaging was performed using a Leica STELLARIS 5 microscope mounted on a Leica DMI8-CS inverted stand and controlled with Leica Application Suite X (LAS X, version 4.7.0). Images were acquired at 1024 × 1024 pixel resolution and 16-bit depth using bidirectional scanning at 400 Hz, with a pinhole size of 1.0 Airy unit. Depending on the experimental application and required spatial resolution, either a 10×/0.40 dry objective or a 20×/0.75 dry objective was used. Typical z-step sizes were 5.0 µm for 10× imaging and 3.0 µm for 20× imaging. Fluorophores were excited using a 405 nm diode laser or the white light laser, and emitted fluorescence was detected using HyD detectors. Frame averaging of 4 to 8 was applied depending on signal intensity. For quantitative comparisons, acquisition settings were kept constant within each experiment.

5.2.5.2 Widefield brightfield and live-cell imaging

Brightfield and live-cell imaging were performed using a Leica DMI8 widefield microscope equipped with a Leica DFC3000 G camera and controlled with LAS X software (version 3.10.1). Images were acquired at 1296 × 966 pixel resolution in 8-bit grayscale using transmitted LED illumination. A 4×/0.10 dry objective or a 10×/0.22 dry objective was used depending on sample size and assay format. Time-lapse recordings for beating analysis and related live-cell assays were typically acquired at approximately 10 frames per second with an exposure time of 100 ms. Standard recordings consisted of 301 frames over approximately 30 s.

5.2.5.3 Automated high-content imaging

Automated image acquisition was performed using an ImageXpress HT.AI system controlled with MetaXpress software (version 6.7.2.290). Images were acquired using a 4× Plan Apo objective and an Andor sCMOS camera at 2048 × 2048 pixel resolution and 16-bit depth. The system was operated in widefield mode with the confocal disk disengaged. Fluorescence acquisitions were performed using FITC-channel excitation with a 470 nm LED light source. Depending on the assay, image series were recorded either in snapshot mode or stream mode. Stream acquisitions typically consisted of 161 frames acquired at approximately 12.36 frames per second, while snapshot

acquisitions consisted of 60 frames acquired over 60 s. Exposure times ranged from 50 to 225 ms depending on assay requirements, with 50 ms used for stream acquisitions.

5.2.6. Fixation and Immunostaining

5.2.6.1. Fixation

For fixation, cardiac spheroids were washed twice with DPBS (-/-) and subsequently transferred into 4 % paraformaldehyde (PFA) solution. Fixation was performed for 40 minutes at room temperature. After fixation, spheroids were washed twice with DPBS (-/-) to remove residual PFA. Samples were either processed immediately for permeabilization and staining or stored in DPBS (-/-) at 4 °C until further use. For 2D iPSC cultures, the fixation time was reduced to 20 minutes under otherwise identical conditions.

5.2.6.2. Permabilistaion

Permeabilization was performed using 0.1 % Triton X-100 in DPBS (-/-). After removal of DPBS from fixed spheroids, the Triton X-100 solution was added and samples were incubated for 10 minutes at room temperature. Subsequently, spheroids were washed twice with DPBS (-/-) to remove residual detergent. Samples were either stored at 4 °C or processed directly for subsequent staining procedures.

5.2.6.3. Nuclear Staining

Nuclei were stained using Hoechst 33342 at a final concentration of 2 μg/mL in DPBS (-/-). Fixed and permeabilized spheroids were incubated with the staining solution for 30 minutes at room temperature. After incubation, samples were washed with DPBS (-/-). Fluorescence imaging was performed using a Leica Stellaris 5 confocal microscope with excitation at 405 nm and emission detection between 415–480 nm.

5.2.6.4. Actin Cytoskeleton Staining

The actin cytoskeleton was visualized using Phalloidin-TRITC. Following fixation and permeabilization, cardiac spheroids were incubated with 100 nM Phalloidin-TRITC diluted in DPBS (-/-) for 60 minutes at room temperature. After staining, samples were washed twice with DPBS (-/-). Fluorescence was detected with excitation at 545 nm and emission at 573 nm.

5.2.6.5. Immunostaining

After fixation and permeabilization, cardiac spheroids were incubated in 3 % bovine serum albumin (BSA) in DPBS (-/-) for 60 minutes at room temperature to block nonspecific binding sites. Primary antibodies were diluted 1:1000 in 3 % BSA and added to the spheroids. Samples were incubated overnight at 4 °C. Following primary antibody incubation, spheroids were washed with DPBS (-/-) to remove unbound antibody. Secondary antibodies (1:500), diluted in 3 % BSA, were then applied and incubated overnight at 4 °C. After secondary antibody incubation, samples were washed with DPBS (-/-) and embedded in 0.5% low-melting-point agarose for confocal microscopy. Imaging was performed using 18-well Ibidi slides.

5.2.6.6. MitoTracker™ staining

Mitochondria were stained using MitoTracker™ Green. Cardiac spheroids were first washed with DPBS (−/−) and subsequently incubated with 125 nM MitoTracker™ Green in maintenance medium for 40 min at 37 °C under 5 % CO_2 in a humidified atmosphere, protected from light. After incubation, the staining solution was removed and the spheroids were washed with DPBS (−/−). Fresh maintenance medium was then added prior to imaging. Fluorescence imaging of the probe was performed using excitation at 490 nm and emission detection at 500–550 nm.

5.2.7. Functionality assessments

5.2.7.1. Brightfield Beating Analysis

Brightfield time-lapse recordings of iPSC-derived ventricular cardiomyocyte spheroids were acquired using a Leica microscope system at a frame rate of 10 frames per second (fps), corresponding to a temporal resolution of approximately 100 ms per frame. Contraction signals were derived using a MuscleMotion-style analysis approach, in which the signal amplitude at each time point was defined as the mean absolute pixel intensity difference relative to a resting reference frame. Raw image stacks were first processed by applying a spatial Gaussian blur ($\sigma = 10$ pixels) to reduce high-frequency noise. A reference frame representing the resting state was selected as the frame closest to the temporal median intensity of the recording. For each frame, the mean absolute deviation from the reference frame was calculated, resulting in a one-dimensional contraction trace. To correct for baseline drift, a rolling 5th-percentile baseline with a sliding window of approximately 3 seconds was subtracted from the signal. Subsequently, each trace was normalized to its 95th percentile value to allow

comparability between samples. Contraction peaks were identified using the scipy.signal.find_peaks function with adaptive thresholds defined as follows:
Prominence threshold: 20 % of the signal's dynamic range
Height threshold: 10 % of the signal maximum
Minimum inter-peak distance: 1.0 second
The minimum inter-peak distance was selected to reflect the physiological lower limit of contraction intervals in iPSC-derived cardiomyocytes. Diastolic troughs were defined as the minimum signal value between two consecutive contraction peaks.

5.2.7.2. Calcium Imaging

To visualize intracellular calcium transients in cardiac spheroids, fluorescence-based calcium imaging was performed using Fluo-4 AM. Cardiac spheroids were incubated in 10 µM Fluo-4 AM solution prepared in maintenance medium (MM) for 60 minutes at 37 °C, 5 % CO_2, and saturated humidity. Following incubation, spheroids were washed three times with MM medium to remove excess dye. Subsequently, samples were incubated for an additional 20 minutes at 37 °C, 5 % CO_2, and saturated humidity in fresh MM medium to allow complete de-esterification of the dye. Live imaging was performed using a Leica DM IL LED microscope. Time-lapse image acquisition was conducted at 10 frames per second (FPS). Fluorescence was recorded with excitation at 494 nm and emission at 516 nm.

5.2.7.3. MTT-Assay

Cell viability of cardiac spheroids was assessed using the MTT assay. Cardiac spheroids were either directly generated in 384-well U-bottom plates or transferred into 384-well plates after formation via the hanging drop method. Spheroids were maintained in 20 µL maintenance medium (MM). For treatment, the respective test substance was diluted to the desired concentration in MM. A complete medium exchange was performed by carefully removing the existing medium and replacing it with 20 µL treatment-containing medium. Control groups received fresh MM without test substance. After 24 hours of incubation at 37 °C, 5 % CO_2, and saturated humidity, 4 µL MTT solution was added to each well. Spheroids were incubated for an additional 4 hours under the same conditions. For the dead control, 2 µL of 20 % Triton X-100 was added prior to MTT incubation to induce complete cell death. Following the 4-hour incubation period, 30 µL stop solution was added to each well to solubilize the formed

formazan crystals. Plates were incubated for 24 hours at 37 °C before absorbance measurement. Absorbance was measured using a SpectraMax 3000 plate reader.

5.2.7.4. ROS assay

Reactive oxygen species (ROS) levels in cardiac spheroids were detected using 2′,7′-dichlorofluorescein diacetate (DCFDA) staining. A 25 µM DCFDA solution in maintenance medium was prepared. Following treatment, the spheroids were transferred to the DCFDA solution and incubated for 45 min at 37 °C in a humidified atmosphere with 5 % CO_2, protected from light. After incubation, ROS levels were quantified either by fluorescence measurements using a SpectraMax 3000 plate reader or by confocal fluorescence microscopy using a Leica STELLARIS 5 microscope. For fluorescence detection, excitation was set to 504 nm and emission to 529 nm. Unstained control samples were cultured under identical conditions but without the addition of DCFDA.

5.2.8. qPCR

5.2.8.1. RNA Extraction

Total RNA was isolated from cardiac spheroids using TRIzol reagent. Cardiac spheroids were washed once with DPBS (-/-), and residual liquid was carefully aspirated. Subsequently, 100 µL TRIzol reagent was added, and samples were homogenized thoroughly by repeated pipetting. Homogenates were either stored at −20 °C for later processing or incubated at room temperature for 5 minutes before phase separation. For phase separation, 40 µL chloroform was added to each sample. Tubes were inverted for 30 seconds and incubated at room temperature for an additional 3 minutes. Samples were briefly vortexed and centrifuged at 12,000 × g for 15 minutes at 4 °C. Following centrifugation, 50 µL of the aqueous phase was transferred to a fresh reaction tube containing 100 µL pre-dispensed isopropanol. Samples were mixed briefly and incubated at room temperature for 10 minutes to precipitate RNA. RNA was pelleted by centrifugation at 12,000 × g for 10 minutes at 4 °C. The supernatant was carefully removed, and the RNA pellet was washed with 75 % ethanol. After 5 minutes of incubation at room temperature, samples were centrifuged at 7,500 × g for 5 minutes at 4 °C. The supernatant was discarded, and the pellet was air-dried for 10 minutes at room temperature to remove residual ethanol. RNA was dissolved in 20 µL nuclease-free water and incubated at 65 °C for 15 minutes with gentle shaking to ensure complete resuspension. RNA concentration and purity were

determined using a NanoDrop spectrophotometer. RNA samples were either stored at −20 °C or immediately used for cDNA synthesis.

5.2.8.2. cDNA

RNA concentrations were adjusted to obtain 1 µg total RNA per sample based on NanoDrop measurements. Each sample was brought to a total volume of 8 µL with nuclease-free water. Subsequently, 1 µL DNase I and 1 µL DNase buffer were added to remove residual genomic DNA. Samples were incubated at 37 °C for 30 minutes in a thermocycler. After DNase treatment, samples were placed on ice, and 1 µL DNase stop solution was added. DNase inactivation was performed at 40 °C for 10 minutes. Next, 0.5 µL (200 µg) random primer mix was added, and primer annealing was performed at 75 °C for 5 minutes. For reverse transcription, 0.5 µL dNTP mix, 3.75 µL nuclease-free water, and 0.25 µL reverse transcriptase were added to each positive sample. For negative controls, reverse transcriptase was replaced with nuclease-free water. cDNA synthesis was performed under the following conditions:

10 minutes at 25 °C
60 minutes at 42 °C
10 minutes at 70 °C

After reverse transcription, 100 µL nuclease-free water was added to each sample. cDNA was stored at −20 °C until further use.

5.2.8.3. cPCR

For endpoint PCR, 3 µL cDNA was mixed with:

4 µL 5× reaction buffer
0.5 µL dNTP mix
1 µL forward primer
1 µL reverse primer
0.5 µL GoTaq DNA polymerase
10.25 µL nuclease-free water

PCR amplification was performed in a thermocycler using the following program:
Initial denaturation:

95 °C for 2 minutes

35 cycles of:

95 °C for 30 seconds
60 °C for 30 seconds

72 °C for 30 seconds

Final extension:

72 °C for 5 minutes

PCR products were analysed on a 2 % agarose gel containing 0.25 μg/mL ethidium bromide alongside a 100 bp DNA ladder.

5.2.8.4. qPCR

qPCR reactions were prepared on ice in 96-well plates. Each reaction contained:

10 μL Promega qPCR master mix

1 μL forward primer

1 μL reverse primer

4 μL nuclease-free water

4 μL cDNA

Plates were sealed and centrifuged at 180 × g for 2 minutes to remove air bubbles.

qPCR was performed using the Bio-Rad CFX96 Real-Time PCR Detection System under the following conditions:

Initial denaturation:

95 °C for 2 minutes

40 cycles of:

95 °C for 15 seconds

60 °C for 60 seconds

Final step:

95 °C for 60 seconds

5.2.9. Automation

5.2.9.1. System Overview

An automated closed-loop platform was developed to iteratively characterize compound dose–response relationships in cardiac spheroids cultured in 384-well plates. The system integrates high-content imaging, robotic liquid handling, viability readout, and computational modelling within a unified control architecture.

Experimental execution was coordinated using Retisoft Genera 6.8.6. Pre-treatment contractility assessment was performed on an ImageXpress HT.AI high-content imager. Compound preparation, dilution, and reagent dispensing were carried out using an Opentrons Flex liquid handling robot. Endpoint absorbance measurements were acquired using a SpectraMax plate reader. A dedicated analysis workstation

executed the closed-loop controller implemented in Python, which integrated imaging-derived exclusion data with viability measurements to guide adaptive concentration selection.

5.2.9.2. OpenTron

Compound Dilution and Dispensing

Five concentrations per compound were generated from stock solutions using automated dilution on the Opentrons Flex platform. Target dilution factors were calculated from stock and desired concentrations. If the required source volume was below the minimum pipettable volume, multi-step serial dilutions were automatically computed. Prepared dilutions were dispensed into 384-well assay plates at 30 µL per well. Dispensing proceeded from lowest to highest concentration within each compound series to minimize cross-contamination. Liquid levels in source containers were dynamically tracked to ensure accurate aspiration.

MTT Viability Assay

Following 24 h compound incubation (37 °C, 5 % CO_2), 4 µL MTT solution (5 mg/mL in PBS) was added per well. Plates were incubated for 4 h to allow formazan formation. Subsequently, 30 µL stop solution (10 % SDS in 0.01 M HCl) was added to each well. Plates were incubated for 12 h to ensure complete solubilization of formazan crystals in the three-dimensional spheroid structures.

5.2.9.3. ImageXpress

Image Acquisition

Prior to compound addition, brightfield image sequences were acquired for all wells at 10 frames per second for 7.5 seconds (75 frames per well). This acquisition window ensured capture of multiple contraction cycles across physiological beating frequencies of iPSC-derived cardiomyocytes.

Contraction Signal Extraction

Contractile activity was quantified using a MuscleMotion-based algorithm (Sala et al., 2018). Image frames were spatially smoothed to reduce acquisition noise. A diastolic reference frame was identified from the temporal median image. For each timepoint, contraction amplitude was calculated as the mean absolute pixel-wise difference between the current frame and the reference frame, generating a one-dimensional contraction trace per well.

Beat Detection and Exclusion Criteria

Baseline drift was removed using a rolling low-percentile estimator, and traces were amplitude-normalized to reduce inter-well variability. Beats were detected using adaptive peak detection scaled to the dynamic range of each signal.

Wells with fewer than two detected beats were classified as non-beating and flagged for exclusion from viability normalization. Wells in which contraction analysis failed were conservatively retained to avoid false exclusion.

5.2.9.4. PlateReader

Absorbance was measured at 570 nm using a SpectraMax plate reader. Raw absorbance values were exported and parsed automatically by the analysis workstation.

Blank correction was applied prior to normalization. Viability for each well was calculated relative to untreated control wells:

Viability (%) = (A_sample / A_control_mean) × 100

For plates containing non-beating spheroids, control means were recalculated excluding flagged wells. Filtered viability values were used for dose–response modelling, while unfiltered data were archived for reference.

5.2.9.5. Closed-Loop

Four-Parameter Logistic Modelling

Dose–response relationships were modeled using a four-parameter logistic (4PL) function:

$$V(C) = V_{bottom} + \frac{V_{top} - V_{bottom}}{1 + \left(\frac{C}{IC_{50}}\right)^{H}}$$

where V represents viability (%), C concentration, V_{bottom} and V_{top} the asymptotes, IC_{50} the half-maximal inhibitory concentration, and H the Hill coefficient.

Nonlinear least-squares fitting was performed under biologically constrained parameter bounds. When replicate variance was available, weighted fitting was applied. Model performance was assessed using R^2 and residual error metrics. Parameter uncertainties were derived from the covariance matrix, and confidence intervals were estimated via Monte Carlo sampling.

Adaptive IC_{50} Refinement

An adaptive Bayesian optimization framework iteratively refined concentration selection. The first iteration employed logarithmically spaced concentrations across the predefined test range. Subsequent iterations selected candidate concentrations using an acquisition function combining prediction uncertainty and proximity to the current IC_{50} estimate in log-concentration space.
Optimization terminated upon satisfaction of predefined convergence criteria for parameter uncertainty and transition zone coverage or upon reaching the maximum number of iterations.

MPR Estimation and Range Escalation
The maximal physiological range (MPR), defined as the highest concentration maintaining ≥90 % viability, was estimated using a Gaussian process surrogate model in log-concentration space. The acquisition strategy prioritized concentrations with high probability of remaining above the 90 % threshold while maintaining adequate exploration.
If viability remained above 50 % at the highest tested concentration, the concentration range was extended toward stock levels and optimization continued within the expanded range.

5.2.10. Statistical Analysis

All statistical analyses were performed in Python (SciPy library). The significance level was set to $\alpha = 0.05$. Results are reported as *$p < 0.05$, **$p < 0.01$, and ***$p < 0.001$ unless otherwise specified. Normality was assessed using the Shapiro–Wilk test and homogeneity of variances using Levene's test.

Parametric Analyses
For comparisons across more than two independent groups, one-way analysis of variance (ANOVA) was applied, followed by Tukey's honest significant difference (HSD) test for post-hoc pairwise comparisons. Welch's two-tailed t-test was used for two-group comparisons when equal variances could not be assumed. Paired t-tests were used for within-replicate comparisons. One-sample t-tests were performed against a theoretical mean of zero for normalized change analyses.

Non-parametric Analyses

When data did not meet parametric assumptions or sample sizes were limited, non-parametric alternatives were employed. The Kruskal–Wallis H test was used for comparisons across more than two independent groups, followed by Mann–Whitney U tests for post-hoc pairwise comparisons. The Friedman test was used for repeated-measures comparisons across treatment phases.

Multiple Comparisons

Multiple testing was controlled using Bonferroni correction for pairwise and dose–response analyses, Dunnett's test for comparisons against a single control group, and the Benjamini–Hochberg procedure (false discovery rate < 0.05) for multi-gene expression analyses.

Effect Sizes

Effect sizes were reported as Hedges' g for two-group comparisons and interpreted according to conventional thresholds.

Gene expression analysis

Relative gene expression was quantified using the 2^(−ΔCt) method normalized to the housekeeping gene HPRT for differentiation time-course experiments. For treatment-response experiments, the 2^(−ΔΔCt) method was used, with untreated samples at each timepoint serving as calibrators. Statistical testing was conducted on ΔCt or ΔΔCt values, as appropriate, while transformed expression values are presented for visualization.

Dose–Response Modelling

Dose–response relationships were characterized by fitting a four-parameter logistic (4PL) model to viability data. For compounds exhibiting stimulatory responses, a sigmoidal E_max model was applied. Parameter uncertainty was estimated by Monte Carlo sampling (8,000 draws from the parameter covariance matrix). Model convergence was assessed based on goodness-of-fit and confidence interval stability.

Bayesian Closed-Loop Optimization

An adaptive Bayesian optimization framework was implemented to refine concentration selection during pharmacological profiling. Initial concentrations were logarithmically spaced across the testable range, and iterative refinement was

performed until predefined convergence criteria for parameter uncertainty and model confidence were reached.

Contractile and calcium signal analysis

Contractile motion was quantified from brightfield time-lapse recordings using a frame-to-frame intensity-difference algorithm. Signals were smoothed and baseline-corrected prior to adaptive peak detection for beat identification. Beat rhythm regularity was assessed using the coefficient of variation of inter-beat intervals and the root mean square of successive differences. Calcium transient traces were extracted as $\Delta F/F_0$ from defined sub-regions within spheroids, with detrending and amplitude normalization performed prior to analysis.

Image Analysis

Confocal z-stacks were processed as maximum or mean intensity projections. Channel intensities were normalized using percentile-based scaling. Spheroid masks were generated using Otsu thresholding with morphological refinement. Reactive oxygen species were quantified as the percentage of spheroid area exceeding a threshold defined from control samples.

Outlier exclusion and sample size criteria

Outliers were identified using the 1.5 × interquartile range method prior to inferential testing and without knowledge of group identity. Groups with fewer than three biological replicates were excluded from inferential analysis. Biological replicates were defined as independent experiments or independent pooled spheroid batches, with per-sample or per-well means used as indicated.

6. List of Abbreviations

2D	two-dimensional
3D	three-dimensional
BPM	beats per minute
CM	Cardiomyocytes
cTnT	cardiac troponin T
DMSO	Dimethylsulfoxid
DPBS	Dulbecco's Phosphate-Buffered Saline
ECM	Extracellular matrix
FCS	fetal calf serum
MBCD	Methyl-β-Cyclodextrin
hiPSC	human induced pluripotent stem cells
iPSC	induced pluripotent stem cells
MM	Maintenance Media
MTT	3-(4,5-Dimethylthiazol-2-yl)-2,5- diphenyltetrazoliumbromid
Oct-4	Octamer binding transcription factor-4
P/S	Penicillin/Streptomycin
RFU	Relative Fluorescence Unit
rpm	revolutions per minute
RT	Room temperature
CVD	Cardiovascular Diseases
IRI	Ischemia Reperfusion Injury
mPTP	mitochondrial permeability transition pore
AU	arbitrary units
ROS	Reactive oxygen species
4PL	Four-parameter logistic model
AR	Alternans ratio
MPR	Maximal physiological range
IBI	Inter beat interval
CV	Coefficient of variation
dMM	Degassed maintenance media
MM	Maintenance media
DD	Differentiation day
SEM	Standard error of the mean

SDNN	Standard deviation of normal-to-normal intervals
RMSSD	Root mean square of successive differences
p_adj	Adjusted p-value
FDR	False discovery rate
RET	Reverse electron transfer
FPS	Frames per second
AAR	Area at risk
OGD	Oxygen-glucose deprivation
AMPK	AMP-activated protein kinase
PFK-1	Phosphofructokinase-1
PDH	Pyruvate dehydrogenase
LCFA	Long chain fatty acids
FAO	Fatty acid oxidation
TCA	Tricarboxylic acid cycle
MMPs	Matrix metalloproteinases
TIMPs	Tissue inhibitors of metalloproteinases
NO	Nitric oxide
ECs	Endothelial cells
CICR	Calcium-induced calcium release
RyR2	Ryanodine receptor 2
ICD	Implantable cardioverter defibrillator
EAD	Early afterdepolarization
DAD	Delayed afterdepolarization
SA	Sinoatrial node
AV	Atrioventricular node
RA	Right atrium
LA	Left atrium
LV	Left ventricle
RV	Right ventricle
hERG	Human Ether-a-go-go-Related Gene
PCI	Percutaneous coronary intervention
HF	Heart failure
OxPhos	Oxidative phosphorylation
Pi	Inorganic phosphate
IC_{50}	Half maximal inhibitory concentration

NCX	Sodium-calcium exchanger
H/R	Hypoxia/reoxygenation
CPT-I	Carnitine palmitoyl transferase I
α-SMA	Alpha smooth muscle actin
AP	Action potential
ETC	Electron transport chain
RET	Reverse electron transport
eCSC	Endogenous cardiac stem cells
FATP	Fatty acid transport protein
BNIP3	BCL2/adenovirus E1B 19 kDA protein-interacting protein 3
Glut1	Glucose transporter 1
HIF-1α	Hypoxia-inducible factor 1
LDHA	Lactate dehydrogenase A
VEGFA	Vascular endothelial growth factor A

7. References

1. World Bank Open Data. Life expectancy at birth, total (years). Available at https://data.worldbank.org/indicator/SP.DYN.LE00.IN (2026).
2. Worldometer. World Demographics 2026 (Population, Age, Sex, Trends) - Worldometer. Available at https://www.worldometers.info/demographics/world-demographics/ (2026).
3. Arora, A. Levels and trends in child mortality 2024. *UNICEF* (2025).
4. Child mortality and causes of death. Available at https://www.who.int/data/gho/data/themes/topics/topic-details/GHO/child-mortality-and-causes-of-death (2026).
5. Saloni Dattani, Veronika Samborska, Hannah Ritchie & Max Roser. Cancer. *Our World in Data* (2024).
6. Cardiovascular diseases (CVDs). Available at https://www.who.int/news-room/fact-sheets/detail/cardiovascular-diseases-(cvds) (2026).
7. Our World in Data. Causes of death. Available at https://ourworldindata.org/grapher/annual-number-of-deaths-by-cause (2026).
8. Murray, C. J. L. The Global Burden of Disease Study at 30 years. *Nature medicine* **28,** 2019–2026; 10.1038/s41591-022-01990-1 (2022).
9. Global Health Estimates: Life expectancy and leading causes of death and disability. Available at https://www.who.int/data/gho/data/themes/mortality-and-global-health-estimates (2026).
10. King, S. J. *et al.* Heart Disease Mortality in the United States, 1970 to 2022. *Journal of the American Heart Association* **14,** e038644; 10.1161/JAHA.124.038644 (2025).
11. Hausenloy, D. J. *et al.* Targeting reperfusion injury in patients with ST-segment elevation myocardial infarction: trials and tribulations. *European heart journal* **38,** 935–941; 10.1093/eurheartj/ehw145 (2017).
12. American Heart Association. 2026 Heart Disease and Stroke Statistics Update Fact Sheet At-a-Glance. Available at https://professional.heart.org/en/science-news/-/media/BC342ED991C24EE38C7DF485238BF0D4.ashx (2026).

13. Global Oncology Trends 2025. Adopting new therapies as modalities shift and expenditures rise. Available at https://www.iqvia.com/insights/the-iqvia-institute/reports-and-publications/reports/global-oncology-trends-2025 (2025).

14. Hartung, T. The (misleading) role of animal models in drug development. *Front. Drug Discov.* **4**; 10.3389/fddsv.2024.1355044 (2024).

15. Cao, Y., Vacanti, J. P., Paige, K. T., Upton, J. & Vacanti, C. A. Transplantation of Chondrocytes Utilizing a Polymer-Cell Construct to Produce Tissue-Engineered Cartilage in the Shape of a Human Ear. *Plastic and Reconstructive Surgery* **100,** 297–302 (1997).

16. Bhavya Lal, Jessica Viola, Dr. Diana Hicks, Ph.D., Dr. Oren Grad, Ph.D., MD. The Emergence of Tissue Engineering as a Research Field.

17. Gandhi, M. A. & Patil, B. K. Sushruta: The Father of Surgery and Ancient Medical Innovations. *Cureus* **16,** e70577; 10.7759/cureus.70577 (2024).

18. Harrison, R. G., Greenman, M. J., Mall, F. P. & Jackson, C. M. Observations of the living developing nerve fiber. *Anat. Rec.* **1,** 116–128; 10.1002/ar.1090010503 (1907).

19. O'Brien, F. J. Biomaterials & scaffolds for tissue engineering. *Materials Today* **14,** 88–95; 10.1016/S1369-7021(11)70058-X (2011).

20. Demirel, G. & Koltuk, G. The importance of 3D cell culture in drug discovery and development. *Frontiers in Life Sciences and Related Technologies* **5,** 224–230; 10.51753/flsrt.1488871 (2024).

21. Lancaster, M. A. & Knoblich, J. A. Organogenesis in a dish: modeling development and disease using organoid technologies. *Science (New York, N.Y.)* **345,** 1247125; 10.1126/science.1247125 (2014).

22. Sato, T. *et al.* Single Lgr5 stem cells build crypt-villus structures in vitro without a mesenchymal niche. *Nature* **459,** 262–265; 10.1038/nature07935 (2009).

23. Rouwkema, J., Rivron, N. C. & van Blitterswijk, C. A. Vascularization in tissue engineering. *Trends in Biotechnology* **26,** 434–441; 10.1016/j.tibtech.2008.04.009 (2008).

24. Carmeliet, P. & Jain, R. K. Angiogenesis in cancer and other diseases. *Nature* **407,** 249–257; 10.1038/35025220 (2000).

25. Liang, P. *et al.* Drug screening using a library of human induced pluripotent stem cell-derived cardiomyocytes reveals disease-specific patterns of cardiotoxicity. *Circulation* **127,** 1677–1691; 10.1161/CIRCULATIONAHA.113.001883 (2013).

26. *Engineering Cardiovascular Tissue Chips for Disease Modeling and Drug Screening Applications* ,

27. Merino, J. L. *et al.* Practical compendium of antiarrhythmic drugs: a clinical consensus statement of the European Heart Rhythm Association of the European Society of Cardiology. *EP Europace* **27**; 10.1093/europace/euaf076 (2025).

28. Regina, A. C., Rehman, R. & Hai, O. *StatPearls. Cardiac Glycoside and Digoxin Toxicity* (Treasure Island (FL), 2025).

29. MedlinePlus. Warfarin sensitivity. Available at https://medlineplus.gov/genetics/condition/warfarin-sensitivity/ (2026).

30. Roden, D. M. Drug-induced prolongation of the QT interval. *The New England journal of medicine* **350,** 1013–1022; 10.1056/NEJMra032426 (2004).

31. Sanguinetti, M. C. & Tristani-Firouzi, M. hERG potassium channels and cardiac arrhythmia. *Nature* **440,** 463–469; 10.1038/nature04710 (2006).

32. Boisaubin, E. V. Cardiology in ancient Egypt. *Texas Heart Institute journal* **15,** 80–85 (1988).

33. Bestetti, R. B., Restini, C. B. A. & Couto, L. B. Development of anatomophysiologic knowledge regarding the cardiovascular system: from Egyptians to Harvey. *Arquivos brasileiros de cardiologia* **103,** 538–545; 10.5935/abc.20140148 (2014).

34. HART, G. D. ASCLEPIUS, GOD OF MEDICINE. *Canadian Medical Association journal* **92,** 232–236 (1965).

35. Mavrodi, A. & Paraskevas, G. Morphology of the heart associated with its function as conceived by ancient Greeks. *International Journal of Cardiology* **172,** 23–28; 10.1016/j.ijcard.2013.12.124 (2014).

36. Shoja, M. M. *et al.* Leonardo da Vinci's studies of the heart. *International Journal of Cardiology* **167,** 1126–1133; 10.1016/j.ijcard.2012.09.078 (2013).

37. NHLBI, N. I. How Blood Flows through the Heart. Available at https://www.nhlbi.nih.gov/health/heart/blood-flow (2026).

38. Rehman, I. & Rehman, A. *StatPearls. Anatomy, Thorax, Heart* (Treasure Island (FL), 2025).

39. Septum of the heart: Function, defects, and more. Available at https://www.medicalnewstoday.com/articles/septum-heart (2022).

40. Kurapati, R., Heaton, J. & Lowery, D. R. *StatPearls. Atrial Kick* (Treasure Island (FL), 2025).

41. 17.2B: Operation of Atrioventricular Valves. *Libretexts* (2018).

42. Secomb, T. W. Hemodynamics. *Comprehensive Physiology* **6,** 975–1003; 10.1002/j.2040-4603.2016.tb00700.x (2016).

43. Vonk Noordegraaf, A. *et al.* Pathophysiology of the right ventricle and of the pulmonary circulation in pulmonary hypertension: an update. *The European respiratory journal* **53**; 10.1183/13993003.01900-2018 (2019).

44. Lang, R. M., Borow, K. M., Neumann, A. & Janzen, D. Systemic vascular resistance: an unreliable index of left ventricular afterload. *Circulation* **74,** 1114–1123; 10.1161/01.CIR.74.5.1114 (1986).

45. Christoffels, V. & Jensen, B. Cardiac Morphogenesis: Specification of the Four-Chambered Heart. *Cold Spring Harbor perspectives in biology* **12**; 10.1101/cshperspect.a037143 (2020).

46. Anderson, R. H., Yanni, J., Boyett, M. R., Chandler, N. J. & Dobrzynski, H. The anatomy of the cardiac conduction system. *Clinical anatomy (New York, N.Y.)* **22,** 99–113; 10.1002/ca.20700 (2009).

47. Accili, E. A., Proenza, C., Baruscotti, M. & DiFrancesco, D. From funny current to HCN channels: 20 years of excitation. *News in physiological sciences : an international journal of physiology produced jointly by the International Union of Physiological Sciences and the American Physiological Society* **17,** 32–37; 10.1152/physiologyonline.2002.17.1.32 (2002).

48. Mangoni, M. E. & Nargeot, J. Genesis and regulation of the heart automaticity. *Physiological reviews* **88,** 919–982; 10.1152/physrev.00018.2007 (2008).

49. Schlotthauer, K. & Bers, D. M. Sarcoplasmic reticulum Ca(2+) release causes myocyte depolarization. Underlying mechanism and threshold for triggered action potentials. *Circulation research* **87,** 774–780; 10.1161/01.RES.87.9.774 (2000).

50. Nagy, N. *et al.* Role of Ca^{2}+-sensitive K+ currents in controlling ventricular repolarization: possible implications for future antiarrhytmic drug therapy. *Current medicinal chemistry* **18,** 3622–3639; 10.2174/092986711796642463 (2011).

51. Ripa, R., George, T., Shumway, K. R. & Sattar, Y. *StatPearls. Physiology, Cardiac Muscle* (Treasure Island (FL), 2025).

52. Watanabe, T., Rautaharju, P. M. & McDonald, T. F. Ventricular action potentials, ventricular extracellular potentials, and the ECG of guinea pig. *Circulation research* **57,** 362–373; 10.1161/01.RES.57.3.362 (1985).

53. Kashani, A. & Barold, S. S. Significance of QRS complex duration in patients with heart failure. *Journal of the American College of Cardiology* **46,** 2183–2192; 10.1016/j.jacc.2005.01.071 (2005).

54. Hope, R. R., Scherlag, B. J., El-Sherif, N. & Lazzara, R. Hierarchy of ventricular pacemakers. *Circulation research* **39,** 883–888; 10.1161/01.RES.39.6.883 (1976).

55. Robinson, R. B. & Siegelbaum, S. A. Hyperpolarization-activated cation currents: from molecules to physiological function. *Annual review of physiology* **65,** 453–480; 10.1146/annurev.physiol.65.092101.142734 (2003).

56. Tse, G. Mechanisms of cardiac arrhythmias. *Journal of arrhythmia* **32,** 75–81; 10.1016/j.joa.2015.11.003 (2016).

57. Early afterdepolarizations: mechanism of induction and block. A role for L-type Ca2+ current.

58. Miake, J., Marbán, E. & Nuss, H. B. Biological pacemaker created by gene transfer. *Nature* **419,** 132–133; 10.1038/419132b (2002).

59. Lei, M., Salvage, S. C., Jackson, A. P. & Huang, C. L.-H. Cardiac arrhythmogenesis: roles of ion channels and their functional modification. *Frontiers in physiology* **15,** 1342761; 10.3389/fphys.2024.1342761 (2024).

60. King, J. H., Huang, C. L.-H. & Fraser, J. A. Determinants of myocardial conduction velocity: implications for arrhythmogenesis. *Frontiers in physiology* **4,** 154; 10.3389/fphys.2013.00154 (2013).

61. Zhou, P. & Pu, W. T. Recounting Cardiac Cellular Composition. *Circulation research* **118,** 368–370; 10.1161/CIRCRESAHA.116.308139 (2016).

62. Stephenson, R. S. *et al.* The functional architecture of skeletal compared to cardiac musculature: Myocyte orientation, lamellar unit morphology, and the helical ventricular myocardial band. *Clinical anatomy (New York, N.Y.)* **29,** 316–332; 10.1002/ca.22661 (2016).

63. Zhao, G., Qiu, Y., Zhang, H. M. & Yang, D. Intercalated discs: cellular adhesion and signaling in heart health and diseases. *Heart failure reviews* **24,** 115–132; 10.1007/s10741-018-9743-7 (2019).

64. Park, S.-Y. *et al.* Cardiac, skeletal, and smooth muscle mitochondrial respiration: are all mitochondria created equal? *American journal of physiology. Heart and circulatory physiology* **307,** H346-52; 10.1152/ajpheart.00227.2014 (2014).

65. Lundby, C. & Jacobs, R. A. Adaptations of skeletal muscle mitochondria to exercise training. *Experimental physiology* **101,** 17–22; 10.1113/EP085319 (2016).

66. Windmueller, R. *et al.* Direct Comparison of Mononucleated and Binucleated Cardiomyocytes Reveals Molecular Mechanisms Underlying Distinct Proliferative Competencies. *Cell reports* **30,** 3105-3116.e4; 10.1016/j.celrep.2020.02.034 (2020).

67. Landim-Vieira, M., Schipper, J. M., Pinto, J. R. & Chase, P. B. Cardiomyocyte nuclearity and ploidy: when is double trouble? *Journal of muscle research and cell motility* **41,** 329–340; 10.1007/s10974-019-09545-7 (2020).

68. Martin, R. R. & Haines, H. Application of Laplace's law to mammalian hearts. *Comparative Biochemistry and Physiology* **34,** 959–962; 10.1016/0010-406X(70)91019-4 (1970).

69. Benitah, J.-P., Perrier, R., Mercadier, J.-J., Pereira, L. & Gómez, A. M. RyR2 and Calcium Release in Heart Failure. *Frontiers in physiology* **12,** 734210; 10.3389/fphys.2021.734210 (2021).

70. Lanner, J. T., Georgiou, D. K., Joshi, A. D. & Hamilton, S. L. Ryanodine receptors: structure, expression, molecular details, and function in calcium release. *Cold Spring Harbor perspectives in biology* **2,** a003996; 10.1101/cshperspect.a003996 (2010).

71. Catterall, W. A. From Ionic Currents to Molecular Mechanisms: The Structure and Function of Voltage-Gated Sodium Channels. *Neuron* **26,** 13–25; 10.1016/S0896-6273(00)81133-2 (2000).

72. Camelliti, P., Borg, T. K. & Kohl, P. Structural and functional characterisation of cardiac fibroblasts. *Cardiovascular research* **65,** 40–51; 10.1016/j.cardiores.2004.08.020 (2005).

73. Souders, C. A., Bowers, S. L. K. & Baudino, T. A. Cardiac fibroblast: the renaissance cell. *Circulation research* **105,** 1164–1176; 10.1161/CIRCRESAHA.109.209809 (2009).

74. Spinale, F. G. Myocardial matrix remodeling and the matrix metalloproteinases: influence on cardiac form and function. *Physiological reviews* **87,** 1285–1342; 10.1152/physrev.00012.2007 (2007).

75. Takawale, A. *et al.* Tissue Inhibitor of Matrix Metalloproteinase-1 Promotes Myocardial Fibrosis by Mediating CD63-Integrin β1 Interaction. *Hypertension (Dallas, Tex. : 1979)* **69,** 1092–1103; 10.1161/HYPERTENSIONAHA.117.09045 (2017).

76. Pope, A. J., Sands, G. B., Smaill, B. H. & LeGrice, I. J. Three-dimensional transmural organization of perimysial collagen in the heart. *American journal of physiology. Heart and circulatory physiology* **295,** H1243-H1252; 10.1152/ajpheart.00484.2008 (2008).

77. Aird, W. C. Phenotypic heterogeneity of the endothelium: I. Structure, function, and mechanisms. *Circulation research* **100,** 158–173; 10.1161/01.RES.0000255691.76142.4a (2007).

78. Brutsaert, D. L. Cardiac endothelial-myocardial signaling: its role in cardiac growth, contractile performance, and rhythmicity. *Physiological reviews* **83,** 59–115; 10.1152/physrev.00017.2002 (2003).

79. Poole, D. C., Musch, T. I. & Colburn, T. D. Oxygen flux from capillary to mitochondria: integration of contemporary discoveries. *European journal of applied physiology* **122,** 7–28; 10.1007/s00421-021-04854-7 (2022).

80. Boland, E., Quondamatteo, F. & van Agtmael, T. The role of basement membranes in cardiac biology and disease. *Bioscience reports* **41**; 10.1042/BSR20204185 (2021).

81. Massion, P. B., Feron, O., Dessy, C. & Balligand, J.-L. Nitric oxide and cardiac function: ten years after, and continuing. *Circulation research* **93,** 388–398; 10.1161/01.RES.0000088351.58510.21 (2003).

82. Karsner, H. T., Saphir, O. & Todd, T. W. The State of the Cardiac Muscle in Hypertrophy and Atrophy. *The American journal of pathology* **1,** 351-372.1 (1925).

83. Beltrami, A. P. *et al.* Adult cardiac stem cells are multipotent and support myocardial regeneration. *Cell* **114,** 763–776; 10.1016/S0092-8674(03)00687-1 (2003).

84. Urbanek, K. *et al.* Stem cell niches in the adult mouse heart. *Proceedings of the National Academy of Sciences of the United States of America* **103,** 9226–9231; 10.1073/pnas.0600635103 (2006).

85. Barker, N. *et al.* Identification of stem cells in small intestine and colon by marker gene Lgr5. *Nature* **449,** 1003–1007; 10.1038/nature06196 (2007).

86. Sender, R. & Milo, R. The distribution of cellular turnover in the human body. *Nature medicine* **27,** 45–48; 10.1038/s41591-020-01182-9 (2021).

87. Arsalan, M. *et al.* Distribution of cardiac stem cells in the human heart. *ISRN cardiology* **2012,** 483407; 10.5402/2012/483407 (2012).

88. Bergmann, O. *et al.* Evidence for cardiomyocyte renewal in humans. *Science (New York, N.Y.)* **324,** 98–102; 10.1126/science.1164680 (2009).

89. Bergmann, O. *et al.* Dynamics of Cell Generation and Turnover in the Human Heart. *Cell* **161,** 1566–1575; 10.1016/j.cell.2015.05.026 (2015).

90. Senyo, S. E. *et al.* Mammalian heart renewal by pre-existing cardiomyocytes. *Nature* **493,** 433–436; 10.1038/nature11682 (2013).

91. van Berlo, J. H. *et al.* c-kit+ cells minimally contribute cardiomyocytes to the heart. *Nature* **509,** 337–341; 10.1038/nature13309 (2014).

92. Elhelaly, W. M. *et al.* C-Kit Cells Do Not Significantly Contribute to Cardiomyogenesis During Neonatal Heart Regeneration. *Circulation* **139,** 559–561; 10.1161/CIRCULATIONAHA.117.033150 (2019).

93. Lunt, S. Y. & Vander Heiden, M. G. Aerobic glycolysis: meeting the metabolic requirements of cell proliferation. *Annual review of cell and developmental biology* **27,** 441–464; 10.1146/annurev-cellbio-092910-154237 (2011).

94. Chaudhry, R. & Varacallo, M. A. *StatPearls. Biochemistry, Glycolysis* (Treasure Island (FL), 2025).

95. Martínez-Reyes, I. & Chandel, N. S. Mitochondrial TCA cycle metabolites control physiology and disease. *Nature communications* **11,** 102; 10.1038/s41467-019-13668-3 (2020).

96. Krebs, H. A. & Johnson, W. A. The role of citric acid in intermediate metabolism in animal tissues. *FEBS Letters* **117**; 10.1016/0014-5793(80)80564-3 (1980).

97. Akram, M. Citric acid cycle and role of its intermediates in metabolism. *Cell biochemistry and biophysics* **68,** 475–478; 10.1007/s12013-013-9750-1 (2014).

98. MITCHELL, P. Coupling of phosphorylation to electron and hydrogen transfer by a chemi-osmotic type of mechanism. *Nature* **191,** 144–148; 10.1038/191144a0 (1961).

99. Boyer, P. D. The ATP synthase--a splendid molecular machine. *Annual review of biochemistry* **66,** 717–749; 10.1146/annurev.biochem.66.1.717 (1997).

100. Rich, P. R. The molecular machinery of Keilin's respiratory chain. *Biochemical Society transactions* **31,** 1095–1105; 10.1042/bst0311095 (2003).

101. Lehman, J. J. & Kelly, D. P. Transcriptional activation of energy metabolic switches in the developing and hypertrophied heart. *Clinical and experimental pharmacology & physiology* **29,** 339–345; 10.1046/j.1440-1681.2002.03655.x (2002).

102. Cha, S.-E., Lee, M. N. & Kim, E.-S. Metabolic impacts of long-chain fatty acids on cardiomyocyte maturation in neonatal mammalian hearts. *Methods (San Diego, Calif.)* **241,** 114–127; 10.1016/j.ymeth.2025.05.010 (2025).

103. Abouleisa, R. R. E., Farraj, K. A., Mehta, S. G. & Mohamed, T. M. A. Cardiomyocyte maturation and proliferation is a flip coin. *BMC cardiovascular disorders* **25,** 880; 10.1186/s12872-025-05360-w (2025).

104. McGarry, J. D. & Brown, N. F. The mitochondrial carnitine palmitoyltransferase system. From concept to molecular analysis. *European journal of biochemistry* **244,** 1–14; 10.1111/j.1432-1033.1997.00001.x (1997).

105. Weis, B. C., Cowan, A. T., Brown, N., Foster, D. W. & McGarry, J. D. Use of a selective inhibitor of liver carnitine palmitoyltransferase I (CPT I) allows quantification of its contribution to total CPT I activity in rat heart. Evidence that the dominant cardiac CPT I isoform is identical to the skeletal muscle enzyme. *Journal of Biological Chemistry* **269,** 26443–26448; 10.1016/S0021-9258(18)47214-6 (1994).

106. Bartelds, B. *et al.* Myocardial carnitine palmitoyltransferase I expression and long-chain fatty acid oxidation in fetal and newborn lambs. *American journal of physiology. Heart and circulatory physiology* **286,** H2243-8; 10.1152/ajpheart.00864.2003 (2004).

107. SHIPP, J. C., OPIE, L. H. & CHALLONER, D. Fatty Acid and Glucose Metabolism in the Perfused Heart. *Nature* **189,** 1018–1019; 10.1038/1891018a0 (1961).

108. Hue, L. & Taegtmeyer, H. The Randle cycle revisited: a new head for an old hat. *American journal of physiology. Endocrinology and metabolism* **297,** E578-91; 10.1152/ajpendo.00093.2009 (2009).

109. Stanley, W. C., Recchia, F. A. & Lopaschuk, G. D. Myocardial substrate metabolism in the normal and failing heart. *Physiological reviews* **85,** 1093–1129; 10.1152/physrev.00006.2004 (2005).

110. Standage, S. W. *et al.* PPARα augments heart function and cardiac fatty acid oxidation in early experimental polymicrobial sepsis. *American journal of physiology. Heart and circulatory physiology* **312,** H239-H249; 10.1152/ajpheart.00457.2016 (2017).

111. Murray, A. J., Anderson, R. E., Watson, G. C., Radda, G. K. & Clarke, K. Uncoupling proteins in human heart. *The Lancet* **364,** 1786–1788; 10.1016/S0140-6736(04)17402-3 (2004).

112. OPIE, L. H. The metabolic vicious cycle in heart failure. *The Lancet* **364,** 1733–1734; 10.1016/S0140-6736(04)17412-6 (2004).

113. van Putten, S., Shafieyan, Y. & Hinz, B. Mechanical control of cardiac myofibroblasts. *Journal of molecular and cellular cardiology* **93,** 133–142; 10.1016/j.yjmcc.2015.11.025 (2016).

114. Gaetani, R. *et al.* When Stiffness Matters: Mechanosensing in Heart Development and Disease. *Frontiers in cell and developmental biology* **8,** 334; 10.3389/fcell.2020.00334 (2020).

115. Brilla, C. G. & Weber, K. T. Reactive and reparative myocardial fibrosis in arterial hypertension in the rat. *Cardiovascular research* **26,** 671–677; 10.1093/cvr/26.7.671 (1992).

116. Brilla, C. G., Matsubara, L. S. & Weber, K. T. Antifibrotic effects of spironolactone in preventing myocardial fibrosis in systemic arterial hypertension. *The American journal of cardiology* **71,** 12A-16A; 10.1016/0002-9149(93)90239-9 (1993).

117. Czubryt, M. P. & Hale, T. M. Cardiac fibrosis: Pathobiology and therapeutic targets. *Cellular signalling* **85,** 110066; 10.1016/j.cellsig.2021.110066 (2021).

118. Frangogiannis, N. G. Cardiac fibrosis. *Cardiovascular research* **117,** 1450–1488; 10.1093/cvr/cvaa324 (2021).

119. Burlew, B. S. & Weber, K. T. Cardiac fibrosis as a cause of diastolic dysfunction. *Herz* **27,** 92–98; 10.1007/s00059-002-2354-y (2002).

120. Ling, L.-H. *et al.* Diffuse ventricular fibrosis in atrial fibrillation: noninvasive evaluation and relationships with aging and systolic dysfunction. *Journal of the American College of Cardiology* **60,** 2402–2408; 10.1016/j.jacc.2012.07.065 (2012).

121. Nguyen, T. P., Qu, Z. & Weiss, J. N. Cardiac fibrosis and arrhythmogenesis: the road to repair is paved with perils. *Journal of molecular and cellular cardiology* **70,** 83–91; 10.1016/j.yjmcc.2013.10.018 (2014).

122. Li, M., Delafontaine, P. & Sukhanov, S. Coronary atherosclerotic plaque composition and classification in hypercholesterimic pigs. *bioRxiv : the preprint server for biology*; 10.1101/2025.06.06.658319 (2025).

123. Pahwa, R. & Jialal, I. *StatPearls. Atherosclerosis* (Treasure Island (FL), 2025).

124. Loftus, I. *Mechanisms of Vascular Disease: A Reference Book for Vascular Specialists. Mechanisms of Plaque Rupture* (Adelaide (AU), 2011).

125. Guldner, N. W. *et al.* Biomechanical hearts: muscular blood pumps, performed in a 1-step operation, and trained under support of clenbuterol. *Circulation* **104,** 717–722; 10.1161/hc3301.092786 (2001).

126. Allen, D. G. & Orchard, C. H. Myocardial contractile function during ischemia and hypoxia. *Circulation research* **60,** 153–168; 10.1161/01.RES.60.2.153 (1987).

127. Jennings, R. B. Historical perspective on the pathology of myocardial ischemia/reperfusion injury. *Circulation research* **113,** 428–438; 10.1161/CIRCRESAHA.113.300987 (2013).

128. Kentish, J. C. The effects of inorganic phosphate and creatine phosphate on force production in skinned muscles from rat ventricle. *The Journal of physiology* **370,** 585–604; 10.1113/jphysiol.1986.sp015952 (1986).

129. Godt, R. E. & Nosek, T. M. Changes of intracellular milieu with fatigue or hypoxia depress contraction of skinned rabbit skeletal and cardiac muscle. *The Journal of physiology* **412,** 155–180; 10.1113/jphysiol.1989.sp017609 (1989).

130. Akaishi, M. *et al.* Analysis of systolic bulging. Mechanical characteristics of acutely ischemic myocardium in the conscious dog. *Circulation research* **58,** 209–217; 10.1161/01.RES.58.2.209 (1986).

131. Ojha, N. & Dhamoon, A. S. *StatPearls. Myocardial Infarction* (Treasure Island (FL), 2025).

132. Theroux, P. *et al.* Regional myocardial function and dimensions early and late after myocardial infarction in the unanesthetized dog. *Circulation research* **40,** 158–165; 10.1161/01.RES.40.2.158 (1977).

133. Reimer, K. A. & Jennings, R. B. Energy metabolism in the reversible and irreversible phases of severe myocardial ischemia. *Acta medica Scandinavica. Supplementum* **651,** 19–27; 10.1111/j.0954-6820.1981.tb03628.x (1981).

134. Kloner, R. A. & Jennings, R. B. Consequences of brief ischemia: stunning, preconditioning, and their clinical implications: part 2. *Circulation* **104,** 3158–3167; 10.1161/hc5001.100039 (2001).

135. Lopaschuk, G. D., Ussher, J. R., Folmes, C. D. L., Jaswal, J. S. & Stanley, W. C. Myocardial fatty acid metabolism in health and disease. *Physiological reviews* **90,** 207–258; 10.1152/physrev.00015.2009 (2010).

136. Hardie, D. G. AMPK: a target for drugs and natural products with effects on both diabetes and cancer. *Diabetes* **62,** 2164–2172; 10.2337/db13-0368 (2013).

137. Hariharan, N., Zhai, P. & Sadoshima, J. Oxidative stress stimulates autophagic flux during ischemia/reperfusion. *Antioxidants & redox signaling* **14,** 2179–2190; 10.1089/ars.2010.3488 (2011).

138. Sun, D., Nguyen, N., DeGrado, T. R., Schwaiger, M. & Brosius, F. C. Ischemia induces translocation of the insulin-responsive glucose transporter GLUT4 to the plasma membrane of cardiac myocytes. *Circulation* **89,** 793–798; 10.1161/01.CIR.89.2.793 (1994).

139. Wheaton, W. W. & Chandel, N. S. Hypoxia. 2. Hypoxia regulates cellular metabolism. *American journal of physiology. Cell physiology* **300,** C385-93; 10.1152/ajpcell.00485.2010 (2011).

140. Valdebenito, G. E., Chacko, A. R. & Duchen, M. R. The mitochondrial ATP synthase as an ATP consumer-a surprising therapeutic target. *The EMBO journal* **42,** e114141; 10.15252/embj.2023114141 (2023).

141. St-Pierre, J., Brand, M. D. & Boutilier, R. G. Mitochondria as ATP consumers: cellular treason in anoxia. *Proceedings of the National Academy of Sciences of the United States of America* **97,** 8670–8674; 10.1073/pnas.140093597 (2000).

142. Schirone, L. *et al.* An Overview of the Molecular Mechanisms Associated with Myocardial Ischemic Injury: State of the Art and Translational Perspectives. *Cells* **11**; 10.3390/cells11071165 (2022).

143. Glitsch, H. G. & Tappe, A. The Na+/K+ pump of cardiac Purkinje cells is preferentially fuelled by glycolytic ATP production. *Pflugers Archiv : European journal of physiology* **422,** 380–385; 10.1007/BF00374294 (1993).

144. Jeremy, R. W., Koretsune, Y., Marban, E. & Becker, L. C. Relation between glycolysis and calcium homeostasis in postischemic myocardium. *Circulation research* **70,** 1180–1190; 10.1161/01.RES.70.6.1180 (1992).

145. Bernardi, P. & Di Lisa, F. The mitochondrial permeability transition pore: molecular nature and role as a target in cardioprotection. *Journal of molecular and cellular cardiology* **78,** 100–106; 10.1016/j.yjmcc.2014.09.023 (2015).

146. Hausenloy, D. J. & Yellon, D. M. The mitochondrial permeability transition pore: its fundamental role in mediating cell death during ischaemia and reperfusion. *Journal of molecular and cellular cardiology* **35,** 339–341; 10.1016/S0022-2828(03)00043-9 (2003).

147. Ong, S.-B., Samangouei, P., Kalkhoran, S. B. & Hausenloy, D. J. The mitochondrial permeability transition pore and its role in myocardial ischemia reperfusion injury. *Journal of molecular and cellular cardiology* **78,** 23–34; 10.1016/j.yjmcc.2014.11.005 (2015).

148. Lemasters, J. J. *et al.* The pH paradox in ischemia-reperfusion injury to cardiac myocytes. *EXS* **76,** 99–114; 10.1007/978-3-0348-8988-9_7 (1996).

149. Becker, L. B. New concepts in reactive oxygen species and cardiovascular reperfusion physiology. *Cardiovascular research* **61,** 461–470; 10.1016/j.cardiores.2003.10.025 (2004).

150. Zorov, D. B., Filburn, C. R., Klotz, L. O., Zweier, J. L. & Sollott, S. J. Reactive oxygen species (ROS)-induced ROS release: a new phenomenon accompanying induction of the mitochondrial permeability transition in cardiac myocytes. *The Journal of experimental medicine* **192,** 1001–1014; 10.1084/jem.192.7.1001 (2000).

151. Chouchani, E. T. *et al.* Ischaemic accumulation of succinate controls reperfusion injury through mitochondrial ROS. *Nature* **515,** 431–435; 10.1038/nature13909 (2014).

152. Bulteau, A. L. *et al.* Oxidative modification and inactivation of the proteasome during coronary occlusion/reperfusion. *Journal of Biological Chemistry* **276,** 30057–30063; 10.1074/jbc.M100142200 (2001).

153. Garcia, L. A. *et al.* Magnesium reduces free radicals in an in vivo coronary occlusion-reperfusion model. *Journal of the American College of Cardiology* **32,** 536–539; 10.1016/S0735-1097(98)00231-9 (1998).

154. Jolly, S. R. & Lucchesi, B. R. Effect of BW755C in an occlusion-reperfusion model of ischemic myocardial injury. *American heart journal* **106,** 8–13; 10.1016/0002-8703(83)90431-3 (1983).

155. Watanabe, M. & Okada, T. Langendorff Perfusion Method as an Ex Vivo Model to Evaluate Heart Function in Rats. *Methods in molecular biology (Clifton, N.J.)* **1816,** 107–116; 10.1007/978-1-4939-8597-5_8 (2018).

156. Muessig, J. M. *et al.* A Model of Blood Component-Heart Interaction in Cardiac Ischemia-Reperfusion Injury using a Langendorff-Based Ex Vivo Assay. *Journal of cardiovascular pharmacology and therapeutics* **25,** 164–173; 10.1177/1074248419874348 (2020).

157. Zhang, R., Li, L., Yuan, L. & Zhao, M. Hypoxic preconditioning protects cardiomyocytes against hypoxia/reoxygenation-induced cell apoptosis via sphingosine kinase 2 and FAK/AKT pathway. *Experimental and molecular pathology* **100,** 51–58; 10.1016/j.yexmp.2015.11.025 (2016).

158. Wen, J. *et al.* The optimization conditions of establishing an H9c2 cardiomyocyte hypoxia/reoxygenation injury model based on an AnaeroPack System. *Cell biology international* **45,** 757–765; 10.1002/cbin.11513 (2021).

159. Iwoń, Z., Krogulec, E., Kierlańczyk, A., Wojasiński, M. & Jastrzębska, E. Hypoxia and re-oxygenation effects on human cardiomyocytes cultured on polycaprolactone and polyurethane nanofibrous mats. *Journal of biological engineering* **18,** 37; 10.1186/s13036-024-00432-5 (2024).

160. Qiu, F. *et al.* A decrease of ATP production steered by PEDF in cardiomyocytes with oxygen-glucose deprivation is associated with an AMPK-dependent degradation pathway. *International Journal of Cardiology* **257,** 262–271; 10.1016/j.ijcard.2018.01.034 (2018).

161. Li, F. *et al.* Quercetin Protects H9c2 Cardiomyocytes against Oxygen-Glucose Deprivation/Reoxygenation-Induced Oxidative Stress and Mitochondrial Apoptosis by Regulating the ERK1/2/DRP1 Signaling Pathway. *Evidence-based complementary and alternative medicine : eCAM* **2021,** 7522175; 10.1155/2021/7522175 (2021).

162. Hidalgo, A. *et al.* Modelling ischemia-reperfusion injury (IRI) in vitro using metabolically matured induced pluripotent stem cell-derived cardiomyocytes. *APL bioengineering* **2,** 26102; 10.1063/1.5000746 (2018).

163. Esumi, K., Nishida, M., Shaw, D., Smith, T. W. & Marsh, J. D. NADH measurements in adult rat myocytes during simulated ischemia. *The American journal of physiology* **260,** H1743-52; 10.1152/ajpheart.1991.260.6.h1743 (1991).

164. Townsend, P. A. *et al.* BAG-1 proteins protect cardiac myocytes from simulated ischemia/reperfusion-induced apoptosis via an alternate mechanism of cell survival independent of the proteasome. *Journal of Biological Chemistry* **279,** 20723–20728; 10.1074/jbc.M400399200 (2004).

165. Vinokurov, A. Y. *et al.* Cytoprotective Action of Sodium Fumarate in an in vitro Model of Hypoxia Using Sodium Dithionite. *Sovremennye tekhnologii v meditsine* **17,** 93–106; 10.17691/stm2025.17.1.09 (2025).

166. Muñoz-Sánchez, J. & Chánez-Cárdenas, M. E. The use of cobalt chloride as a chemical hypoxia model. *Journal of applied toxicology : JAT* **39,** 556–570; 10.1002/jat.3749 (2019).

167. Rinderknecht, H. *et al.* The Art of Inducing Hypoxia. *Oxygen* **1,** 46–61; 10.3390/oxygen1010006 (2021).

168. Veldhuizen, J. *et al.* Cardiac ischemia on-a-chip to investigate cellular and molecular response of myocardial tissue under hypoxia. *Biomaterials* **281,** 121336; 10.1016/j.biomaterials.2021.121336 (2022).

169. Rexius-Hall, M. L. *et al.* A myocardial infarct border-zone-on-a-chip demonstrates distinct regulation of cardiac tissue function by an oxygen gradient. *Science advances* **8,** eabn7097; 10.1126/sciadv.abn7097 (2022).

170. Lynch, T. & Price, A. The effect of cytochrome P450 metabolism on drug response, interactions, and adverse effects. *American family physician* **76,** 391–396 (2007).

171. Duarte, J. D. & Cavallari, L. H. Pharmacogenetics to guide cardiovascular drug therapy. *Nature reviews. Cardiology* **18,** 649–665; 10.1038/s41569-021-00549-w (2021).

172. Zhang, H. *et al.* Impact of CYP2C19 gene polymorphism on warfarin maintenance doses in patients with non-valvular atrial fibrillation. *Gene* **591,** 80–84; 10.1016/j.gene.2016.06.046 (2016).

173. Veerman, C. C., Wilde, A. A. M. & Lodder, E. M. The cardiac sodium channel gene SCN5A and its gene product NaV1.5: Role in physiology and pathophysiology. *Gene* **573,** 177–187; 10.1016/j.gene.2015.08.062 (2015).

174. Yang, L., Katchman, A., Morrow, J. P., Doshi, D. & Marx, S. O. Cardiac L-type calcium channel (Cav1.2) associates with gamma subunits. *FASEB journal : official publication of the Federation of American Societies for Experimental Biology* **25,** 928–936; 10.1096/fj.10-172353 (2011).

175. Splawski, I. *et al.* Ca(V)1.2 calcium channel dysfunction causes a multisystem disorder including arrhythmia and autism. *Cell* **119,** 19–31; 10.1016/j.cell.2004.09.011 (2004).

176. Duan, J. *et al.* Anticancer drugs-related QTc prolongation, torsade de pointes and sudden death: current evidence and future research perspectives. *Oncotarget* **9,** 25738–25749; 10.18632/oncotarget.25008 (2018).

177. Dorange, I. & Swahn, B.-M. Recent Progress in the Discovery of Kv7 Modulators (Elsevier2011), Vol. 46, pp. 53–65.

178. Vornanen, M. DESIGN AND PHYSIOLOGY OF THE HEART | Action Potential of the Fish Heart. In *Encyclopedia of Fish Physiology* (Elsevier2011), pp. 1038–1044.

179. Carmeliet, E. Repolarization reserve in cardiac cells. *Journal of Medical and Biological Engineering* **26,** 97–105 (2006).

180. Wei, X., Yohannan, S. & Richards, J. R. *StatPearls. Physiology, Cardiac Repolarization Dispersion and Reserve* (Treasure Island (FL), 2025).

181. Cesarovic, N., Lipski, M., Falk, V. & Emmert, M. Y. Animals in cardiovascular research: Clinical relevance and translational limitations of animal models in cardiovascular medicine; 10.3929/ethz-b-000391688 (2020).

182. Moriwaki, T., Tani, H. & Tohyama, S. Human induced pluripotent stem cell-derived cardiomyocytes for disease modeling and drug discovery. *Frontiers in bioengineering and biotechnology* **13,** 1687840; 10.3389/fbioe.2025.1687840 (2025).

183. Schwartz, P. J., Crotti, L. & Insolia, R. Long-QT syndrome: from genetics to management. *Circulation. Arrhythmia and electrophysiology* **5,** 868–877; 10.1161/CIRCEP.111.962019 (2012).

184. Smith, L., Quelch-Cliffe, R., Liu, F., Aguilar, A. H. & Przyborski, S. Evaluating Strategies to Assess the Differentiation Potential of Human Pluripotent Stem Cells: A Review, Analysis and Call for Innovation. *Stem cell reviews and reports* **21,** 107–125; 10.1007/s12015-024-10793-5 (2025).

185. Rajala, K., Pekkanen-Mattila, M. & Aalto-Setälä, K. Cardiac differentiation of pluripotent stem cells. *Stem cells international* **2011,** 383709; 10.4061/2011/383709 (2011).

186. Tsoi, C. *et al.* Temporal Control of the WNT Signaling Pathway During Cardiac Differentiation Impacts Upon the Maturation State of Human Pluripotent Stem Cell Derived Cardiomyocytes. *Frontiers in molecular biosciences* **9,** 714008; 10.3389/fmolb.2022.714008 (2022).

187. Lindsley, R. C., Gill, J. G., Kyba, M., Murphy, T. L. & Murphy, K. M. Canonical Wnt signaling is required for development of embryonic stem cell-derived mesoderm. *Development (Cambridge, England)* **133,** 3787–3796; 10.1242/dev.02551 (2006).

188. Yilbas, A. E. *et al.* Activation of GATA4 gene expression at the early stage of cardiac specification. *Frontiers in chemistry* **2,** 12; 10.3389/fchem.2014.00012 (2014).

189. Zhang, J. *et al.* Cardiac differentiation of human pluripotent stem cells using defined extracellular matrix proteins reveals essential role of fibronectin. *eLife* **11**; 10.7554/eLife.69028 (2022).

190. Lauschke, K., Volpini, L., Liu, Y., Vinggaard, A. M. & Hall, V. J. A Comparative Assessment of Marker Expression Between Cardiomyocyte Differentiation of Human Induced Pluripotent Stem Cells and the Developing Pig Heart. *Stem cells and development* **30,** 374–385; 10.1089/scd.2020.0184 (2021).

191. Nakashima, Y. & Tsukahara, M. Effect of iPS cell culture medium on the differentiation potential of induced cardiac tissues. *Scientific reports* **15,** 28301; 10.1038/s41598-025-13259-x (2025).

192. Chambers, I. & Tomlinson, S. R. The transcriptional foundation of pluripotency. *Development (Cambridge, England)* **136,** 2311–2322; 10.1242/dev.024398 (2009).

193. Rizzino, A. Concise review: The Sox2-Oct4 connection: critical players in a much larger interdependent network integrated at multiple levels. *Stem cells (Dayton, Ohio)* **31,** 1033–1039; 10.1002/stem.1352 (2013).

194. Shi, G. & Jin, Y. Role of Oct4 in maintaining and regaining stem cell pluripotency. *Stem cell research & therapy* **1,** 39; 10.1186/scrt39 (2010).

195. Radzisheuskaya, A. *et al.* A defined Oct4 level governs cell state transitions of pluripotency entry and differentiation into all embryonic lineages. *Nature cell biology* **15,** 579–590; 10.1038/ncb2742 (2013).

196. Theunissen, T. W. *et al.* Reprogramming capacity of Nanog is functionally conserved in vertebrates and resides in a unique homeodomain. *Development (Cambridge, England)* **138,** 4853–4865; 10.1242/dev.068775 (2011).

197. Rebuzzini, P., Zuccotti, M., Redi, C. A. & Garagna, S. Achilles' heel of pluripotent stem cells: genetic, genomic and epigenetic variations during prolonged culture. *Cellular and molecular life sciences : CMLS* **73,** 2453–2466; 10.1007/s00018-016-2171-8 (2016).

198. Yang, S., Cho, Y. & Jang, J. Single cell heterogeneity in human pluripotent stem cells. *BMB reports* **54,** 505–515; 10.5483/BMBRep.2021.54.10.094 (2021).

199. Efrat, S. Epigenetic Memory: Lessons From iPS Cells Derived From Human β Cells. *Frontiers in endocrinology* **11,** 614234; 10.3389/fendo.2020.614234 (2020).

200. Poursani, E. M., Mohammad Soltani, B. & Mowla, S. J. Differential Expression of OCT4 Pseudogenes in Pluripotent and Tumor Cell Lines. *Cell journal* **18,** 28–36; 10.22074/cellj.2016.3984 (2016).

201. Schmidt, M., Zeevaert, K., Elsafi Mabrouk, M. H., Goetzke, R. & Wagner, W. Epigenetic biomarkers to track differentiation of pluripotent stem cells. *Stem cell reports* **18,** 145–158; 10.1016/j.stemcr.2022.11.001 (2023).

202. Aghlara-Fotovat, S. *et al.* Delivery of cytokines via encapsulated human astrocytes for neural immunomodulation. *Biomaterials* **326,** 123650; 10.1016/j.biomaterials.2025.123650 (2026).

203. Ren, J. *et al.* A Step-by-Step Refined Strategy for Highly Efficient Generation of Neural Progenitors and Motor Neurons from Human Pluripotent Stem Cells. *Cells* **10**; 10.3390/cells10113087 (2021).

204. Lian, X. *et al.* Directed cardiomyocyte differentiation from human pluripotent stem cells by modulating Wnt/β-catenin signaling under fully defined conditions. *Nature protocols* **8,** 162–175; 10.1038/nprot.2012.150 (2013).

205. Tereshchenko, Y., Petkov, S. G. & Behr, R. The Efficiency of In Vitro Differentiation of Primate iPSCs into Cardiomyocytes Depending on Their Cell Seeding Density and Cell Line Specificity. *International journal of molecular sciences* **25**; 10.3390/ijms25158449 (2024).

206. Lu, T. *et al.* Cardiomyocyte differentiation of rat bone marrow multipotent progenitor cells is associated with downregulation of Oct-4 expression. *Tissue engineering. Part A* **16,** 3111–3117; 10.1089/ten.tea.2010.0036 (2010).

207. Gaspar, J. A. *et al.* Unique metabolic features of stem cells, cardiomyocytes, and their progenitors. *Circulation research* **114,** 1346–1360; 10.1161/circresaha.113.302021 (2014).

208. Barak, Y., Hemberger, M. & Sucov, H. M. Phases and Mechanisms of Embryonic Cardiomyocyte Proliferation and Ventricular Wall Morphogenesis. *Pediatric cardiology* **40,** 1359–1366; 10.1007/s00246-019-02164-6 (2019).

209. Boheler, K. R. *et al.* Differentiation of pluripotent embryonic stem cells into cardiomyocytes. *Circulation research* **91,** 189–201; 10.1161/01.RES.0000027865.61704.32 (2002).

210. Lukacheva, A. V. *et al.* Oct4 Contributes to Mesodermal Differentiation by Sustaining the Proliferative Capacity of Early Mesodermal Progenitors. *International journal of molecular sciences* **27**; 10.3390/ijms27010054 (2025).

211. Benecke, B. J., Ben-Ze'ev, A. & Penman, S. The control of mRNA production, translation and turnover in suspended and reattached anchorage-dependent fibroblasts. *Cell* **14,** 931–939; 10.1016/0092-8674(78)90347-1 (1978).

212. Liu, Y. *et al.* p53 Promotes Differentiation of Cardiomyocytes from hiPSC through Wnt Signaling-Mediated Mesendodermal Differentiation. *International journal of stem cells* **14,** 410–422; 10.15283/ijsc21051 (2021).

213. Bowman, P. R. T., Smith, G. L. & Gould, G. W. GLUT4 expression and glucose transport in human induced pluripotent stem cell-derived cardiomyocytes. *PloS one* **14,** e0217885; 10.1371/journal.pone.0217885 (2019).

214. Tonack, S., Rolletschek, A., Wobus, A. M., Fischer, B. & Santos, A. N. Differential expression of glucose transporter isoforms during embryonic stem cell differentiation. *Differentiation; research in biological diversity* **74,** 499–509; 10.1111/j.1432-0436.2006.00091.x (2006).

215. Krug, A. *et al.* Three-dimensional spheroid models for cardiovascular biology and pathology. *Mechanobiology in medicine* **3,** 100144; 10.1016/j.mbm.2025.100144 (2025).

216. Agger, P. & Stephenson, R. S. Assessing Myocardial Architecture: The Challenges and Controversies. *Journal of cardiovascular development and disease* **7**; 10.3390/jcdd7040047 (2020).

217. Li, Y. *et al.* The molecular mechanisms of cardiac development and related diseases. *Signal transduction and targeted therapy* **9,** 368; 10.1038/s41392-024-02069-8 (2024).

218. STEMCELL Technologies. ROCK Inhibitor Y-27632. Available at https://www.stemcell.com/products/y-27632.html (2026).

219. Khalil, A. S., Xie, A. W. & Murphy, W. L. Context clues: the importance of stem cell-material interactions. *ACS chemical biology* **9,** 45–56; 10.1021/cb400801m (2014).

220. Velecela, V. *et al. WNT inhibition primes the transcriptional landscape of mesoderm to initiate a phased ventricular cardiomyocyte specification programme* (2025).

221. Graham, N. *et al. Conserved roles of GATA4 and its target gene TBX2 in regulation of human cardiogenesis* (2025).

222. Liu, F. *et al.* The Biphasic Effect of Retinoic Acid Signaling Pathway on the Biased Differentiation of Atrial-like and Sinoatrial Node-like Cells from hiPSC. *International journal of stem cells* **15,** 247–257; 10.15283/ijsc21148 (2022).

223. Machiraju, P. *et al. Early Inhibition of Retinoic Acid Signaling Rapidly Generates Cardiomyocytes Expressing Ventricular Markers from Human Induced Pluripotent Stem Cells* (2019).

224. Pinto, A. R. *et al.* Revisiting Cardiac Cellular Composition. *Circulation research* **118,** 400–409; 10.1161/CIRCRESAHA.115.307778 (2016).

225. Williams, A. E. *et al.* Impact of Endothelial Diversity and Dysfunction on Cardiovascular Disease. *Comprehensive Physiology* **15,** e70064; 10.1002/cph4.70064 (2025).

226. Zamani, M., Karaca, E. & Huang, N. F. Multicellular Interactions in 3D Engineered Myocardial Tissue. *Frontiers in cardiovascular medicine* **5,** 147; 10.3389/fcvm.2018.00147 (2018).

227. Doppler, S. A. *et al.* Cardiac fibroblasts: more than mechanical support. *Journal of thoracic disease* **9,** S36-S51; 10.21037/jtd.2017.03.122 (2017).

228. Vestweber, D. VE-cadherin: the major endothelial adhesion molecule controlling cellular junctions and blood vessel formation. *Arteriosclerosis, thrombosis, and vascular biology* **28,** 223–232; 10.1161/atvbaha.107.158014 (2008).

229. Hsieh, P. C. H., Davis, M. E., Lisowski, L. K. & Lee, R. T. Endothelial-cardiomyocyte interactions in cardiac development and repair. *Annual review of physiology* **68,** 51–66; 10.1146/annurev.physiol.68.040104.124629 (2006).

230. Singhal, A. K., Symons, J. D., Boudina, S., Jaishy, B. & Shiu, Y.-T. Role of Endothelial Cells in Myocardial Ischemia-Reperfusion Injury. *Vascular disease prevention* **7,** 1–14; 10.2174/1874120701007010001 (2010).

231. Zhang, P., Su, J. & Mende, U. Cross talk between cardiac myocytes and fibroblasts: from multiscale investigative approaches to mechanisms and functional consequences. *American journal of physiology. Heart and circulatory physiology* **303,** H1385-96; 10.1152/ajpheart.01167.2011 (2012).

232. Tai, Y. *et al.* Myofibroblasts: Function, Formation, and Scope of Molecular Therapies for Skin Fibrosis. *Biomolecules* **11**; 10.3390/biom11081095 (2021).

233. Holm Nielsen, S. *et al.* Serological Assessment of Activated Fibroblasts by alpha-Smooth Muscle Actin (α-SMA): A Noninvasive Biomarker of Activated Fibroblasts in Lung Disorders. *Translational oncology* **12,** 368–374; 10.1016/j.tranon.2018.11.004 (2019).

234. Toba, H. *et al.* Cellular and molecular signals of cardiac wound healing after myocardial infarction. *American journal of physiology. Heart and circulatory physiology* **330,** H594-H609; 10.1152/ajpheart.00891.2025 (2026).

235. Achilli, T.-M., Meyer, J. & Morgan, J. R. Advances in the formation, use and understanding of multi-cellular spheroids. *Expert opinion on biological therapy* **12,** 1347–1360; 10.1517/14712598.2012.707181 (2012).

236. Zhu, L., Liu, K., Feng, Q. & Liao, Y. Cardiac Organoids: A 3D Technology for Modeling Heart Development and Disease. *Stem cell reviews and reports* **18,** 2593–2605; 10.1007/s12015-022-10385-1 (2022).

237. Radisic, M. *et al.* Oxygen gradients correlate with cell density and cell viability in engineered cardiac tissue. *Biotechnology and bioengineering* **93,** 332–343; 10.1002/bit.20722 (2006).

238. Park, G., Kim, S. S., Shim, J. & Lee, S.-J. V. Brief guide to immunostaining. *Molecules and cells* **48,** 100157; 10.1016/j.mocell.2024.100157 (2025).

239. Piña, R. *et al.* Ten Approaches That Improve Immunostaining: A Review of the Latest Advances for the Optimization of Immunofluorescence. *International journal of molecular sciences* **23**; 10.3390/ijms23031426 (2022).

240. McKinnon, K. M. Flow Cytometry: An Overview. *Current protocols in immunology* **120,** 5.1.1-5.1.11; 10.1002/cpim.40 (2018).

241. Shcherbakova, A. *et al.* Factors Affecting Cell Viability during the Enzymatic Dissociation of Human Endocrine Tumor Tissues. *Biology* **13**; 10.3390/biology13090665 (2024).

242. Zhao, L. *et al.* Single-cell profiling of cellular changes in the somatic peripheral nerves following nerve injury. *Frontiers in pharmacology* **15,** 1448253; 10.3389/fphar.2024.1448253 (2024).

243. Mayourian, J. *et al.* Physiologic, Pathologic, and Therapeutic Paracrine Modulation of Cardiac Excitation-Contraction Coupling. *Circulation research* **122,** 167–183; 10.1161/CIRCRESAHA.117.311589 (2018).

244. Lundy, S. D., Zhu, W.-Z., Regnier, M. & Laflamme, M. A. Structural and functional maturation of cardiomyocytes derived from human pluripotent stem cells. *Stem cells and development* **22,** 1991–2002; 10.1089/scd.2012.0490 (2013).

245. Shen, S. *et al.* Physiological calcium combined with electrical pacing accelerates maturation of human engineered heart tissue. *Stem cell reports* **17,** 2037–2049; 10.1016/j.stemcr.2022.07.006 (2022).

246. Adeniran, I., MacIver, D. H., Hancox, J. C. & Zhang, H. Abnormal calcium homeostasis in heart failure with preserved ejection fraction is related to both reduced contractile function and incomplete relaxation: an electromechanically detailed biophysical modeling study. *Frontiers in physiology* **6,** 78; 10.3389/fphys.2015.00078 (2015).

247. Strom, M., Wan, X., Poelzing, S., Ficker, E. & Rosenbaum, D. S. Gap junction heterogeneity as mechanism for electrophysiologically distinct properties across the ventricular wall. *American journal of physiology. Heart and circulatory physiology* **298,** H787-94; 10.1152/ajpheart.00887.2009 (2010).

248. Han, M. Limitations of the use of MTT assay for screening in drug discovery. *J. Chin. Pharm. Sci.* **19**; 10.5246/jcps.2010.03.027 (2010).

249. Hasenfuss, G. *et al.* Energetics of calcium cycling in nonfailing and failing human myocardium. *Basic research in cardiology* **87 Suppl 2,** 81–92; 10.1007/978-3-642-72477-0_8 (1992).

250. Guan, X. *et al.* Development of hydrogels for regenerative engineering. *Biotechnology journal* **12**; 10.1002/biot.201600394 (2017).

251. Zhu, J. & Marchant, R. E. Design properties of hydrogel tissue-engineering scaffolds. *Expert review of medical devices* **8,** 607–626; 10.1586/erd.11.27 (2011).

252. Wei, Z. *et al.* Hydrogels with tunable mechanical plasticity regulate endothelial cell outgrowth in vasculogenesis and angiogenesis. *Nature communications* **14,** 8307; 10.1038/s41467-023-43768-0 (2023).

253. Sahan, A. Z., Baday, M. & Patel, C. B. Biomimetic Hydrogels in the Study of Cancer Mechanobiology: Overview, Biomedical Applications, and Future Perspectives. *Gels (Basel, Switzerland)* **8**; 10.3390/gels8080496 (2022).

254. Azevedo, P. S., Polegato, B. F., Minicucci, M. F., Paiva, S. A. R. & Zornoff, L. A. M. Cardiac Remodeling: Concepts, Clinical Impact, Pathophysiological Mechanisms and Pharmacologic Treatment. *Arquivos brasileiros de cardiologia* **106,** 62–69; 10.5935/abc.20160005 (2016).

255. Curtis, M. W. & Russell, B. Micromechanical regulation in cardiac myocytes and fibroblasts: implications for tissue remodeling. *Pflugers Archiv : European journal of physiology* **462,** 105–117; 10.1007/s00424-011-0931-8 (2011).

256. Abdoulkader, M. S. & Komai, K. A Modified Fick's First Law Incorporating a Flux Correction Factor for Nutrient Diffusion in Intertidal Sediments. *Water* **17,** 2958; 10.3390/w17202958 (2025).

257. Liang, N.-W. *et al.* Under-oil neuronal cell culture: Enhanced system stability, yield, and modulated oxygen environment. *Journal of neuroscience methods* **422,** 110511; 10.1016/j.jneumeth.2025.110511 (2025).

258. Nielsen, S. H. *et al.* Understanding cardiac extracellular matrix remodeling to develop biomarkers of myocardial infarction outcomes. *Matrix biology : journal of the International Society for Matrix Biology* **75-76,** 43–57; 10.1016/j.matbio.2017.12.001 (2019).

259. Richardson, W. J., Clarke, S. A., Quinn, T. A. & Holmes, J. W. Physiological Implications of Myocardial Scar Structure. *Comprehensive Physiology* **5,** 1877–1909; 10.1002/cphy.c140067 (2015).

260. Hall, C., Gehmlich, K., Denning, C. & Pavlovic, D. Complex Relationship Between Cardiac Fibroblasts and Cardiomyocytes in Health and Disease. *Journal of the American Heart Association* **10,** e019338; 10.1161/JAHA.120.019338 (2021).

261. Park, S., Ranjbarvaziri, S., Zhao, P. & Ardehali, R. Cardiac Fibrosis Is Associated With Decreased Circulating Levels of Full-Length CILP in Heart Failure. *JACC. Basic to translational science* **5,** 432–443; 10.1016/j.jacbts.2020.01.016 (2020).

262. Yoganathan, T. *et al.* Acute stress induces long-term metabolic, functional, and structural remodeling of the heart. *Nature communications* **14,** 3835; 10.1038/s41467-023-39590-3 (2023).

263. Cohn, P. F. Total ischemic burden: Pathophysiology and prognosis. *The American journal of cardiology* **59,** C3-C6; 10.1016/0002-9149(87)90188-3 (1987).

264. Sandau, K. E. *et al.* Update to Practice Standards for Electrocardiographic Monitoring in Hospital Settings: A Scientific Statement From the American Heart Association. *Circulation* **136,** e273-e344; 10.1161/CIR.0000000000000527 (2017).

265. Patel, L. *et al.* Substrate stiffness-dependent metabolic reprogramming of iPSC-derived cardiomyocytes on physiological PDMS polymers. *Metabolic engineering communications* **21,** e00266; 10.1016/j.mec.2025.e00266 (2025).

266. Lavrentev, F. V. *et al.* Diffusion-Limited Processes in Hydrogels with Chosen Applications from Drug Delivery to Electronic Components. *Molecules (Basel, Switzerland)* **28**; 10.3390/molecules28155931 (2023).

267. Gałdyszyńska, M., Radwańska, P., Szymański, J. & Drobnik, J. The Stiffness of Cardiac Fibroblast Substrates Exerts a Regulatory Influence on Collagen Metabolism via $\alpha 2\beta 1$ Integrin, FAK and Src Kinases. *Cells* **10**; 10.3390/cells10123506 (2021).

268. Sun, X., Nkennor, B., Mastikhina, O., Soon, K. & Nunes, S. S. Endothelium-mediated contributions to fibrosis. *Seminars in cell & developmental biology* **101,** 78–86; 10.1016/j.semcdb.2019.10.015 (2020).

269. Foster, M. N. & Coetzee, W. A. KATP Channels in the Cardiovascular System. *Physiological reviews* **96,** 177–252; 10.1152/physrev.00003.2015 (2016).

270. Rhana, P. *et al.* Fueling the heartbeat: Dynamic regulation of intracellular ATP during excitation-contraction coupling in ventricular myocytes. *Proceedings of the National Academy of Sciences of the United States of America* **121,** e2318535121; 10.1073/pnas.2318535121 (2024).

271. Barbuti, A. & DiFrancesco, D. Control of cardiac rate by "funny" channels in health and disease. *Annals of the New York Academy of Sciences* **1123,** 213–223; 10.1196/annals.1420.024 (2008).

272. Cano-Jorge, M., Gómez, S., Toonder, J. den, Wang, Y. & Passier, R. In vitro approaches to mimic cardiac mechanical load dynamics for enhancing maturation and disease modelling. *Cardiovascular research* **121,** 2484–2502; 10.1093/cvr/cvaf247 (2025).

273. Mora, M. T., Zaza, A. & Trenor, B. Insights from an electro-mechanical heart failure cell model: Role of SERCA enhancement on arrhythmogenesis and myocyte contraction. *Computer methods and programs in biomedicine* **230,** 107350; 10.1016/j.cmpb.2023.107350 (2023).

274. Hajjar, R. J. & Gwathmey, J. K. Cross-bridge dynamics in human ventricular myocardium. Regulation of contractility in the failing heart. *Circulation* **86,** 1819–1826; 10.1161/01.CIR.86.6.1819 (1992).

275. Ma, Y. *et al.* Bioinspired high-power-density strong contractile hydrogel by programmable elastic recoil. *Science advances* **6**; 10.1126/sciadv.abd2520 (2020).

276. Crossman, D. C. The pathophysiology of myocardial ischaemia. *Heart (British Cardiac Society)* **90,** 576–580; 10.1136/hrt.2003.029017 (2004).

277. Idris, A. H. *et al.* Oxidant injury occurs rapidly after cardiac arrest, cardiopulmonary resuscitation, and reperfusion. *Critical care medicine* **33,** 2043–2048; 10.1097/01.CCM.0000174104.50799.BD (2005).

278. Solaini, G., Baracca, A., Lenaz, G. & Sgarbi, G. Hypoxia and mitochondrial oxidative metabolism. *Biochimica et biophysica acta* **1797,** 1171–1177; 10.1016/j.bbabio.2010.02.011 (2010).

279. Zhao, C. & MacKinnon, R. Molecular structure of an open human KATP channel. *Proceedings of the National Academy of Sciences of the United States of America* **118**; 10.1073/pnas.2112267118 (2021).

280. Stein, P. K., Domitrovich, P. P., Hui, N., Rautaharju, P. & Gottdiener, J. Sometimes higher heart rate variability is not better heart rate variability: results of graphical and nonlinear analyses. *Journal of cardiovascular electrophysiology* **16,** 954–959; 10.1111/j.1540-8167.2005.40788.x (2005).

281. Bravi, A. *et al.* Do physiological and pathological stresses produce different changes in heart rate variability? *Frontiers in physiology* **4,** 197; 10.3389/fphys.2013.00197 (2013).

282. Gañán-Calvo, A. M. & Fajardo-López, J. Universal structures of normal and pathological heart rate variability. *Scientific reports* **6,** 21749; 10.1038/srep21749 (2016).

283. Griffiths, E. J. *et al.* Mitochondrial calcium transporting pathways during hypoxia and reoxygenation in single rat cardiomyocytes. *Cardiovascular research* **39,** 423–433; 10.1016/S0008-6363(98)00104-7 (1998).

284. Murphy, E. & Steenbergen, C. Mechanisms underlying acute protection from cardiac ischemia-reperfusion injury. *Physiological reviews* **88,** 581–609; 10.1152/physrev.00024.2007 (2008).

285. Bertero, E., Popoiu, T.-A. & Maack, C. Mitochondrial calcium in cardiac ischemia/reperfusion injury and cardioprotection. *Basic research in cardiology* **119,** 569–585; 10.1007/s00395-024-01060-2 (2024).

286. Wang, J. *et al.* Thermal Marangoni natural convection enables directional transport across immiscible liquids. *Nature communications* **16,** 5727; 10.1038/s41467-025-60930-y (2025).

287. O'Donnell, J. M., Pound, K., Xu, X. & Lewandowski, E. D. SERCA1 expression enhances the metabolic efficiency of improved contractility in post-ischemic heart. *Journal of molecular and cellular cardiology* **47,** 614–621; 10.1016/j.yjmcc.2009.08.031 (2009).

288. Li, Q. *et al.* Energy metabolism: A critical target of cardiovascular injury. *Biomedicine & pharmacotherapy = Biomedecine & pharmacotherapie* **165,** 115271; 10.1016/j.biopha.2023.115271 (2023).

289. Rose, H. & Kammermeier, H. Contraction and metabolic activity of electrically stimulated cardiac myocytes from adult rats. *Pflugers Archiv : European journal of physiology* **407,** 116–118; 10.1007/bf00580731 (1986).

290. Ronald J. Korthuis. Exercise Hyperemia and Regulation of Tissue Oxygenation During Muscular Activity. In *Skeletal Muscle Circulation,* edited by R. J. Korthuis (Morgan & Claypool Life Sciences2011).

291. Kamel, K. S., Oh, M. S. & Halperin, M. L. L-lactic acidosis: pathophysiology, classification, and causes; emphasis on biochemical and metabolic basis. *Kidney international* **97,** 75–88; 10.1016/j.kint.2019.08.023 (2020).

292. Della Bella, P. *et al.* Increased cardiac electrical instability concomitant with pacing induced repolarisation abnormalities. *British heart journal* **57,** 118–124; 10.1136/hrt.57.2.118 (1987).

293. Baloglu, E. Hypoxic Stress-Dependent Regulation of Na,K-ATPase in Ischemic Heart Disease. *International journal of molecular sciences* **24**; 10.3390/ijms24097855 (2023).

294. Gusarova, G. A. *et al.* Hypoxia leads to Na,K-ATPase downregulation via Ca(2+) release-activated Ca(2+) channels and AMPK activation. *Molecular and cellular biology* **31,** 3546–3556; 10.1128/MCB.05114-11 (2011).

295. Sun, J. *et al.* Hypoxia-induced BNIP3 facilitates the progression and metastasis of uveal melanoma by driving metabolic reprogramming. *Autophagy* **21,** 191–209; 10.1080/15548627.2024.2395142 (2025).

296. Bellot, G. *et al.* Hypoxia-induced autophagy is mediated through hypoxia-inducible factor induction of BNIP3 and BNIP3L via their BH3 domains. *Molecular and cellular biology* **29,** 2570–2581; 10.1128/mcb.00166-09 (2009).

297. Huo, Q., Zhang, Y., Zhao, J., Bai, N. & Wang, J. HIF-1α/BNIP3-mediated mitophagy mitigates cerebral ischemia/reperfusion injury in rats by suppressing NLRP3 inflammasome activation. *European journal of medical research* **31,** 251; 10.1186/s40001-026-03954-4 (2026).

298. Mingyuan, X. *et al.* Hypoxia-inducible factor-1α activates transforming growth factor-β1/Smad signaling and increases collagen deposition in dermal fibroblasts. *Oncotarget* **9,** 3188–3197; 10.18632/oncotarget.23225 (2018).

299. Biernacka, A., Dobaczewski, M. & Frangogiannis, N. G. TGF-β signaling in fibrosis. *Growth factors (Chur, Switzerland)* **29,** 196–202; 10.3109/08977194.2011.595714 (2011).

300. Butler, P. *et al.* RNA disruption is a widespread phenomenon associated with stress-induced cell death in tumour cells. *Scientific reports* **13,** 1711; 10.1038/s41598-023-28635-8 (2023).

301. Nesci, S. & Rubattu, S. Mitochondrial Permeability Transition Pore: The Cardiovascular Disease's Molecular Achilles Heel. *Biomedicines* **13**; 10.3390/biomedicines13123014 (2025).

302. Kalogeris, T., Baines, C. P., Krenz, M. & Korthuis, R. J. Ischemia/Reperfusion. *Comprehensive Physiology* **7,** 113–170; 10.1002/cphy.c160006 (2016).

303. Boyette, L. C. & Manna, B. *StatPearls. Physiology, Myocardial Oxygen Demand* (Treasure Island (FL), 2025).

304. Jurcau, A. & Ardelean, A. I. Oxidative Stress in Ischemia/Reperfusion Injuries following Acute Ischemic Stroke. *Biomedicines* **10**; 10.3390/biomedicines10030574 (2022).

305. Chen, T. & Vunjak-Novakovic, G. In vitro Models of Ischemia-Reperfusion Injury. *Regenerative engineering and translational medicine* **4,** 142–153; 10.1007/s40883-018-0056-0 (2018).

306. Deng, Y., Li, Y. & Li, L. Experimental investigation of nitrogen isotopic effects associated with ammonia degassing at 0–70 °C. *Geochimica et Cosmochimica Acta* **226,** 182–191; 10.1016/j.gca.2018.02.007 (2018).

307. Steenbergen, C., Murphy, E., Levy, L. & London, R. E. Elevation in cytosolic free calcium concentration early in myocardial ischemia in perfused rat heart. *Circulation research* **60,** 700–707; 10.1161/01.res.60.5.700 (1987).

308. Zhou, B. & Tian, R. Mitochondrial dysfunction in pathophysiology of heart failure. *The Journal of clinical investigation* **128,** 3716–3726; 10.1172/JCI120849 (2018).

309. Shattock, M. J. *et al.* Na+/Ca2+ exchange and Na+/K+-ATPase in the heart. *The Journal of physiology* **593,** 1361–1382; 10.1113/jphysiol.2014.282319 (2015).

310. Lipskaia, L., Chemaly, E. R., Hadri, L., Lompre, A.-M. & Hajjar, R. J. Sarcoplasmic reticulum Ca(2+) ATPase as a therapeutic target for heart failure. *Expert opinion on biological therapy* **10,** 29–41; 10.1517/14712590903321462 (2010).

311. Halestrap, A. P. Calcium, mitochondria and reperfusion injury: a pore way to die. *Biochemical Society transactions* **34,** 232–237; 10.1042/BST0340232 (2006).

312. Dwyer, K. D., Snyder, C. A. & Coulombe, K. L. K. Cardiomyocytes in Hypoxia: Cellular Responses and Implications for Cell-Based Cardiac Regenerative Therapies. *Bioengineering (Basel, Switzerland)* **12**; 10.3390/bioengineering12020154 (2025).

313. Verma, S. *et al.* Fundamentals of reperfusion injury for the clinical cardiologist. *Circulation* **105,** 2332–2336; 10.1161/01.CIR.0000016602.96363.36 (2002).

314. Lindsey, M. L. *et al.* Guidelines for experimental models of myocardial ischemia and infarction. *American journal of physiology. Heart and circulatory physiology* **314,** H812-H838; 10.1152/ajpheart.00335.2017 (2018).

315. Zuurbier, C. J. *et al.* Cardiac metabolism as a driver and therapeutic target of myocardial infarction. *Journal of cellular and molecular medicine* **24,** 5937–5954; 10.1111/jcmm.15180 (2020).

316. Clusin, W. T., Buchbinder, M. & Harrison, D. C. Calcium overload, "injury" current, and early ischaemic cardiac arrhythmias--a direct connection. *The Lancet* **1,** 272–274; 10.1016/s0140-6736(83)91688-4 (1983).

317. Brook, J. *et al.* Development of a pro-arrhythmic ex vivo intact human and porcine model: cardiac electrophysiological changes associated with cellular uncoupling. *Pflugers Archiv : European journal of physiology* **472,** 1435–1446; 10.1007/s00424-020-02446-6 (2020).

318. Zha, X.-M., Xiong, Z.-G. & Simon, R. P. pH and proton-sensitive receptors in brain ischemia. *Journal of cerebral blood flow and metabolism : official journal of the International Society of Cerebral Blood Flow and Metabolism* **42,** 1349–1363; 10.1177/0271678X221089074 (2022).

319. Bøgh, N. *et al.* Cardiac pH-Imaging With Hyperpolarized MRI. *Frontiers in cardiovascular medicine* **7,** 603674; 10.3389/fcvm.2020.603674 (2020).

320. Laurita, K. R. & Rosenbaum, D. S. Cellular mechanisms of arrhythmogenic cardiac alternans. *Progress in biophysics and molecular biology* **97,** 332–347; 10.1016/j.pbiomolbio.2008.02.014 (2008).

321. Kulkarni, K. *et al.* Cardiac Alternans: Mechanisms and Clinical Utility in Arrhythmia Prevention. *Journal of the American Heart Association* **8,** e013750; 10.1161/JAHA.119.013750 (2019).

322. Bhullar, S. K. & Dhalla, N. S. Status of Mitochondrial Oxidative Phosphorylation during the Development of Heart Failure. *Antioxidants (Basel, Switzerland)* **12**; 10.3390/antiox12111941 (2023).

323. Vite, A. *et al.* Functional Impact of Alternative Metabolic Substrates in Failing Human Cardiomyocytes. *JACC. Basic to translational science* **9,** 1–15; 10.1016/j.jacbts.2023.07.009 (2024).

324. Gu, H.-O., Noh, S. W., Kim, O.-H. & Oh, B.-C. Crucial roles of calcium ATPases and phosphoinositides: Insights into pathophysiology and therapeutic strategies. *Molecules and cells* **48,** 100254; 10.1016/j.mocell.2025.100254 (2025).

325. Yano, M., Ikeda, Y. & Matsuzaki, M. Altered intracellular Ca2+ handling in heart failure. *The Journal of clinical investigation* **115,** 556–564; 10.1172/JCI24159 (2005).

326. Siasos, G. *et al.* Mitochondria and cardiovascular diseases-from pathophysiology to treatment. *Annals of translational medicine* **6,** 256; 10.21037/atm.2018.06.21 (2018).

327. Kuznetsov, A. V. *et al.* The Role of Mitochondria in the Mechanisms of Cardiac Ischemia-Reperfusion Injury. *Antioxidants (Basel, Switzerland)* **8**; 10.3390/antiox8100454 (2019).

328. Langer, G. A., Weiss, J. N. & Schelbert, H. R. Cardiac ischemia. Part I--Metabolic and physiologic responses. *The Western journal of medicine* **146,** 713–723 (1987).

329. Ferrari, R. *et al.* Metabolic derangement in ischemic heart disease and its therapeutic control. *The American journal of cardiology* **82,** 2K-13K; 10.1016/s0002-9149(98)00531-1 (1998).

330. Pang, Q. *et al.* Temporal regulation of genetic programs governing multiple cell death during myocardial ischemia-reperfusion injury. *Frontiers in genetics* **16,** 1632867; 10.3389/fgene.2025.1632867 (2025).

331. Gourdin, M. & Dubois, P. Impact of Ischemia on Cellular Metabolism. In *Artery Bypass,* edited by W. S. Aronow (InTech2013).

332. Huang, H. *et al.* Cellular succinate metabolism and signaling in inflammation: implications for therapeutic intervention. *Frontiers in immunology* **15,** 1404441; 10.3389/fimmu.2024.1404441 (2024).

333. Rutter, J., Winge, D. R. & Schiffman, J. D. Succinate dehydrogenase - Assembly, regulation and role in human disease. *Mitochondrion* **10,** 393–401; 10.1016/j.mito.2010.03.001 (2010).

334. Dery, K., Chiu, R., Kasargod, A. & Kupiec-Weglinski, J. Feedback Loops Shape Oxidative and Immune Interactions in Hepatic Ischemia–Reperfusion Injury. *Antioxidants* **14,** 944; 10.3390/antiox14080944 (2025).

335. Milliken, A. S., Kulkarni, C. A. & Brookes, P. S. Acid enhancement of ROS generation by complex-I reverse electron transport is balanced by acid inhibition of complex-II: Relevance for tissue reperfusion injury. *Redox biology* **37,** 101733; 10.1016/j.redox.2020.101733 (2020).

336. Yusof, N. L. M., Yellon, D. M. & Davidson, S. M. The contribution of cardiomyocyte hypercontracture to the burden of acute myocardial infarction: an update. *Basic research in cardiology* **120,** 619–639; 10.1007/s00395-025-01120-1 (2025).

337. Li, C. *et al.* SERCA overexpression reduces reperfusion-mediated cardiac microvascular damage through inhibition of the calcium/MCU/mPTP/necroptosis signaling pathways. *Redox biology* **36,** 101659; 10.1016/j.redox.2020.101659 (2020).

338. Kiernan, Z., Labate, G., Chen, Q. & Quader, M. Reducing mitochondrial dysfunction through combination therapy to limit ischemia-reperfusion injury in male DCD rats. *Frontiers in cardiovascular medicine* **12,** 1625385; 10.3389/fcvm.2025.1625385 (2025).

339. Perrelli, M.-G., Pagliaro, P. & Penna, C. Ischemia/reperfusion injury and cardioprotective mechanisms: Role of mitochondria and reactive oxygen species. *World journal of cardiology* **3,** 186–200; 10.4330/wjc.v3.i6.186 (2011).

340. Pinton, P., Giorgi, C., Siviero, R., Zecchini, E. & Rizzuto, R. Calcium and apoptosis: ER-mitochondria Ca2+ transfer in the control of apoptosis. *Oncogene* **27,** 6407–6418; 10.1038/onc.2008.308 (2008).

341. Görlach, A., Bertram, K., Hudecova, S. & Krizanova, O. Calcium and ROS: A mutual interplay. *Redox biology* **6,** 260–271; 10.1016/j.redox.2015.08.010 (2015).

342. Su, Y., Ke, C., Li, C., Huang, C. & Wan, C. Intermittent hypoxia promotes the recovery of motor function in rats with cerebral ischemia by regulating mitochondrial function. *Experimental biology and medicine (Maywood, N.J.)* **247,** 1364–1378; 10.1177/15353702221098962 (2022).

343. Kashihara, T. *et al.* YAP mediates compensatory cardiac hypertrophy through aerobic glycolysis in response to pressure overload. *The Journal of clinical investigation* **132**; 10.1172/JCI150595 (2022).

344. Reddan, B. & Cummins, E. P. The regulation of cell metabolism by hypoxia and hypercapnia. *The Journal of biological chemistry* **301,** 108252; 10.1016/j.jbc.2025.108252 (2025).

345. Sherman, A. J. *et al.* Myofibrillar disruption in hypocontractile myocardium showing perfusion-contraction matches and mismatches. *American journal of*

physiology. Heart and circulatory physiology **278,** H1320-34; 10.1152/ajpheart.2000.278.4.h1320 (2000).

346. Verburg, E., Murphy, R. M., Stephenson, D. G. & Lamb, G. D. Disruption of excitation-contraction coupling and titin by endogenous Ca2+-activated proteases in toad muscle fibres. *The Journal of physiology* **564,** 775–790; 10.1113/jphysiol.2004.082180 (2005).

347. Iqbal, S. & Hood, D. A. Oxidative stress-induced mitochondrial fragmentation and movement in skeletal muscle myoblasts. *American journal of physiology. Cell physiology* **306,** C1176-83; 10.1152/ajpcell.00017.2014 (2014).

348. Tombo, N., Imam Aliagan, A. D., Feng, Y., Singh, H. & Bopassa, J. C. Cardiac ischemia/reperfusion stress reduces inner mitochondrial membrane protein (mitofilin) levels during early reperfusion. *Free radical biology & medicine* **158,** 181–194; 10.1016/j.freeradbiomed.2020.06.039 (2020).

349. Geto, Z., Molla, M. D., Challa, F., Belay, Y. & Getahun, T. Mitochondrial Dynamic Dysfunction as a Main Triggering Factor for Inflammation Associated Chronic Non-Communicable Diseases. *Journal of inflammation research* **13,** 97–107; 10.2147/JIR.S232009 (2020).

350. Gorza, L., Menabò, R., Vitadello, M., Bergamini, C. M. & Di Lisa, F. Cardiomyocyte troponin T immunoreactivity is modified by cross-linking resulting from intracellular calcium overload. *Circulation* **93,** 1896–1904; 10.1161/01.cir.93.10.1896 (1996).

351. Momeni, H. R. Role of calpain in apoptosis. *Cell journal* **13,** 65–72 (2011).

352. Enomoto, A. & Fukasawa, T. The role of calcium-calpain pathway in hyperthermia. *Frontiers in molecular medicine* **2,** 1005258; 10.3389/fmmed.2022.1005258 (2022).

353. Liu, G.-Y. *et al.* Calpain: the regulatory point of myocardial ischemia-reperfusion injury. *Frontiers in cardiovascular medicine* **10,** 1194402; 10.3389/fcvm.2023.1194402 (2023).

354. Vázquez-Galán, Y. I., Guzmán-Silahua, S., Trujillo-Rangel, W. Á. & Rodríguez-Lara, S. Q. Role of Ischemia/Reperfusion and Oxidative Stress in Shock State. *Cells* **14**; 10.3390/cells14110808 (2025).

355. Powell, S. R., Gurzenda, E. M. & Wahezi, S. E. Actin is oxidized during myocardial ischemia. *Free radical biology & medicine* **30,** 1171–1176; 10.1016/S0891-5849(01)00514-7 (2001).

356. Murphy, E. *et al.* Signaling by S-nitrosylation in the heart. *Journal of molecular and cellular cardiology* **73,** 18–25; 10.1016/j.yjmcc.2014.01.003 (2014).

357. Buelna-Chontal, M., García-Niño, W. R., Silva-Palacios, A., Enríquez-Cortina, C. & Zazueta, C. Implications of Oxidative and Nitrosative Post-Translational Modifications in Therapeutic Strategies against Reperfusion Damage. *Antioxidants (Basel, Switzerland)* **10**; 10.3390/antiox10050749 (2021).

358. Kalinina, E. & Novichkova, M. Glutathione in Protein Redox Modulation through S-Glutathionylation and S-Nitrosylation. *Molecules (Basel, Switzerland)* **26**; 10.3390/molecules26020435 (2021).

359. Chakraborty, S. *et al.* S-Denitrosylation: A Crosstalk between Glutathione and Redoxin Systems. *Antioxidants (Basel, Switzerland)* **11**; 10.3390/antiox11101921 (2022).

360. Ulfig, A. & Jakob, U. Cellular oxidants and the proteostasis network: balance between activation and destruction. *Trends in biochemical sciences* **49,** 761–774; 10.1016/j.tibs.2024.07.001 (2024).

361. Lim, J. C. *et al.* Irreversible oxidation of the active-site cysteine of peroxiredoxin to cysteine sulfonic acid for enhanced molecular chaperone activity. *Journal of Biological Chemistry* **283,** 28873–28880; 10.1074/jbc.M804087200 (2008).

362. Binek, A. *et al.* Oxidative Post-translational Protein Modifications upon Ischemia/Reperfusion Injury. *Antioxidants (Basel, Switzerland)* **13**; 10.3390/antiox13010106 (2024).

363. Atsma, D. E., Bastiaanse, E. M., Jerzewski, A., van der Valk, L. J. & van der Laarse, A. Role of calcium-activated neutral protease (calpain) in cell death in cultured neonatal rat cardiomyocytes during metabolic inhibition. *Circulation research* **76,** 1071–1078; 10.1161/01.RES.76.6.1071 (1995).

364. Neuhof, C. & Neuhof, H. Calpain system and its involvement in myocardial ischemia and reperfusion injury. *World journal of cardiology* **6,** 638–652; 10.4330/wjc.v6.i7.638 (2014).

365. Sangeetha, M., Pillai, M. S., Philip, L., Lakatta, E. G. & Shivakumar, K. NF-κB inhibition compromises cardiac fibroblast viability under hypoxia. *Experimental cell research* **317,** 899–909; 10.1016/j.yexcr.2010.12.024 (2011).

366. Clarke, M., Bennett, M. & Littlewood, T. Cell death in the cardiovascular system. *Heart (British Cardiac Society)* **93,** 659–664; 10.1136/hrt.2006.088203 (2007).

367. Scarabelli, T. M. *et al.* Different signaling pathways induce apoptosis in endothelial cells and cardiac myocytes during ischemia/reperfusion injury. *Circulation research* **90,** 745–748; 10.1161/01.res.0000015224.07870.9a (2002).

368. Nguyen, B. Y. *et al.* Mitochondrial function in the heart: the insight into mechanisms and therapeutic potentials. *British journal of pharmacology* **176,** 4302–4318; 10.1111/bph.14431 (2019).

369. Martínez, M. S. *et al.* Energetic metabolism in cardiomyocytes: molecular basis of heart ischemia and arrhythmogenesis. *VP* **1**; 10.20517/2574-1209.2017.34 (2017).

370. Li, X. *et al.* Metabolic Adaptation to a Disruption in Oxygen Supply during Myocardial Ischemia and Reperfusion Is Underpinned by Temporal and Quantitative Changes in the Cardiac Proteome. *Journal of Proteome Research* **11,** 2331–2346; 10.1021/pr201025m (2012).

371. Colomer-Saucedo, J. *et al.* SERCA Inhibition by Drugs - A Potential Therapeutic Strategy in Ischemia. *The Journal of Pharmacology and Experimental Therapeutics* **385,** 302; 10.1124/jpet.122.538430 (2023).

372. Sgarbi, G. *et al.* Hypoxia decreases ROS level in human fibroblasts. *The international journal of biochemistry & cell biology* **88,** 133–144; 10.1016/j.biocel.2017.05.005 (2017).

373. Popov, L.-D. Mitochondrial biogenesis: An update. *Journal of cellular and molecular medicine* **24,** 4892–4899; 10.1111/jcmm.15194 (2020).

374. Di Lisa, F. & Bernardi, P. Mitochondria and ischemia-reperfusion injury of the heart: fixing a hole. *Cardiovascular research* **70,** 191–199; 10.1016/j.cardiores.2006.01.016 (2006).

375. Tappia, P. S., Shah, A. K., Ramjiawan, B. & Dhalla, N. S. Modification of Ischemia/Reperfusion-Induced Alterations in Subcellular Organelles by Ischemic Preconditioning. *International journal of molecular sciences* **23**; 10.3390/ijms23073425 (2022).

376. Zhao, L. *et al.* Ischemic duration determines extent of cardiac remodeling, and both early and delayed reperfusion prevent fatal cardiac rupture: Model comparison. *PloS one* **20,** e0328001; 10.1371/journal.pone.0328001 (2025).

377. Mager, W. H. & Kruijff, A. J. de. Stress-induced transcriptional activation. *Microbiological reviews* **59,** 506–531; 10.1128/mr.59.3.506-531.1995 (1995).

378. Moro, C. *et al.* Delayed expression of cytokines after reperfused myocardial infarction: possible trigger for cardiac dysfunction and ventricular remodeling. *American journal of physiology. Heart and circulatory physiology* **293,** H3014-9; 10.1152/ajpheart.00797.2007 (2007).

379. Sanjaya, A. Transcriptomic dynamics of cardiac remodeling after myocardial infarction. *Scientific reports* **15,** 36720; 10.1038/s41598-025-20736-w (2025).

380. Leancă, S. A. *et al.* Left Ventricular Remodeling after Myocardial Infarction: From Physiopathology to Treatment. *Life (Basel, Switzerland)* **12**; 10.3390/life12081111 (2022).

381. Smart, N. *et al.* De novo cardiomyocytes from within the activated adult heart after injury. *Nature* **474,** 640–644; 10.1038/nature10188 (2011).

382. Kucherenko, M. M. & Shcherbata, H. R. miRNA targeting and alternative splicing in the stress response - events hosted by membrane-less compartments. *Journal of cell science* **131**; 10.1242/jcs.202002 (2018).

383. Agnew, E. J. *et al.* Scar Formation with Decreased Cardiac Function Following Ischemia/Reperfusion Injury in 1 Month Old Swine. *Journal of cardiovascular development and disease* **7**; 10.3390/jcdd7010001 (2019).

384. Briganti, F. & Wang, Z. Alternative Splicing in the Heart: The Therapeutic Potential of Regulating the Regulators. *International journal of molecular sciences* **25**; 10.3390/ijms252313023 (2024).

385. Shinde, A. V., Humeres, C. & Frangogiannis, N. G. The role of α-smooth muscle actin in fibroblast-mediated matrix contraction and remodeling. *Biochimica et biophysica acta. Molecular basis of disease* **1863,** 298–309; 10.1016/j.bbadis.2016.11.006 (2017).

386. Giordano, C., Francone, M., Cundari, G., Pisano, A. & d'Amati, G. Myocardial fibrosis: morphologic patterns and role of imaging in diagnosis and

prognostication. *Cardiovascular pathology : the official journal of the Society for Cardiovascular Pathology* **56,** 107391; 10.1016/j.carpath.2021.107391 (2022).

387. Heilig, C. *et al.* Implications of glucose transporter protein type 1 (GLUT1)-haplodeficiency in embryonic stem cells for their survival in response to hypoxic stress. *The American journal of pathology* **163,** 1873–1885; 10.1016/S0002-9440(10)63546-8 (2003).

388. Sun, X. *et al.* Glucose transporter GLUT1 expression is important for oriental river prawn (Macrobrachium nipponense) hemocyte adaptation to hypoxic conditions. *The Journal of biological chemistry* **299,** 102748; 10.1016/j.jbc.2022.102748 (2023).

389. Kierans, S. J. & Taylor, C. T. Regulation of glycolysis by the hypoxia-inducible factor (HIF): implications for cellular physiology. *The Journal of physiology* **599,** 23–37; 10.1113/JP280572 (2021).

390. Cao, M. *et al.* Mitochondrial dysfunction and metabolic reprogramming in acute kidney injury: mechanisms, therapeutic advances, and clinical challenges. *Frontiers in physiology* **16,** 1623500; 10.3389/fphys.2025.1623500 (2025).

391. Sorby-Adams, A. *et al.* A model of mitochondrial superoxide production during ischaemia-reperfusion injury for therapeutic development and mechanistic understanding. *Redox biology* **72,** 103161; 10.1016/j.redox.2024.103161 (2024).

392. Chen, H., Tang, Y., Ren, P. & Wu, W. The unmet promise: a critical review of antioxidant strategies in myocardial ischemia-reperfusion injury and the path towards precision medicine. *Frontiers in pharmacology* **16,** 1693441; 10.3389/fphar.2025.1693441 (2025).

393. Jomova, K. *et al.* Several lines of antioxidant defense against oxidative stress: antioxidant enzymes, nanomaterials with multiple enzyme-mimicking activities, and low-molecular-weight antioxidants. *Archives of toxicology* **98,** 1323–1367; 10.1007/s00204-024-03696-4 (2024).

394. Zorov, D. B., Juhaszova, M. & Sollott, S. J. Mitochondrial reactive oxygen species (ROS) and ROS-induced ROS release. *Physiological reviews* **94,** 909–950; 10.1152/physrev.00026.2013 (2014).

395. Bao, Y. *et al.* Mitochondrial Reverse Electron Transport: Mechanisms, Pathophysiological Roles, and Therapeutic Potential. *Biology* **14**; 10.3390/biology14091140 (2025).

396. Bernardi, P. *et al.* Identity, structure, and function of the mitochondrial permeability transition pore: controversies, consensus, recent advances, and future directions. *Cell death and differentiation* **30,** 1869–1885; 10.1038/s41418-023-01187-0 (2023).

397. Bugger, H. & Pfeil, K. Mitochondrial ROS in myocardial ischemia reperfusion and remodeling. *Biochimica et biophysica acta. Molecular basis of disease* **1866,** 165768; 10.1016/j.bbadis.2020.165768 (2020).

398. Samuel, T. J., Rosenberry, R. P., Lee, S. & Pan, Z. Correcting Calcium Dysregulation in Chronic Heart Failure Using SERCA2a Gene Therapy. *International journal of molecular sciences* **19**; 10.3390/ijms19041086 (2018).

399. Peletier, M., Zhang, X., Klein, S. & Kroon, J. Multicellular 3D models to study myocardial ischemia-reperfusion injury. *Frontiers in cell and developmental biology* **12,** 1494911; 10.3389/fcell.2024.1494911 (2024).

400. Francisco, J. & Del Re, D. P. Inflammation in Myocardial Ischemia/Reperfusion Injury: Underlying Mechanisms and Therapeutic Potential. *Antioxidants (Basel, Switzerland)* **12**; 10.3390/antiox12111944 (2023).

401. Gruber, A., Reizenstein, P. & Peterson, C. Effect of verapamil in vitro and in vivo on the accumulation of vincristine in leukemic cells from patients with low malignant lymphoma. *Anticancer research* **9,** 9–12 (1989).

402. Chaitrakoonthong, T., Ampornaramveth, R. & Kamolratanakul, P. Rinsing with L-Ascorbic Acid Exhibits Concentration-Dependent Effects on Human Gingival Fibroblast In Vitro Wound Healing Behavior. *International journal of dentistry* **2020,** 4706418; 10.1155/2020/4706418 (2020).

403. Palande, N. V., Bhoyar, R. C., Biswas, S. P. & Jadhao, A. G. Short-term exposure to L-type calcium channel blocker, verapamil, alters the expression pattern of calcium-binding proteins in the brain of goldfish, Carassius auratus. *Comparative biochemistry and physiology. Toxicology & pharmacology : CBP* **176-177,** 31–43; 10.1016/j.cbpc.2015.07.006 (2015).

404. Gęgotek, A. & Skrzydlewska, E. Ascorbic acid as antioxidant. *Vitamins and hormones* **121,** 247–270; 10.1016/bs.vh.2022.10.008 (2023).

405. Herrera-Pérez, S., Rueda-Ruzafa, L., Campos-Ríos, A., Fernández-Fernández, D. & Lamas, J. A. Antiarrhythmic calcium channel blocker verapamil inhibits trek currents in sympathetic neurons. *Frontiers in pharmacology* **13,** 997188; 10.3389/fphar.2022.997188 (2022).

406. Juricic, S. *et al.* Molecular and Cellular Mechanisms of Myocardial Ischemia and Reperfusion Injury: A Narrative Review. *Cells* **15**; 10.3390/cells15030265 (2026).

407. Deng, Y. *et al.* Myocardial Ischemia/Reperfusion Injury: Mechanism and Targeted Treatment for Ferroptosis. *Anatolian journal of cardiology* **28,** 133–141; 10.14744/AnatolJCardiol.2023.3606 (2024).

408. Soares, R. O. S., Losada, D. M., Jordani, M. C., Évora, P. & Castro-E-Silva, O. Ischemia/Reperfusion Injury Revisited: An Overview of the Latest Pharmacological Strategies. *International journal of molecular sciences* **20**; 10.3390/ijms20205034 (2019).

409. Trujillo-Rangel, W. Á. *et al.* Therapeutic Targets for Regulating Oxidative Damage Induced by Ischemia-Reperfusion Injury: A Study from a Pharmacological Perspective. *Oxidative medicine and cellular longevity* **2022,** 8624318; 10.1155/2022/8624318 (2022).

410. Wang, R. *et al.* Calenduloside E suppresses calcium overload by promoting the interaction between L-type calcium channels and Bcl2-associated athanogene 3 to alleviate myocardial ischemia/reperfusion injury. *Journal of advanced research* **34,** 173–186; 10.1016/j.jare.2020.10.005 (2021).

411. Cain, B. S. *et al.* Clinical L-type Ca(2+) channel blockade prevents ischemic preconditioning of human myocardium. *Journal of molecular and cellular cardiology* **31,** 2191–2197; 10.1006/jmcc.1999.1039 (1999).

412. Hajnóczky, G., Robb-Gaspers, L. D., Seitz, M. B. & Thomas, A. P. Decoding of cytosolic calcium oscillations in the mitochondria. *Cell* **82,** 415–424; 10.1016/0092-8674(95)90430-1 (1995).

413. Balaban, R. S. The role of Ca(2+) signaling in the coordination of mitochondrial ATP production with cardiac work. *Biochimica et biophysica acta* **1787,** 1334–1341; 10.1016/j.bbabio.2009.05.011 (2009).

414. Isha, I., Choudhary, D. K. & Paul, S. Impact of Calcium Channel Blocker on Mitochondrial Metabolism in Acute Myeloid Leukemia. *Int. J. Res. Publ. Rev.* **5,** 813–822; 10.55248/gengpi.5.0924.2504 (2024).

415. Viola, H. M. & Hool, L. C. Cross-talk between L-type Ca2+ channels and mitochondria. *Clinical and experimental pharmacology & physiology* **37,** 229–235; 10.1111/j.1440-1681.2009.05277.x (2010).

416. Benitah, J.-P., Alvarez, J. L. & Gómez, A. M. L-type Ca(2+) current in ventricular cardiomyocytes. *Journal of molecular and cellular cardiology* **48,** 26–36; 10.1016/j.yjmcc.2009.07.026 (2010).

417. Bhosale, G., Sharpe, J. A., Sundier, S. Y. & Duchen, M. R. Calcium signaling as a mediator of cell energy demand and a trigger to cell death. *Annals of the New York Academy of Sciences* **1350,** 107–116; 10.1111/nyas.12885 (2015).

418. Ohtsuka, M. *et al.* Role of Na+-Ca2+ exchanger in myocardial ischemia/reperfusion injury: evaluation using a heterozygous Na+-Ca2+ exchanger knockout mouse model. *Biochemical and biophysical research communications* **314,** 849–853; 10.1016/j.bbrc.2003.12.165 (2004).

419. Mochizuki, S. & Jiang, C. Na+/Ca++ exchanger and myocardial ischemia/reperfusion. *Japanese heart journal* **39,** 707–714; 10.1536/ihj.39.707 (1998).

420. Fukushima, C. T. *et al.* Reactive Oxygen Species Generation by Reverse Electron Transfer at Mitochondrial Complex I Under Simulated Early Reperfusion Conditions. *bioRxiv : the preprint server for biology*; 10.1101/2023.11.21.568136 (2023).

421. Schieber, M. & Chandel, N. S. ROS function in redox signaling and oxidative stress. *Current biology : CB* **24,** R453-62; 10.1016/j.cub.2014.03.034 (2014).

422. Poljsak, B., Šuput, D. & Milisav, I. Achieving the balance between ROS and antioxidants: when to use the synthetic antioxidants. *Oxidative medicine and cellular longevity* **2013,** 956792; 10.1155/2013/956792 (2013).

423. Talukder, M. A. H., Zweier, J. L. & Periasamy, M. Targeting calcium transport in ischaemic heart disease. *Cardiovascular research* **84,** 345–352; 10.1093/cvr/cvp264 (2009).

424. Bochaton, T. & Ovize, M. Why Did All Treatments of Reperfusion Injury Failed in Humans? In *Coronary Microvascular Obstruction in Acute Myocardial Infarction* (Elsevier2018), pp. 295–307.

425. Alsadder, L. & Hamadah, A. Cardiac Ischaemia-Reperfusion Injury: Pathophysiology, Therapeutic Targets and Future Interventions. *Biomedicines* **13**; 10.3390/biomedicines13092084 (2025).

426. Kolwicz, S. C., Purohit, S. & Tian, R. Cardiac metabolism and its interactions with contraction, growth, and survival of cardiomyocytes. *Circulation research* **113,** 603–616; 10.1161/circresaha.113.302095 (2013).

427. Sala, L. *et al.* MUSCLEMOTION: A Versatile Open Software Tool to Quantify Cardiomyocyte and Cardiac Muscle Contraction In Vitro and In Vivo. *Circulation research* **122,** e5-e16; 10.1161/CIRCRESAHA.117.312067 (2018).

428. Hou, J. *et al.* Hyperoside alleviates myocardial ischemia-reperfusion injury in heart transplantation by promoting mitochondrial fusion via activating the Stat3-Tom70-Opa1 pathway. *Frontiers in pharmacology* **16,** 1566674; 10.3389/fphar.2025.1566674 (2025).

429. Ghasemi, M., Turnbull, T., Sebastian, S. & Kempson, I. The MTT Assay: Utility, Limitations, Pitfalls, and Interpretation in Bulk and Single-Cell Analysis. *International journal of molecular sciences* **22**; 10.3390/ijms222312827 (2021).

430. Habimana, R. *et al.* Endotoxin Pretreatment Mitigates Myocardial Ischemia-Reperfusion Injury Through Preservation of Mitochondrial Respiration: A Combined Assessment of In Vivo, Ex Vivo, and In Vitro Data. *International journal of molecular sciences* **26**; 10.3390/ijms262211162 (2025).

431. Blinova, K. *et al.* International Multisite Study of Human-Induced Pluripotent Stem Cell-Derived Cardiomyocytes for Drug Proarrhythmic Potential Assessment. *Cell reports* **24,** 3582–3592; 10.1016/j.celrep.2018.08.079 (2018).

432. American Chemical Society. Adrenaline. Available at https://www.acs.org/molecule-of-the-week/archive/a/adrenaline.html (2026).

433. Baumgart, D. *et al.* Impact of alpha-adrenergic coronary vasoconstriction on the transmural myocardial blood flow distribution during humoral and neuronal adrenergic activation. *Circulation research* **73,** 869–886; 10.1161/01.RES.73.5.869 (1993).

434. Hennis, K., Piantoni, C., Biel, M., Fenske, S. & Wahl-Schott, C. Pacemaker Channels and the Chronotropic Response in Health and Disease. *Circulation research* **134,** 1348–1378; 10.1161/CIRCRESAHA.123.323250 (2024).

435. Alhayek, S. & Preuss, C. V. *StatPearls. Beta 1 Receptors* (Treasure Island (FL), 2025).

436. Ditchey, R. V., Goto, Y. & Lindenfeld, J. Myocardial oxygen requirements during experimental cardiopulmonary resuscitation. *Cardiovascular research* **26,** 791–797; 10.1093/cvr/26.8.791 (1992).

437. Roden, D. M. *et al.* Cardiovascular pharmacogenomics. *Circulation research* **109,** 807–820; 10.1161/CIRCRESAHA.110.230995 (2011).

438. Naderi, N., Jolfayi, A. G., Azimi, A., Maleki, M. & Kalayinia, S. Pharmacogenomics in cardiac therapy: Personalizing treatment for heart health. *Biomedicine & pharmacotherapy = Biomedecine & pharmacotherapie* **190,** 118392; 10.1016/j.biopha.2025.118392 (2025).

439. Tamargo, J. *et al.* Gender differences in the effects of cardiovascular drugs. *European heart journal. Cardiovascular pharmacotherapy* **3,** 163–182; 10.1093/ehjcvp/pvw042 (2017).

440. Wang, Y., Mi, J., Lu, K., Lu, Y. & Wang, K. Comparison of Gating Properties and Use-Dependent Block of Nav1.5 and Nav1.7 Channels by Anti-Arrhythmics Mexiletine and Lidocaine. *PloS one* **10,** e0128653; 10.1371/journal.pone.0128653 (2015).

441. Docken, S. S., Clancy, C. E. & Lewis, T. J. Rate-dependent effects of lidocaine on cardiac dynamics: Development and analysis of a low-dimensional drug-channel interaction model. *PLoS computational biology* **17,** e1009145; 10.1371/journal.pcbi.1009145 (2021).

442. Fernández-Sada, E. *et al.* Cardiac responses to β-adrenoceptor stimulation is partly dependent on mitochondrial calcium uniporter activity. *British journal of pharmacology* **171,** 4207–4221; 10.1111/bph.12684 (2014).

443. Kelley, E. F., Johnson, B. D. & Snyder, E. M. Beta-2 Adrenergic Receptor Genotype Influences Power Output in Healthy Subjects. *Journal of strength and conditioning research* **31,** 2053–2059; 10.1519/JSC.0000000000001978 (2017).

444. Abbes, H., Soria-Chacartegui, P., Omezzine, A., Abad-Santos, F. & Zubiaur, P. Impact of Genetic Variation in Adrenergic Receptors on β-Blocker Effectiveness and Safety in Cardiovascular Disease Management: A Systematic Review. *Pharmaceuticals (Basel, Switzerland)* **18**; 10.3390/ph18040493 (2025).

445. Wu, H. *et al.* Epigenetic Regulation of Phosphodiesterases 2A and 3A Underlies Compromised β-Adrenergic Signaling in an iPSC Model of Dilated Cardiomyopathy. *Cell stem cell* **17,** 89–100; 10.1016/j.stem.2015.04.020 (2015).

446. Zhu, W. Z. *et al.* Dual modulation of cell survival and cell death by beta(2)-adrenergic signaling in adult mouse cardiac myocytes. *Proceedings of the National Academy of Sciences of the United States of America* **98,** 1607–1612; 10.1073/pnas.98.4.1607 (2001).

447. Zhu, W.-Z. *et al.* Linkage of beta1-adrenergic stimulation to apoptotic heart cell death through protein kinase A-independent activation of Ca2+/calmodulin kinase II. *The Journal of clinical investigation* **111,** 617–625; 10.1172/JCI16326 (2003).

448. Zheng, M., Han, Q.-D. & Xiao, R.-P. Distinct beta-adrenergic receptor subtype signaling in the heart and their pathophysiological relevance. *Sheng li xue bao : [Acta physiologica Sinica]* **56,** 1–15 (2004).

449. Zhao, Y., Xu, J., Gong, J. & Qian, L. L-type calcium channel current up-regulation by chronic stress is associated with increased alpha(1c) subunit expression in rat ventricular myocytes. *Cell stress & chaperones* **14,** 33–41; 10.1007/s12192-008-0052-2 (2009).

450. Papa, A. *et al.* Rad regulation of CaV1.2 channels controls cardiac fight-or-flight response. *Nature cardiovascular research* **1,** 1022–1038; 10.1038/s44161-022-00157-y (2022).

451. Tong, C. & Zhou, B. Cardioprotective strategies in myocardial ischemia-reperfusion injury: Implications for improving clinical translation. *Journal of molecular and cellular cardiology plus* **11,** 100278; 10.1016/j.jmccpl.2024.100278 (2025).

452. Buja, L. M. Pathobiology of Myocardial Ischemia and Reperfusion Injury: Models, Modes, Molecular Mechanisms, Modulation, and Clinical Applications. *Cardiology in review* **31,** 252–264; 10.1097/CRD.0000000000000440 (2023).

453. Sebastião, M. J. *et al.* Bioreactor-based 3D human myocardial ischemia/reperfusion in vitro model: a novel tool to unveil key paracrine factors upon acute myocardial infarction. *Translational research : the journal of laboratory and clinical medicine* **215,** 57–74; 10.1016/j.trsl.2019.09.001 (2020).

454. Welt, F. G. P. *et al.* Reperfusion Injury in Patients With Acute Myocardial Infarction: JACC Scientific Statement. *Journal of the American College of Cardiology* **83,** 2196–2213; 10.1016/j.jacc.2024.02.056 (2024).

455. Li, F., Silva, M. D., Sotak, C. H. & Fisher, M. Temporal evolution of ischemic injury evaluated with diffusion-, perfusion-, and T2-weighted MRI. *Neurology* **54,** 689–696; 10.1212/wnl.54.3.689 (2000).

456. Wang, R., Wang, M., He, S., Sun, G. & Sun, X. Targeting Calcium Homeostasis in Myocardial Ischemia/Reperfusion Injury: An Overview of Regulatory Mechanisms and Therapeutic Reagents. *Frontiers in pharmacology* **11,** 872; 10.3389/fphar.2020.00872 (2020).

457. Cadenas, S. ROS and redox signaling in myocardial ischemia-reperfusion injury and cardioprotection. *Free radical biology & medicine* **117,** 76–89; 10.1016/j.freeradbiomed.2018.01.024 (2018).

458. Hausenloy, D. J., Duchen, M. R. & Yellon, D. M. Inhibiting mitochondrial permeability transition pore opening at reperfusion protects against ischaemia-reperfusion injury. *Cardiovascular research* **60,** 617–625; 10.1016/j.cardiores.2003.09.025 (2003).

459. Moon, C.-M., Kim, Y.-H., Ahn, Y.-K., Jeong, M.-H. & Jeong, G.-W. Metabolic alterations in acute myocardial ischemia-reperfusion injury and necrosis using in vivo hyperpolarized 1-13C pyruvate MR spectroscopy. *Scientific reports* **9,** 18427; 10.1038/s41598-019-54965-7 (2019).

460. Kuhn, D. E., Roy, S., Radtke, J., Khanna, S. & Sen, C. K. Laser microdissection and capture of pure cardiomyocytes and fibroblasts from infarcted heart regions: perceived hyperoxia induces p21 in peri-infarct myocytes. *American journal of physiology. Heart and circulatory physiology* **292,** H1245-53; 10.1152/ajpheart.01069.2006 (2007).

461. Dewald, O. *et al.* Of Mice and Dogs: Species-Specific Differences in the Inflammatory Response Following Myocardial Infarction. *The American journal of pathology* **164,** 665–677; 10.1016/S0002-9440(10)63154-9 (2004).

462. Davidson, S. M. *et al.* Multitarget Strategies to Reduce Myocardial Ischemia/Reperfusion Injury: JACC Review Topic of the Week. *Journal of the American College of Cardiology* **73,** 89–99; 10.1016/j.jacc.2018.09.086 (2019).

463. Baron, V. *et al.* Effects of electro-mechanical uncouplers, hormonal stimulation and pacing rate on the stability and function of cultured rabbit myocardial slices. *Frontiers in bioengineering and biotechnology* **12,** 1363538; 10.3389/fbioe.2024.1363538 (2024).

464. Saito, T. *et al.* Effect of Continuous-Flow Mechanical Circulatory Support on Microvasculature Remodeling in the Failing Heart. *Artificial organs* **43,** 350–362; 10.1111/aor.13348 (2019).

465. Hong, D. *et al.* Detection assays of mitochondrial permeability transition pore: Current status and future prospects. *Acta histochemica* **127,** 152278; 10.1016/j.acthis.2025.152278 (2025).

466. Kumar, R. & Gullapalli, R. R. High Throughput Screening Assessment of Reactive Oxygen Species (ROS) Generation using Dihydroethidium (DHE) Fluorescence Dye. *Journal of visualized experiments : JoVE*; 10.3791/66238 (2024).

467. Mckinney, W. pandas: a Foundational Python Library for Data Analysis and Statistics. *Python High Performance Science Computer* (2011).

468. Virtanen, P. *et al.* SciPy 1.0: fundamental algorithms for scientific computing in Python. *Nature methods* **17,** 261–272; 10.1038/s41592-019-0686-2 (2020).

469. Hunter, J. D. Matplotlib: A 2D Graphics Environment. *Comput. Sci. Eng.* **9,** 90–95; 10.1109/MCSE.2007.55 (2007).

470. Harris, C. R. *et al.* Array programming with NumPy. *Nature* **585,** 357–362; 10.1038/s41586-020-2649-2 (2020).

8. Curriculum Vitae

Eric Pohl

Academic Positions

04/2023 – Present	Research Associate Institute for Functional Interfaces (IFG) Karlsruhe Institute of Technology (KIT), Karlsruhe, Germany
03/2024 – Present	Member of the Excellence Cluster 3D Matter Made to Order (3DMM2O) Karlsruhe Institute of Technology (KIT) / Heidelberg University

Education

11/2023 – Present	PhD Candidate in Chemistry Karlsruhe Institute of Technology (KIT), Germany Graduate Program: HEiKA Graduate School on Functional Materials (3DMM2O) Supervisor: Prof. Dr. Ute Schepers Dissertation Title: *Development of a Three-Dimensional iPSC-Derived Cardiac Spheroid Model of Ischemia–Reperfusion Injury: From Classical Tissue Engineering to Closed-Loop Bayesian Optimized Engineering for Genotype-Dependent Drug Response Profiling* Official acceptance as doctoral candidate: **14 November 2023**
10/2020 – 09/2022	Master of Science (M.Sc.) Biology Karlsruhe Institute of Technology (KIT), Germany Master's Thesis: *Organ-on-a-Chip Disease Model of the Outer Blood–Retinal Barrier*

10/2017 – 09/2020	Bachelor of Science (B.Sc.) Biology Karlsruhe Institute of Technology (KIT), Germany Bachelor's Thesis: *Analysis of the Transformation Efficiency and T-DNA Integration in Arabidopsis thaliana*

Additional Qualifications

05/2024 – 06/2025	MBA Fundamentals Program HECTOR School of Engineering and Management, Karlsruhe Institute of Technology

Publications

No.	Authors	Title	Journal	Year	DOI
1	Yousefshahi, S.; **Pohl, E.**; Sehn, T.; Jungbluth, M.; *et al.*	3D-Printed Hydrogels from Recycled Cellulose for Biomedical Applications	*ChemSusChem*	2025	10.1002/cssc.202501734
2	Qiu, X.; **Pohl, E.**; Jung, A.; Cai, Q.; *et al.*	Modulating the Photolysis of Aryl Azides in a Supramolecular Host to Develop Photoactivatable Fluorophores	*Chem. Commun.*	2024	10.1039/D4CC03907F
3	Qiu, X.; Cai, Q.; **Pohl, E.**; Jung, A.; *et al.*	A Simple Method to Modulate the Selectivity of Aryl Azide Photolysis Using Cucurbit[8]uril	*Chem. Commun.*	2024	10.1039/D4CC04209C
4	Qiu, X.; **Pohl, E.**; Jung, A.; Cai, Q.; *et al.*	Modulating and Accelerating Photolysis of Aryl Azides in a Supramolecular Host	*Adv. Funct. Mater.*	2024	10.1002/adfm.202401938
5	Saghafi, M. K.; Vasantham, S. K.; Hussain, N.; *et al.*; **Pohl, E.**	Printed Electronic Devices and Systems for Interfacing with Single Cells up to Organoids	*Adv. Funct. Mater.*	2023	10.1002/adfm.202308613